



COMOTI
ROMANIAN RESEARCH &
DEVELOPMENT INSTITUTE FOR
GAS TURBINES

TURBO

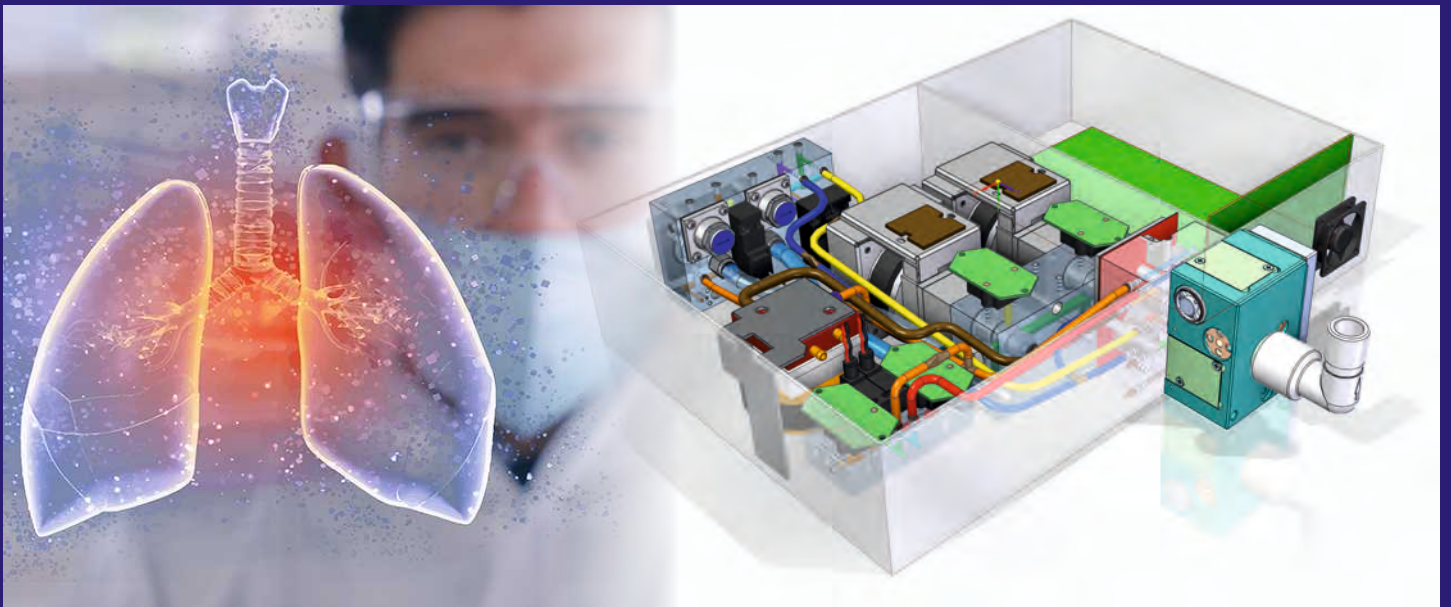
Scientific Journal

vol. VII (2020), no. 1

Covid-19

We care about those around us!

Romanian PULMONARY VENTILATOR Prototype



COMOTI
ROMANIAN RESEARCH &
DEVELOPMENT INSTITUTE FOR
GAS TURBINES



Cum o nouă „Coroană” ne-a schimbat viața (I)

Să vorbim despre noutate astăzi a devenit pasionant pentru toți. Sunt noi primele gesturi ale dimineții și e nou felul în care ne gândim ținuta pentru ieșirea din casă cu tot ritualul de protecție și grijă. E nou modul de lucru și modul de relaționare cotidiană și e inedit sfârșitul de zi când un ritual nou de igienă ne stăpânește. Întrebările ce ne bântuie nopțile fac și ele parte, mai mult sau mai puțin din sfera condițiilor noi de viață și de raportare la social.

Ca și cum am fi văzut un accident de mașină la ralanti, cea mai mare parte a aspectelor cotidiene au tranzitat în trecut, făcând loc unei stări de lucruri noi și de neimaginat până de curând.

Coronavirusul, ca o gheară a încleștat deja întreaga lume: granițe închise, state întregi în carantină. Nimeni nu știe când se va sfârși pandemia dar toți suntem de acord: post-pandemie lumea pe care o știam se va schimba dramatic, așa cum în secolul trecut s-a întâmplat după războaiele mondiale, după revoluții și după căderea Zidului Berlinului.

Wladimir Kaminer, scriitor berlinez de succes, născut la Moscova - în 2017 a fost invitat la Cluj la Centrul Cultural German - citește în această perioadă pe internet dintr-o carte „Germania aplaudă de la balcoane” pe care a început să o scrie la începutul pandemiei:

„Acești oameni nu sunt acolo. Nu știu dacă mă ascultă sau nu. Poate că răsucesc țigări în acest moment, sau gătesc cina sau se uită la hochei la televizor. Deși ce hochei ... Deja nu mai există nimic! Sper că nu va trebui să termin de scris această carte, că aceste două capitole pe care le voi citi, le voi pune undeva pe raft. Și voi uita un vis teribil.”

Acum, fără a părăsi locuința participăm și ne bucurăm de lecturi științifice ori literare și de reprezentării live pe întreg globul. Fără a părăsi biroul sau locuința stabilim acorduri și propuneri de colaborare. Cel mai important însă, gândim proiecte de cercetare comune, dar fără emoția întâlnirilor directe, mutate acum în on-line, căci este un moment de reconsiderare a direcțiilor și perspectivelor de interacțiune a științei cu societatea pentru dezvoltarea inovativă, în condițiile cu totul și cu totul noi ale aspectelor medicale, geopolitice și economice.

Strategii politici vorbesc despre perimarea ideilor de globalizare și revenirea la statele naționale, despre dominația tot mai evidentă a Chinei și despre probabilitatea apariției de țări falimentare. La Riyadh era plănuț summitul G20 în toamna acestui an. Străngerile călduroase de mână, fotografia de grup ori reglementarea bugetelor prin negociere față în față, astăzi nu mai sunt posibile. Pe 26 martie 2020 membrii G20 au organizat un summit de urgență prin videoconferință, menținând distanțarea socială pe fondul noii crize, pentru a planifica un răspuns global împotriva pandemiei.

La Bruxelles Parlamentul European este aproape pustiu, cei 750 de parlamentari au votat proiectele de lege de acasă. A apărut întrebarea oportunității păstrării uriașului aparat parlamentar european în forma actuală știut fiind că se va recurge în continuare la ședințe de lucru online, cu posibilitatea votului de la distanță. Chiar dacă Europa a sărbătorit a 25-a aniversare a intrării în vigoare a Schengen granițele nu mai sunt cele stabilite prin acest acord pentru că astăzi Europa funcționează cu totul în afara regulilor Schengen.

Distanțarea socială devine treptat obișnuință, iar relațiile tradiționale sunt deja neprețuite prin plasarea lor în trecut. Călătoriile aeriene și nu numai, se află într-un uriaș impas; din cauza reducerii traficului activitatea companiilor de transport va scădea semnificativ în întreaga lume. Cât vor rezista hub-urile aeriene? Cererea mică de combustibil va menține prețul petrolului la un nivel scăzut, fapt ce va atrage noi și nebănuite aspecte economice. Probabil turismul de masă va reveni timid, cu schimbări semnificative, asemenea sectoarelor divertismentului și industriei educaționale.

Într-un articol pentru Financial Times, Yuval Noah Harari - istoric israelian, autorul bestseller-urilor Sapiens. Scurtă istorie a omenirii, Homo deus. Scurtă istorie a viitorului și 21 de lecții pentru secolul XXI, invitat la Brand Minds București 2019 - prezice că lumea va supraviețui după războiul cu COVID-19, dar va fi complet diferită.

Cum o nouă „Coroană” ne-a schimbat viața (2)

„Cred că istoricii din viitor vor privi asta ca pe un moment de cotitură din istoria secolului 21. Dar încotro se vor îndrepta lucrurile - aceasta depinde de deciziile noastre.”

O astfel de decizie majoră ar putea fi aceea care să transforme în acest moment interdisciplinaritatea cercetărilor științifice în cel mai puternic factor de dezvoltare inovativă. Și cum la nivel global se caută soluții și extrem de necesare direcții noi, începând cu așteptata imunizare a populației și până la maximizarea impactului cercetării în tot ceea ce reprezintă noile priorități dictate de pandemie, este de așteptat o cooperare optimă și eficientă pe fondul acestei inedite și sobre provocări societale.

Ce este important în această criză este reconsiderarea a ceea ce admitem a fi evident, prin adaptare și luptă continuă. În prezent incertitudinile sunt majore, iar în cercetare, în mod firesc, fiecare ajunge la o altă concluzie. Cum facem față? Cum răspundem? Cum ne implicăm? Cum identificăm adevărata necesitate în criză?

Expresia „criza nu poate fi prevăzută pentru că ceea ce este prevăzut nu va fi o criză” se dovedește a fi foarte adevărată, fostul CFO Lufthansa, Simone Menne, spune că o astfel de situație nu ar fi putut fi prevăzută - interviu pentru Handelsblatt. Ea crede că problemele pentru companii nu vor sta numai în întreruperea producției, ci și în contextul incert: nimeni nu știe ce piață se va prăbuși prima, cât de puternic și pentru cât timp.

Cu toate aspectele noi care afectează întregul mapamond prin impactul asupra piețelor financiare, afacerilor, societăților, pandemia Covid-19 a devenit o mare surpriză. Știam că economia lumii trăiește în conformitate cu propriile legi, asemenea vieții biologice, iar unicul semn de întrebare semnificativ în ultimii ani a fost asupra încălzirii globale. Dar pentru OMS, pentru sistemele naționale de sănătate, pentru guverne, pandemia nu ar fi trebuit să vină totuși ca o surpriză știut fiind că specialiști competenți au avertizat în mod repetat despre posibilitatea unei pandemii virale.

N-ar fi trebuit, dar s-a întâmplat! Așadar avem un tip de nouitate perfidă, căci nimeni nu și-a imaginat o carantină mondială în zilele noastre. Știam cu toții că s-a recurs la carantină încă din perioada Morții Neagre în secolul XIV. Dar carantina reprezintă și astăzi o jertfă sacră, pentru înlănzirea unui demon necruțător. Teama de contaminare se răsfrânge masiv asupra aspectului economic: prin scăderea activității sociale se ajunge la scăderea consumului parțial, iar starea de spirit depresivă duce la scăderea consumului total la nivel mondial.

Încetinirea semnificativă a oricăror modificări legislative, de implementare, structurale, toate datorate anulării sau amânării evenimentelor, drept consecință a inhibării stării de lucruri, reprezintă o nouitate căreia trebuie să-i facem față. Acest lucru înseamnă că litigiile, emiterea de permise și licențe, aprobarea proiectelor, actualizarea acordurilor vor încetini, se vor amâna ori se vor opri.

Există și analiști optimiști! Epidemia se va încheia fără afectarea afacerilor imobiliare, fabricilor, uzinelor ori transporturilor, iar natura nu va avea de suferit, căci tot ce înseamnă exploatare se va relansa cu un impact mai curat, care să stimuleze consumul și investițiile. Stimulente pentru dezvoltare vor fi acordate asistenței medicale, industriei farmaceutice și cercetărilor imunologice. Lumea va deveni mult mai on-line, mai multe persoane vor lucra de acasă, se vor face cumpărături, tranzacții și negocieri pe internet. Va fi un excelent moment de preluare a serviciilor off-line de către on-line, care și-a consolidat poziția în timpul carantinei.

La un an sau doi după încheierea epidemiei, va urma o perioadă de creștere pe termen lung a prețurilor acțiunilor și o perioadă de stagnare a piețelor datoriilor și de creștere economică. Să fie această pandemie noua graniță a epocilor?

Severa criză a existenței noastre ar putea fi punctul de plecare al solidarității ce se cere, într-un târziu, echilibrată. Și cum perspectiva vidului nu este încurajatoare, o nouitate majoră ar fi aceea a modificării comportamentul uman în situație de criză, devenind pe termen nedefinit, altruist.

Autor: ec. Elena Banea
Iunie 2020

The way a new “Corona” has changed our lives (1)

Talking about innovation today has become an exciting preoccupation for us all. There is novelty in our first morning activities, as well as in the way we conceive our outdoors outfit, with all the protection and safety routine associated to it. Our daily working approach and socializing habits are entirely changed and so is the end of the day, which includes a new hygiene routine for all of us. The questions that keep haunting us during the night have to do, more or less, with the new living conditions and social reference as well.

As if we were witnesses to a car accident taking place at low speed, most daily aspects are a matter of the past, leaving place to a novel state of affairs, unimaginable to us not very long ago.

The corona virus has already gripped the whole world like a claw: closed borders and entire states placed under quarantine. Nobody knows when the pandemic is going to end, but we all agree to one certain fact: the world we were used to will bring over dramatic changes in the post pandemic era, as it happened after the World Wars, the revolutions or after the fall of the Berlin Wall a century ago.

These days, Wladimir Kaminer, a successful writer from Berlin, but originally from Moscow, who was invited to Cluj at the German Cultural Centre in 1917, is lecturing on the internet from his book called *”Germany Is Applauding from the Balconies”* (Deutschland raucht auf dem Balkon), which he started writing at the beginning of this pandemic:

“These people are not there. I am not certain that they are listening to me or not. They may be rolling cigarettes right now or making dinner or watching hockey on TV. Though speaking about hockey ... There is nothing left there already! I hope I shall not have to finish this book, and that I shall put away, on a shelf somewhere, these two chapters I’m going to read. And that I shall forget this awful dream.”

These days, without leaving our homes, we are taking part to and enjoying on-line scientific or literary lectures or live shows from all over the world. Without leaving our office or personal precincts, we make deals and settle proposals of collaboration. But, most important of all, we are conceiving common research projects, which lack the excitement of direct meetings, and that are being transferred on-line, as this is a time of reconsideration of the trends and perspectives of interaction of science and society, towards innovative development in these particularly novel circumstances, which involve medical, geopolitical and economical aspects.

Political strategists are talking about the ideas concerning globalization as becoming obsolete, and about the reconsideration of the concept of national states, but also about the more and more evident domination of China and of the possible financial collapse of certain states. This fall, the G20 Summit was supposed to take place in Riyadh. Warm handshakes, group photographs or budget settlement during face-to-face negotiations are no longer possible these days. On March 26, the G20 members organized an urgent video conference summit, thus keeping social distancing imposed by this new crisis, in order to deliver a global response against this pandemic.

The European Parliament in Brussels is almost empty, the 750 parliamentary members have voted the project bills from their homes. Thus, a new issue has emerged, that is the necessity of keeping in use this massive European parliamentary machinery as such, since it is sure that working meetings are due to be taking place on-line for some time onwards, and with the instrument of on-line voting at hand. Even if Europe has celebrated the 25th anniversary of the Schengen space coming into force, the borders are no longer the same, as stipulated by this treaty, due to the fact that Europe is functioning today entirely beyond the Schengen rules.

Social distancing is slowly becoming a routine and traditional relationships have already become precious less, due to their sliding into the past. Air travelling, and not only, is in a deadlock, and the activity of the transportation companies is going to turn significantly low around the globe, due to traffic reduction. How long are the air hubs going to resist? Low fuel demand is going to keep oil prices down, which in its turn will trigger new and unforeseen economic problems. Mass tourism will probably timidly return to its old pace eventually, with significant changes though, and so will the entertainment and educational industry sectors.

In an article for The Financial Times, Yuval Noah Harari - Jewish historian and author of the bestsellers *Sapiens. A Brief History of Humankind*, *Homo Deus: A Brief History of Tomorrow* and *21 Lessons for the 21st Century*, when a guest at Brand Minds in Bucharest 2019 - predicted that humankind will survive the COVID-19 war, but that it would suffer massive changes.

The way a new “Corona” has changed our lives (2)

” I believe that future historians will see this as a turning point in the history of the 21st century. Wherever things may get to, this is a matter entirely depending on our decisions.”

One such major decision could imply the turning of the present interdisciplinary scientific research into the most powerful factor of innovative development. And since there is a global preoccupation for searching both solutions and extremely necessary novel trends, starting with the much expected immunization of the population and going as far as maximizing the impact of research on each and every aspect of what represents the new priorities dictated by the pandemic, a most favorable and efficient cooperation is expected to occur on the background of this new and serious social challenge. An important aspect, along this crisis, is the reconsideration of the things that we currently admit to be obvious, through sustained adaptation and endeavor. Today, incertitude of all kinds is at its highest peak, and obviously, as far as the research activity is concerned, everyone involved is identifying distinct solutions. How are we coping with this? What is our response going to be? How are we getting involved into this? How are we identifying the true need during this crisis?

The affirmation “crisis cannot be predicted since what it is predicted is not going to be a crisis anymore” proves to be entirely true, the former Lufthansa CFO, Simone Menne, says in an interview for Handelsblatt that such a situation could not have been predicted”. She believes that, among other problems that the companies will have to deal with, such as production cutting, will also include the uncertain circumstances: nobody knows which market is going to fall first, how serious that fall is going to be and for how long.

The COVID-19 pandemic has come as a major surprise, with all the new aspects that affect humankind on a global scale, due to its impact on the financial markets, businesses and societies. We all have been aware of the fact that the world market functions according to its own laws, similar to biological life, and the only significant uncertainty, during the recent years, has been that related to global warmth. But for WHO, for the national health systems and for governments, the pandemic should not have come, though, as a surprise, as it is well known that competent specialists have repeatedly warned about the possible occurrence of a viral pandemic.

It shouldn't have come as a surprise, yet it did! Therefore, we are facing a certain type of perfidious change, as no one has conceived the whole world being put into quarantine these days. We were aware that quarantine had been the solution adopted ever since the Black Death during the 14th century. But, even today, quarantine represents a sacred sacrifice made to team a fierce beast. The fear of contamination has a direct impact on the economic aspect: a lower social activity is leading to a partially lower consumption, while the depressive mood is leading to a lower global consumption.

The significant slowing down of the legislative system activity, in terms of modifications, implementation and structurally speaking, all due to the cancelling or postponement of events, as a direct consequence of the restricted state of facts, represents a change that we all have to overcome. This means that litigations, permit and license issuing, project approval and resettlement of deals are not going to take place at the normal rate, they are going to be postponed or cancelled.

There are also optimistic analysts as well! The pandemic will end without any damage to the real estate businesses, factories, plants or transportation, and nature will not be affected, since any exploitation will be launched anew with a clean impact on it, besides it will stimulate consumption and investments. Various stimulants for development will be made available to the medical assistance sector, the pharmaceutical industry and to the immunological research. Mankind will be more present on-line, more people will be home working, shopping, transactions and negotiations will all take place on the internet. This is going to be an excellent opportunity for the off-line services to be overtaken by the on-line that has consolidated its position during the quarantine.

A year or two after the pandemic is over, a long term raises in share hold prices, a stagnation of the debt markets and of economic growth. Could this pandemic mark the new frontier between distinct époques?

This severe existential crisis might be the starting point of the solidarity that, more than ever, needs to be reached in balance. And, since the perspective of the void is not an encouraging one, a major change during such times of crisis would be the one taking place in human conduct, that is it becoming altruistic indefinitely.

Author: ec. Elena Banea

June 2020

EDITORIAL BOARD



COMOTI
ROMANIAN RESEARCH &
DEVELOPMENT INSTITUTE FOR
GAS TURBINES

2300 Siles Avenue, 061126 Bucharest 6, ROMANIA-PO 76, POB 174
Phone: +40 0214340198, +40 0214340240; Fax: +40 0214340241
E-mail: comoti@comoti.ro, www.comoti.ro
Nr. Of. Com. Reg. 340/4880/1997, CF: RO445238



PRESIDENT:

Dr. Eng. Valentin SILIVESTRU

VICE-PRESIDENT:

Dr. Eng. Cristian CĂRLĂNESCU

Dr. Eng. Romulus PETCU

SECRETARY:

Dr. Eng. Jeni VILAG

MEMBERS:

Prof. Dr. Virgil STANCIU

Prof. Dr. Corneliu BERBENTE

Prof. Dr. Dan ROBESCU

Prof. Dr. Sterian DĂNĂILĂ

Dr. Eng. Gheorghe MATACHE

Dr. Eng. Ene BARBU

Dr. Eng. Gheorghe FETEA

Dr. Eng. Ionuț PORUMBEL

Dr. Eng. Mircea Dan IONESCU

Dr. Eng. Lucia Raluca MAIER

Dr. Eng. Mihaiella CREȚU

Dr. Eng. Cleopatra CUCIUMIȚA

Dr. Eng. Sorin GABROVEANU

EDITOR IN CHIEF:

Prof. Dr. Lăcrămioara ROBESCU

EDITORS:

Eng. Mihaela Raluca CONDRUZ

Ec. Elena BANEA

ADMINISTRATIVE

SECRETARY:

Eng. Mihaela GRIGORESCU

TRANSLATION CHECKING:

Dr. Eng. Paul RĂDULESCU

Laura COMĂNESCU

Oana HRIȚCU

GRAPHICS:

Victor BEȘLEAGĂ

CONTENTS

GAS TURBINE ENGINES AUTOMATICS

Experimental Identification for Microturbine Engine Components and Electronics Dynamics

Taranu A.A., Ciobanu R., Stanciuc R.E..... pp 7

Optimization of the Electronic Control System for the ST40M Gas Turbine

Niculescu F., Vasile M.L., Savescu A., Codoban R...pp.24

GAS TURBINE ENGINES AND AERONAUTICAL APPLICATIONS

Investigation Methodology for Turbine Cavities Flow Fields

Nicoara R., Vilag V., Prisecariu E., Suciu C.,
Dombrovski M., Dobromirescu C..... pp 34

Spiral Plate Heat Exchanger with High Heat Transfer Coefficient for Microturbine

Tipa T., Totu A.G., Radu A., Dombrovski M., Olariu C.,
S. Voicu..... pp 44

Flowfield Analysis of Different Test Cells Configurations

Gherman B., Ciobotaru D., Dombrovski M.pp 54

MATERIALS AND TECHNOLOGIES (1)

Experimental Investigation for WEDM Influence on 17-4PH Surface Roughness Based on Taguchi Method

Condurachi F., Zamfir L.C., Zaharia C..... pp. 60

Isothermal Oxidation Behavior and Thermal Shock Resistance of Thermal Barrier Coatings

Badea T.A., Paraschiv A., Condruz M.R., Frigioescu T.F.,
Zamfir L.C., Ionica I pp 65

INFO



COMOTI
ROMANIAN RESEARCH &
DEVELOPMENT INSTITUTE FOR
GAS TURBINES

2300 Siles-Mediu Ave., 661126 Bucharest 6, ROMANIA-PO 76, POB 174
Phone: +40 021/4340198, +40 021/4340240; Fax: +40 021/4340241
E-mail: comoti@comoti.ro, www.comoti.ro
No. Of. Com. Reg. 340/4880/1997, CF: RO445238

TURBO
Scientific Journal

More information regarding the scientific journal can be found at:
http://www.comoti.ro/ro/jurnalul_scientific_turbo.html
turbojournal@comoti.ro
jeni.vilag@comoti.ro

ISSN: 2559-608X
ISSN-L: 1454-2897

Scientific Journal **TURBO** is included in:

-**ICI World of Journals:**
ICV 2018: 63,88
<https://journals.indexcopernicus.com/search/details?id=48512>

-**Directory of Open Access Scholarly Resources (ROAD)**
<https://portal.issn.org/resource/ISSN/2559-608X#>

-**Directory of Research Journals Indexing (DRJI):**
<http://olddrji.lbp.world/JournalProfile.aspx?jid=2559-608X>

CONTENTS

MATERIALS AND TECHNOLOGIES (2)

System and Method Design for TBC Degradation Detection

Frigioescu T.F., Condruz M.R., Paraschiv A., Badea T.A., Zamfir L.C., Ionica I. pp 73

Increased Productivity of Welded Joints by Using the MIG/MAG Process with SpinArc

Zamfir L.C., Condurachi F., Campurean A.H. pp 79

Replacement of Conventional Couplings with 3D Printed Couplings

Stănescu T., Stan N.D., Badea G., Vasile E., Borcea R., Ilies A., Șervescu H. pp 87

Designing a High Efficiency Additively Manufactured Heat Exchanger

Tipa T., Totu A.G., Radu A., Dombrovski M., Olariu C., S. Voicu pp 92

Finite Element Analysis on Temperature Distribution of Thermal Barrier Coatings

Frigioescu T.F., Paraschiv A., Condruz M.R., Badea T.A., Zamfir L.C., Ionica I. pp 101

MACHINE ELEMENTS

Test Bench with 500 Nm Hydraulic Brake for Simulating Nonlinear Loads on Electric Actuators

Ciobanu R., Tomescu S., Petrescu V., Ungureanu A., Taranu A., Vasile E., Stanciuc R.E. pp. 108

COMPRESSORS BLOWERS

Stress Reduction Methods for Centrifugal Impellers

Totu A.G., Crunteanu D.E., Dobre A.C., Sima M... pp. 121

June 2020

EXPERIMENTAL IDENTIFICATION FOR MICROTURBINE ENGINE COMPONENTS AND ELECTRONICS DYNAMICS

Alexandra-Andreea TARANU^{1,2}, Razvan CIOBANU¹, Ramona Elena STANCIUC¹

ABSTRACT: This article presents dynamic system identification and analysis thru means of experimental methods for microturbine engine mechanical, hydraulic and electronic components which are designated for remotely piloted aircraft systems. Dynamic systems are used to mathematically describe the component's behaviour in terms of state space system or transfer functions outputs in relation with system inputs. The scope of this study was to model all microturbine auxiliary components in order to design and develop an electronic controller. All components were experimentally tested and compared with a reference in order to map input vs. output function both linear and nonlinear. System analysis theory was used in order to create a global deterministic state space system. All components were mapped as dynamic system blocks in order to design closed loop controllers. The control loops were analysed for stability and robustness in terms of step and Dirac impulse response for fine tuning.

KEYWORDS: System Dynamics, Microturbine, Controller, System Analysis, Experimental Identification, Curve Fitting, Mathematical Dynamic Model

NOMENCLATURE

AI – Artificial Intelligence	Mf – Modulation frequency
CC – Centrifugal Clutch	NCC – Centrifugal Clutch Input Speed
DC – Direct Current	NGT - Gas Turbine Rotational Speed
ECU – Engine Control Unit	NSG – Starter Generator Rotational Speed
EGT – Exhaust Gas Temperature	OAT – Outside Air Temperature
EHCV – Electro Hydraulic Check Valve	P60 – Commercial Name of the Engine
EMF – Electromotive Force	PHT2 – Commercial Name of the Power Plant
FI – Fuel Injector	Q - Flow
FP – Fuel Pump	R – Resistance
GP – Glow Plug	RPAS – Remotely Piloted Aircraft Systems
GPT – Glow Plug Temperature	rpm – Revolutions per Minute
HIL – Hardware In-the Loop	SG – Starter Generator
$H_{(s)}^{SG}$ – Starter Generator Transfer Function	Simulink – Design Software Developed by Mathworks
I – Current	s – Laplace Variable
J – Inertia	T - Torque
JetCat – Producer of the Power Plant	TF – Transfer Function
K_b – Back EMF constant	U – Voltage
K_t – Torque coefficient	u_{res} – Resolution Standard Uncertainty
L – Inductance	
LiPO – Lithium Polymer	

¹ Romanian Research and Development Institute for Gas Turbines COMOTI, Bucharest, Romania

² University Politehnica of Bucharest, Romania

1. INTRODUCTION

This article presents the methods used to determine the dynamic system via means of experimental identification in order to simulate and design a mathematical model for the PHT2 microturbine engine and its auxiliary components. This was done in order to design and develop an electronic control unit for the engine.

The PHT2 power plant from Jet CAT is based on a centrifugal compressor, single spool, turbine engine rated at 2.7kW that has three output shafts, main rotor, tail rotor and an auxiliary drive train. The PHT2 power plant is designed for unmanned rotor type aircraft. The PHT2 power plant is controlled and operated via means of auxiliary equipment such as fuel pump, electrohydraulic check valves, fuel injector, glow plug, starter-generator and utilises a control loop based on turbine rotational speed and exhaust gas temperature. All drive trains in the PHT2 system are based on timing belts and pulleys and a crown bevel gears for final output shafts.

The objective of the present study was to determine the dynamic system for the components in order to future design and develop an innovative ECU that uses intelligent neural algorithms for control loops.

All components were experimentally tested and compared with a reference in order to map input vs. output both linear and nonlinear functions. System analysis theory was used in order to create a global deterministic state space system. All components were mapped as dynamic system blocks in order to design closed loop controllers which were then analyzed for stability and robustness in terms of step and Dirac impulse response for fine tuning.

The determined transfer functions and other component dynamics where modeled as function blocks and/or control loops in order to test for stability, controllability and robustness of the global dynamic system of the PHT2 power plant. The following study will present the methods and systems used for experimental identification and also illustrate test results and performances.

2. EXPERIMENTAL DYNAMICS SYSTEM IDENTIFICATION

This article is based on the study of developing test systems and architectures in order to identify electromechanical, electrical, hydraulic and mechanical components dynamics. As a state-of-the-art in the field of testing and identifying system dynamics for such types of components we looked at National Instruments [1] which are currently one of the leaders in the field of experimental hardware testing, simulation and HIL for the aerospace and defence industries. National Instruments utilises test architectures that are adaptable in means of signal generation and simulation for HIL type experimental identifications for hardware dynamics. They are also utilising MathWorks's Simulink software for its versatility and highly capable system simulation on target hardware, either desktop computers, clusters or other external systems such as its Compact RIO (product name) range programmable logic controllers.

The PHT2 power plant (fig. 1) is designed around a P60 Jet CAT turbine engine modified for fuel injector start-up and mechanical drive train.

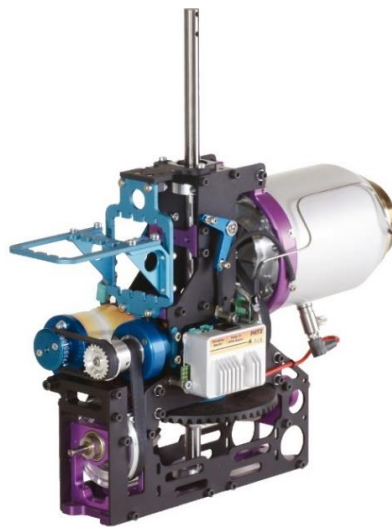


Fig. 1 PHT2 power plant for rotor aircraft type RPAS with modified P60 turbine engine [2]

For system dynamics identification we first had to determine the position, role and dependencies of each auxiliary equipment. This was done as a form of a general block diagram (fig. 2) and was used to map the final dynamic system block diagrams designed in Simulink software. The block “TRU CVD” stands for transformer rectifier unit whit constant voltage drive [5][6].

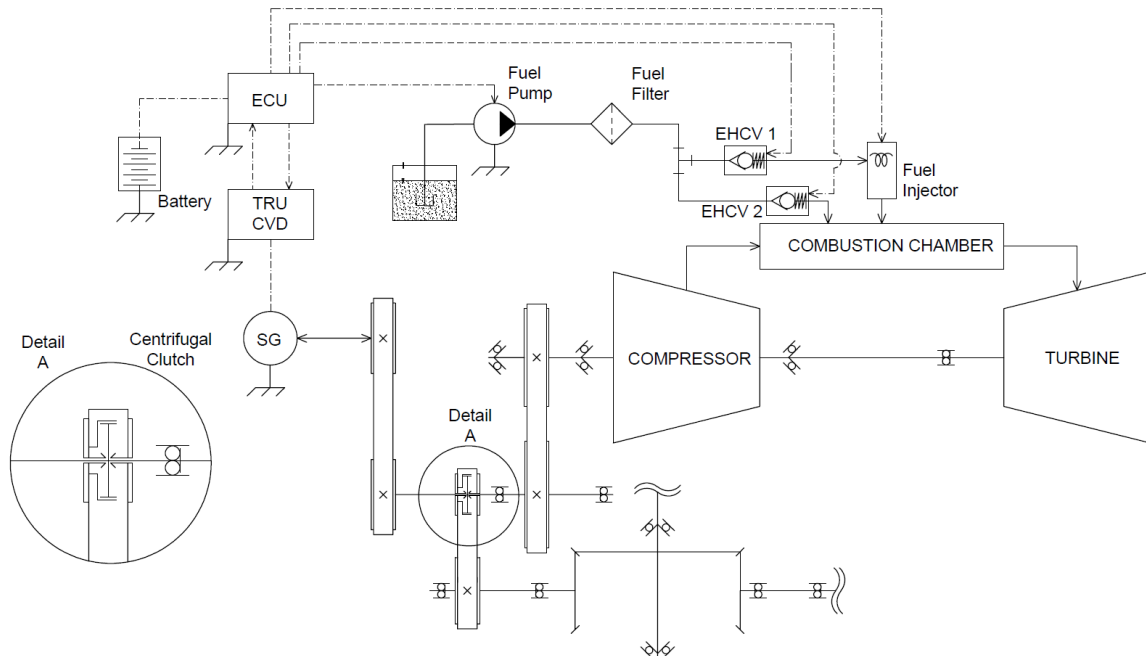


Fig. 2 PHT2 power plant block diagram

After the identification of the components was carried out, we determined all drive train ratios and dependencies. From experimental engine testing we concluded that the CC of the PHT2 system will fully engage only after 63.000 rpm. Thus, all drive systems after the CC will be at 0 rpm. The CC (fig.3a) of the PHT2 power plant has three aluminium shoes which are deformed under centrifugal forces and a drum constructed out of anodised 6065 aluminium. The CC was modelled using a linear dynamic dependency with the engaging delay modelled as a TF in a kinematic response block from Simulink software (fig. 3b).

The drive train (fig. 4 – top) of the PHT2 system is used to transfer power in duplex mode from the SG to the turbine and from the turbine to other output shafts. Drive ratios where determined by means of pulley tooth ratios and modelled as linear multiplier blocks (fig. 4 - bottom). PHT2 drive ratios for different stages are presented in table 1.



Fig. 3a Centrifugal Clutch mechanism

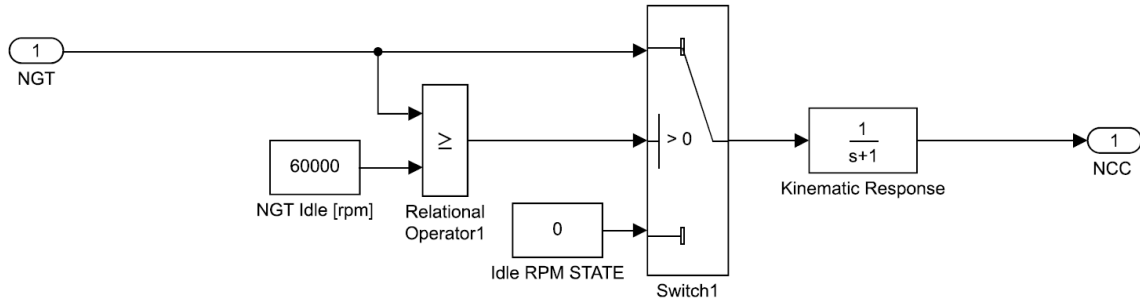


Fig. 3b Clutch system model (bottom).

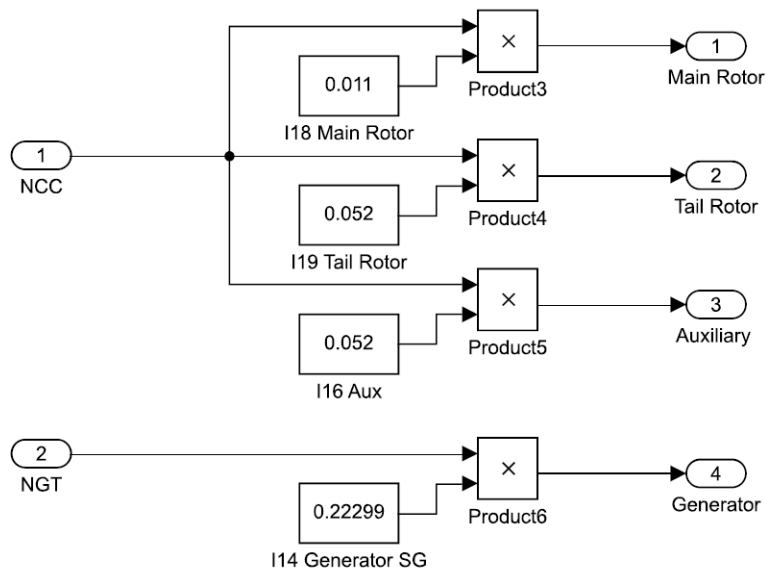


Fig. 4 PHT2 Drive train (top) and system model (bottom)

Table 1. Drive train transmission ratios

Gear	Ration	Output
I18	0.011	Main Rotor
I19	0.052	Tail Rotor
I16	0.052	Auxiliary
I14	0.22299	Generator
I41	4.484	Starter

The SG (fig. 5) is used to provide rotational speed at engine start-up and to generate electrical power beyond idle rpm in order to recharge the on-board LiPO battery.



Fig. 5 Starter Generator

For experimental determination of the transfer function of the SG we used a rotary speed encoder to measure rpm response in relation with supply voltage and current. The experimental testing carried out is illustrated in figure 6 and the experimental configuration block diagram in figure 7.



Fig. 6 Starter Generator testing.

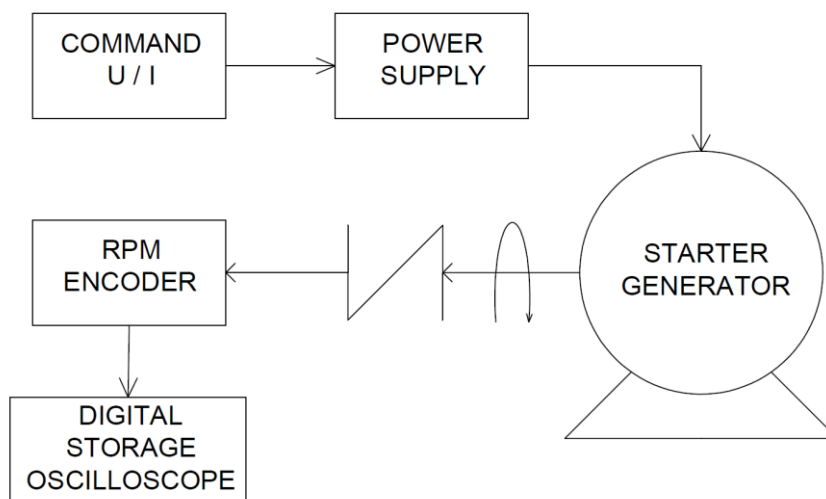


Fig. 7 Starter Generator experimental setup

After testing and identifying the SG's electrical and mechanical characteristics we could plot its characteristic response curve (fig. 8 a & b)

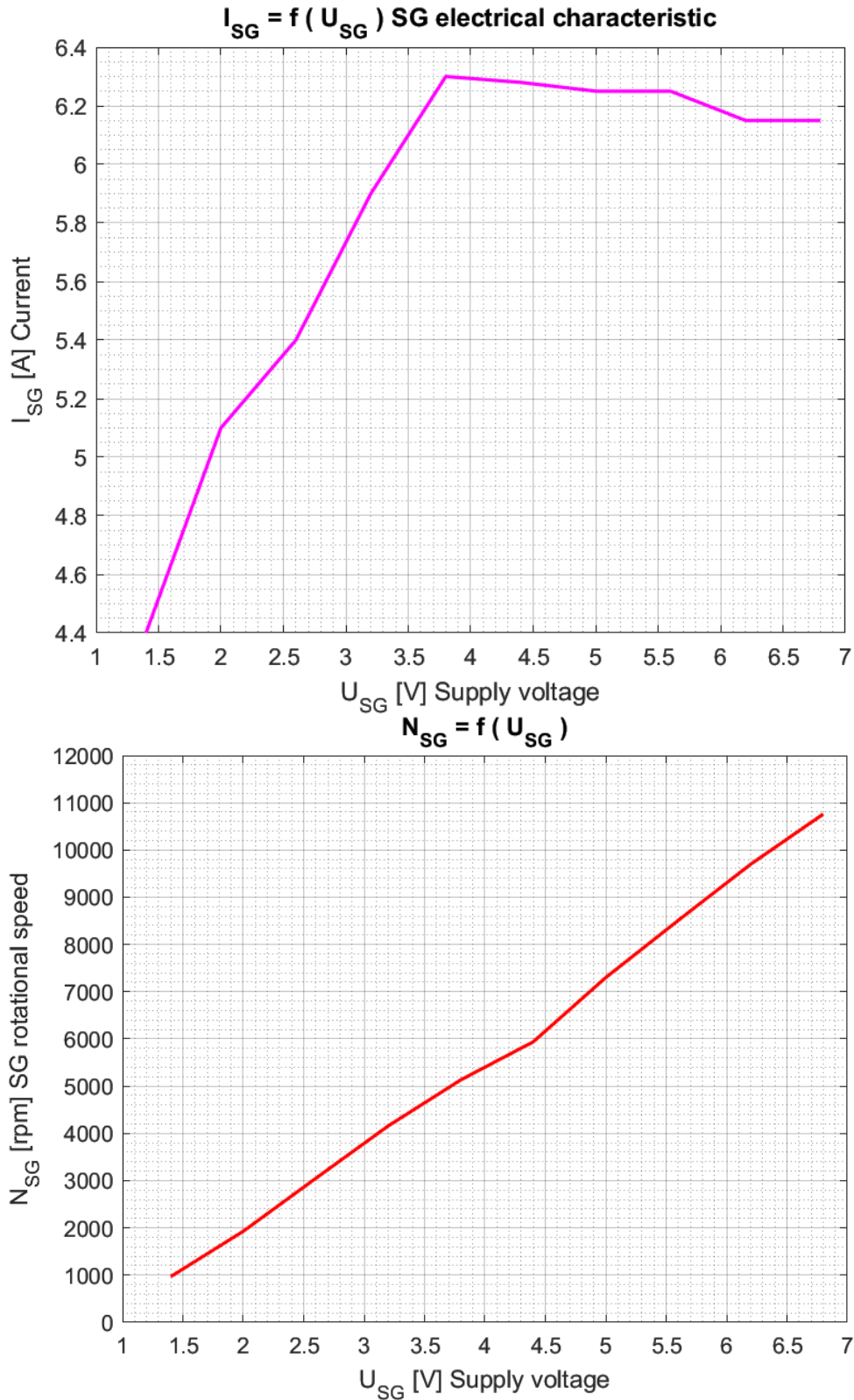


Fig. 8 b SG rpm vs supply voltage

As a nonlinear second order system we modelled the TF of the SG by using formula (1) listed below. Thus, resulting a system model as per figure 9. [3][4]

$$H_{(s)}^{SG} = \frac{K_t}{(J*s+K_b)*(L*s+R)+K_b^2} \quad (1)$$

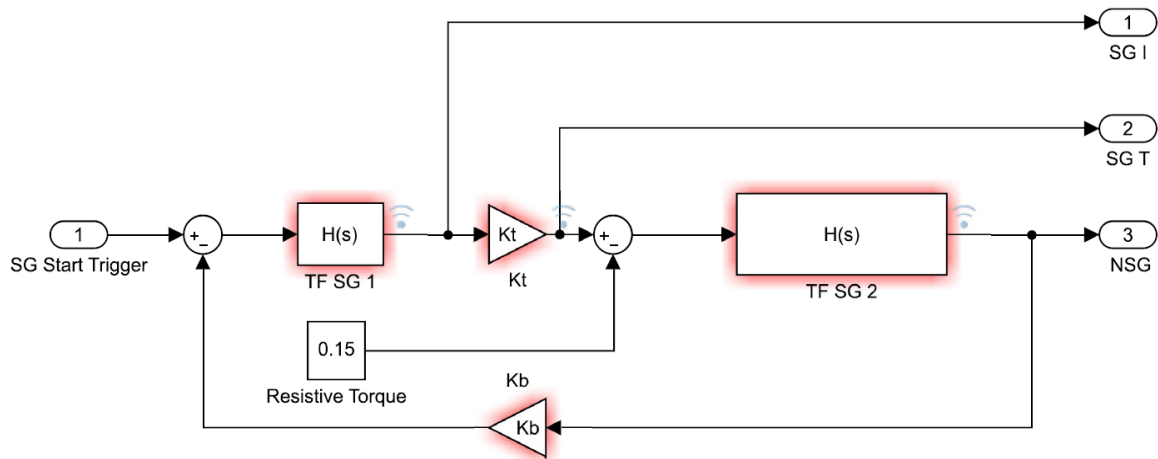
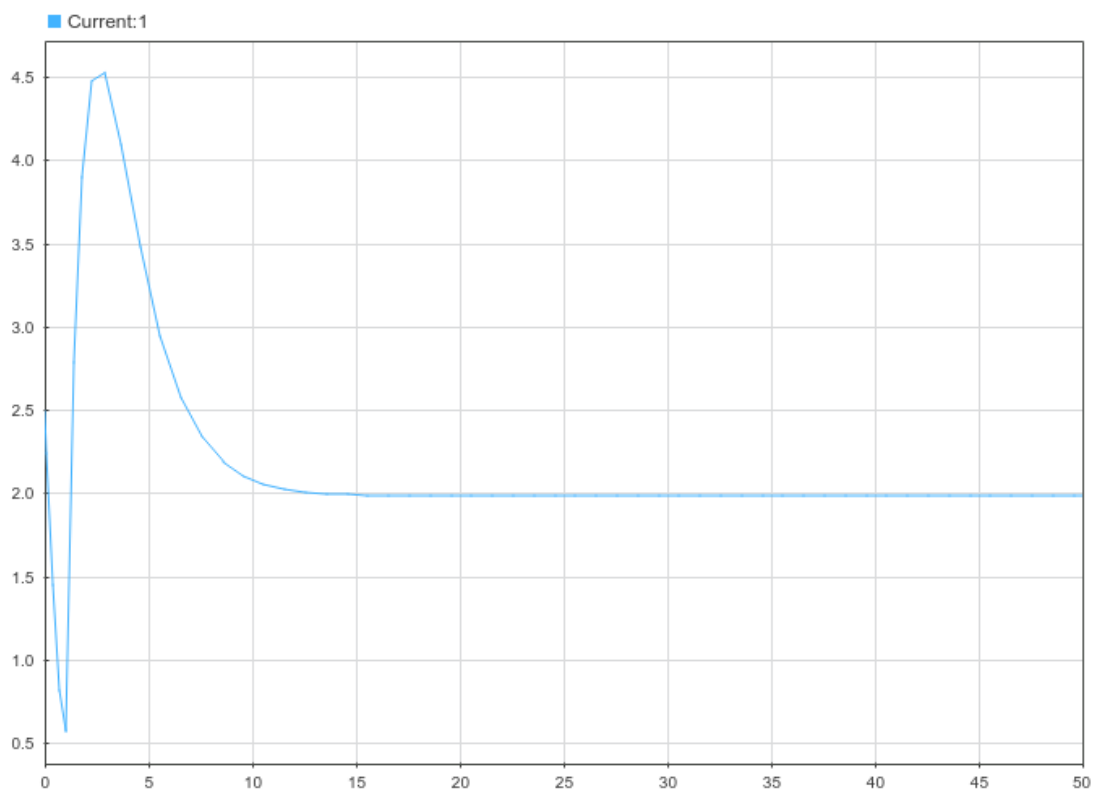


Fig. 9 SG system model

In order to visualise the SGs response for any input command we used step response analysis as shown in figure 10, where the top plot illustrates current consumption in Amps, the centre plot illustrates generated speed in RPM and the bottom plot illustrates torque response all in time basis.



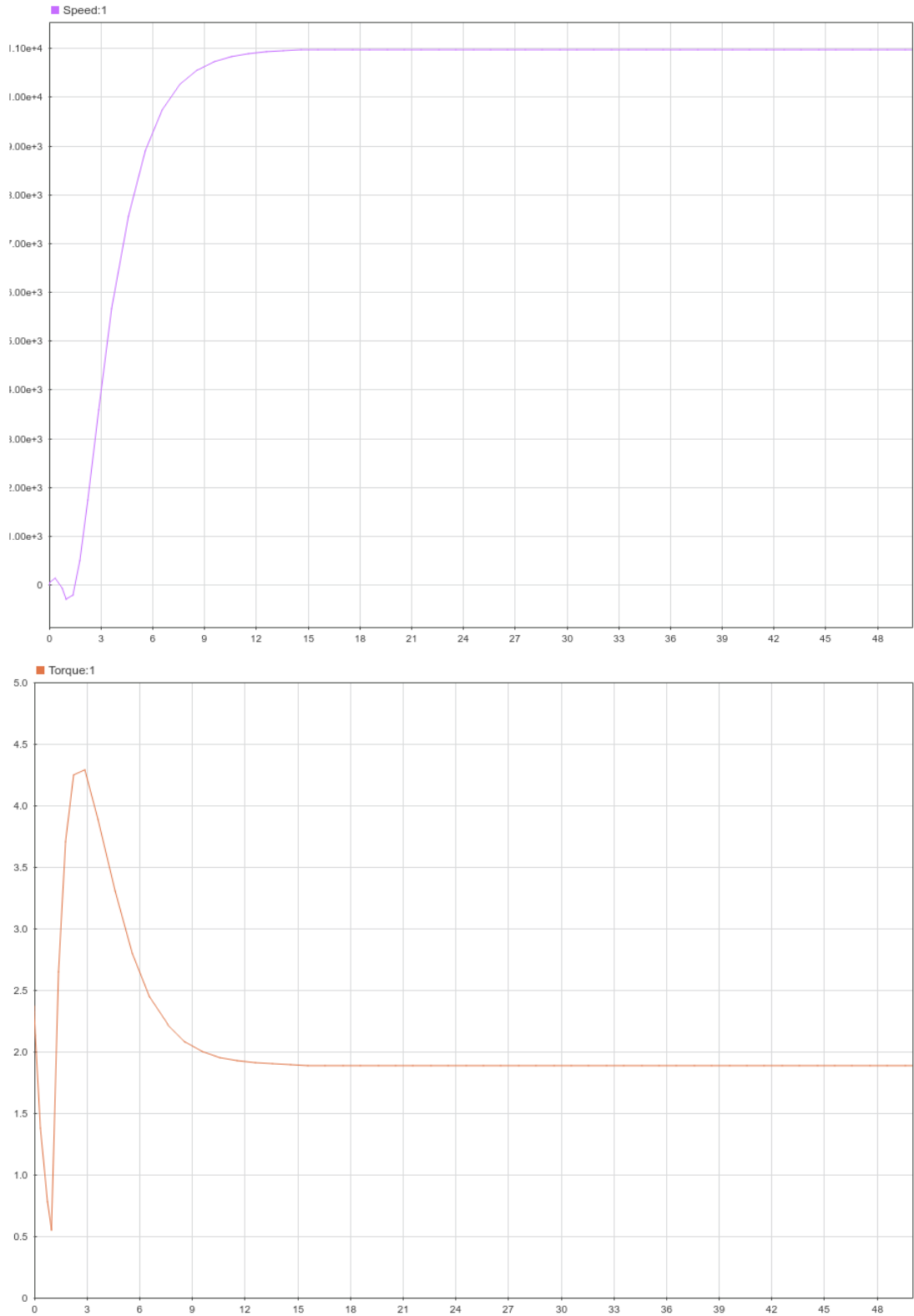


Fig. 10 SG step response

For testing the FI EHCV (fig. 11) we had to develop a test setup (fig. 12) which replicates fuel flow according to the real configuration of the system. In addition, we added a bypass flow line upstream of the EHCV in order to eliminate any FP surges and delay that might result in fuel line pressure increase thus leading to false reading of modulated flow.

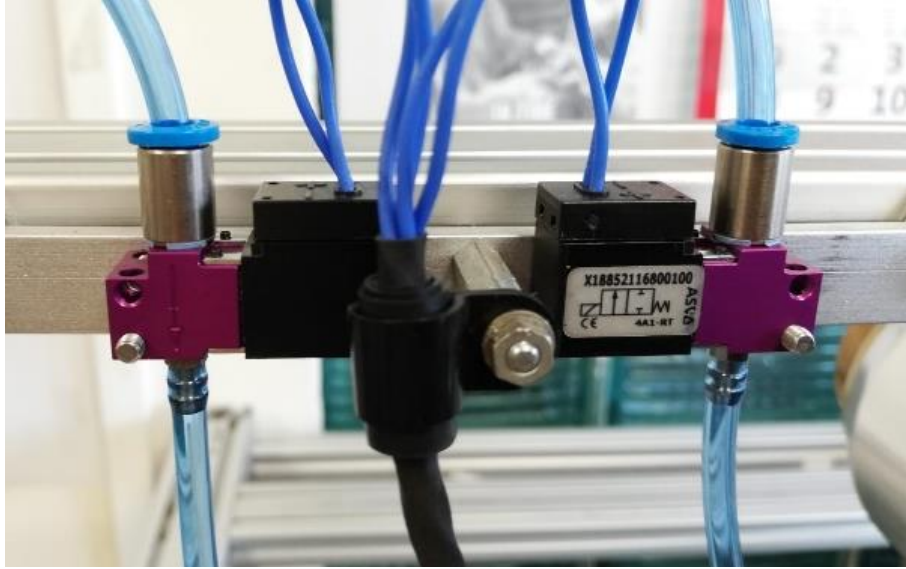


Fig. 11 Fuel Injector EHCV (left) and Combustion Chamber EHCV (right)

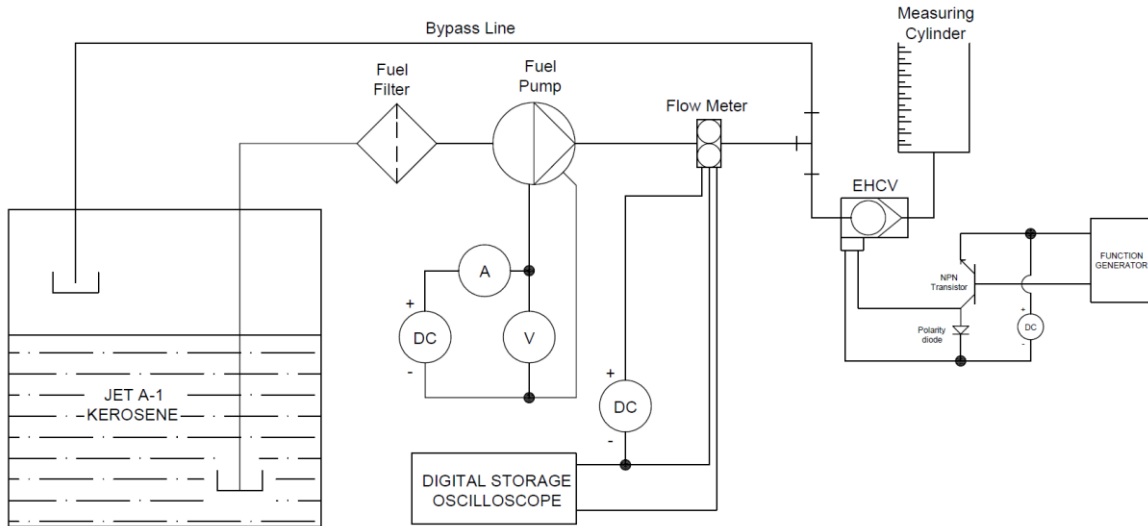


Fig. 12 Fuel supply system test setup used for experimental identification of fuel injector EHCV

For measuring the fuel flow, we used a precise test tube with an associated uncertainty of ± 0.11 mL according to equation (2) used to express the standard uncertainty for measurement resolution.

$$u_{res} = \sqrt{\frac{1}{3} * \left(\frac{division}{interpolation} \right)^2} [\pm \delta ml] \quad (2)$$

The FI EHCV modulate fuel flow by shutting on and off at a certain frequency and duty cycle (50%) thus resulting in a precise method of supplying fuel into the fuel injector without the risk of drawing too much heat energy from the FI's GP.

By conducting experimental testing with the PHT2 engine we concluded that the optimal modulation frequency for a guaranteed consecutive and successful fuel ignition inside the combustion chamber is in the range of (6~9) Hz.

For experimental FI EHCV dynamic identification we used 5, 10, 15, 20 and 25 Hz modulation frequency at three different power maps for the FP, i.e. 2.3V, 3.3V and 4.3V as per table 2.

Table 2. Fuel Injector EHCV test results

I FP [A]	U FP [V]	Flow freq. [Hz]	Flow [L/min]
1.65	2.3	650	0.342766743
ECHV Mod. Freq. [Hz]	On time [sec]	Measured Vol. [mL]	TEST 1
5	5	2.2	
10	5	1.9	
15	5	1.9	
20	5	2.1	
25	5	1.4	
I FP [A]	U FP [V]	Flow freq. [Hz]	Flow [L/min]
2.1	3.3	1000	0.527333451
ECHV Mod. Freq. [Hz]	On time [sec]	Measured Vol. [mL]	TEST 2
5	5	4	
10	5	3.2	
15	5	2.9	
20	5	2.8	
25	5	2.6	
I FP [A]	U FP [V]	Flow freq. [Hz]	Flow [L/min]
2.5	4.3	1400	0.738266831
ECHV Mod. Freq. [Hz]	On time [sec]	Measured Vol. [mL]	TEST 3
5	5	5.8	
10	5	5	
15	5	3.8	
20	5	4	
25	5	3.8	

The data was processed as curve fitting dependencies in MATLAB software. The plot in figure 13 illustrates fuel flow maps according to FP supply voltage and EHCV modulation frequencies. The blue line corresponds to 2.3V, the red line to 3.3V and the yellow line to 4.3V supply applied to the FP.

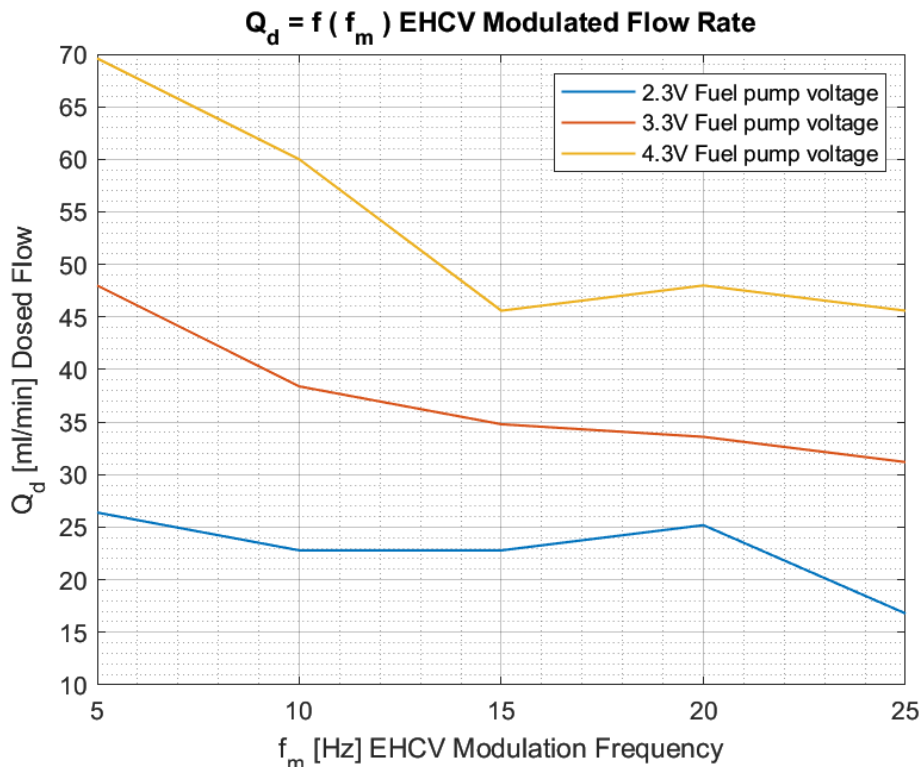


Fig. 13 Fuel Injector EHCV fuel flow curve fitting map plot.

For creating a nonlinear system block (fig. 14) designed to model the FI EHCV we used curve fitting techniques and plot mapping blocks which are dependent to FP supply voltage signal and a trigger system (fig. 15) signal for controlling the start sequence of the EHCV.

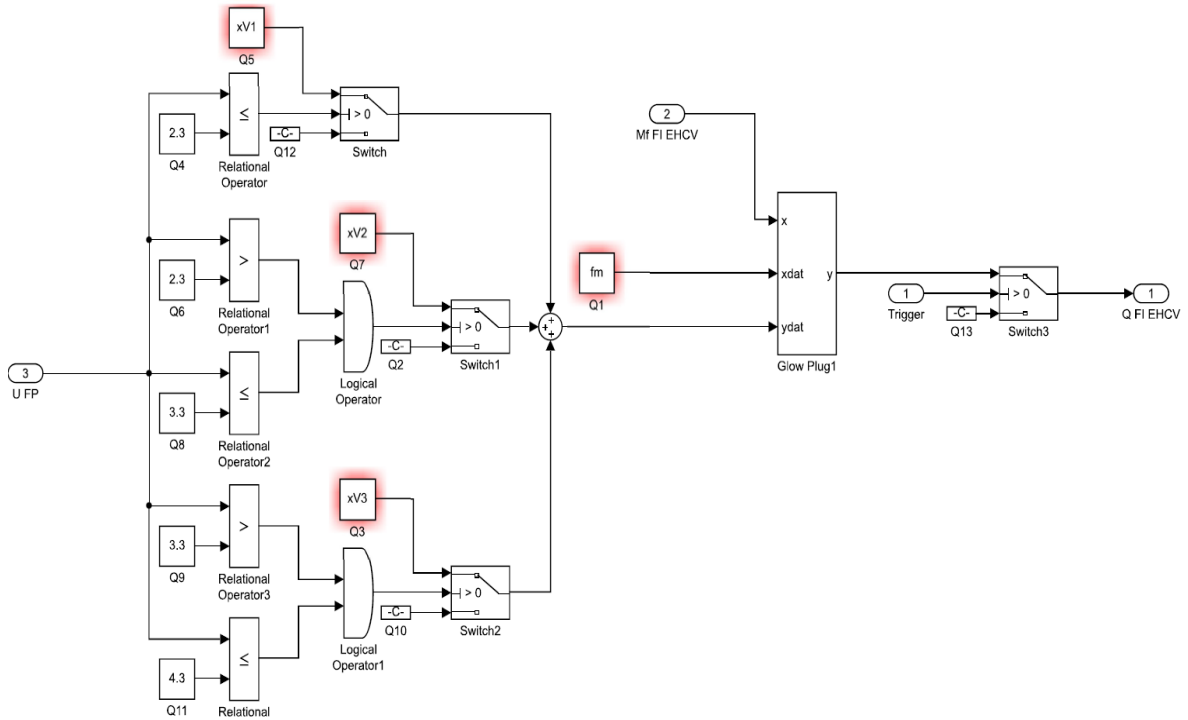


Fig. 14 FI EHCV system model

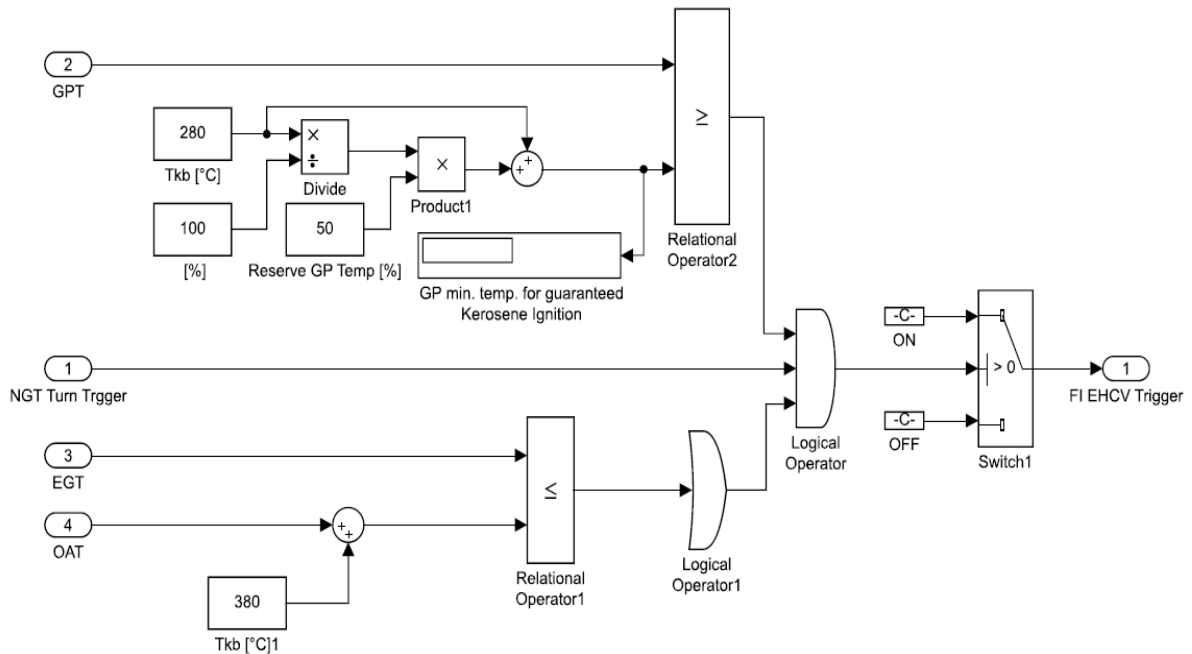
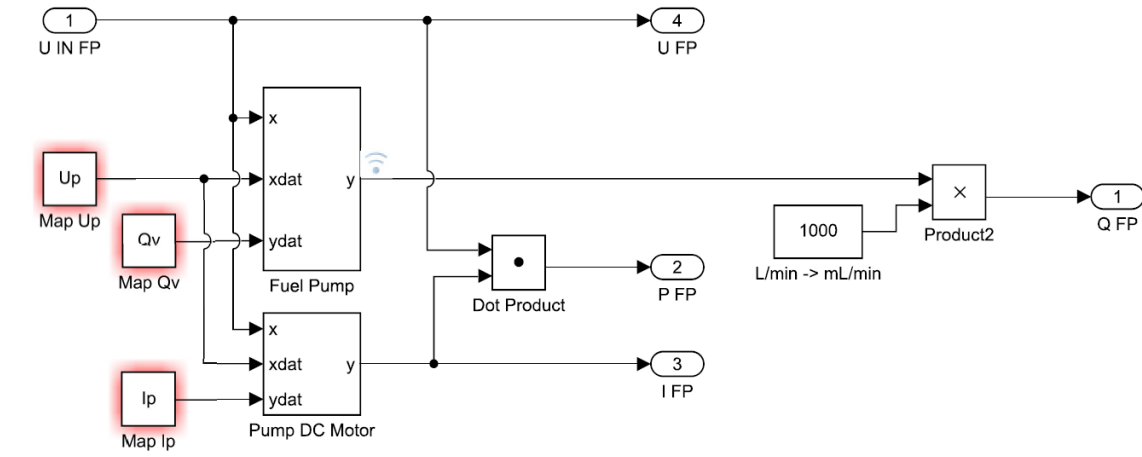


Fig. 15 FI EHCV trigger block

The fuel pump was also modelled via a curve fitting logic in means of fuel flow vs supply dependency and thus the FP characteristic response is illustrated in the model and plot from figure 16. Where the blue line represents the actual FP fuel flow in mL, the green line is a linearization of the FP response, both according to supply voltage. At maximum load, the fuel pump provides a fuel flow of 975.6 mL/min.



$$Q_v = f(I_p) \text{ Fuel Flow}$$

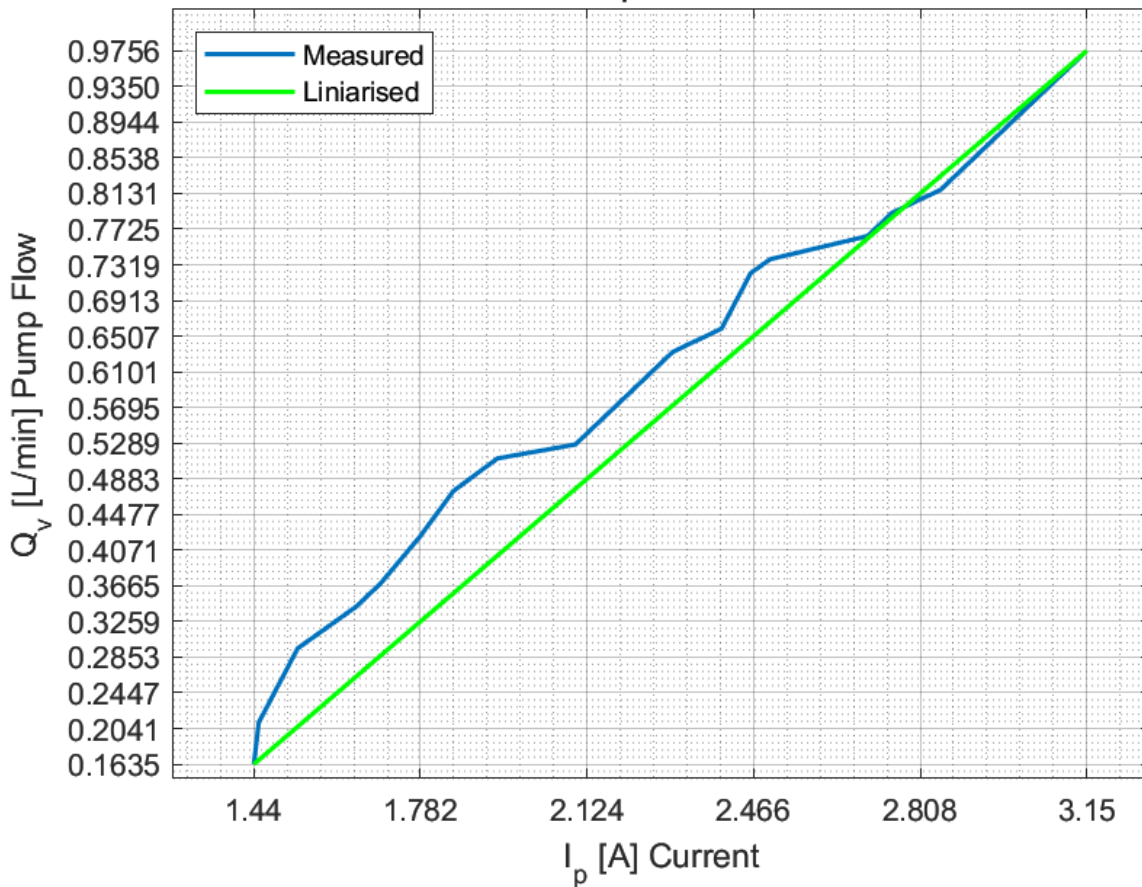


Fig. 16 FP system model (top), FP response curve (bottom)

The fuel injector's GP was tested according to test configuration diagram illustrated in figure 17. The testing was done in order to determine the temperature output vs control voltage and current consumption. The testing of the GP is presented in the images from figure 18. The output data of the GP temperature vs supply dependency is shown in the plot from figure 19.

The GP's block system model is shown in figure 20 and it is based on a nonlinear data mapping block.

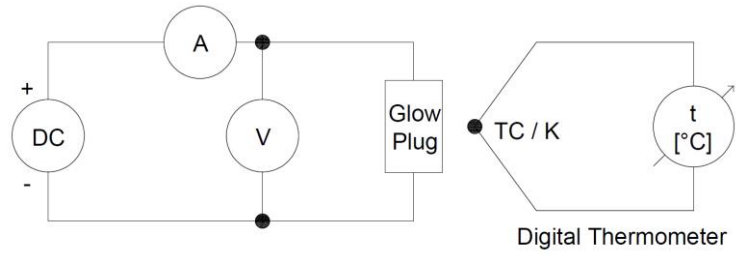


Fig. 17 GP test diagram



Fig. 18 GP testing (from left up to right down corner: internal resistance, low power glow, maximum power glow, temperature reading of GP tip)

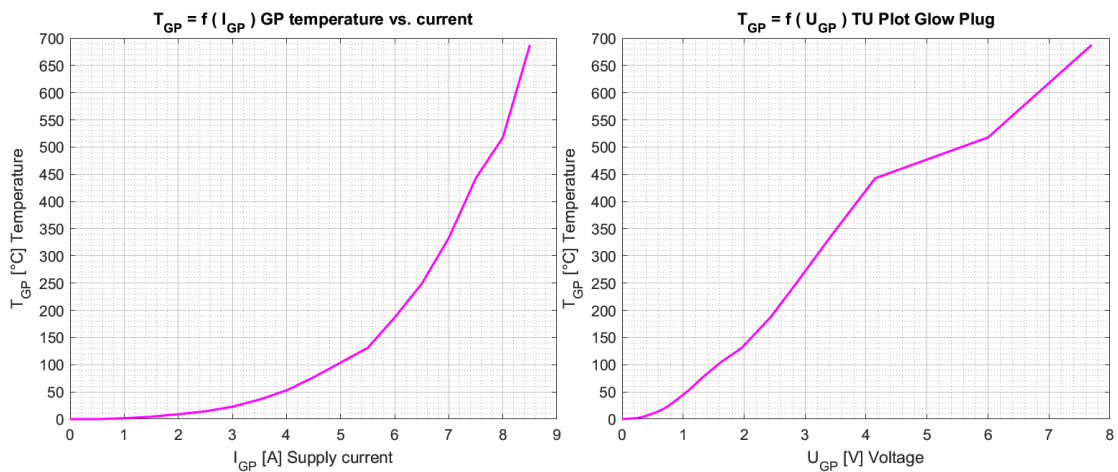


Fig. 19 GP temperature vs. supply current (left) and temperature vs. supply voltage (right)

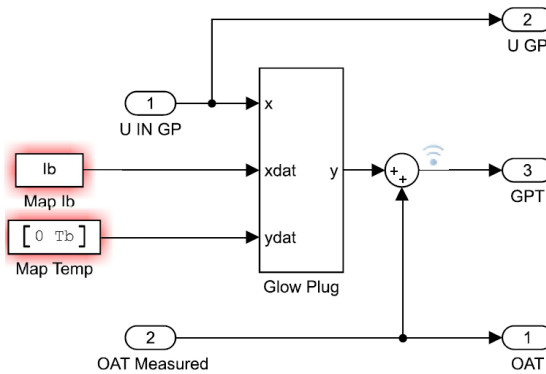


Fig. 20 GP block system model

After modelling all components as individual dynamic blocks we created a global dynamic system (fig. 21) which recreates the PHT2 power plant as a mathematical model. This model will be used to design and develop in further studies an innovative AI based control loop ECU. For testing and validating the resulted dynamic system model and the future build ECU we will develop an HIL type testing stand. This reducing all physical experimental factors and test time by up to 80% while allowing for safe, ultra-reliable and robust development of control hardware i.e. ECU. The rotary knobs are used in local simulation for varying certain input parameters such as, FP supply voltage, SG supply voltage, EGT and OAT.

The blue blocks are the components modelled thru experimental identification, the orange blocks are state variable and measured inputs, the green blocks are output commands and variables, the red signals represent ECU variables and the yellow ones are trigger, threshold and conditioning blocks. [3]

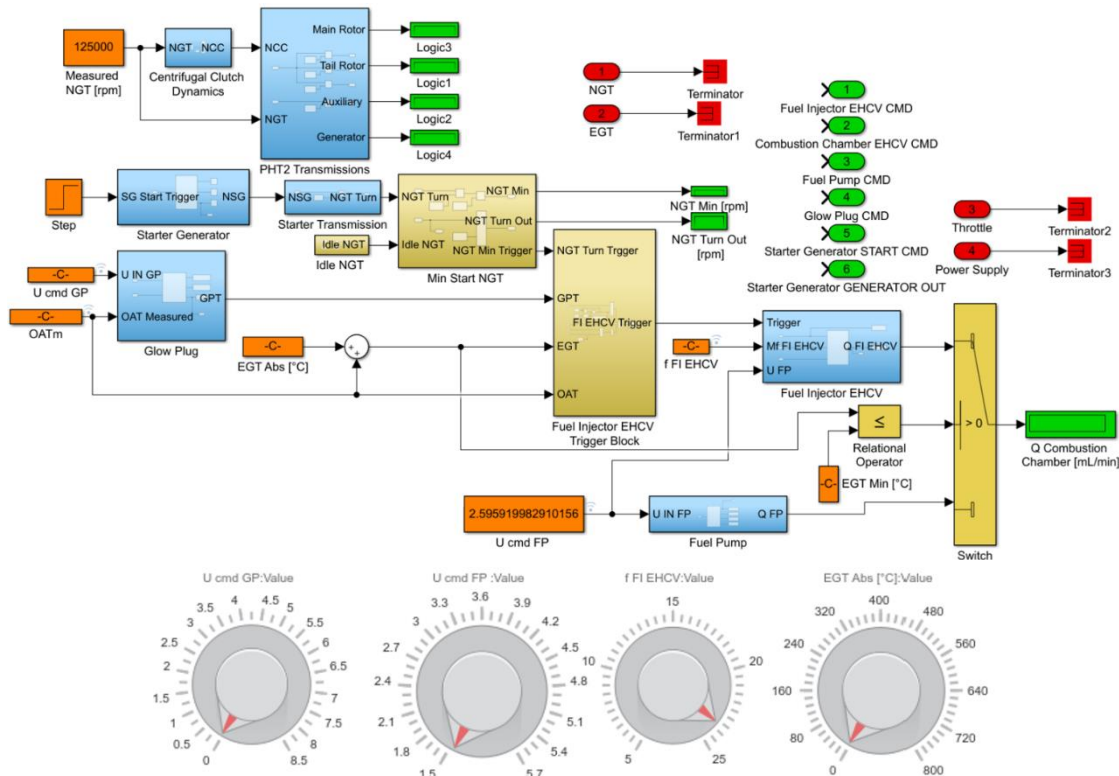


Fig. 21 PHT2 dynamic system model including all auxiliary components

In order to achieve better control performance and highly optimised control loops we will further research and develop experimental dynamics identification test conditions and diagrams and study the usage of more performant feedback systems and measuring devices on the PHT2 power plant.

In the graph illustrated in figure 22 is the starter generator RPM response in time during experimental testing with the PH2 turbine engine. At time 0 the SG receives the ON command thru the command block illustrated in figure 23. [7]

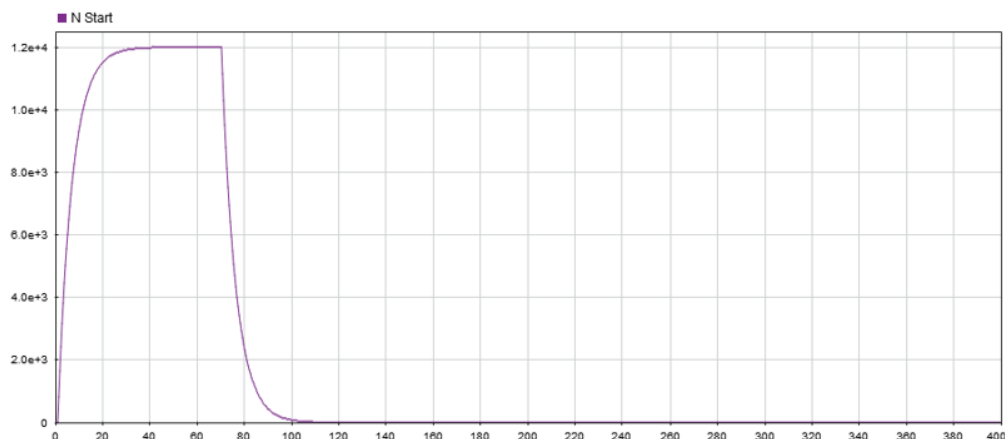


Fig. 22 SG RPM experimental testing

During experimental turbine engine testing, we concluded that the starter generator has the exact same response as its mathematical transfer function. The SG tops out at 12000 RPM for 40 seconds until minimum EGT level is achieved such that the turbine engine is in self sustained mode, after which the SG shuts OFF. [7]

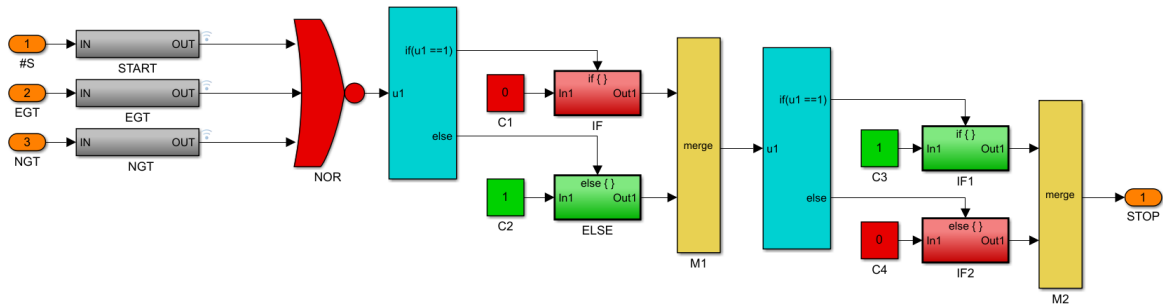


Fig. 23 SG command block for start and stop

Starter generator shut off is conditioned by three input variables such as start attempt count, exhaust gas temperature and turbine speed. When all these three variables, simultaneously, satisfy certain threshold conditions they will all enable the logic NOR (standard name for logic operator) operator to trigger the SG stop command.

In the plot illustrated in figure 24 we can observe exhaust gas temperature response during start up and at idle. The overshoot in temperature at the time interval between 80 and 100 seconds is due to several factors such as fuel pump inertia, fuel line pressure build up and turbine inertia. The 30 seconds delay between the time the SG starts up until the rise in EGT is due to the fact that a minimum of 8000 RPM is needed in order to trigger the fuel injector. If not, the combustion chamber can be flooded with unburned fuel. The vertex point in EGT at 420°C is due to the transition of fuel supply from the fuel injector to the combustion chamber pipe injection system, which in term leads to a drop in fuel pressure. [7]

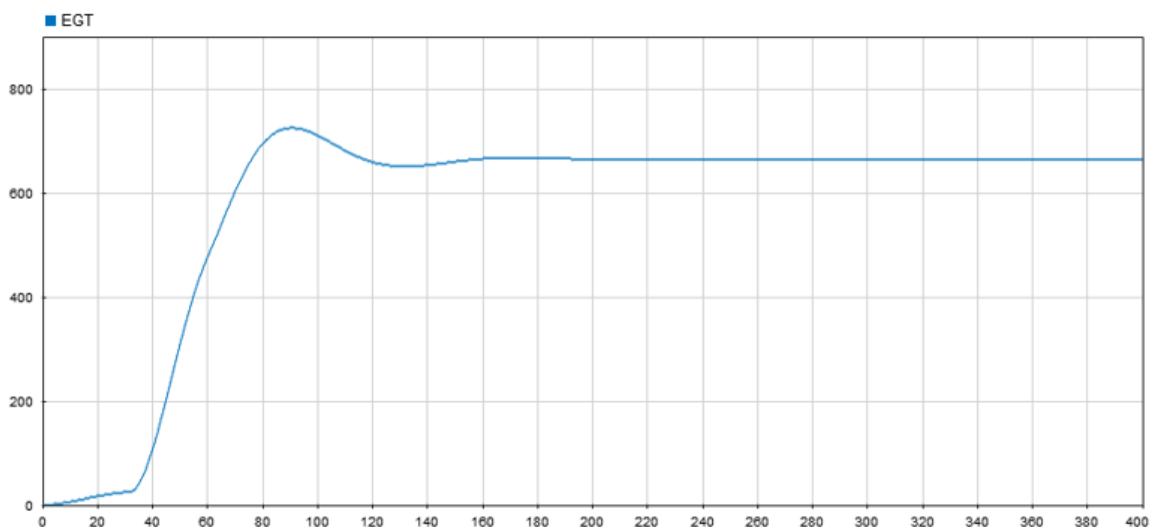
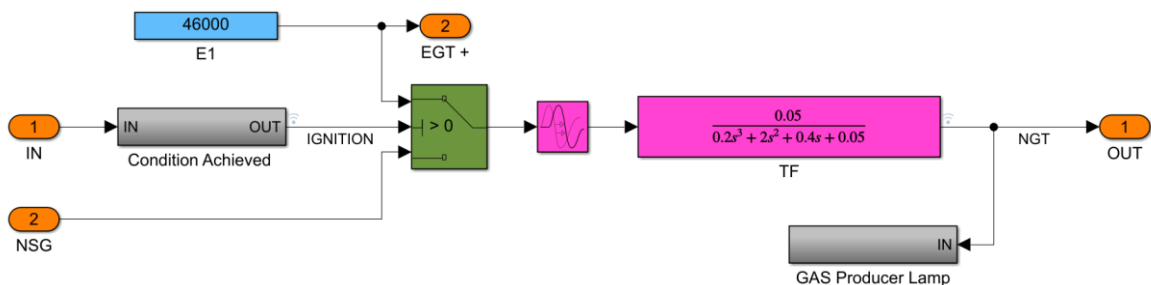


Fig. 24 Exhaust gas temperature during start up and idle



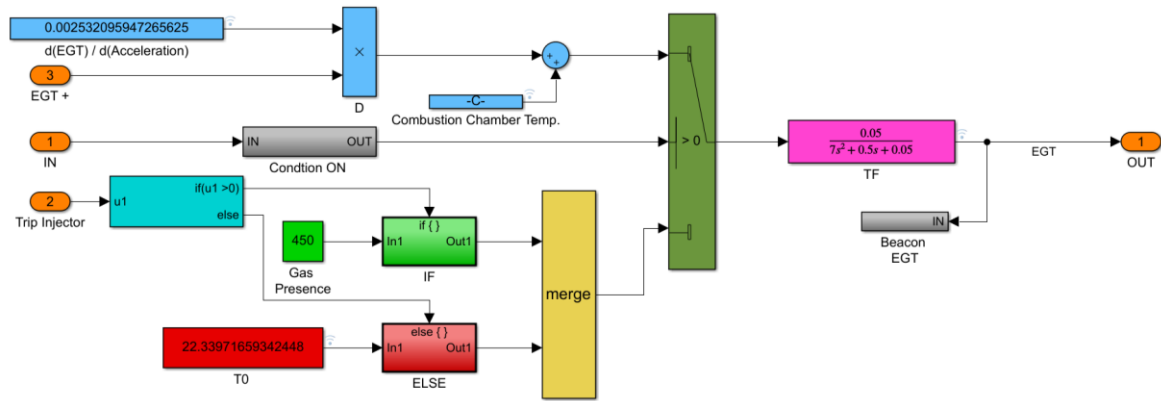


Fig. 25 Gas turbine and combustion chamber mathematical model

The block diagram illustrated in figure 25 is used to mathematically simulate the gas turbine speed response (upper transfer function and transport delay) and combustion chamber temperature response in terms of EGT. Turbine speed response utilises two input variables E1 (desired speed) and NSG (starter generator speed) as input vectors for the upper transfer function. In order to simulate temperature response for the combustion chamber, we used the ratio of difference in EGT over difference in acceleration (NGT speed), correlated with ambient temperature T0 and an empirical power map [10] for internal combustion chamber temperature, derived from the specific heat generated by a certain level of injected fuel.

3. CONCLUSIONS

In this article we addressed the problems and requirements of determining and modeling a dynamic system for a microturbine engine. The challenges that we faced were related to determining command and control logics for the power plant via means of test bench experimentation, identifying signal values and limits for engine control loops and developing accurate and repeatable test conditions.

We successfully managed to identify all component dynamics and to model them as dynamic system blocks into a global design cluster which stands at the basis of ECU design and development. The designed and modeled global system was tested for all types of input signal simulated via means of previous data acquisitions from the PHT2 power plant and performed as expected. Thus, concluding that the designed system is validated after final simulation testing. In conclusion, the designed dynamic model is eligible for use in developing an ECU prototype in further research.

ACKNOWLEDGEMENT

The present research data is part of the “Nucleu” Programs TURBO 2020+ and TURBOPROP, supported by the Romanian Ministry of Research and Innovation, project number PN 19.05.01.01 and ongoing project phases.

REFERENCES

- [1] www.ni.com/ro-ro/innovations/case-studies/19/collins-aerospace-saves-time-money-and-labor-by-developing-a-unified-test-architecture-for-electromechanical-systems.html
- [2] www.jetcat.de/jetcat/produkte/hobby/pht2/pht2serie.jpg
- [3] A. Taranu, O. Grigore Muller; 2016; Modernizarea instalatiei electrice a unei aeronave pentru monitorizarea mediului; Universitatea Politehnica Bucuresti, Facultatea de Inginerie Aerospaciala, Catedra Ingineria Sistemelor Aeronautice “Nicolae Titei”; Bucuresti Romania;
- [4] R. Ciobanu, O. Grigore Muller; 2016; Actionarea unei drone autonome cu monitorizarea si back-up de la sol; Universitatea Politehnica Bucuresti, Facultatea de Inginerie Aerospaciala, Catedra Ingineria Sistemelor Aeronautice “Nicolae Titei”; Bucuresti Romania;

- [5] A. Taranu, O. Grigore Muller; 2018; Comanda inteligenta a unui UAV; Universitatea Politehnica Bucuresti, Facultatea de Inginerie Aerospatiale, Catedra Ingineria Sistemelor Aeronautice "Nicolae Tipei", Masterat Avionica si Navigatie Aeriana; Bucuresti Romania;
- [6] R. Ciobanu, O. Grigore Muller; 2018; Metode de navigatie inteligente a unui UAV; Universitatea Politehnica Bucuresti, Facultatea de Inginerie Aerospatiale, Catedra Ingineria Sistemelor Aeronautice "Nicolae Tipei", Masterat Avionica si Navigatie Aeriana; Bucuresti Romania;
- [7] R. Ciobanu, A. Stoicescu, C. Nechifor, A. Taranu; 2018; Self-Learning Control System Concept for APU Test Cells; MATEC Web of Conferences; Vol. 210, 02009; 22nd International Conference on Circuits, Systems, Communications and Computers (CSCC); Majorca, Spain; July 14-17, 2018;
- [8] M.V. Cook; 2007; Flight Dynamics Principles; Jordan Hill, Oxford OX2 8DP; ISBN: 978-0-7506-6927-6;
- [9] A. M. Khatkhate, E. Keller; 2006; Modelling and System Identification of an Experimental Apparatus for Anomaly Detection in Mechanical Systems; Department of Mechanical Engineering, The Pennsylvania State University, University Park, PA 16802-1412, United States;
- [10] M. Witters, J. Sweres; 2009; Optimal experiment design for the black box identification of a semi-active damper; Department of Mechanical Engineering, Katholieke Universiteit Leuven, Celestijnenlaan 300B, B-3001 Heverlee, Belgium;
- [11] M. Deflorian, S. Zaglauer; 2011; Design of Experiments for nonlinear dynamic system identification; The International Federation of Automatic Control Milano (Italy);
- [12] A. Khalil, G. El-Bayoumi; 2013; Flight Dynamics, Stability and Control of a Flexible Airplane; Conference: 15th International Conference on Aerospace Sciences & Aviation Technology (ASAT – 15)At: Cairo, Egypt;
- [13] J. Schoukens, L. Ljung; 2019; Nonlinear System Identification A User-Oriented Roadmap; IEEE Control Systems Magazine;
- [14] R. A. Bunge; 2015; Aircraft Flight Dynamics; Stanford University, USA;
- [15] V. Bures; 2015; Comparative Analysis of System Dynamics Software Packages; International Review on Modelling and Simulations (I.R.E.M.O.S.);
- [16] D. A. Caughey; 2011; Introduction to Aircraft Stability and Control Course Notes for M&AE 5070; Sibley School of Mechanical & Aerospace Engineering Cornell University Ithaca, New York;
- [17] G. I. Stry, D. J. Mook; 1991; An Experimental Study of Nonlinear Dynamic System Identification; Department of Mechanical and Aerospace Engineering, State University of New York at Buffalo, Buffalo, New York, USA;
- [18] L. Derafa, T. Madani, A. Benallegue; 2007; Dynamic Modelling and Experimental Identification of Four Rotors Helicopter Parameters; Proceedings of the IEEE International Conference on Industrial Technology. 1834 - 1839. 10.1109/ICIT.2006.372515;
- [19] D. Kaplan, L. Glass; 1995; Understanding nonlinear dynamics; McGill University 3655 Drummond Street Montreal, Quebec, Canada H3G 1Y6;
- [20] M. Vidyasagar; 1993; Nonlinear systems analysis; ISBN 0-13-623463-1;
- [21] R. Ciobanu, C. Nechifor, A. Stoicescu, A. Taranu; 2019, Cercetare fundamentala model instrumentare pentru ECU si FADEC; AICSAT, INCDT COMOTI;

OPTIMIZATION OF THE ELECTRONIC CONTROL SYSTEM FOR THE ST40M GAS TURBINE

Filip NICULESCU¹, Mirela-LetițiaVASILE¹, Adrian SAVESCU¹, Radu CODOBAN¹

ABSTRACT: Gas turbines used in propulsion ensure increased efficiency and safety, with a very good power / weight ratio, low maintenance and operation costs. The characteristics of the ST40M gas turbine have made it suitable for the propulsion of fast ships. The ST40M gas turbine electronic system ensures control, monitoring and alarm functions, including over speed protection. A local control panel interfacing the logic controller displays the engine parameters, commands, also providing maintenance and calibration sequences. The proposed solution enables both the local and the remote control of the gas turbine. The paper presents the optimization of the electronic control system from the initial form proposed in the project to the form with which the ST40M turbine was tested on the ship. In conclusion, the optimization process took into account the engine configuration and the control requirements of the group propulsion. Future efforts will be aimed towards the continual optimization of the power supply, integration into the control system on the ship and improvement of the control software.

KEYWORDS: turbines, control, marine technology, optimization, command and control systems

NOMENCLATURE

FADEC	Full Authority Digital Engine Control
CCS	Command Control System
PLC	Programmable Logic Controller
LCP	Local Control Panel
CPU	Central Processing Unit
LVDT	Linear Variable Differential Transformer
XDC	Position of the fuel metering valve
XDCN	Scaled position of the fuel metering valve
PQC	Position of the metering valve dual torque motor.

1. INTRODUCTION

1.1 The global situation of control systems for marine gas turbine

The use of gas turbines on board ships for specific advantages involves the development of automatic control for this type of propulsion. A typical marine gas turbine propulsion system installation consists of separate controls for not only the gas turbine but also the ship systems, reduction gearbox and exhaust system (Fig. 1). Advantages in reduction complexity, lower weight, ease of installation/ maintenance can be achieved by minimizing the quantity of individual subsystem controls [1].

¹ Romanian Research and Development Institute for Gas Turbine COMOTI, Bucharest, Romania

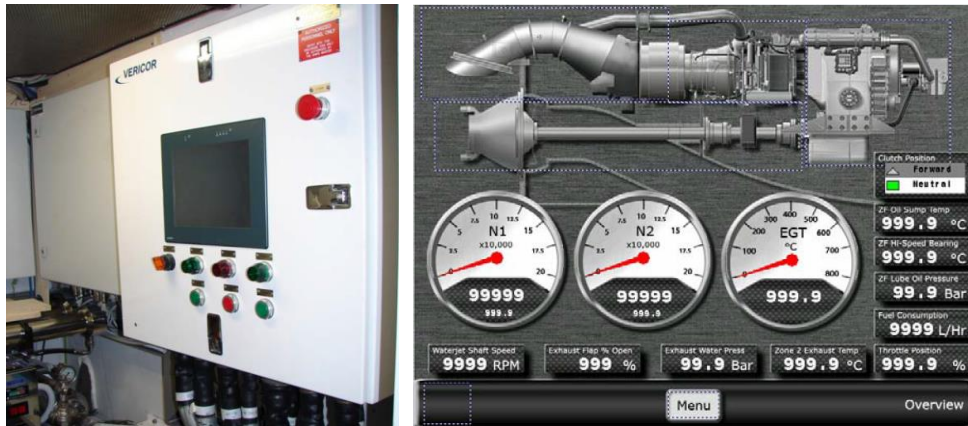


Fig. 1 Control system for marine gas turbine [1]

1.2 ST40M gas turbine

The ST40M is an aero derivative gas turbine, manufactured by Pratt & Whitney Canada, whose performance is correlated with the performance of the PW150A gas turbine. The power turbine (free turbine) consisting of two axial stages remained basically unchanged except that the power shaft of the last two stages was lengthened to comply with the width of the new intake device.

The PW150A gearbox was removed and the air intake was changed for radial-symmetrical air intake to the gas turbine axis. The compressors remained unchanged being the same as in the PW150A. The low pressure axial compressor has 3 axial stages being driven by a low pressure axial turbine with 1 stage. The high pressure axial compressor has a single centrifugal stage being driven by a high pressure axial turbine with 1 stage (Fig. 2).

The combustion chamber is the same as inverted ring type but with the modified geometry for the use of diesel instead of aviation fuel. Kerosene was replaced with standard naval diesel fuel for economic reasons [2]. The ST40M gas turbine has been modified to meet the marine standard, i.e. treated for resistance to salt mist corrosion.

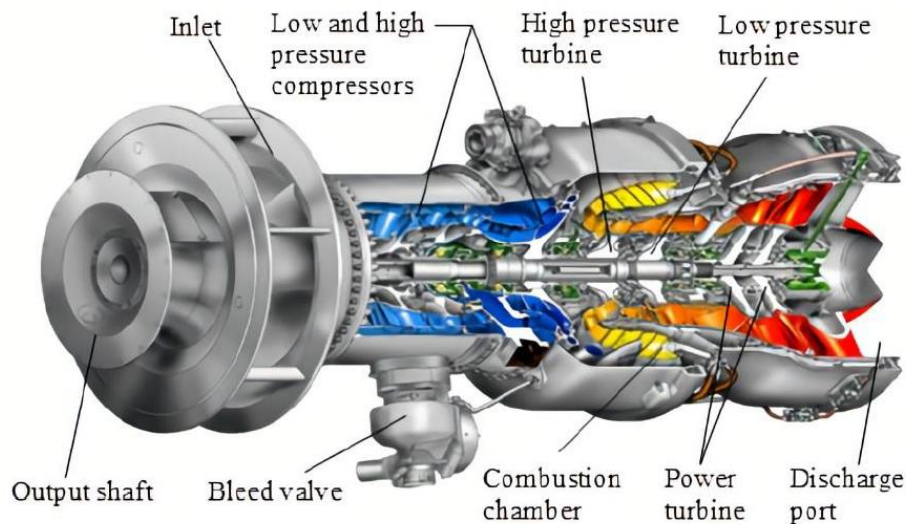


Fig. 2 Section through the model of ST40M gas turbine [2]

The ST40M engine has an advanced air-cooling system of turbine stator and rotor blades which allows a thermal efficiency of 33%.

To achieve the specified high thermal efficiency ($\eta=33\%$) the compressor compression ratio has a high value being $\pi_c=18$.

Other engine parameters are:

- Air flow $M_a=14.44$ kg/sec ;
- Continuous power $P = 4039$ kW ;

1.3 ST40M gas turbine control system

The ST40 engine in its use for aviation has a control system based on FADEC. Although many system upgrades have been made since its conception, the lack of flexibility of the FADEC system for implementing logical functions or for adding additional inputs, limits its use in marine installations. That is why its use was abandoned and it is replaced with a new control system to take over its functions.

The PLC platform chosen for the engine control system was VERSAMAX from General Electric. The assembly contains voltage source, CPU drive, analog inputs, analog outputs, digital inputs, digital outputs and counter inputs (Fig. 3). The PLC assembly located in the local control cabinet is connected to the voltage and current adapters located in the junction boxes near the engine.

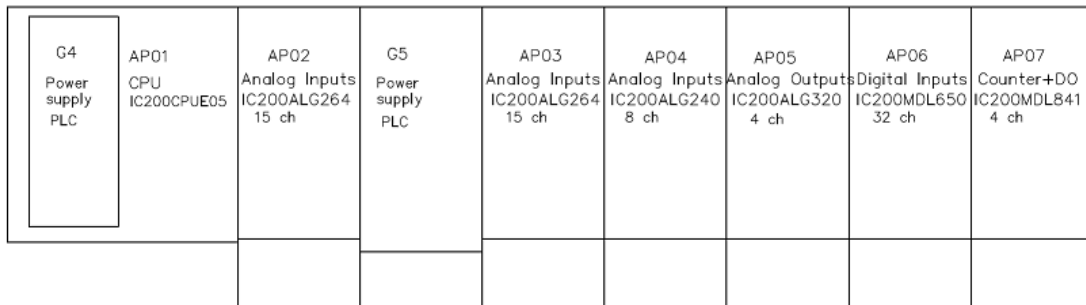


Fig. 3 PLC layout

The CPU communicates over Ethernet with the operator panel in the local control cabinet and with the computer control in the engine command room. The number of tests to validate a project with components used in other applications, where they proved their reliability, was evaluated as much lower than that required for a control system with different components. This has led to a low implementation cost and the ability to quickly change design once a need has been identified. A new control and control system has been developed, as well as the piping required to switch the suction with the exhaust air in such a way as to match those of the mechanical installation (Fig. 4).

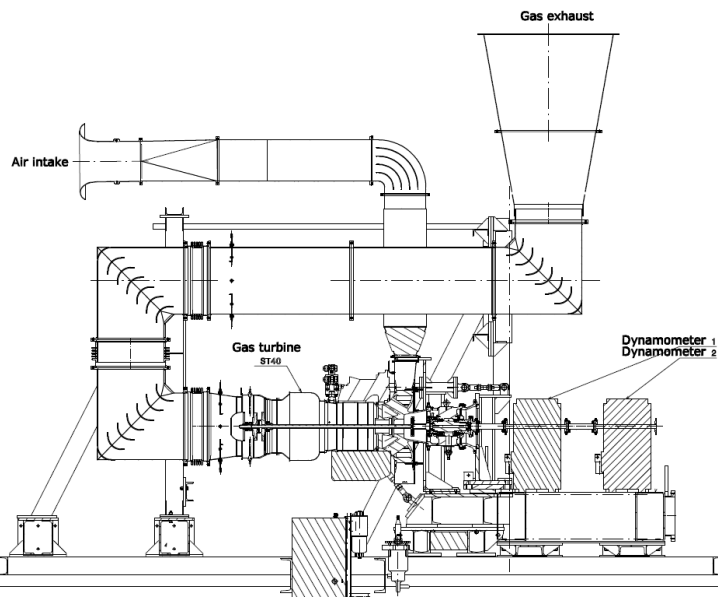


Fig. 4 Section through the installation of ST40M gas turbine on test bench

An automated electronic control system was designed, built, installed and tested together with the ST40M engine for naval application. Among the available control systems [3], the electronic control currently offers the highest reliability and adaptability, and can easily and rapidly be tailored for any arising situation or parameter change [4].

In the new configuration tests were carried out on the test bench until the maximum power from the manufacturer's sheet was obtained.

In Fig. 5 is showed the ST40M installed on test bench.



Fig. 5 Installation of the ST40M engine in the test bench

2. Hardware optimizing

2.1 Power from two sources - power from one source.

In the initial project, the idea was to use two 24Vdc power supplies. One power supply was dedicated for PLC power supply, temperature adapters, speed adapters, pressure transducers and vibration units. The other power supply was intended to supply the ignition unit to which the spark plugs of the motor are connected.

Voltage	28V DC, Nominal. 16V minimum, 32Vmax
Average Current.	1.5A Max. (In rush current 33A).

Fig. 6 The characteristics of the ignition module given by engine manufacturer

This was decided because the current consumption of the ignition module was estimated to be high (data from factsheet 33A inrush, Fig. 6).

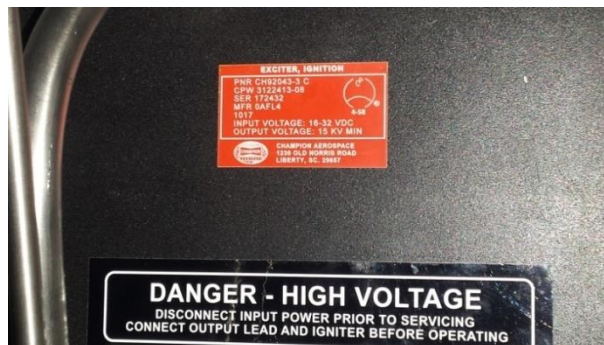


Fig. 7 The engine ignition unit [2]

With the connection of the equipment and the beginning of the tests it was found that this source dedicated to the ignition unit (Fig.7) is even limiting, the measured current being about 30 A. The source of 20 A was replaced with one of 45 and the tests were continued (Fig. 8).

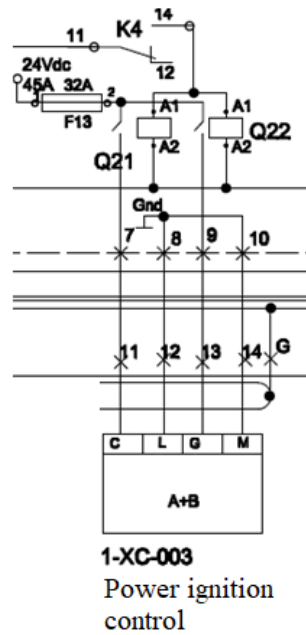


Fig. 8 The connection diagram of the engine ignition unit

Because in this configuration, the current measured indicate a value above the value in Fig. 6, the engine supplier was contacted in order to confirm the correctness of the connections.

Table 1. The connector AE6 pin allocation [2]

Ignition Exciter	AE6	L	Channel A Ground
		C	Channel A Power supply +
		A	Ignition Command (Channel A Ignitor A #1)
		D	Ignition Command (Channel A Ignitor A #2)
		B	Ignition Command (Channel B Ignitor B #1)
		E	Ignition Command (Channel B Ignitor B #2)
		G	Channel B Power Supply +
		M	Channel B Ground

After the verification, it was found that according to the provided diagram (Table 1), there was an inversion to the supply of channel B. Pin G had to be connected to ground and pin M to Power supply +. By remarking the connections it was found that the supply current decreased to a maximum value of 1 A. It was decided to supply the other modules in the LCP, as well as the ignition unit from the same source of 20A / 24Vdc (Fig. 9).



Fig. 9 The power supply of the LCP

The tests performed confirmed the normal functioning of the circuits supplied in this way. It was decided to eliminate a source and simplify the power circuit.

2.2 Operator panel removing

The initial project provided for the engine room two operator panels. One mounted on the local control cabinet and one mounted in a position that allows easy access to the engine's controls for the operator (Fig. 10).

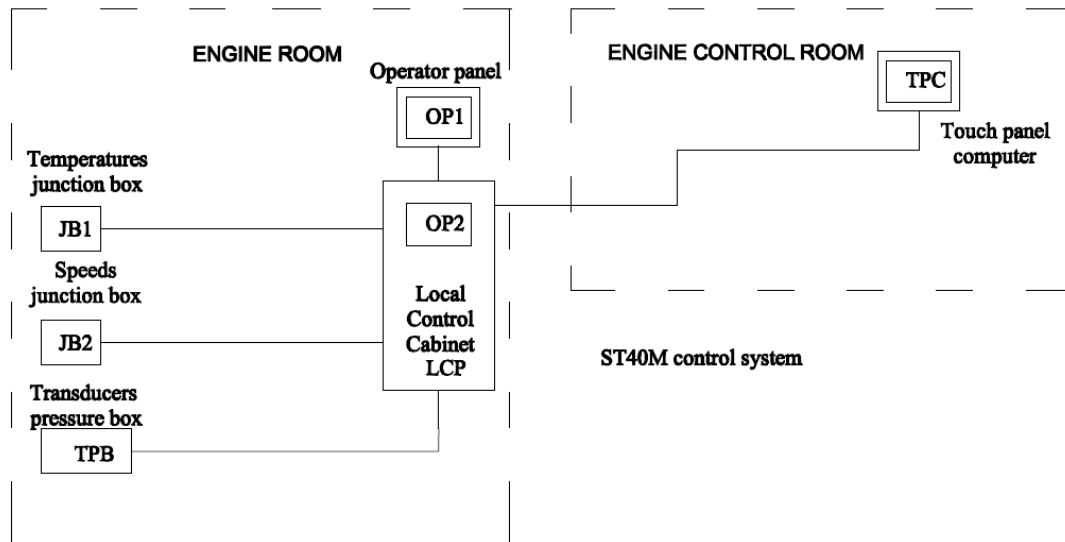


Fig. 10 The initial block diagram of the system

After careful analysis it was found that the local control cabinet does not occupy a large dedicated space and can be positioned so that the operator has easy access to the panel included in it, the second operator panel in the engine room is no longer necessary. Therefore the use of the second panel was abandoned, in the final scheme only the panel in the local control cabinet is provided (Fig. 11).

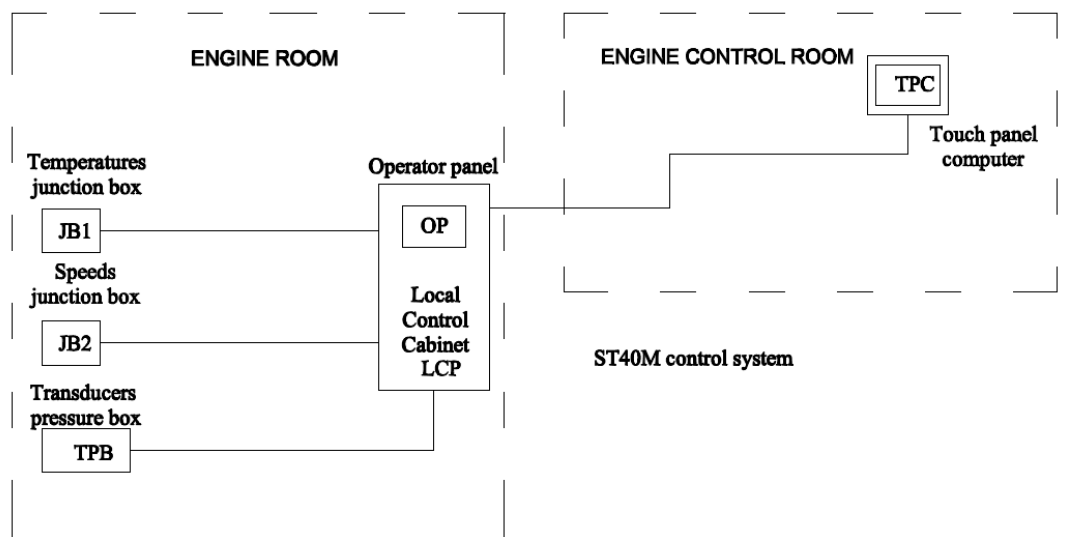


Fig. 11 The final block diagram of the system

In Fig. 12 it can be seen the location of the local control panel, the temperature and samples speeds junction box at sea tests, on ship board.

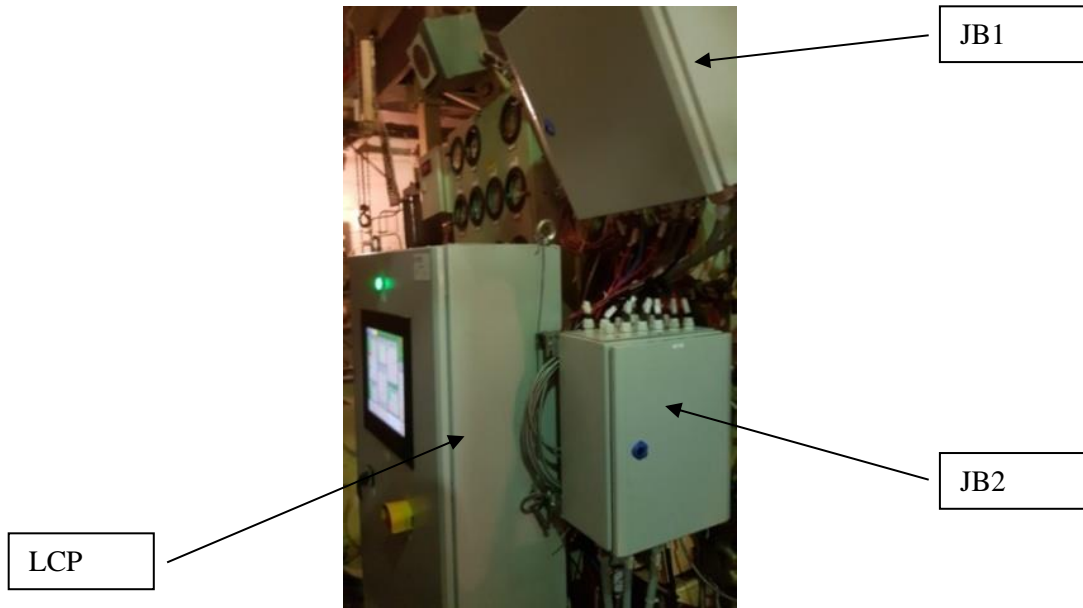


Fig. 12 The position of the junction boxes and LCP on sea tests

Tests were performed with the control system of the ST40M gas turbine on board the F222, the ship having a two-propeller configuration (of engine) and, when respecting the configuration shown in Fig. 12, the results were excellent.

Traction of the propulsion group was tried in several cases, one of the cases being the one in which the motor installed at the port moved the propeller on its side, the other propeller being towed.

3. SOFTWARE OPTIMIZATION

The control application was written in the programming environment Proficy Machine Edition v9.50, a very versatile programming environment developed by General Electric, in which both dedicated PLC applications and operator panel applications can be developed [5]. Starting from the basic functions necessary for the controlling and monitoring the engine's parameters, an application has been developed that is perfectly compatible with the equipment of the propulsion group. The software functions have been optimized to fully meet the engine requirements imposed by the equipment beneficiary.

In this paper it will show comparative optimization of the control function of the fuel dosing valve so that its control is carried out according to expectations.

The initial equations implemented in the logic block (Fig. 13) are given below. The relationship between the position of the fuel metering valve XDC and the position of the metering valve dual torque motor PQC, based on experience with another turbo engine, was established to [6]:

$$\Delta XDC = XDC0 - XDC \quad [\%] \quad (2)$$

$$\Delta PQC = 0.6 \times \Delta XDC \quad [\%] \quad (3)$$

$$PQC_n = 5.76 + \Delta PQC \quad [\%] \quad (4)$$

where:

XDC – Real position of fuel metering valve

XDC0 - Setting position of the fuel metering valve

PQC_{n-1} – Previous position of the metering valve dual torque motor

PQC_n – Present position of the metering valve dual torque motor

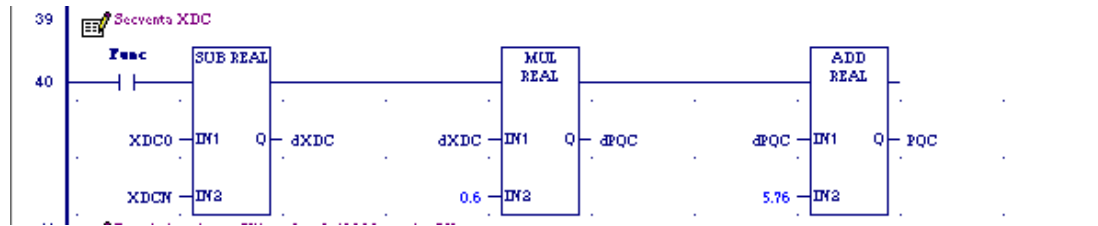


Fig. 13. The ladder diagram of the XDC routine (initial case)

After tests the above formulas have been changed. The deviation is calculated with formula 2. The chosen solution was the implementation of a proportional type regulator, but which has the proportionality factor variable with the deviation size.

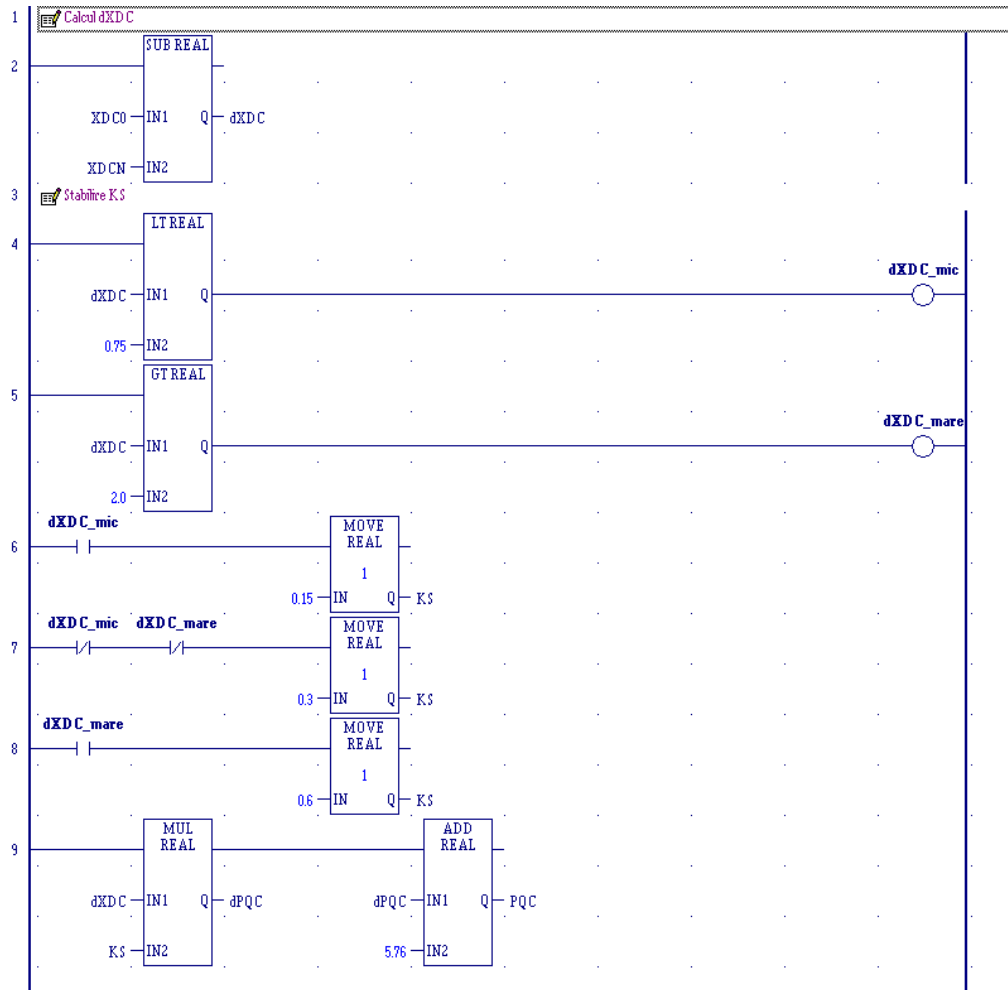


Fig. 14. The ladder diagram of the XDC routine (final case)

The proportionality factor KS is variable and depends on the deviation.

- If $\Delta XDC < 0.75$, then:

$$KS = 0.15 \tag{5}$$

- If $0.75 < \Delta XDC < 2$, then

$$KS = 0.30 \tag{6}$$

- If $\Delta XDC > 2$ rpm, then

$$KS = 0.60 \tag{7}$$

Then the equation (3) becomes

$$\Delta PQC = KS \times \Delta XDC \text{ [%]} \quad (8)$$

The relationship (4) remains the same. By this transformation of the multiplication factor it is intended that the fuel metering system responds faster to high values of deviation and less to values close to equilibrium. The transposition of equations into lines of code is shown in Fig. 14.

4. APPLICATION SCREEN OPTIMIZATION

The screens of the application of the control system of the ST40M turbine have been optimized in the sense of improving the clarity and ergonomics of the parameter display, adding some essential information for the smooth operation of the control and grouping the parameters so that they can be viewed more easily.

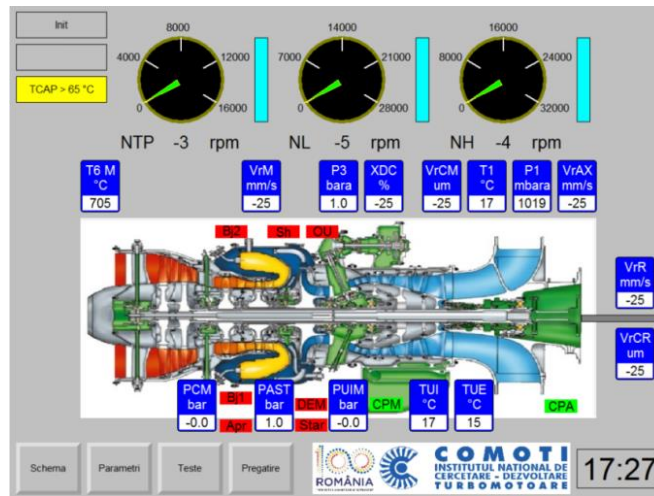


Fig. 15. Initial „Schema” screen

Thus, in the case of the "Schema" screen, compared to the initial version (Fig. 15), the ITT parameter was added – intra turbine exhaust gas temperatures, which is a very important indication of the engine's functioning. It also added information representing the number of hot starts and engine operating hours, which are important for maintenance.

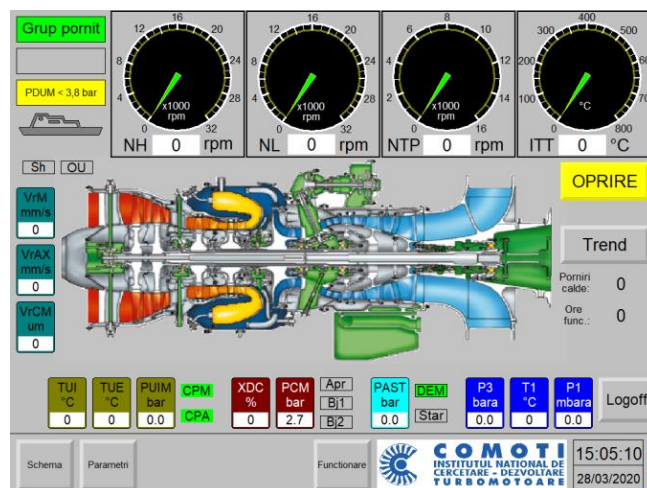


Fig. 16. Final „Schema” screen

On the right side of the screen was placed the “OPRIRE” button for normal engine timing in this screen without allowing the application screens anymore. On the same side was placed the “Trend” button that can be used especially at startup to visualize the trend of the compressor speed and temperature of the gas.

Also on the right side appeared the **Logon / Logoff** button, this being necessary to increase the degree of system protection for operator who can access the system and start the engine. In the lower right corner were placed 3 LEDs that provide information on the status of the data transmission between the operator panel and PLC, as well as on the state of the internal battery of the PLC.

The color of the digital indicators has been changed so as to give information about the category they belong to, so that the operator can quickly get an idea about the installation of the engine it represents. The accuracy of the analogue dials has been improved so that the operator can quickly see the area where the engine speed or temperature is (Fig. 16).

5. CONCLUSIONS

The optimization has resulted in a robust and reliable system. The control system has achieved its objectives, control the gas turbine, displaying functioning parameters and accomplish turbine limit protection. Ease of operation and safety make it easy to modernize and use the ST40M engine in the application. In the design process, the chosen configuration has proven compatibility with the application as well as ease of adaptation for similar projects. System optimization respects the general principles in which for the hardware part, the goal is to reduce the number of components and reduce costs, while for software the aim is to adapt it to the application requirements and ease of use of interfaces. In the case of the command and control system for the gas turbine ST40M, a new solution based on reliable components was obtained, having a user interface with innovative elements obtained through successive optimizations.

Integration into the control system on the ship and improvement of the control software will be the goal of our future efforts. Taking into account the power supply characteristics, it will be tested to supply the local cabinet and the oil pump motor at 400V / 60Hz. The optimization will be continued with the implementation of the solution for future projects.

REFERENCES

- [1] J.H. McMurry, T.B. Keefer, L. Previsani, „Marine gas turbine propulsion system controls: an integrated approach”, Proceedings of ASME Turbo Expo 2008: Power for Land, Sea and Air GT2008, June 9-13, 2008, Berlin, Germany
- [2] *** - ST40M Marine Gas Turbine – Installation Manual
- [3] A. Thomasson, “Modeling and Control of Co-Surge in Bi-Turbo Engines”, World Congress, (2011)
- [4] B. Maclsaac, R. Langton, “Marine Propulsion Systems”, Gas Turbine Propulsion Systems, (2011)
- [5] *** GE-Proficy Machine Edition v9.0
- [6] F. Niculescu, and A. Savescu, “Aspects regarding the control and regulation of an industrial turbine”, ATEE, 2019
- [7] S. Dimitriu, V. Manoliu, E.Alexandrescu, Al. Mihailescu, Gh. Ionescu, A. Stefan, “Advanced structural multilayer architecture for turbo engines”, Metalurgia international (2013)
- [8] A.Pilkington, B. Rosic, S. Horie, “Methods for Controlling Gas Turbine Casing Flows During Engine Shutdown”, Article, 2018
- [9] F.Niculescu, M.L.Vasile, C.Nechifor, A.Stoicescu – “Comparative Analysis between Gas Turbine and Electric Combined Propulsion”, EV2019 - ELECTRICAL VEHICLE INTERNATIONAL CONFERENCE & SHOW”, Bucharest, Octombrie 3-4, 2019

INVESTIGATION METHODOLOGY FOR TURBINE CAVITIES FLOW FIELDS

Razvan Nicoara¹, Valeriu Vilag¹, Emilia Prisacariu¹, Cosmin Suci¹, Madalin Dombrowschi¹, Cristian Dobromirescu¹

ABSTRACT: In the context of increasing air traffic and regulations in this increasingly tight industry, the aim is to reduce greenhouse gas emissions by increasing the thermal efficiency of aviation engines. Thus, it is expected that the aircraft produced in the near future to be powered by an advanced turbofan engine (ultra-high bypass turbofans or geared turbofans). An important component of these engines is the low-pressure turbine, by improving the efficiency of this component a considerable reduction in fuel consumption and greenhouse gas emissions can be obtained. Turbine stages have been extensively studied from an aerodynamic point of view, but its interaction with secondary systems (like cooling and sealing systems) is still a source of important losses. To characterize these flows and interactions, in order to optimize the systems, it is necessary to reproduce the phenomena on dedicated experimental installations. Due to geometry complexity, limited space for instrumentation and high demands in terms of functional parameters requirements, a test cell capable of reproducing the exact operational conditions it is not feasible. Instead a simplified rig must be designed in order to acquire relevant information on the phenomenon of interest. In this paper, a methodology to determine the configuration of an experimental installation for characterizing flows through the inner cavities and labyrinths of a turbine stage is presented and analysed. The methodology is validated through numerical studies and a dedicated experimental installation is proposed.

KEYWORDS: Design methodology, Turbine cavities, Numerical study, Experimental installation, Flow interaction

NOMENCLATURE

b - outer disc radius;
 \dot{m} - purge flow rate;
 S_c - seal clearance;
 C_w – radial velocity;
 $C_{w_{min}}$ - the minimum value of **C_w** required to avoid ingestion;
 Re_θ -rotational Reynolds number;
 μ - fluid viscosity;
 ρ - fluid density;
 Ω - angular velocity;

1. INTRODUCTION

Due to complex construction, cooling requirements and the relative movement between different components of the gas turbine engine, secondary air is extracted from the compressor and used in cooling and sealing systems. A schematic of the secondary air systems in a turbine is presented in fig. 1. In the turbine stage geometry, a gap is required between the fast-rotating disc and the non-moving stator. The swirl inside the cavity is caused by the interaction between the boundary layer and the disc. The interaction between the cooling flow and the main flow through the stage near the sealing labyrinth has an important contribution to the overall losses in the turbine stage. Fluid ingestion from the main flow into the cavity is possible, additional cooling air may be used in order to prevent this phenomenon.

¹ Romanian Research and Development Institute for Gas Turbines COMOTI, Bucharest, Romania

The cavity in question is formed in front of the turbine disc and it is connected to the main annulus flow by a sealing labyrinth. In this context the design of the sealing labyrinth between the two elements has an important role in determining the losses due to fluids interactions and the cooling efficiency of the turbine disc.

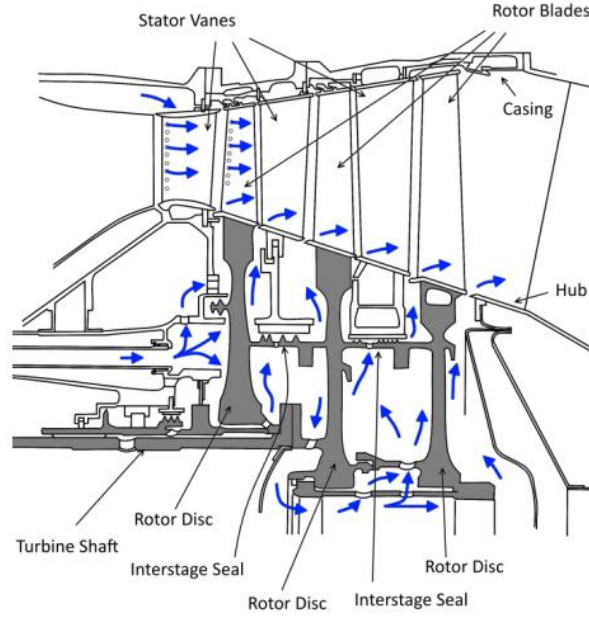


Fig. 1 Secondary air systems in a turbine [1]

The interaction between the cooling flow and the boundary layer developed on the turbine disc determines the formation of a complex swirl system, that moves inside the cavity, with high to low pressure cells. Cao et al. [2] have determined in a numerical and experimental study for a two stage turbine that eight unsteady structures formed and are moving at 90% to 97% of the rotor speed. The structures were found to be independent of the blade passing.

The scientific studies available in literature present significant success correlating experimental data, but it is still apparent that the flow physics is not fully understood. One of the first openly published research was by Bayley and Owen [3]. They presented equation 1 as a correlation of experimental results for a minimum flow rate required to seal a rotor/stator disc cavity with a simple axial clearance at the outer radius and no external flow.

$$Cw_{min} = 0.61 G_c Re_{\phi} \quad (1)$$

$$Cw = \dot{m} / \mu b \quad (2)$$

$$G_c = S_c / b \quad (3)$$

$$Re_{\phi} = \rho \Omega b^2 / \mu \quad (4)$$

An elementary model to deduce the minimum seal flow required to prevent ingestion was presented in Chew [4] and Chew et al. [5]. Using momentum integral methods to estimate the disc boundary layer flow approaching the seal an expression was derived for the pressure drop across the seal, with the minimum sealing flow corresponding to the condition in which the pressure drop equals zero. The model included an empirical factor (k) that was obtained for a number of different seals by comparison with published experimental data.

The importance of external flow, and particularly the associated circumferential pressure variation was established in early experimental studies by Abe et al. [6], Kobayashi et al. [7], Phadke and Owen [8] and Hamabe and Ishida [9]. The pressure-driven mechanism for ingestion is shown in fig. 2.

A 3.5 MW in-line natural gas heater was installed in order to reach a temperature of 675 K at maximum mass flow. A diagram and picture of the installation assembly are presented in fig. 4 and can it be determined that technical and cost requirements for development and operation of this test rig are high.

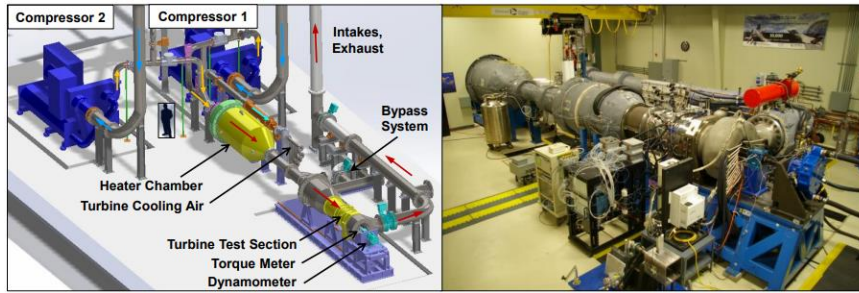


Fig. 4 START experimental installation [17]

2. INVESTIGATION METHODOLOGY

In order to reproduce the phenomena related to cavity flows and flow interactions, with high fidelity at lower costs and demands, a new test rig is proposed. The installation aims at reproducing the thermodynamic parameters on a reduced working channel, with reduced blades span. Turbine vanes and blades correspond to the blade span affected by the interaction with the secondary flow. In this paper the methodology to determine the blade span affected by the flow interactions in order to determine the necessary geometry and parameters will be discussed and numerically analysed on a low-pressure turbine.

These simplified test rigs enable the test of multiple labyrinth geometries on a high-fidelity turbine stage without the need to dissipate a high power and with a lower time and cost for manufacturing.

A proper height of the channel is needed in order to assure that the vortex of interest does not interfere with walls or other vortices due to a small channel. The channel height will be determined by conducting a CFD study on the reference geometry. A numerical simulation will determine first the influence of the turbine hub and shroud, as well as turbine blade profiles on the flow through the stage by employing an ideal geometry without the rotating cavity and clearance tip. Another numerical simulation will determine the influence of the presents of rotating cavities on the flow. In this case, there is no clearance tip and cooling flow for the rotor disc, also no labyrinth geometry will be used. It is expected to encounter fluid ingestion from the working channel to the rotating cavity. At last, another simulation will determine the disturbance in the flow due to cooling air from the cavity. Multiple relevant mass flows will be employed for cooling in order to determine the worst case from the point of view of flow disturbance. From these results, the flow through the stage can be characterized, and it can be determined the minimum height of the blade from which the vortices of interest are not influenced by the height of the channel. By comparing the simplified geometry results with the results for the reference geometry, the present procedure will be validated. The procedure for determining the blade height influenced by the cooling flow from the inner cavities is represented in fig. 5.

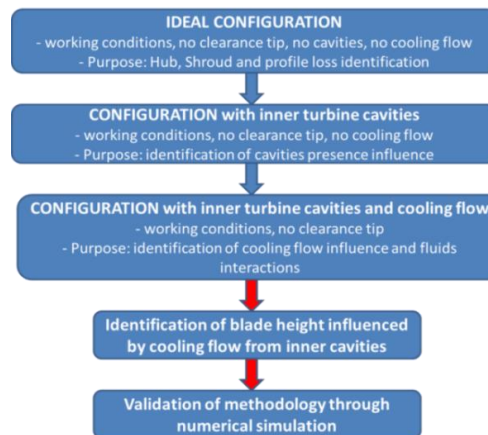


Fig. 5 The procedure for determining the blade height influenced by the cooling flow from the inner cavities by numerical simulations

3. NUMERICAL STUDY

Following the procedure described above, a RANS (Reynolds-averaged Navier-Stokes) numerical study was conducted to determine the blade height affected by the injection of cooling fluid into the working channel on a 1500 KW turbine design by COMOTI. An ideal configuration was numerical studied in order to determine the characteristics of the turbine; ideal configuration assumed here implies geometry without clearance tip, cavities and cooling flow. The numerical studies were conducted in symmetrical flow hypotheses between blade channels. Thus, a single channel was geometrical reproduced. In fig. 6 the numerical grids for the guided vane and the rotor blade are presented. The numerical grid was constructed with 1 mm cells and even smaller ones near the walls; the guide vane grid has approximately 950000 nodes and the blade grid approximately 300000.

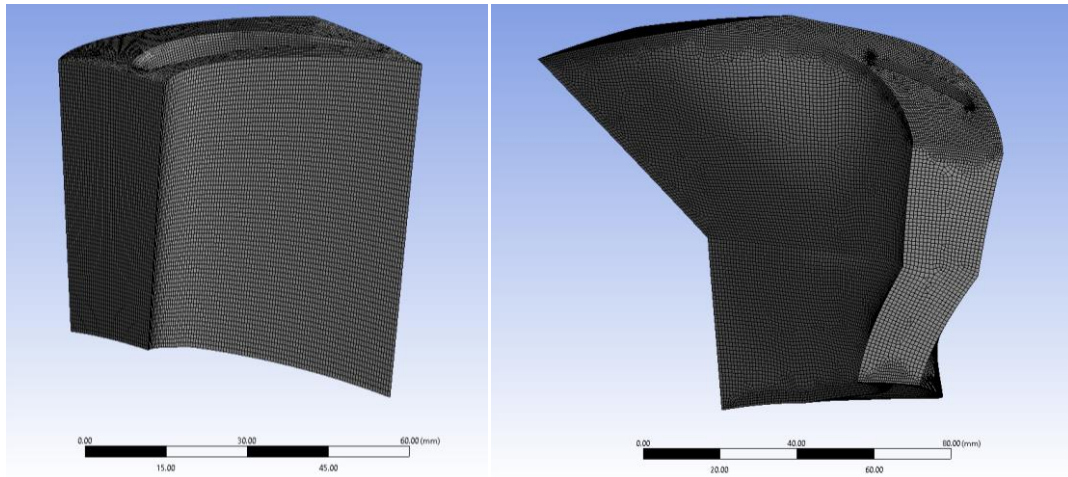


Fig. 6 Numerical grid for Stator and Rotor blades

The boundary conditions were set in order to impose the fluid properties at the stage inlet and to determine the properties at the stage outlet. A constant mass flow hypothesis in the turbine stage was used. Thus, Inlet boundary conditions was set at the guide vane inlet, setting the total temperature and pressure, Outlet boundary conditions at the rotor outlet, setting the mass flow and wall boundary conditions for hub, shroud and profiles. Periodic conditions were used in order to reduce the computational demands of the numerical study. The k-epsilon turbulence model was employed to determine the flow field. Table 1 presents the boundary conditions used for the numerical study.

Table 1. Boundary conditions

No.	Boundary	Type	Condition
1	INLET	inlet	Total pressure = 2.64 bar Temperature = 977 K
2	OUTLET	outlet	Mass flow = 8 (total for all sectors)
3	WALL	wall	No slip wall
4	PERIODIC	periodic	One sector out of 44 for the Stator One sector out of 53 for the Rotor
5	STATOR-ROTOR INTERFACE	Frozen rotor	-

In fig. 7 the fluid domain, boundary conditions and the resulting y^+ are presented. The y^+ values are acceptable considering the turbulence model used and the fluid evolution through the stage.

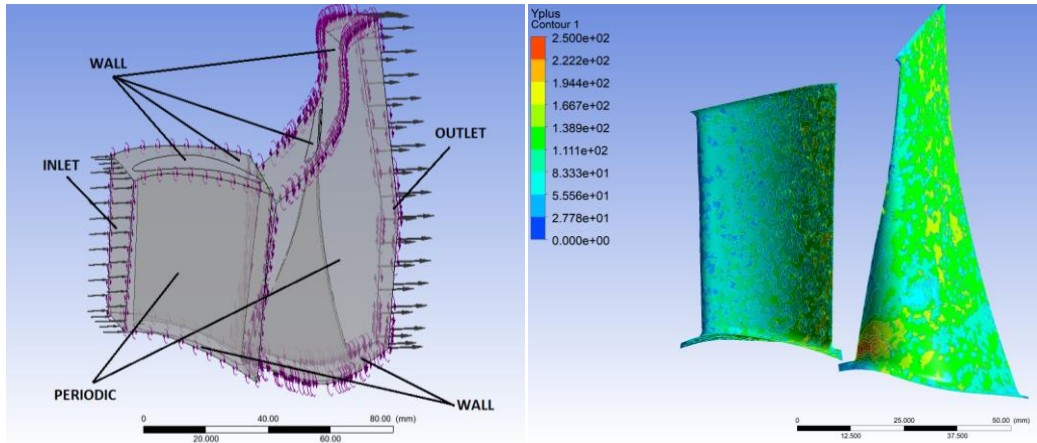


Fig. 7 Numerical case boundary conditions and the resulting y^+

By analysing the results, it was concluded that the stage was properly design without radial circulation as it can be determined from the velocity streamlines distribution presented in fig. 8.

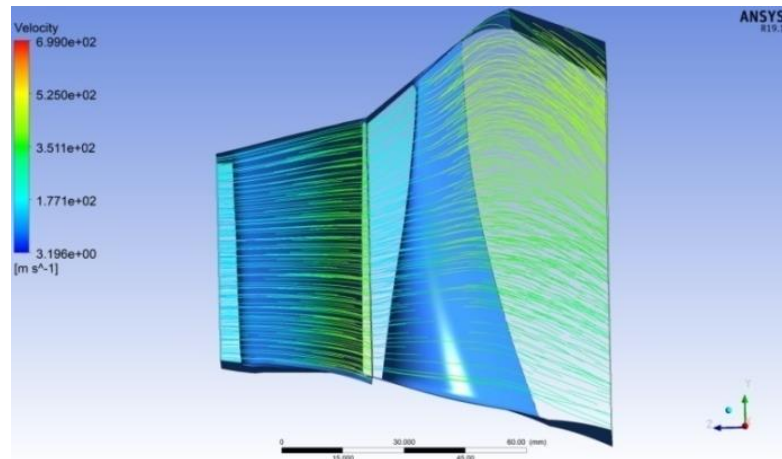


Fig. 8 Velocity streamlines through the turbine stage assuming the ideal configuration described above

The next step was to simulate the inner rotating cavity without the cooling flow in order to determine the influence of the cavity. For this case the geometry was created in order to recreate the inner cavity of the turbine, the cavity being delimited by the stator assembly geometry (below stator hub) and the rotor disc. Also the cavity downstream the rotor disc was created. In this numerical study it is expected that ingestion from the main working channel into the cavity to occur but the influence of this phenomena to the flow through the main channel to be reduced. In fig. 9 the velocity streamlines are presented and can be determined that the ingestion phenomenon was determined in this study.

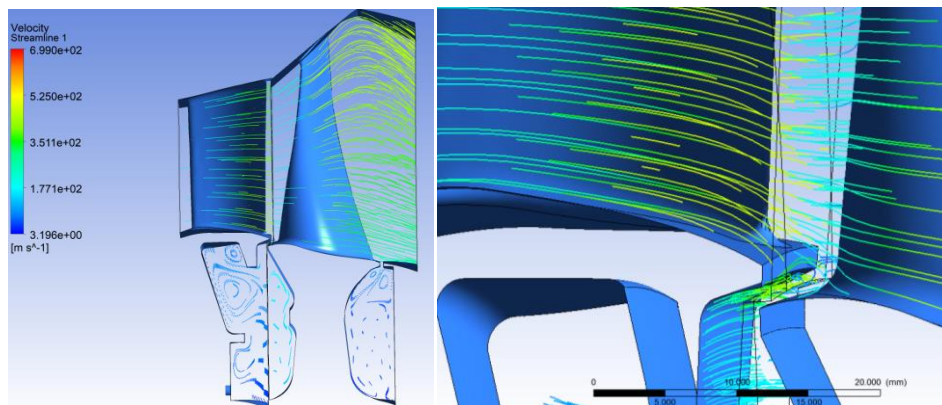


Fig. 9 Velocity streamlines through the turbine stage with inner cavities

In order to determine the influence of the cooling fluid on the flow through the working channel, 3 values of the cooling fluid mass flow were simulated as described in Table 2. The cooling fluid mass flow used in this numerical study are higher than the values used in modern gas turbine engines in order to assume the worst case scenario.

Table 2. Cooling fluid mass flow

No.	Cooling mass flow [kg/s]	Cooling mass flow [% working mass flow]
1	0.05	0.625
2	0.15	1.875
3	0.25	3.125

The cooling flow injection has the effect of eliminating the ingestion phenomenon from the working channel but the interaction with the main flow near the hub of the rotor blade leads to the formation of additional vortices. The cooling mass flow has a direct impact on these vortices, thus by increasing the mass flow of the cooling fluid leads to an increase in turbulence near the hub and downstream of the rotor blades. This effect can be observed from fig. 10, which presents velocity streamlines for the 3 cooling flows studied.

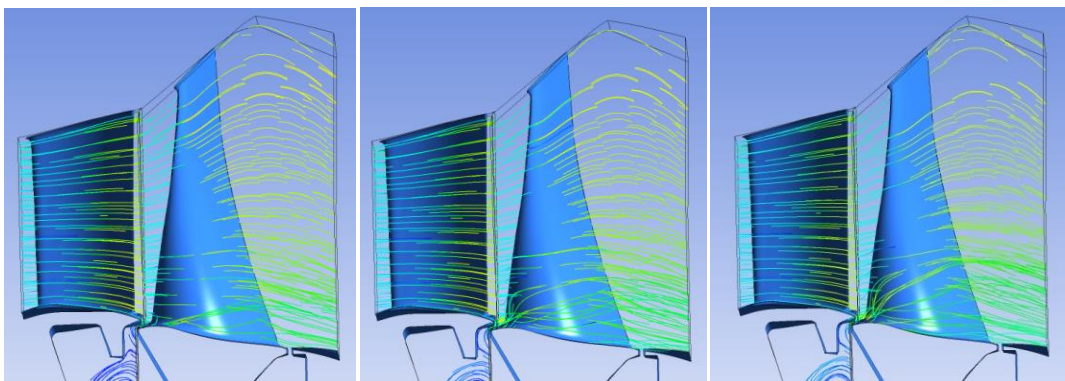


Fig. 10 Velocity streamlines through the turbine stage with cooling flow for 3 mass flow rates (0.05, 0.15, 0.25 kg/s)

In order to determine the blade height affected by the interaction of the secondary flow with the main annulus flow the turbulence kinetic energy was analysed in a plane downstream of the rotor blade by comparison between the cases with and without cooling flow.

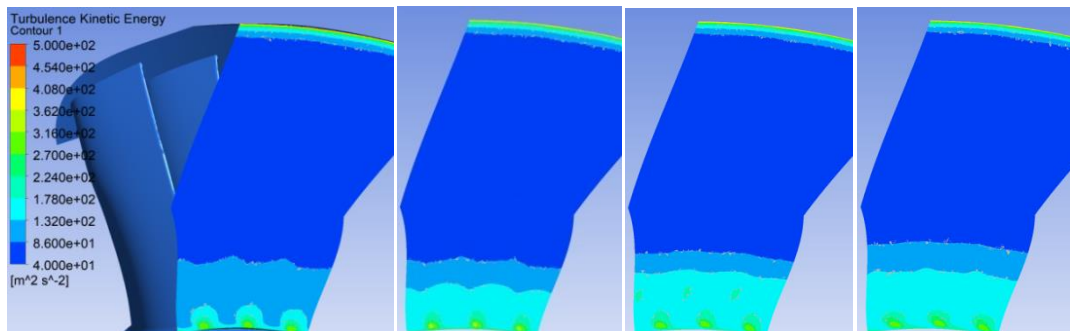


Fig. 11 Turbulent kinetic energy downstream the rotor blade for: no cooling flow, 0.05 k/s, 0.15 and 0.25 kg/s cooling flow

Based on the streamlines distribution and the turbulent kinetic energy analysis, presented in fig. 10 respectively fig. 11, it was determined that one third of the rotor blade is affected by the interactions of the two flow systems. Thus, the study of these phenomena can be conducted, with satisfactory precision, only on this part of the working channel. In the analysis of the affected blade height, the effect of the shroud was taken into account beside that of the vortices near the blade hub.

A reduced geometry was created with only a third of the blades in order to reproduce the phenomena of interest with less demanding parameters. The flow through the turbine was reproduce by calculating the inlet parameters respective to the reduce geometry. Thus, the pressure and the temperature were kept constant and the mass flow rate of the main working fluid was calculated in order to obtain the same flow velocities.

The mass flow rate of the cooling flow was kept constant at 0.15 kg/s. Fig. 12 presents the velocity streamlines for the reduce geometry. The streamlines distribution shows a similar behaviour compared with the complete geometry case.

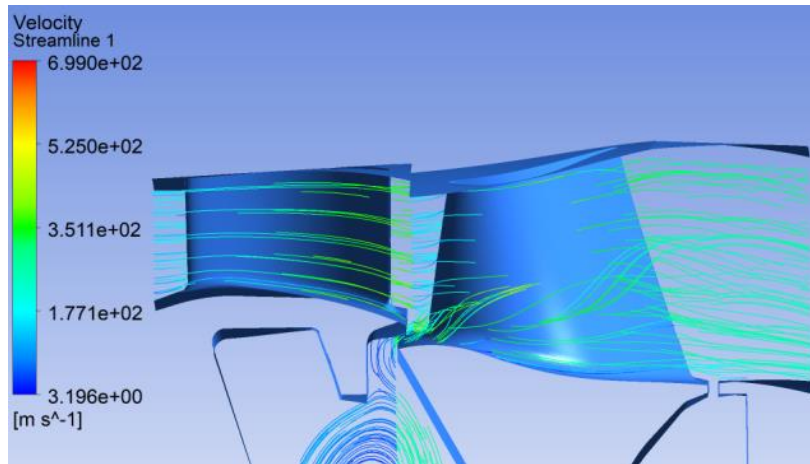


Fig. 12 Velocity streamlines through the reduced geometry

From the turbulent kinetic energy analysis downstream the rotor, fig. 13, can be determined, by comparison with the complete geometry results, that the two cases show similar results. Similar structures can be observed with a similar blade height characterized by a higher turbulence. From this analysis, it can be seen that the height of the channel was correctly determined, thus the high turbulence zone near the hub, characteristic of flow interactions, is separated from the turbulence zone near the shroud by a low turbulence zone. This is similar to the complete geometry case, the difference being the area of the low turbulence zone. The turbulent structures near the hub are formed in the same location, for the two cases, with a minimum difference in intensity.

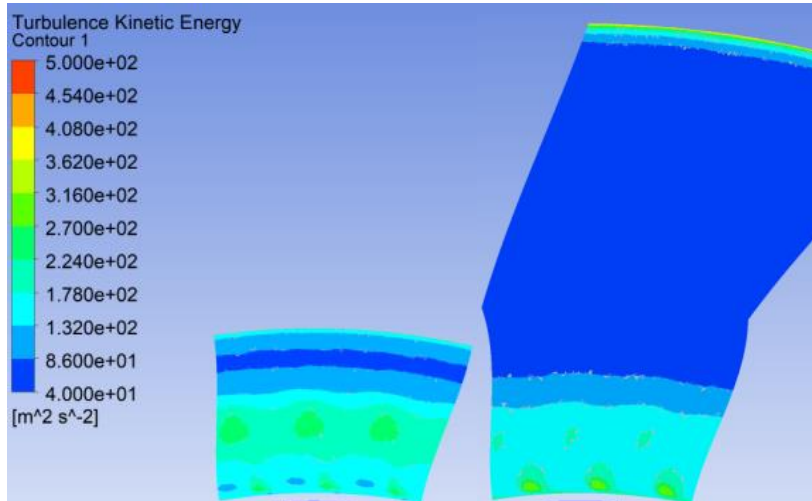


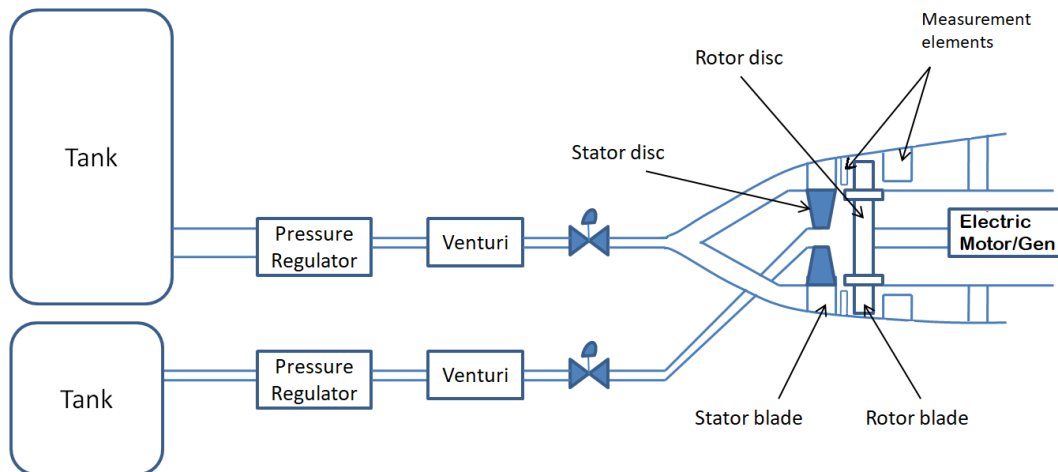
Fig. 13. Turbulent kinetic energy downstream the rotor blade for reduced and complete geometry

As the results for the two cases, the reduced and complete geometry, are similar it can be concluded that the study of the effect of the cooling flow on the flow through the working flow can be completed on a simplified rig with a lower channel height and less demanding parameters. Thus, the methodology proposed in this paper is validated through numerical study. The advantages in studying the flows through the inner cavities and labyrinths of a turbine stage and the effects of the cooling flow on the main flow through the stages can be deduced from table 3, which presents the performances and parameters of the complete and reduced geometry cases. As resulted from the table 3, the inlet temperature and pressure are the same, in order to reproduce the flow conditions through the stage accurately. The main advantages of the reduce geometry are the lower mass flow used with a reduce geometry configuration, less than 30%, and lower power that needs to be dissipated during the experiment, less than 22%.

Table 3. Comparison of complete and reduced geometry parameters

Parameter	Complete geometry	Reduced geometry
Inlet temperature [K]	977	977
Inlet pressure [bara]	2.64	2.64
Mass flow [kg/s]	8	2.374
Power generated [KW]	850	184

A dedicated test rig capable of identifying the phenomena characteristic of flow interaction determined by the cooling flow is proposed in fig. 14. The experimental installation comprise of a high volume, high pressure fluid tank, which works as a working fluid source, pressure regulators and mass flow measurements in order to reproduce the necessary inlet conditions. Depending on the required working temperatures, one can also choose to introduce a heat source on the working fluid path (e.g. combustion chamber) or to use similarity parameters to reproduce the necessary regime. The flow through the experimental stage is similar to the reference geometry but reproducing only the blade height necessary as was presented in this paper. The power produced by the rotor is dissipated (converted into electrical energy) by an electric generator. The cooling fluid is introduced through a separate route, this being recommended for better control over its parameters (flow, pressure and temperature). The source of this cooling flow can be, as in the previous case, a compressor or a tank.

**Fig. 14 Proposed experimental installation scheme**

3. CONCLUSIONS

In this paper a methodology to determine the geometry of a simplified experimental installation, capable to characterise the flow fields and flow interactions as a result of cooling flow injection in the main working channel, was proposed and numerical analysed. The methodology is composed of 5 steps in order to eliminate the influence of different phenomena (blade, hub, shroud and cavity effects), that lead to a proper channel height with similar flow fields. The numerical cases were presented resulting that for the turbine stage analysed only a one third channel height was affected by the vortices determined by the flow interactions. A simplified geometry, consisting in a one third blade height, was numerically tested and compared with the complete geometry case. By comparison of the two cases it was determined that similar results were obtained, thus validating the methodology.

The effect of cooling mass flow on the flow through the turbine was also studied, 3 mass flow rates were simulated and compared with the case with no cooling flow. From this study resulted that the turbulence determined by the interaction of cooling flow with the main working flow increases with the increase of cooling flow.

By using the simplified geometry, the mass flow needed to reproduce the turbine regime was approximately 30% of the mass flow needed for the complete geometry case and the power generated by the rotor blades was approximately 21% from the nominal power of the turbine stage. These values are only informative because the cooling mass flow rates used in this paper are higher than those used in gas turbine engines and also the effect of the clearance tip was not accounted for. Nonetheless, they underline the advantages of this method. Based on the method discussed in this paper, an experimental installation was proposed.

Future work should analyse the effect of the tip clearance with the aim of improving the methodology. By taking into account the tip clearance, an increase of the channel height needed in order to maintain a low turbulence zone between the vortices near the hub and shroud of the rotor can be required. Another analysis should be conducted to study the effect of the unsteady behaviour identified in the articles mentioned in this paper.

ACKNOWLEDGEMENT

This work was carried out within “Nucleu” Program 2N/2019, supported by the Romanian Minister of Research and Innovation.

REFERENCES

- [1] Rolls-Royce plc, 1996, *The Jet Engine*, Rolls-Royce plc, Derby, England, ISBN:0 902121 2 35.
- [2] Cao, C.; Chew, J.W.; Millington, P.R.; Hogg, S.I. Interaction of Rim Seal and Annulus Flows in an Axial Flow Turbine. *ASME J. Eng. Gas Turb. Power* 2004, 126, 786–793
- [3] Bayley FJ and Owen JM. The fluid dynamics of a shrouded disk system with a radial outflow of coolant. *J Eng Power* 1970; 92: 335-341.
- [4] Chew JW. A theoretical study of ingress for shrouded rotating disc systems with radial outflow. *ASME J Turbomach* 1991; 113: 91-97.
- [5] Chew JW, Dadkhah S and Turner AB. Rim sealing of rotor-stator wheel spaces in the absence of external flow. *ASME J Turbomach* 1992; 114: 433-438.
- [6] Abe T, Kikuchi J and Takeuchi H. An investigation of turbine disc cooling. In: *Third CIMAC congress, Vienna 1979*, paper no. GT30.
- [7] Kobayashi N, Matsumoto M and Shizuya M. An experimental investigation of a gas turbine disk cooling system. *ASME J Eng Gas Turbines power* 1984; 106: 136-141.
- [8] Phadke UP and Owen JM. Aerodynamic aspects of the sealing gas-turbine rotor-stator systems part 1-3. *Int J Heat Fluid Flow* 1988; 9: 98-117
- [9] Hamabe K and Ishida K. Rim seal experiments and analysis of a rotor-stator system with non-axisymmetric main flow. *ASME paper 92-GT-160*, 1992.
- [10] Chew, John & Gao, Feng & Palermo, Donato. (2018). Flow mechanisms in axial turbine rim sealing. *Proceedings of the Institution of Mechanical Engineers, Part C: Journal of Mechanical Engineering Science*. 10.1177/0954406218784612.
- [11] Jakoby R, Zierer T, Lindblad K, et al. Numerical simulation of the unsteady flow field in an axial gas turbine rim seal configuration. In *Proceedings of the ASME turbo expo 2004,2004*, paper no. GT2004-53829
- [12] Schadler R, Kalfas AI, Abhari RS, et al. Modulation and radial migration of turbine cavity modes by rim seal purge flow. *ASME J turbomach* 2016; 139:011011-011011-10.
- [13] Roy RP, Feng JJ, Nazary DD, et al. Experiments on gas ingestion through axial-flow turbine rim seals. *ASME J Eng Gas Turbine Power* 2005; 127: 127: 573-582.
- [14] Camci, Cengiz & Averbach, Michael & Town, Jason. (2019). Unsteady Flow Structures within a Turbine Rim Seal Cavity in the Presence of Purge Flow—An Experimental and Computational Unsteady Aerodynamics Investigation. *Aerospace*. 6. 60. 10.3390/aerospace6050060.
- [15] Guida, Roberto &Lengani, Davide & Simoni, Daniele & Ubaldi, M. & Zunino, Pietro. (2018). New Facility Setup for the Investigation of Cooling Flow, Viscous and Rotational Effects on the Interstage Seal Flow Behavior of a Gas Turbine. *V05BT15A017*. 10.1115/GT2018-75630.
- [16] Barringer, Michael & Coward, Andrew & Clark, Ken & Thole, Karen & Schmitz, John & Wagner, Joel & Alvin, Mary Anne & Burke, Patcharin & Dennis, Rich. (2014). The Design of a Steady Aero Thermal Research Turbine (START) for Studying Secondary Flow Leakages and Airfoil Heat Transfer. *V05CT16A013*. 10.1115/GT2014-25570.
- [17] Berdanier, Reid & Monge-Concepción, I. & Knisely, Brian & Barringer, M.D. & Thole, Karen & Grover, E.A.. (2019). Scaling sealing effectiveness in a stator-rotor cavity for differing blade spans. *Journal of Turbomachinery*. 141. 10.1115/1.4042423.

SPIRAL PLATE HEAT EXCHANGER WITH HIGH HEAT TRANSFER COEFFICIENT FOR MICROTURBINE

Traian TIPA¹, Andrei George TOTU¹, Andrei RADU¹, Madalin DOMBROVSCHI¹
Cristian OLARIU¹, Sebastian VOICU¹

ABSTRACT: This paper proposes a unique heat exchanger, spiral form, with high convection coefficient, compact geometry and lightweight destined to be applied for the manufacturing of the microturbines to increase its thermal efficiency. This type of heat exchanger is unique through its constructive scheme composed of one type of corrugated thin welded plates which separate fluids and the heat transfer occurs directly across the plates. Due to its spiral form, the heat exchanger has a high heat transfer coefficient, both working fluids traveling a larger path through the heat exchanger, while a large energy exchange takes place in this way. At the same time, this paper focuses on the benefits of using recuperative thermodynamic cycles in gas turbines. The main heat exchanger parameters were analytical and numerical approached to demonstrate its benefits.

KEYWORDS: microturbine, recuperative thermodynamic cycle, spiral plate heat exchanger, thermal and hydraulic performance;

NOMENCLATURE

A	heat transfer surface area [m ²]	p ₁	compressor inlet pressure [bar]
CFD	computational fluid dynamics	p ₂	compressor outlet pressure [bar]
K	heat transfer coefficient [W/m ² K]	p ₃	turbine inlet pressure [bar]
L	plate length [mm]	p ₄	turbine outlet pressure [bar]
M _a	air flow rate [kg/s]	p ₅	combustor inlet pressure [bar]
M _g	gas flow rate [kg/s]	p ₆	exhaust pressure [K]
Nu	Nusselt number	w	fluid velocity [m/s]
Pr	Prandtl number		
Q	heat exchanger load [W]		Greek symbols
Re	Reynolds number	α	convection coefficient
SFC	Specific Fuel Consumption [g/kWh]	δ	plate thickness [mm]
T ₁	compressor inlet temperature [K]	ε	thermal effectiveness
T ₂	compressor outlet temperature [K]	η _t	microturbine thermal efficiency
T ₃	turbine inlet temperature [K]	θ	T ₃ /T ₁
T ₄	turbine outlet temperature [K]	λ	thermal conductivity [W/mK]
T ₅	combustor inlet temperature [K]	μ	dynamic viscosity [Ns/m ²]
T ₆	exhaust temperature [K]	ν	kinematic viscosity [m ² /s]
ΔT _{med}	logarithmic mean temperature difference [K]	π _c	pressure ratio
c _p	specific heat [J/kgK]	ρ	fluid density [kg/m ³]
d _e	hydraulic diameter [m]		
f	friction factor		
h	specific enthalpy [kJ/kg]		
k	adiabatic index		

¹ Romanian Research and Development Institute for Gas Turbines COMOTI

1. INTRODUCTION

A lot of the power needs from driving tanks, jets and helicopters to power generation and industrial power uses are fulfilled by gas turbines who have been receiving important attention over the past several decades because of the growing demand for environmentally friendly engines with lower emissions and improved specific consumption and, thus, operation costs. These requirements can be met by incorporating heat exchangers into gas turbines (Regenerative Brayton cycle), which leads to an increase of the gas-turbine cycle efficiency by transferring the heat from the hot exhausted burnt gases to compressed air before entering the combustion chamber "Fig.1".

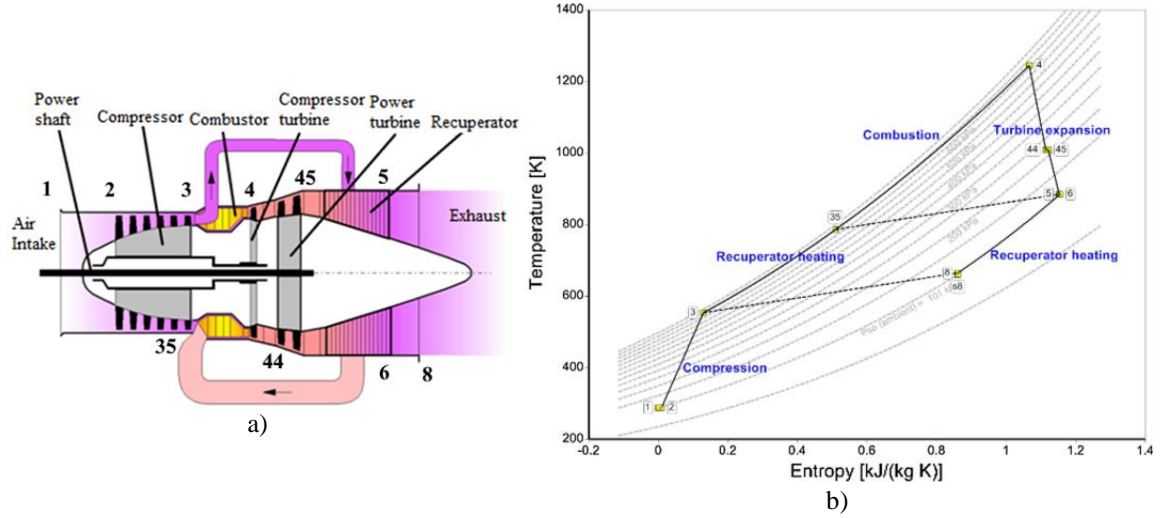


Fig.1 (a). Illustration of a recuperated turboshaft engine; (b). T-s diagram for the recuperated cycle based on GasTurb13 [1]

In the case of the Regenerative Brayton cycle, besides the main parameters such as pressure ratio and turbine inlet temperature, the gas turbine performance depends on thermal effectiveness also. This parameter is defined as the ratio between the heat flux received by the compressed air and maximum heat flux available:

$$\varepsilon = \frac{T_5 - T_2}{T_4 - T_2} \quad [2] \quad (1)$$

Usually, the thermal effectiveness can take values in the range (0,1), the extreme values cannot be reached. Higher thermal effectiveness requires a large heat transfer area which leads to a large-sized heat exchanger. An important constrain in the regenerative Brayton cycle is that $T_2 < T_4$, otherwise, heat recovery is not efficient. As it is known that:

$$\frac{T_4}{T_2} = \frac{T_4 T_3 T_1}{T_3 T_1 T_2} = \theta \left(\frac{p_4}{p_3}\right)^{\frac{k-1}{k}} \left(\frac{p_1}{p_2}\right)^{\frac{k-1}{k}} = \frac{\theta}{\pi_c^{\frac{k-1}{k}}} \quad [2] \quad (2)$$

it can be concluded that heat recovery can be realized only if:

$$\pi_c < \sqrt{\frac{k}{\theta^{k-1}}} \quad [2] \quad (3)$$

and the thermal efficiency of the gas turbine in the case of regenerative Brayton cycle will be:

$$\eta_t^{(rec)} = \frac{\left(\theta - \pi_c^{\frac{k-1}{k}}\right) \left(\pi_c^{\frac{k-1}{k}} - 1\right)}{\theta \pi_c^{\frac{k-1}{k}} - \pi_c^{\frac{k-1}{k}} - \varepsilon \left(\theta - \pi_c^{\frac{k-1}{k}}\right)} \quad [2] \quad (4)$$

In the case of the regenerative Brayton cycle, the variation of the main engine parameters such as thermal efficiency, specific fuel consumption, thermal effectiveness, pressure ratio, and turbine inlet temperature can be seen in the following figures. As is shown in “Fig.2 a)-b)”, the thermal effectiveness has a high influence on engine thermal efficiency and specific fuel consumption. Thus, for small pressure ratio ($\pi_c=4$) the thermal efficiency of the engine, is the higher the θ is higher, and the specific fuel consumption decreases considerably as thermal effectiveness is greater.

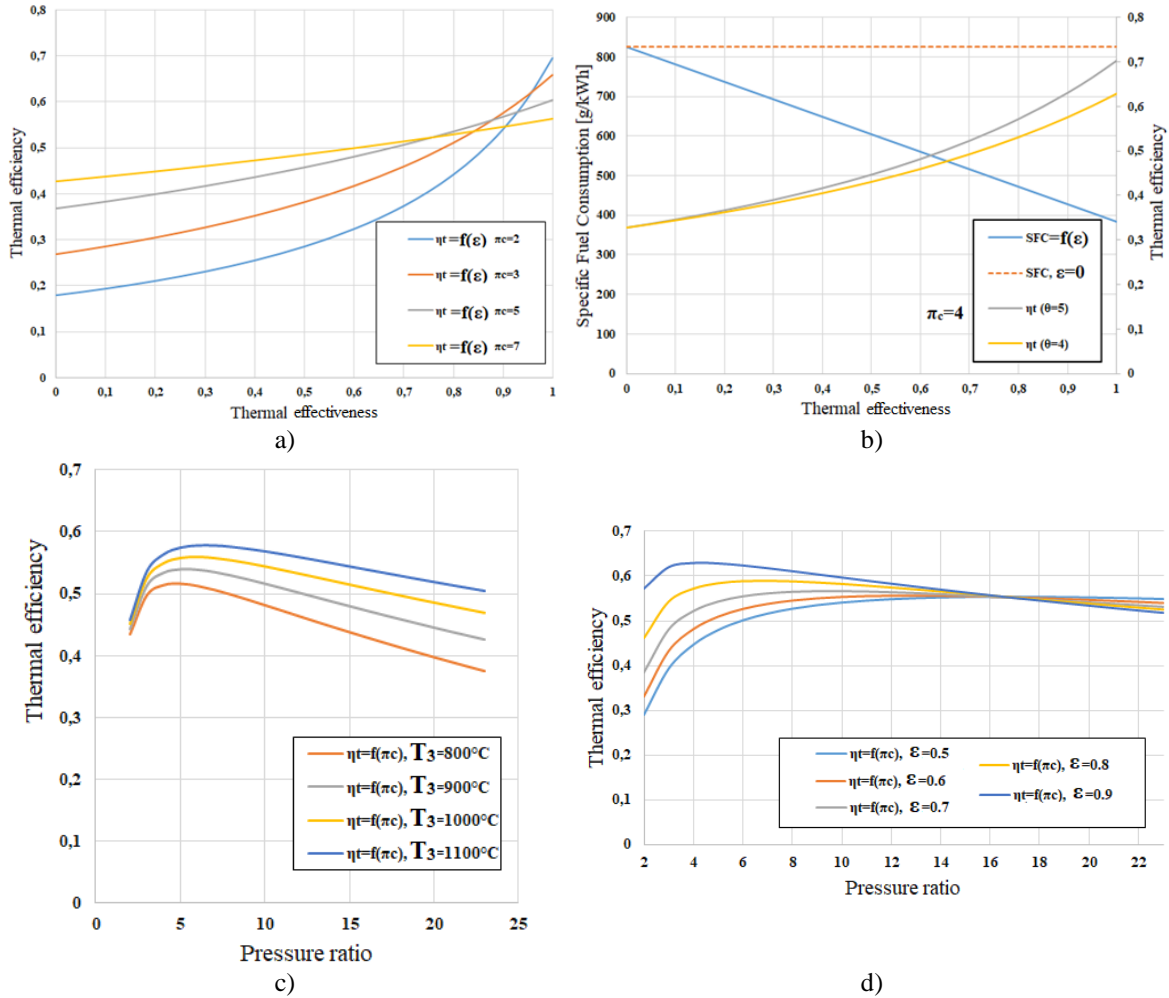


Fig.2 Main parameters variation in the case of Regenerative Brayton cycle

“Fig.2 c)-d)” relates the variation of the thermal efficiency with pressure ratio for different thermal effectiveness and inlet turbine temperature. It can be concluded that for small thermal effectiveness values, the thermal efficiency has an increasing appeal for small pressure ratio (up to 8), and as π_c increases (values greater than 8), the efficiency decreases. It can be concluded that exist an optimum π_c for the regeneration.

2. RECUPERATOR TECHNOLOGY STATUS

Initial heat exchangers, including recuperators, that have been used in the gas turbine systems, were essentially designed based on size limitation, reliability, and costs [3]. For this reason, many new types of recuperators with smaller sizes, lower costs, and higher effectiveness have recently been proposed. They are usually classified into three types according to their heat transfer surface geometry, such as primary-surface, plate-fin, and tubular recuperators.

2.1 Primary-surface recuperators

The primary surface recuperators comprises of thin corrugated sheets stacked together with gas (hot) stream and air (cold) stream flowing through alternate layers. The main characteristic of this kind of construction is that heat transfer takes place directly through these thin plates without secondary surface fin efficiency effects.

The primary surface recuperator is suitable for relatively low pressure (LP) ratio engine applications, like many turboshafts engines (≈ 15 bar). In addition, it is not feasible to incorporate this type of recuperator into high pressure (HP) ratio engines due to the lack of supporting structural elements between flow passages.

The manufacturing of primary surface recuperators is amenable to high volume manufacturing processes, which leads to lower cost. Produced by pressing, stamping or folding of thin metal sheets, the primary surface heat exchanger has different patterns including cross-corrugated (CC), cross-undulated (CU) and cross-wavy (CW) [4]. Recently, unlike traditional periodic profiles with simple geometry construction, some novel primary surfaces, having more complex 3D CC geometries are shown in "Fig.3". In comparison with the conventional sinusoidal corrugation, a pressure drop reduction was estimated for the antiphase and full-wave rectified secondary corrugation models without big changes to the predicted heat transfer capacity "Fig.3 (a-c)" [5]. Considering the different operating pressure and pressure drop requirements on the hot and cold sides, it was investigated that the aerothermal performance of CC primary surface recuperator having asymmetric cross-sectional profiles, as shown in "Fig.3 (d)". Based on the calculation results, it is observed that the asymmetric profile can balance the pressure drops on both sides with reduced weight and volume of heat exchanger matrix, though this comes with a slight loss of effectiveness [5].

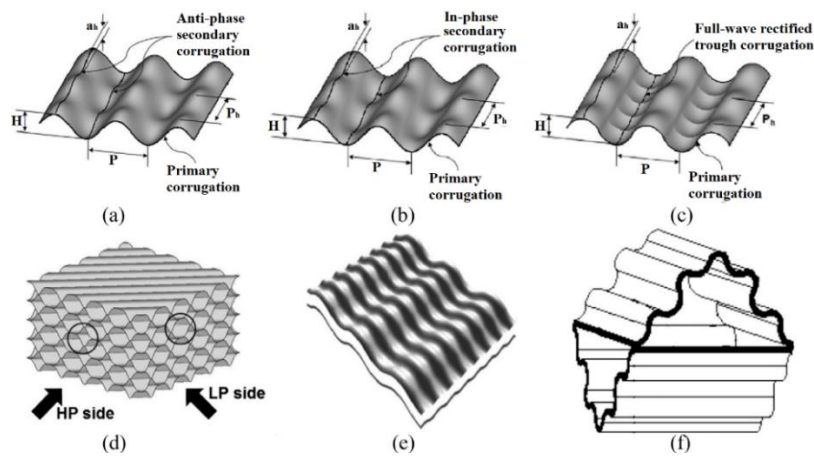


Fig. 3 Configurations of modified primary surfaces [5]

Primary-surface recuperators have been developed by many companies since the 1970s. In "Fig.4" are related some important types of recuperators, with different configurations and different types of flow, counterflow, crossflow, or parallel-flow.

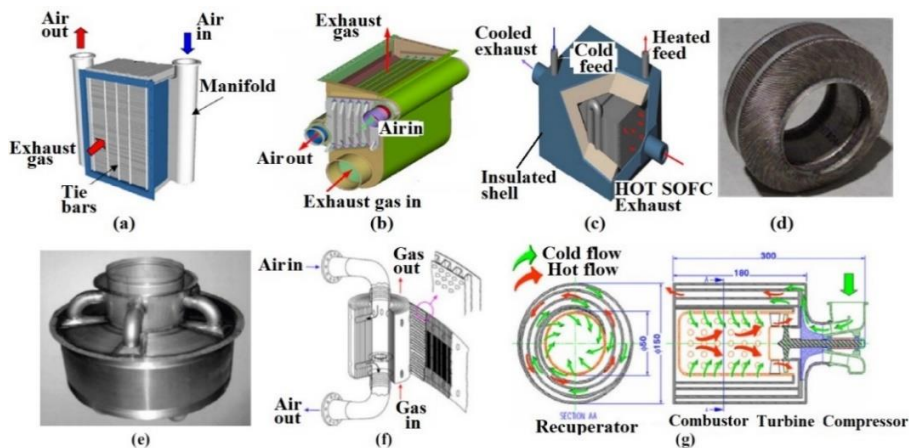


Fig.4 Pictures of recuperators from: a) RSAB [6]; b) Honeywell [7]; c) SIC [8]; d) Capstone [9]; e) ACTE [10]; f) Rolls-Royce [11]; g) Swiss-Roll [12]

2.2 Plate-fin recuperators

Plate-fin recuperators mainly consist of a series of fin surfaces together with flat separators known as parting sheets. The main attribute of the plate-fin surface is that the introduced fins work as secondary heat transfer surface and provide mechanical support against internal pressure differentials between layers.

Ingersoll-Rand began to develop plate-fin recuperators, which adopts offset fins in the heat exchange area, as shown in "Fig.5" [13]. AlliedSignal produced an industrial gas-turbine plate-fin recuperator with offset plate-fin surfaces, and the entire heat exchanger (plate, fins, headering bars, and manifolds) was brazed to form a very strong monolithic unit [14]. Abiko invented a plate-fin heat exchanger for micro gas turbines with four different embodiments of their invention [15].

2.3. Tubular recuperators

Tubular recuperators consist of a series of tubes within an outer shell. As shown in "Fig.6", MTU developed a cross-counter flow recuperator that consisted of two manifold tubes and a bundle of profile tubes.

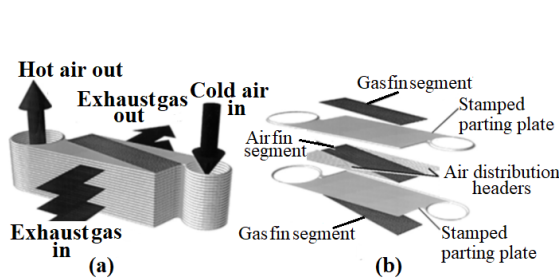


Fig.5 Flow paths (a) and a unit cell (b) of an Ingersoll-Rand's plate-fin recuperator [13]

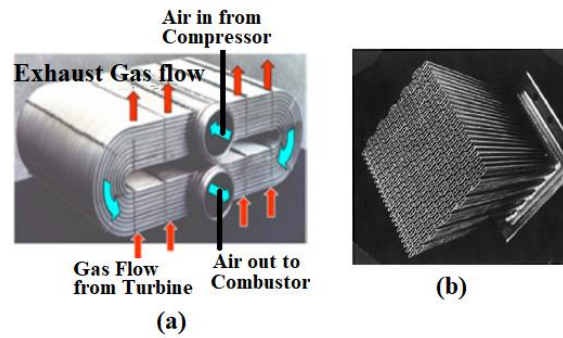


Fig. 6 MTU tubular recuperator: (a) Fluids flow; (b) Cross-section [13]

3. RECUPERATOR ARCHITECTURE

The much greater heat transfer demands required for a recuperator suitable for use with a 200 kW microturbine led the assignee of the present paper to develop a completely new design for an annular counter-flow primary surface heat exchanger, "Fig. 7" shows a cross-section of the microturbine having the annular heat exchanger. The physical dimensions of the microturbine, combined with the surface area required to provide the necessary heat transfer, led to the construction of an annular heat exchanger having a relatively high ratio of radial width to axial length. Thus, in this paper is proposed a unique recuperator (heat exchanger) with high α (convection coefficient), compact geometry and lightweight, for preheating air before it enters the combustion chamber of the micro gas turbine.

As it can be seen in "Fig.7", the air enters the microturbine through inlet air passage, then is compressed by the compressor and high-pressure air exits compressor via the recuperator air passage which directs the compressed air through the recuperator along spiral (helix) path. The compressed air is pre-heated in the recuperator and guided toward the combustor chamber when it is combined with fuel in a known manner and the heated products of combustion are directed via turbine inlet passage to the turbine which drives the compressor and generator with common shaft. Hot exhaust gas from the turbine is carried via turbine exhaust passage back to the recuperator.

The exhaust gas flows in the same spiral path, as the compressed air but in a counter direction. The spent low-pressure exhaust gas is exhausted via outlet passage after it passes through the recuperator. The heat exchanger can be generally described as a spiral annular counter flow recuperator that surrounds the compressor and turbine of the microturbine. Also, in this way, the working fluids have a smooth flow, without any complicated cross areas, this fact leading to minimum pressure losses.

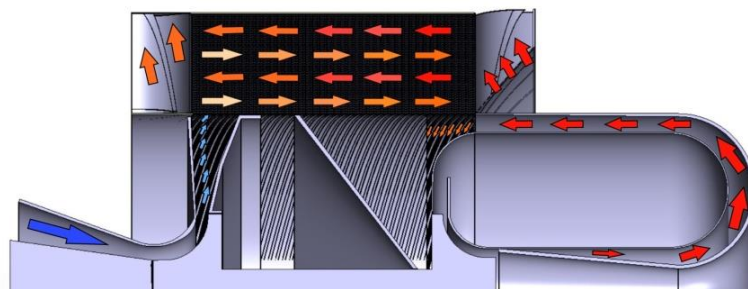


Fig.7 Cross section microturbine equipped with spiral annular recuperator

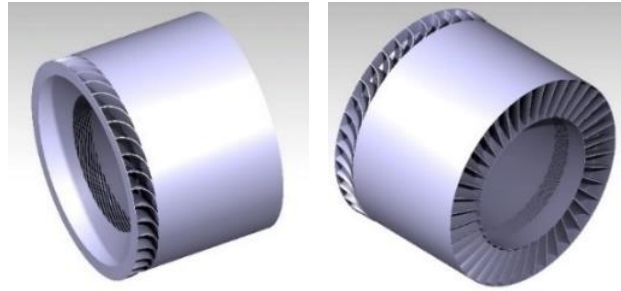


Fig. 8 External shape of the designed recuperator

The recuperator is made up of a large number of single pattern corrugation spiral thin plates, stacked together back to back composing the fluids passing channels in this way. The back to back set of the plates provides minimum welding operations in forming the core of the recuperator. The plates are supported by each other and the problem regarding the different pressure of the cold and hot fluids which require good construction and technological solutions is solved in this way.

As it was said above, the core of the recuperator is made out of multiple welded thin metal plates with a spiral shape that will force the working fluids to make a longer way through the recuperator. This will increase the amount of energy transferred between exhausted hot gas and compressed air. After the cutting of the metal plates, as the one you can see in "Fig.9.a)", the cut plates are corrugated and formed in a spiral shape. After that, all the spiral plates are "threaded" one by one to form the core of the heat exchanger "Fig.9 b)".

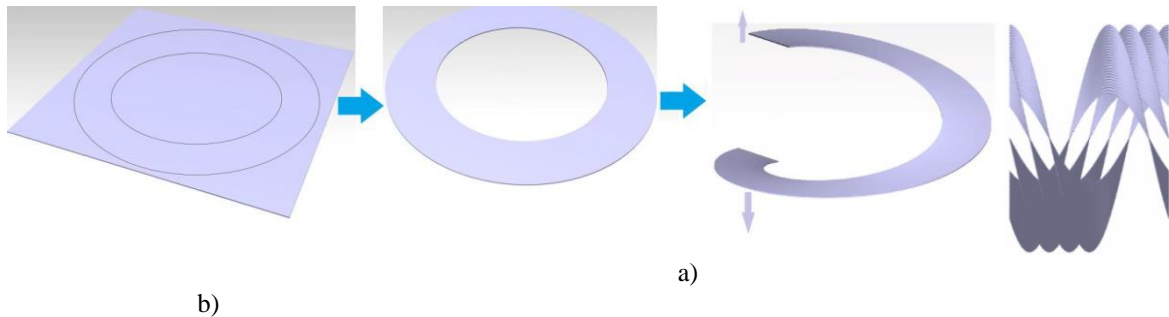


Fig. 9 Recuperator core obtaining: a) cutting plates and spiral forming; b) "threading" operation to form the passing channels

Taking into account that the corrugated thin spiral plates are forming an annular core of the recuperator, with an inner and outer diameter, the pattern corrugation of the plates, is in the sinusoidal wave shape with a constant pitch, but with variable amplitude to solve the problem occurred by the difference of the diameters.

"Fig.10" relates the passing channel form for both fluids, hot and cold, which are formed by putting in contact the variable amplitude corrugated plates.

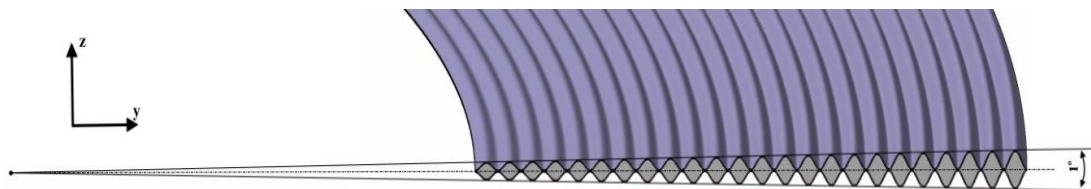


Fig.10 Corrugated pattern variable amplitude

This unique recuperator consists of 180 annular spiral plate pairs, formed by laser welding together 0.25 mm thick 625 nickel alloy steel plates with surface flow configuration as shown in "Fig.11". These plates are resistance welded at the inner and outer diameters to form the complete heat exchanger core which has a high ratio of radial width to axial length (500/350mm).

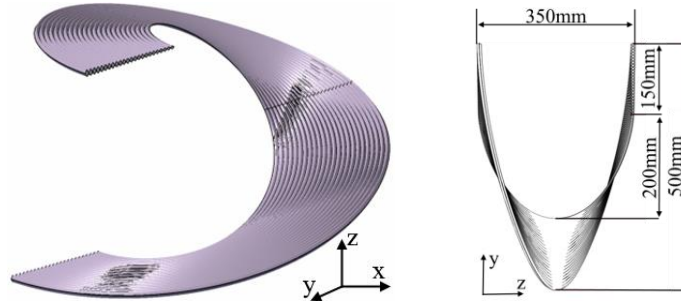


Fig. 11. Annular spiral plate pair

4. ANALYTICAL AND NUMERICAL APPROACH

The hot and cold fluid streams enter into and leave from the opposite sides of the core region, providing a counter-flow arrangement in most parts of the recuperator except for the inlet and outlet region in each fluid stream. Thus, all the analytical and numerical calculations were done only for the annular spiral side, counter-flow arrangement. In future work, it will be completed with heat transfer and pressure drop calculation for the inlet and outlet region as well. So it is known, the recuperator will equip a microturbine, thus, some of the microturbines cycle parameters were used as inputs for recuperator calculations. These parameters are summarized in "Table 1" beside all the temperatures in every section of the engine obtained after analytical calculation.

Table 1. Main microturbine parameters used in recuperator calculations

No.	Parameter	Values [Unit]	No.	Parameter	Values [Unit]
1	M_a	1 [kg/s]	6	T_4	1093 [K]
2	π_c	4.2	7	T_5	924 [K]
3	T_1	288 [K]	8	T_6	570 [K]
4	T_2	470 [K]	9	Q	600 [kW]
5	T_3	1457 [K]			

One of the most vital characteristics in recuperator researches is the heat transfer which can be expressed as:

$$Q = K \cdot A \cdot \Delta T_{med} = M_a \cdot \int_{T_2}^{T_5} c_p(T) dT = M_g \cdot \int_{T_4}^{T_6} c_p(T) dT = 575 \text{ kW} \quad [17] \quad (5)$$

when the whole heat transfer area is $A=88\text{m}^2$ knowing the dimensions of the plate mentioned above. The ratio between heat transfer area and effective volume of the recuperator is $1280 \text{ m}^2/\text{m}^3$, which can be concluded that in a small room there is a large heat transfer area thanks to the spiral shape of the plates, that offers a high ratio of radial width to axial length as well. Assuming the counter-flow arrangements, the temperature inside the recuperator was calculated as:

$$\Delta T_{med} = \frac{(T_4 - T_5) - (T_6 - T_2)}{\ln\left(\frac{T_4 - T_5}{T_6 - T_2}\right)} = 71.76^\circ \quad [17] \quad (6)$$

and the heat transfer coefficient:

$$K = \frac{1}{\frac{1}{\alpha_a} + \frac{\delta}{\lambda} + \frac{1}{\alpha_g}} = 100.163 \text{ [W/m}^2\text{K]} \quad [17] \quad (7)$$

The convection coefficient for both fluids was calculated using Reynolds criteria:

$$Re = \frac{w \cdot d_e}{\nu} \quad [17] \quad (8)$$

$$Nu = \frac{\alpha \cdot d_e}{\lambda} = a \cdot Re^b \cdot Pr^{0.33} \quad [17] \quad (9)$$

Table 2. Convection coefficient for both fluids using Reynolds criteria

No.	Compressed Air side (Cold fluid)		Burnt Gas side (Hot fluid)	
1	Re	1911	Re	1065
2	Pr	0.704	Pr	0.727
3	a	0.122	a	0.122
4	b	0.685	b	0.685
5	Nu	29.22	Nu	13.06
6	α	177.34 [W/m ² K]	α	230.81 [W/m ² K]

The Prandtl number depends on the temperature and pressure of the working fluids and was chosen using [18]. The constants a and b, depend on the plate corrugation angle and Reynolds number [17]. The analytical calculated thermal effectiveness is $\epsilon=0.7$.

Another vital characteristic in recuperator researches is pressure loss, especially for the recuperators used to increase microturbine efficiency when the pressure plays an important role. The pressure loss for both fluids was calculated with the formula below, and the values obtained were insignificant (up to 0.02bar, which means under 1%) which is very good for the entire assembly efficiency.

$$\Delta p = 4 \cdot f \cdot \frac{\rho \cdot w^2}{2} \cdot \frac{L}{d_e} \quad [17] \quad (10)$$

Besides analytical and numerical calculations, CFD simulations were done to demonstrate the recuperator benefits. In “Table 3” are summarized the variation of the temperature of the fluids along the channel length. The variation of the corrugated plate temperature (wall temperature), obtained by CFD simulations is related in “Table 3” as well.

To use computational resources more efficiently, the analysis of a single full-length sector (comprising the two fluids and the solid plate between them) was chosen. The length of the sector used is that corresponding to the helix located at the average radius (1100mm) and the amplitude of the corrugations is the average amplitude of the corrugations of all the flow passages.

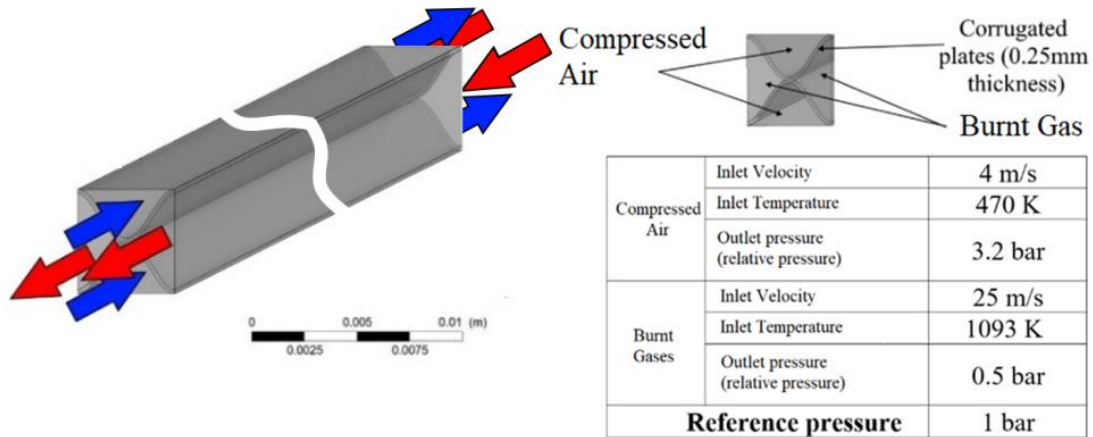


Fig. 12 Boundary conditions

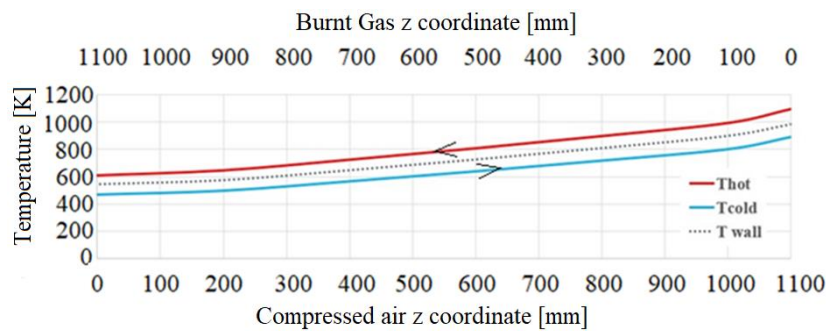
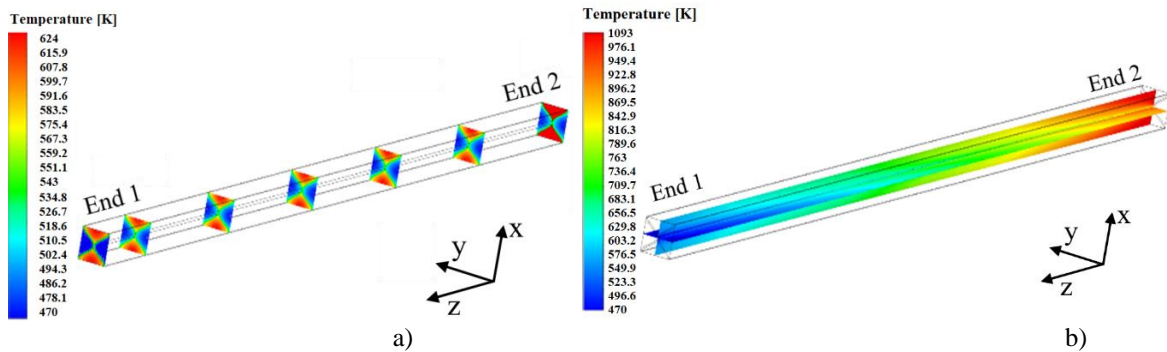
For the simulation, a grid consisting of structured quadrilateral elements was used near the walls and unstructured triangular elements in the remaining part of the geometry. The boundary conditions are presented in „Fig.12”.

The study case was a steady one in which thermal radiation was not taken into consideration. An important feature of this case is represented by the wall thickness, more precisely for this case, the walls are considered surfaces with 0 thicknesses and the material used for the solid body was steel.

Table 3. CFD simulation results

z coordinate [mm]	Burnt Gas Temperature [K]			Compressed Air Temperature [K]			Wall temperature [K]
	Near wall	One quarter channel width	Mid channel	Near wall	One quarter channel width	Mid channel	
0	1093	1093	1093	907.9	884.3	872.6	981
200	1014.23	998.4	959.9	818.7	795.9	784.8	896.6
400	916.83	902.1	866.1	734.2	712.84	702.5	807
600	825.84	812.1	778.6	655.3	635.3	625.6	723.4
800	740.88	728	696.7	581.7	563	553.9	645.3
1000	661.55	649.6	620.4	512.3	495.1	487.2	572.5
1100	624	612	585.3	470	470	470	543

As mentioned above, the hot (burnt gas) and cold (compressed air) fluid streams enter into and leave from opposite sides of the recuperator core, in a counter-flow arrangement. The “Fig.13” relates the variation curves of the temperature of the fluids.

**Fig.13 Variation of the averaged temperature of the fluids along recuperator core****Fig.14 CFD simulation heat transfer**

“Fig.14 (a)” shows the temperature distribution both on the hot air area and on the cold air area, as well as the variation of wall temperature in different sections of the working channel. The temperature distribution along two perpendicular planes passing through the maximum amplitudes of the channel is shown in “Fig. 14 (b)”. After the numerical simulations, the thermal effectiveness obtained is $\epsilon=0.67$. If this value is compared with analytical calculated thermal effectiveness value, it can be seen a difference of only 0.03.

5. CONCLUSIONS

In the first part, this paper provides a comprehensive review of benefits brought by operating in the regenerative cycle of the gas turbines and a state of the art in the recuperators domain. In the second part, the paper provides the design stage including analytical and numerical calculation and CFD simulation as well. With the previously analyzed design, the main objective of recuperator (to determine a compromise among the heat transfer effectiveness, pressure drop, small recuperator size, and low-cost requirements) seems to have been achieved.

The recuperator designed in this paper formed by an array of corrugated thin plate pairs is very compact and delivers a high heat transfer area in a small volume. Analyzing the results of the numerical analysis it can be concluded that the design is viable and offers a significant recovery of the energy of the gases that normally would have been lost. It is obvious that this solution is not optimal but it is an accessible solution, which can be materialized relatively simply, the future direction of research is the development of a recuperator (also of cylindrical shape to minimize the overall dimensions), for which the exhaust gas flow will be on the radial direction which would lead to a cross-flow in the recuperator.

6. REFERENCES

- [1]. J. Kurzke, I. Halliwell, "Propulsion and Power", Springer International Publishing AG, ISBN 978-3-319-75977-7, <https://doi.org/10.1007/978-3-319-75979-1>
- [2]. Dorin Stanciu, Mircea Marinescu, *Termodinamică Tehnică*, Editura Printech 2002
- [3]. McDonald CF. The increasing role of heat exchangers in gas turbine plants.
- [4]. Gang Xiao, *Recuperators for micro gas turbines: A review*, 2017.
- [5]. Chengyu Zhang, Volker Gummer, High temperature heat exchangers for recuperated rotorcraft powerplants, *Applied Thermal Engineering* 154 (2019)
- [6]. Lagerstrom G., Xie M. High performance and cost effective recuperator for micro-gas turbine, 2002.
- [7]. Shah RK. Presented at Fifth international conference on enhanced, compact and ultra-compact heat exchangers: science, engineering and technology. Hoboken, NJ, USA, 2005.
- [8]. Wilson MA, Recknagle KP, Brooks K. Design and development of a low-cost, high temperature silicon carbide microchannel recuperator. ASME Paper No. GT2005-69143; 2005.
- [9]. Treece B, Vessa P, McKeirnan R. Microturbine recuperator manufacturing and operating experience; 2002.
- [10]. Jeong JH, Kim LS, Lee JK, Ha MY, Kim KS, Ahn YC. Review of heat exchanger studies for high-efficiency gas turbines; 2007.
- [11]. Tsai B, Wang YL. A novel Swiss-Roll recuperator for the microturbine engine. *Appl Therm Eng* 2009;29:216–2.
- [12]. Kesseli J, Wolf T, Nash J, Freedman S. Micro, industrial, and advanced gas turbines employing recuperators; 2003.
- [13]. McDonald CF. Compact buffer zone plate-fin IHX—The key component for high-temperature nuclear process heat realization with advanced MHR. *Appl Therm Eng* 1996;16:3–32.
- [14]. Abiko T, Tujii J, Eta T. Plate fin type heat exchanger for high temperature. Google Patents; 2005.
- [15]. Proeschel RA. Proe 90TM recuperator for microturbine applications; 2002.
- [16]. Schönenborn H, Ebert E, Simon B, Storm P. Thermomechanical design of a heat exchanger for a recuperative aero engine; 2004.
- [17]. Necula, H., Badea, A., Ionescu, C. *Schimbătoare de căldură compacte*. Editura AGIR, București, 2006
- [18]. https://www.peacesoftware.de/einigewerte/luft_e.html

FLOWFIELD ANALYSIS OF DIFFERENT TEST CELLS CONFIGURATIONS

Bogdan GHERMAN¹, Dan CIOBOTARU¹, Madalin DOMBROVSCI¹

ABSTRACT: This research concentrates on studying the importance of a controlled environment for engine testing. Two main cases are described: baseline case with two air inlets and a modified geometry with one intake. Flow field patterns for both cases were determined using numerical simulation, based on a steady RANS approach. Aerodynamic interactions between the jet engine and the test cell components was also analysed. The results of the paper, drawn attention to test cell structures with two air intakes. In the present case, for a turbojet with afterburning, secondary intake played an important role in decreasing jet length and affecting its stability.

KEYWORDS: CFD, test cell, secondary intake, operation stability, turbojet engine

NOMENCLATURE

ε - dissipation
k – turbulent kinetic energy
CFD – Computational Fluid Dynamics
TKE – Turbulent Kinetic Energy

1. INTRODUCTION

A test cell represents a facility build in order to reproduce the operating conditions of an engine, aircraft etc, respecting the manufacture guidelines. Aerodynamic performances and operational stability of the tested product is influenced by the components that link the test structure, such as: intake section, augments tube, flow splitters, exhaust system, instrumentation system etc. In the case of an engine test cell, engine performances are affected by turbulence, vortex formation, flow separation, pressure loss, chaotic distribution of the temperature and pressure near the engine etc. [1].

The intake section should provide a uniform air flow through chamber room that will be accelerated into the engine. Engine size and test cell bypass ratio represent challenges that need to be taken into account when designing such a structure. Cell bypass ratio, represents one criteria which helps determine the vortex formation in a test cell; thus for bypass ratios greater than 50-70% no vortices are formed, and for values lower than 20-30% the vortices are stable [2].

With the increase of the engine size, adverse effects can compromise the engine operation, also could lead to engine damage [3]. Air stability can be compromised due to cell depression. Engine working conditions are not going to be influenced, if the difference between ambient and chamber static pressure are up to 150 mm H₂O [4].

One of the differences between indoor and outdoor engine testing is given by the wall presence. Thus, for an inside engine test cell, the thrust measured is lower, being affected by the peripheral velocity; which should be less than 10 m/s for low correction factors [5]. Design of the test bed and devices, such as: noise attenuators, exhaust nozzles etc., installed on engine for testing could modify its parameters and must be the same when correlations are made [6].

Augments tube size controls the velocity of the gas at exhaust and the quantity of the secondary air flow [7]. According to Al-Alshaikh [8], if the air flow through the test chamber is too low will result recirculation of exhaust gases that could cause engine surge and overheating.

¹Romanian Research and Development Institute for Gas Turbines COMOTI, Bucharest, Romania

Otherwise, large static pressure gradients will be generated leading to large thrust correction factor.

The distance from engine to augmentor tube influences the pressure around the engine nozzle; the greater the distance, the lower the pressure depression is [9]. Pressure depression being responsible for peripheral air flow entrainment. If flow uniformization is influenced by the mixing among the augmentor, second intake at the augmentor entry section can be used as a solution. Also, the second air inlet needs to assure additional air for cooling the exhaust system. Is very important, in a test cells with two intakes, to monitor the air flow patterns, avoiding thus the air from the secondary intake to be drawn by the primary one.

Exhaust system represents another factor that can influence engine performances, being able to control the back pressure on the engine and noise reduction.

While, experimental test facilities have limitation in flow representation and also cost implications, the CFD requires only computer speed and memory, which has increased a lot lately, more than computational costs. Thus, CFD techniques have become an important component in developing, testing and evaluation of test facilities.

This paper presents a comparative study between a test cell configuration with two entrances and a test cell with secondary intake closed. The main purpose of the work, being to illustrate the importance of a proper test cell configuration capable of assure a uniform flow distribution through the engine and the entire facility.

2. CFD SETUP

The geometrical parameters defining the test cell configuration are presented in Table 1, but also in [10]. For both cases, the parameters are the same, the only difference is given by the elimination of second entrance, see Fig. 1. Another difference between the two structures is the presence of turning vanes for the case with two air inlets, to guide the air into horizontal direction.

For the second case, the turning vanes arrangement was eliminated, even if its scope is to generate uniform velocity upstream of the engine inlet. Their presence, in this case, doesn't affect the engine operation and jet stability.

In order to determine the test cell capabilities, Tumansky R11-F300 turbojet engine with afterburner was used as test case. If the test cell system is capable of providing operation stability of the afterburner version, we can deduce that for the versions without afterburning, the experimental test cell can assure a controlled environment for engines testing.

Table 1. Design parameters defining the test cell [10]

Domain	Dimensions [mm]
Test cell length	27315
Test cell width	5800
Primary intake length	2615
Primary intake width	4780
Secondary intake length	3500
Secondary intake width	4000
Outlet domain length	14000
Outlet domain width	14020
Engine length	5000
Distance between engine and augmentor tube	500

The numerical simulations performed for the present study, were realized using ANSYS CFX software. Both cases were discretized using an unstructured grid, due to geometrical complexity; thus the number of elements is around 13 million per case.

Table 2 shows the general boundary conditions for the main domains. As working fluid was used air ideal gas with a reference pressure of 1 bar.

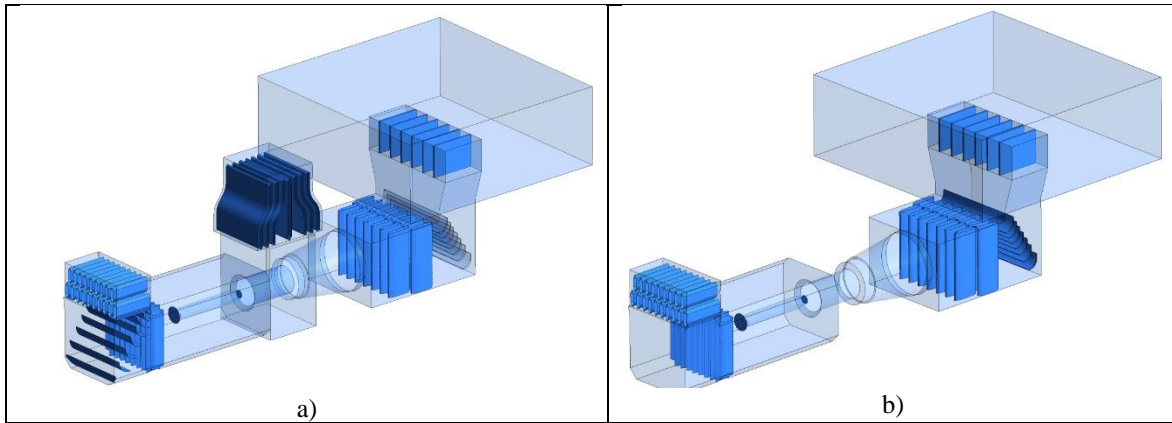


Fig. 1 Test cell configuration: a) baseline case, b) secondary intake closed

Table 2. Main domains boundary conditions

Domain	Value
Domain inlet – total pressure [bar]	0
Domain inlet – total temperature [K]	288.15
Engine inlet – mass flow [kg/s]	64
Engine exhaust – mass flow [kg/s]	68
Engine exhaust – total temperature [K]	983
Domain outlet – opening pressure and direction [bar]	0
Domain outlet – opening temperature [K]	300.15

The numerical simulations performed are steady RANS calculations, capable of providing accurate results for this paper purpose. Also, turbulent flow conditions, are represented using turbulence model - $k-\epsilon$, which is one of the most wide validated model, due to his good convergence ratio and lower computational resources [11].

3. RESULTS AND DISCUSSION

The following results present only the behaviour of the air flow through the system, influence of the second entrance and jet engine pattern, without making any observation about position and design of other facility components.

Figure 2 illustrates velocity variation in the facility, for both cases. Immediately, the differences between the two jets stands out. The first being the jet instability and the second one its jet length. The second inlet influences the jet stability, especially due to differences in pressure on the upper and lower zone of the second entrance chamber.

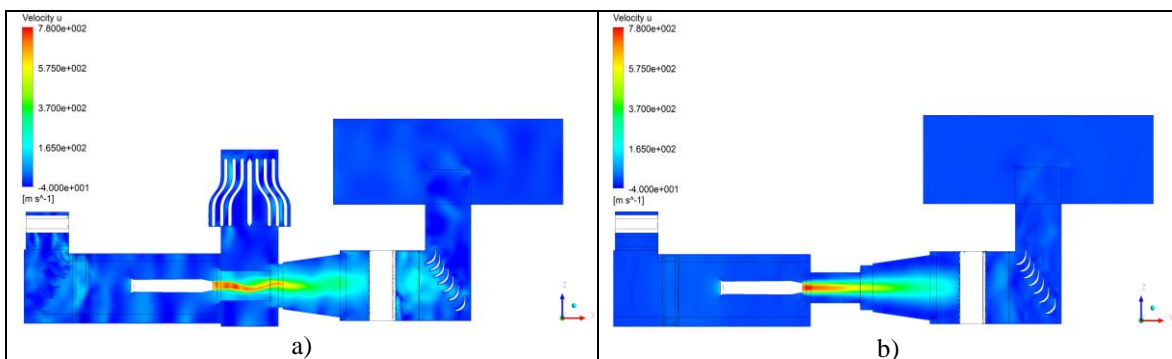


Fig. 2 Velocity variation along X axis: a) baseline case, b) secondary intake closed

Streamline field highlights the presents of boundary layer separation in the augments tube and diffuser area, Fig.3b). The velocity profiles are developed symmetrical towards the jet core, especially where the pressure is much lower compared with the nearby flow field. One way to avoid flow separation after the engine exhaust is to use lower divergence angles for the diffuser section, smoothing thus the cross section area and assuring low velocity and high pressure for an ideal flow pattern.

Secondary intake influence on engine jet characteristics is presented in Fig.4. The total temperature fields are positioned at middle of augments tube on YX direction. A reduction of jet core is observed in Fig.4a) due to the air bypassing the augments tube.

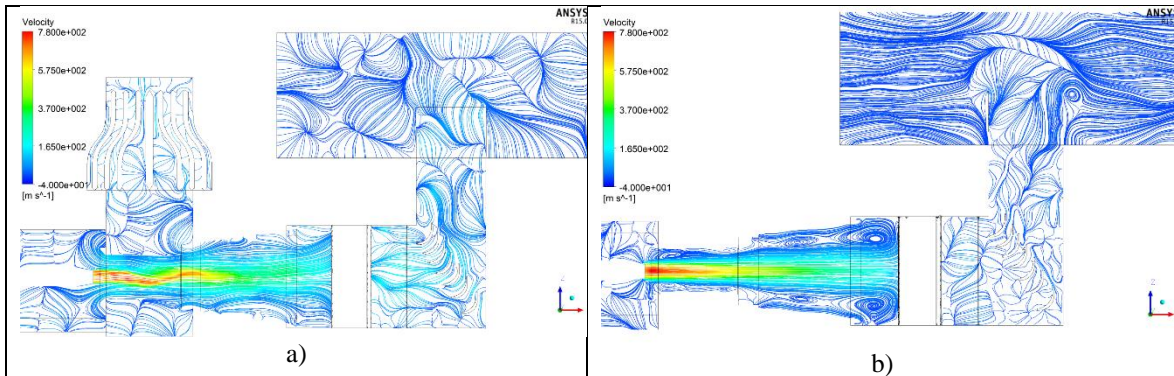


Fig. 3 Surface streamline at 50% from test cell width: a) baseline case, b) secondary intake closed

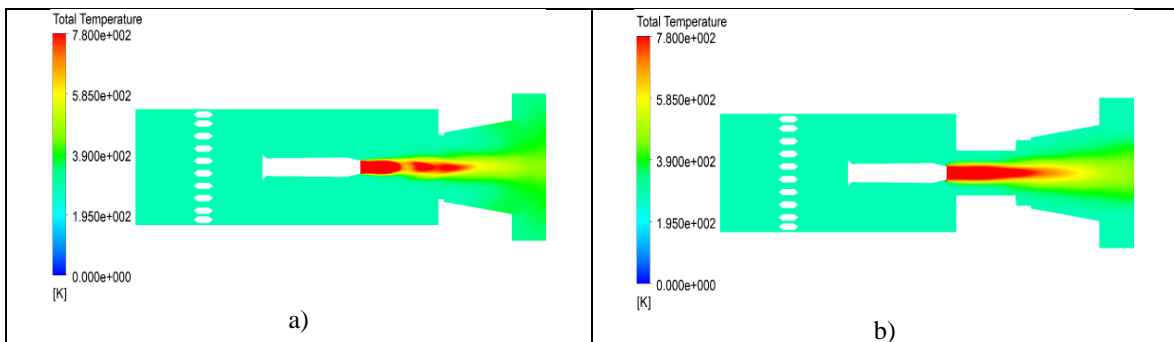


Fig. 4 Total temperature distribution on YX plane: a) baseline case, b) secondary intake closed

Velocity field represented in ZY plane, plane - situated before the acoustic buffer arrangement - Fig.5, displays jet shape, its intensity and velocity variation near the exhaust stack. If Fig.5b) illustrates a symmetry of velocity profile, Fig. 5a) presents a chaotic distribution of velocity in the chamber with an increased jet core value.

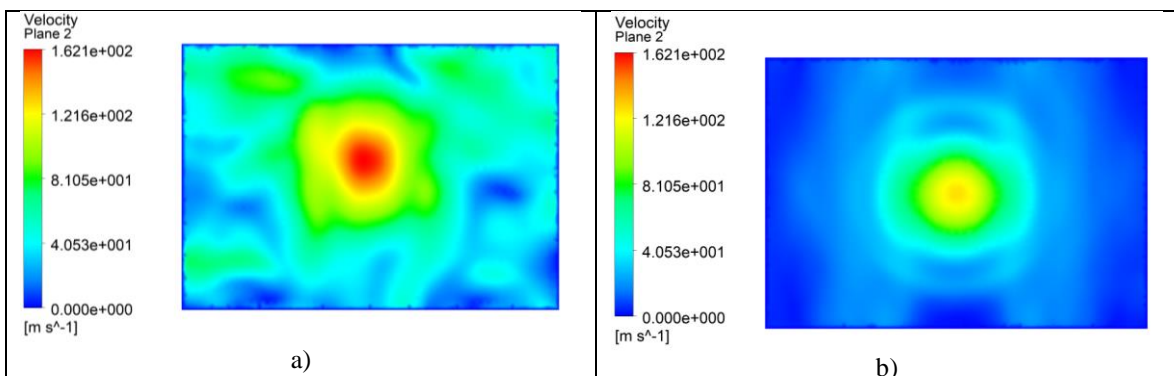


Fig. 5 Velocity profile before the acoustic buffer: a) baseline case, b) secondary intake closed

Figure 6 and 7 presents the variation of total temperature and velocity among X direction, from the engine exhaust up to the acoustic baffle arrangement in exhaust stack. Three measurements line were positioned considering the jet core pattern: upper, middle and lower areas of the engine exhaust. The two cases were compared from potential cores point of view. The maximum differences between the two cases reach up to approximately 300 m / s.

It can be observed not only a difference on the two jet cores, but also a velocity profile asymmetry given by second entrance. Thereby, both velocity and temperature profiles varies dramatically for the upper and lower series, presented in Fig. 6 and 7.

Jet core maximum temperature reaches 1000 K and decreases as the jet approaches the acoustic baffle arrangement.

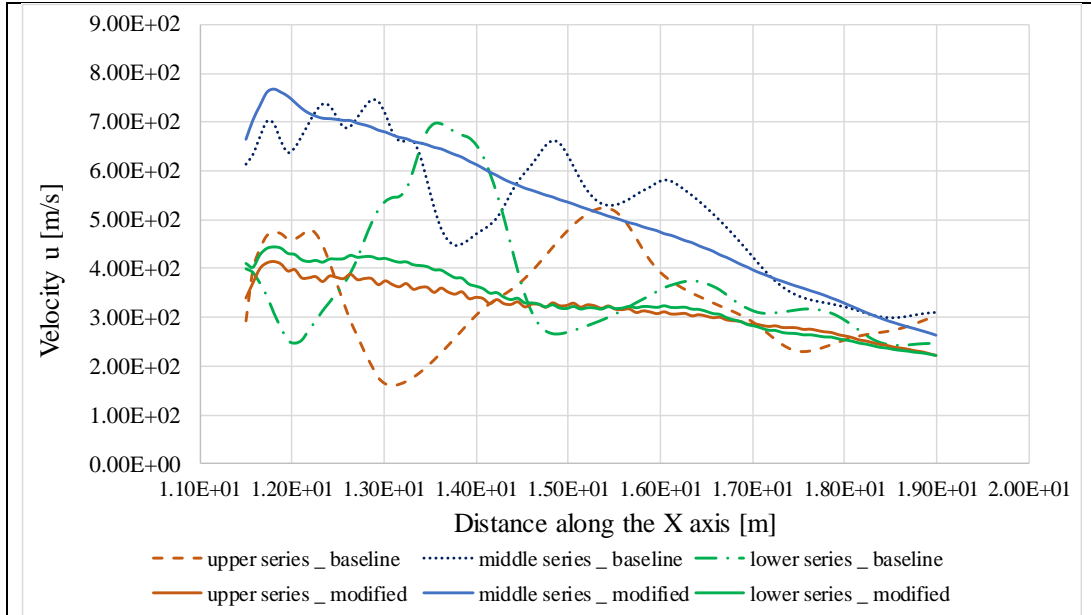


Fig. 6 Velocity variation along the x direction: a) baseline case, b) secondary intake closed

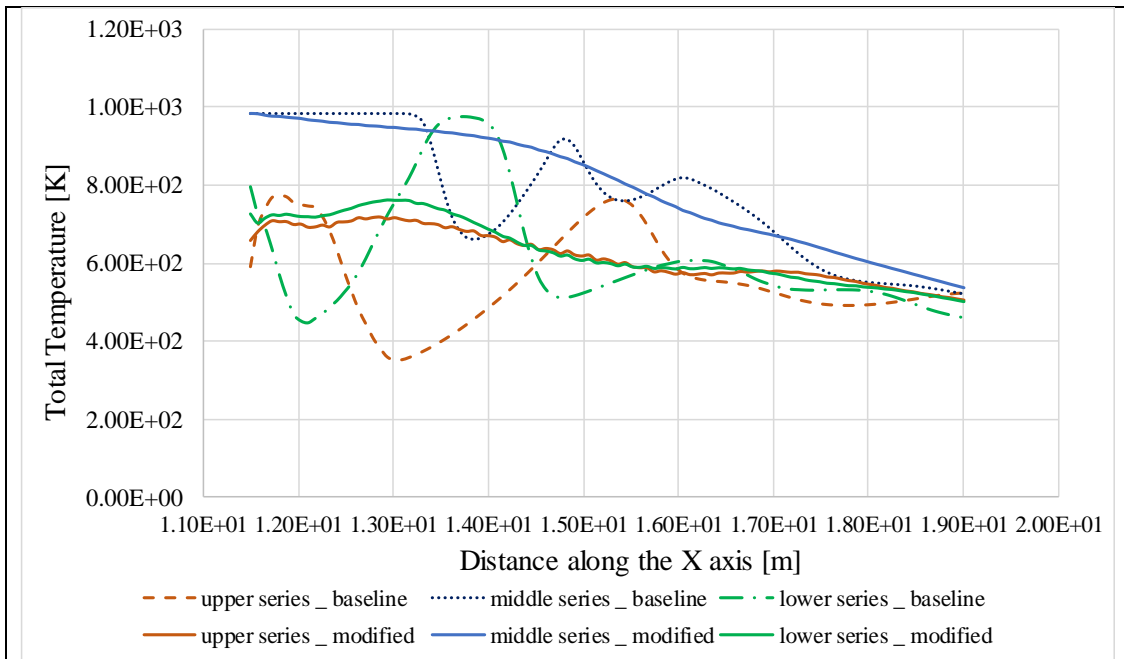


Fig. 7 Total temperature along the x direction: a) baseline case, b) secondary intake closed

4. CONCLUSIONS

This paper presents the numerical simulation of two test cells: baseline case with two air intakes and a modified structure having the secondary inlet closed. The entire case study was performed using RANS calculation and as turbulence model $k - \epsilon$. Both cases present results that can be improved. The major disturbance of a test cell with a secondary inlet is the influence on jet stability and the chaotic velocity profiles

after augmenter tube. Also, secondary intake flow that bypasses the engine affects the pressure distribution around it.

For the second case, with only one primary inlet, the problem is given by the boundary layer separation and its impact on performances. Flow separation, that can be avoided by using conical diffusers with smoother cross section areas. Although, above, are mentioned some factors that can influence the proper testing of an engine, it is necessary to perform more advanced numerical analyzes (using other engine sizes) to determine how large their impact is on the existing test cell configuration.

REFERENCES

- [1]. J. J. Ballough, 2002, Correlation, operation, design, and modification of turbofan/jet engine test cells, Federal Aviation Administration, AC 43-207
- [2]. Ho Wei Hua, M. Jermy, 2007, Validated CFD simulations of vortex formation in jet engine test cells, 16 th Australasian Fluid Mechanics Conference, Crown Plaza, Gold Coast, Australia;
- [3]. S.L.Kromer, D.A.Dietrich, 1985, Flowfield Analysis of Low Bypass Ratio Test Cells, J.Aircraft, Vol.22, No.2, February 1985
- [4]. R. Jacques, 1984, Operation and performance measurement on engines in sea level test facilities, Mar. 1984. AGARD Lecture Series No.132.
- [5]. D.M. Rudnitski, 1984, Performance derivation of turbojet and turbofans from tests in sea-level tests cells, 1984. AGARD-LS-132.
- [6]. S. Fábry, M. Spodniak, P.Gašparovič, P. Koščák, 2019, Aircraft Gas Turbine Engine Testing, Acta Avionica, Volume XXI, 41 – No. 2, DOI: 10.35116/aa.2019.0016
- [7]. R. Hastings, 1983, Simulation of a Jet Engine Test Cell, National Research Council, Canada;
- [8]. A. Al-Alshaikh, 2011, An Experimental and Numerical Investigation of the Effect of Aero Gas Turbine Test Facility Aspect Ratio on Thrust Measurement, PhD Thesis, Cranfield University;
- [9]. G. B. Ramos, 2015, Study of a Test Cell for Commercial Jet Engines, Master Degree, Instituto Superior Técnico, University of Lisbon, Portugal
- [10]. O.Dumitrescu, G. B.Gherman, I.Porumbel, 2018, Importance of a second entrance in a test cell, INCAS BULLETIN, Volume 10, Issue 1/ 2018, pp. 63 – 72 (P) ISSN 2066-8201, (E) ISSN 2247-4528;
- [11]. D. C. Wilcox, 1998, Turbulence Modeling for CFD, Second edition, Anaheim: DCW Industries, pp. 174;

EXPERIMENTAL INVESTIGATION FOR WEDM INFLUENCE ON 17-4PH SURFACE ROUGHNESS BASED ON TAGUCHI METHOD

Florentin CONDURACHI¹, Lucian-Cosmin ZAMFIR¹, Cristin ZAHARIA²

ABSTRACT: Electrical discharge machining is an important manufacturing process used for machining hard alloys, or those that would be very difficult to machine with traditional techniques, and to reproduce complex geometries. It's used in mold-making and die industries, aerospace industry, automobile and electronics industries in which production quantities are relatively low. This paper presents a study of the influence of setup parameters of wire electrical discharge machining for one metal alloy: 17-4 PH steel. The experimental methodology includes the analysis by design of experiments under Taguchi method. The results show significant influence of the following EDM parameters: discharge current, discharge frequency and wire speed on surface roughness.

KEYWORDS: WEDM, surface roughness, 17-4 PH steel, Taguchi

NOMENCLATURE

SR	Surface roughness
WEDM	Wire electrical discharge machining
EDM	Electrical discharge machining
I	Discharge current [A]
P	Discharge frequency [Hz]
Aw	Wire speed [m/min]
Ra	Roughness average [μm]
Rq	Root mean square [μm]
Rsk	Skewness of the assessed profile
Rk	Core roughness depth [μm]
Rz	Peak-peak [μm]
Rmax	Complement for Rz [μm]
Rp	Maximum peak height [μm]
Mr1	Upper material ratio delimiting core area 1 [%]
Mr2	Lower material ratio delimiting core area 2 [%]
Yi	Observed response value
n	Number of imitations
(S/N)	Signal to noise
LB	Lower is better
NB	Normal is better
HB	Higher is better

1. INTRODUCTION

Electrical discharge wire cutting, more commonly known as wire-EDM, is a spark erosion process used to produce complex two and three-dimensional shapes through electrically conductive workpieces by

¹ Romanian Research and Development Institute for Gas Turbines COMOTI, Bucharest, Romania

² University Politehnica of Bucharest, Romania

using wire electrode. The sparks will be generated between the workpiece and a wire electrode flushed with or immersed in a dielectric fluid. The degree of accuracy of workpiece dimensions obtainable and the fine surface finishes make WEDM particularly valuable for applications involving manufacture of stamping dies, extrusion dies and prototype parts. Without WEDM the fabrication of precision workpieces requires many hours of manual grinding and polishing.

The most important performance measures in WEDM are material removal rate/cutting speed, workpiece surface roughness and kerf. Discharge current, discharge frequency, pulse width, pulse frequency, wire speed, wire tension and dielectric flushing conditions are the machining parameters which affect the performance measures.

The profile roughness parameters are included in ISO 4287:2000 British standard, identical with the ISO 4287:1997 standard. [1]

There are many different roughness parameters in use, but Ra (equation 1) is by far the most common, other common parameters include Rz, Rq, Rsk.

$$Ra = \frac{1}{n} \sum_{i=1}^n |y_i| \quad [2] \quad (1)$$

The EDM process has 2D (wire) or 3D (electrode) patterns. Even when mechanical drawing typically specifies Ra, many functional requirements of engineering surfaces are evaluated through functional roughness parameters that have not been in general treated in relationship with EDM setup. This experimental study presents a contribution of the qualitative and quantitative influence on those roughness parameters, focused on functional surface roughness parameters.[3]

2. MATERIAL AND METHOD

The material that was analyzed is 17-4 PH and is a precipitation-hardening martensitic stainless steel. The work piece used for the experiments is in the form of a rectangular plate with dimensions of 60mm x 25mm x 5mm (Fig.1). In Table 1 typical physical properties are included.

Table 1. Physical properties

Material	17-4 PH
Melting range [°C]	1404-1440
Hardness	35 HRC
Density [g/cm ³]	7,75
Thermal Conductivity [W/m.K]	18,3

The WEDM machine is AgieCharmilles CUT E 350 (Fig. 2.), operated with a brass wire AC CUT AH 0.25 mm diameter and de-ionized water as dielectric fluid.



Fig.1 Tested specimens



Fig.2 AgieCharmilles CUT E350

To compare the influence of the machine parameters of EDM on SR the following parameters are taken into account: I discharge current [A], P discharge frequency [Hz] and Aw wire speed [m/min].

Taguchi developed a particular design of orthogonal arrays to study the whole parameter space with a little amount of experiments. Then transformed the experimental results to taken with a signal-to-noise ratio. It utilizes the signal to noise percentage to estimate the quality characteristics dissimilar from or nearing to the preferred values. [4]

Depending on the particular design problem, different S/N ratios are applicable, including “lower is better” (LB), “nominal is best” (NB), or “higher is better” (HB). S/N ration can be calculated as a logarithmic transformation of loss function. The characteristics selected for SR is “Lower is better”,as given in equation 2. Lower is better was used because minimum surface roughness was required.[5]

$$\frac{S}{N}ratio = -10 \log_{10} \frac{1}{n} \sum_{i=1}^n y_i^2 \quad [4] \quad (2)$$

Where y_i = observed response value and n = number of imitations.

Selection of particular orthogonal array from the standard orthogonal array depends on the number of factors, levels of each factor and Fthe total degrees of freedom.

- Number of control factors = 3;
- Number of levels for each control factors = 3;
- Number of experiments to be conducted = 9;

Based on these values and the required minimum number of experiments to be conducted, the nearest Orthogonal Array is L9 (Table 2).

Table2.Experimental design. Taguchi array L9 and control factor level.

Experiment	I	P	Aw
1	1	1	1
2	1	2	2
3	1	3	3
4	2	1	2
5	2	2	3
6	2	3	1
7	3	1	3
8	3	2	1
9	3	3	2

Level	A (I)	B (P)	C(Aw)
1	2	87	7,2
2	4	80	8,1
3	11	66	9

Using different levels of the process parameters the specimens have been machined accordingly. Roughness measurement was accomplished by a roughness tester MarfSurfPS1 (Fig.3). Every machined surface was cleaned with acetone and tested in parallel with machining feed direction, the length of the measurement was 17.5mm with 5 cut-offs.



Fig.3 MarfSurf PS1 roughness tester

3. RESULTS AND DISCUSSION

The experimental graphics and values are included in Table 3 and Table 4.

Table 3. Experimental graphics

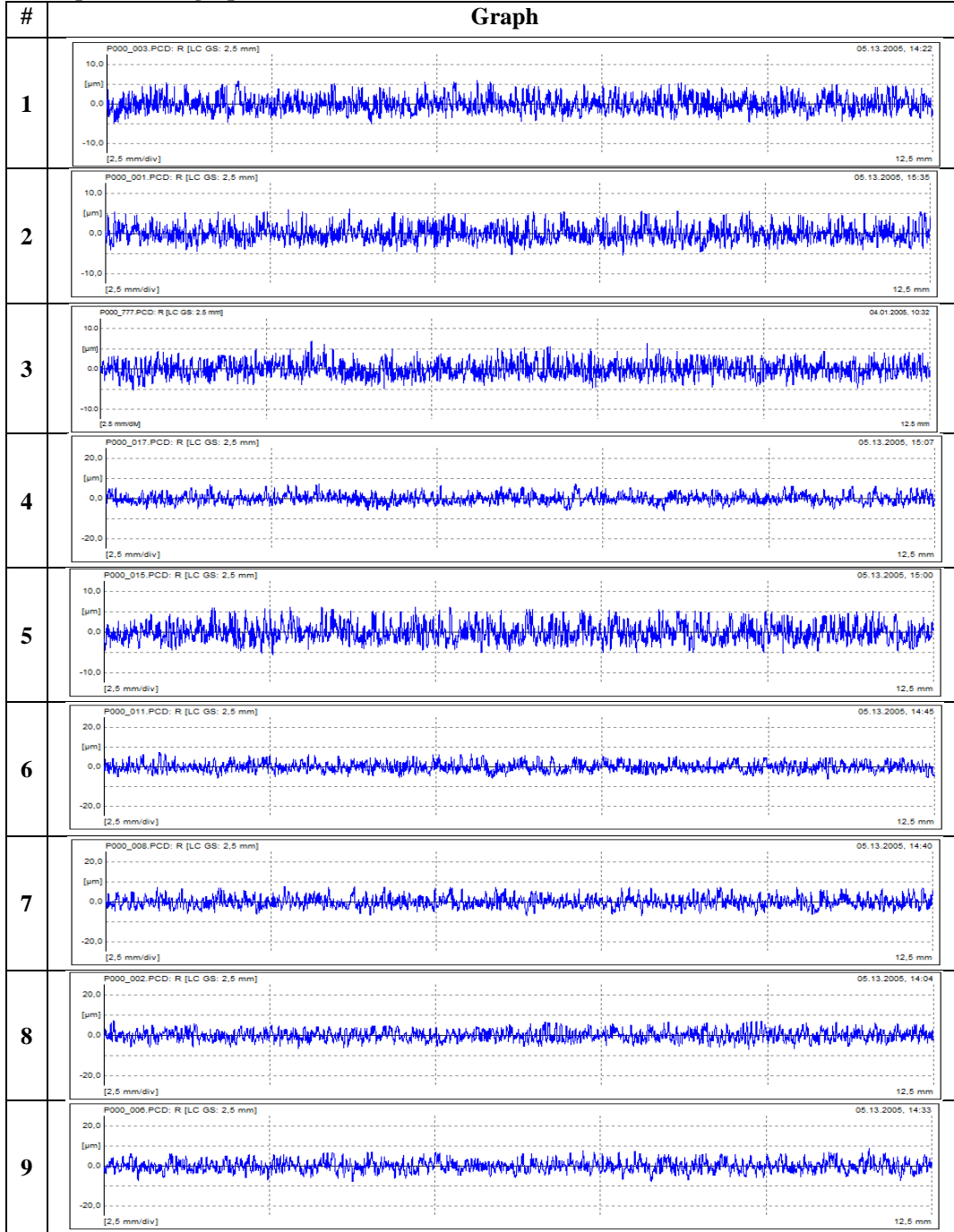


Table 4. Experimental values

Experiment	Ra[µm]	Rq[µm]	Rsk	Rk[µm]	Rz[µm]	Rmax[µm]	Rp[µm]	Mr1%	Mr2%
1	1,544	1.915	0.427	4.80	10.20	10.60	5.51	14	92.9
2	1.542	1.930	0.448	4.90	10.30	11.00	5.6	13	93.4
3	1.508	1.861	0.289	4.90	10.40	11.60	5.7	12.6	92.4
4	1.792	2.247	0.419	5.64	12.30	13.00	6.57	13.4	92.6
5	1.733	2.148	0.341	5.27	11.00	11.70	5.8	15.0	92.7
6	1.836	2.283	0.331	5.63	11.60	12.80	6.08	13.8	91.6
7	2.119	2.634	0.364	6.80	14.00	14.60	7.43	12.5	93.2
8	2.079	2.543	0.198	6.98	12.80	14.00	6.46	11.1	92.6
9	2.175	2.713	0.235	6.88	14.50	16.30	7.39	12.2	91.3

The results of the experiments have been shown in (Fig.4). Confirmation test have also been conducted to validate optimal results. From Figure 4, it is observed that, the surface roughness is high at high I, Aw and low P, decreasing from low I, Aw and high P. Taguchi’s robust design methodology has been successfully implemented to identify the optimum settings for control parameters in order to reduce surface roughness. The optimum settings are found in Table 5. This optimum settings combination is validated by conducting confirmation test Table 6.

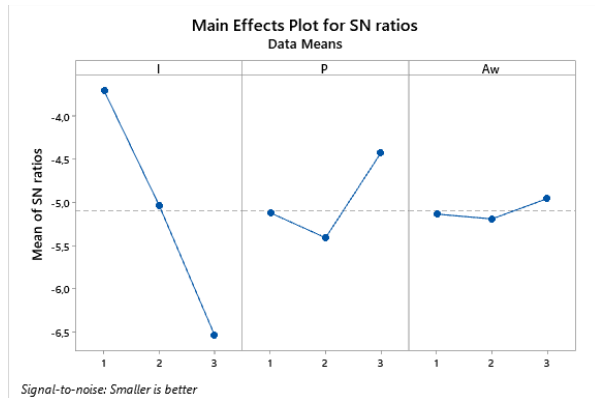


Fig.4 Main effects SN ratios Taguchi method

Table 5. Optimum parameters for SR

I[A]	P[Hz]	Aw[m/min]
8	87	7.2

Table 6. Validation test

Experiment	Ra[μm]	Rq[μm]	Rsk	Rk[μm]	Rz[μm]	Rmax[μm]	Rp[μm]	Mr1%	Mr2%
VALIDATION	1.497	1.851	0.279	4.80	10.30	11.50	5.5	12.6	92.4

4. CONCLUSIONS

This paper investigates the optimal input process parameters for machining of 17-4PH steel for minimum surface roughness. Experimental examination on wire electrical discharge machining of stainless steel 17-4PH was performed utilizing brass wire of 0.25mm diameter with de-ionized water as dielectric fluid.

With Taguchi method this study is focused in controlling the roughness results, an analysis of signal-to-noise ratio under the smaller is better criteria has been carried out to reveal the main influences for optimized the input parameters resulting the minimum surface roughness. The parameters I, P, Aw shown significant effect. The optimal combination of input parameters and their levels for minimization of surface roughness are A2B1C1.

REFERENCES

[1] ISO 4287:2000, Geometrical product specification (GPS). Surface texture. Profile method. Terms, definitions and surface texture parameters.
 [2] Degarmo, E. Paul; Black, J.; Kohser, Ronald A. (2003), *Materials and Processes in Manufacturing (9th ed.)*, Wiley, p. 223, ISBN 0-471-65653-4.
 [3] T.R. Thomas, Roughness and function, *Surf. Topogr.:Metrol. Prop.* 2 (2014) 014001 (10pp).
 [4] Taguchi Method Based Optimization for Surface Roughness in Drilling Operation of EN-31 Steel Material and DOE Approach.
 [5] Experimental investigation of EDM Process parameters in Machining of 17-4 PH Steel using Taguchi Method.

ISOTHERMAL OXIDATION BEHAVIOR AND THERMAL SHOCK RESISTANCE OF THERMAL BARRIER COATINGS

Teodor-Adrian BADEA¹, Alexandru PARASCHIV^{1,2}, Mihaela Raluca CONDRUZ^{1,2},
Tiberius-Florian FRIGIOESCU¹, Lucian Cosmin ZAMFIR¹, Ion IONICA³

ABSTRACT: The thermal shock resistance and isothermal oxidation behavior of a plasma-sprayed thermal barrier coating (TBC) with yttria-stabilized zirconia as top coat and NiCrAlY alloy as bond coat were investigated. The TBC were deposited by atmospheric plasma spraying on Ni-based superalloy Nimonic 86. Isothermal oxidation tests were performed at 1100°C for 100, 200 and 300 hours using an atmospheric electrical furnace. Thermal shock resistance of TBC was evaluated by furnace cyclic oxidation test performed in the temperature range of 40-1300°C using the same atmospheric electrical furnace. The isothermal oxidation behavior was evaluated by measuring the sample's weight gain during oxidation and microstructural investigation. The experimental results indicated an increase of the weight and thermally grown oxides as a function of oxidation duration. To evaluate the thermal shock resistance a failure criterion of 20% spallation of the TBC surface was considered. Based on the cyclic furnace oxidation test results, it was concluded that the investigated TBC has a maximum shock resistance of 35 thermal cycles.

KEYWORDS: Thermal shock, thermal barrier coatings, cycling, isothermal oxidation.

1. INTRODUCTION

Improving the efficiency of gas turbine engines can be accomplished by increasing the turbine inlet temperatures (TIT) [1,2]. In order to withstand the aggressive environments and high working temperatures which may exceed the melting point of superalloys, the metallic components must be protected by cooling systems and TBCs [3].

A typical TBC system (Figure 1) consists of a Ni-based superalloy substrate, a metallic bond coat for oxidation resistance (usually MCrAlY, where M is Ni, Co, or combinations), a ceramic top coat based on yttria-stabilized zirconia - YSZ (ZrO_2 -6-8% Y_2O_3) for thermal insulation and a thermally grown oxide layer (TGO) which is formed at the bond coat-top coat interface during oxidation [3-5].

For the preparation of TBCs, two techniques are most commonly used: electrical beam-physical vapor deposition (EB-PVD) and atmospheric plasma spray (APS). The particularity of the EB-PVD technique consists in the formation of columnar grain and inner sub-grain distributed between the columnar grains, while by the conventional APS method a lamellar structure of the layer is obtained [6].

During thermal cycles, the TBCs has relatively short lifetime due to differences between the thermal expansion coefficients of the metallic and ceramic layers and substrate. Thermal residual stresses also occurred due to the increasing of thermally grown oxides (TGO). These residual stresses could originate microcracks including debonding and delamination which deeply affect the thermal protection of metallic substrate. So, a good understanding of these phenomena is fundamental for the prediction and evaluation of the performances and lifetime of TBCs [7].

Various thermal shock and isothermal oxidation tests are carried out by the gas turbine manufacturers in order to evaluate the quality and lifetime of the TBCs. The engine manufacturers has developed testing systems for simulation of real thermal conditions in engines which consist of jet engine thermal shock testing units, furnace cycle tests and burner rig thermal shock testing units [8-12].

Despite many testing systems were developed, a standardized method is still lacking due to the difficulty to simulate the real thermal conditions.

¹ Romanian Research and Development Institute for Gas Turbines COMOTI

² University Politehnica of Bucharest, Romania

³ SC Plasma Jet SRL

The present study is focused to evaluate the thermal shock resistance and isothermal oxidation behavior of a plasma-sprayed thermal barrier coating (TBC) with yttria-stabilized zirconia as top coat and NiCrAlY alloy as bond coat on Ni-based superalloy Nimonic 86 substrate.

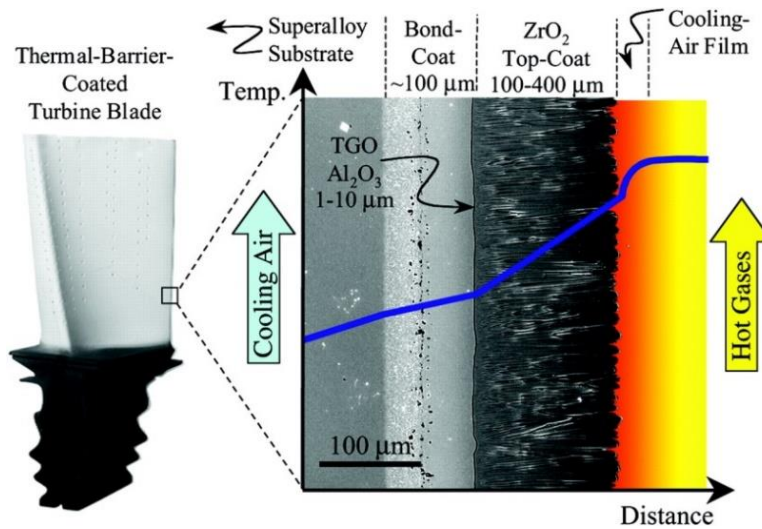


Fig. 1. The basic configuration of a TBCs deposited on a turbine blade [13]

2. MATERIALS AND METHODS

2.1. Preparation of TBCs Specimens

Nimonic 86 was used as substrate while YSZ and NiCrAlY were used as top coat and bond coat. The chemical compositions of the Nimonic 86 superalloy is presented in Table 1. Four samples with dimensions 20x10x2 mm were cut from a Nimonic 86 sheet and were prepared by sand blasting with corundum to obtain a rough surface ($R_a = 8-10 \mu\text{m}$) in order to facilitate the bonding between the substrate and the coating. Thermal spray deposition of TBCs was performed by atmospheric plasma spraying (APS) using the Metco 7M installation with F4 gun (Figure 2a) and parameters from Table 2.



Fig. 2. Thermal spray deposition process of TBCs using Metco 7M installation with F4 gun (a) and the coated specimens (b)

Table. 1. Chemical composition of Ni superalloy 86.

Elements	Ni	Cr	Mo	Fe	Si	Mn	C	Ti
Nimonic 86	Balance	25.3	10.2	5.0	1.0	1.0	0.05	0.3

Table 2. Thermal spraying parameters used for bond coat and the ceramic layer by APS.

Parameters for bondcoat (APS)		Parameters for ceramic layer (APS)	
Argon [bar]	5.2	Argon [bar]	4.5
Hydrogen [bar]	6.7	Hydrogen [bar]	6.0
Voltage [V]	60	Voltage [V]	50
Amperage [A]	520	Amperage [A]	550
Distance [mm]	200	Distance [mm]	170

2.2. Isothermal oxidation test

For isothermal oxidation tests, three coated samples were placed in alumina crucibles and heat treated using Nabertherm LH 30/14 furnace (Tmax. = 1400°C). The oxidation heat treatment consisted in heating from room temperature to 1100°C (heating rate of 15°C/min) with 100 h holding at temperature followed by slow cooling in the furnace. Three stages of 100 h holding were realised in order to ensure a total holding period of 300 h. Before oxidation test and after each 100 h stage, the weight-gain data was recorded by sample’s weighing using an analytical balance Ohaus Pioneer PA214C (accuracy 0.1 mg). After each stage of 100 h, the furnace was allowed to cool and one sample was investigated by scanning electron microscopy (SEM).

In order to evaluate the influence of isothermal oxidation at high temperature on microstructure of TBCs, the oxidized samples with TBCs tested at 100, 200 and 300 hours and a reference specimen (specimen not exposed to isothermal oxidation) were metallographically prepared by grinding and polishing and investigated by SEM. The oxidability characteristics were investigated in the cross section of the samples.

2.3. Thermal-Shock test

The evaluation of thermal shock resistance of TBCs was performed by furnace cycle tests (FCT) with short thermal cycles performed in the temperature range of 40-1300°C by using the same atmospheric electrical furnace with a sliding and clamping system of samples which allows the insertion and removal of samples through an acces hole located above the furnace, a type K thermocouple which shall record the temperature at the surface of the sample and a compressed air cooling system. The sliding device was fixed on a support which was positioned above the furnace acces hole (Figure 3).

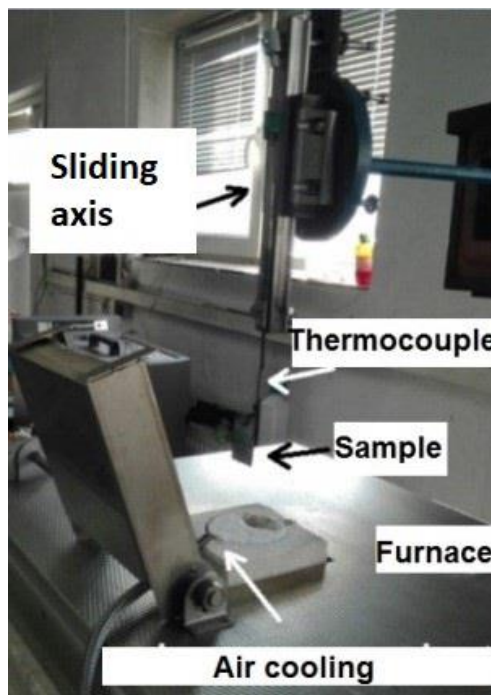


Fig. 3. The thermal shock test installation

A cycle of thermal shock consisted in maintaining the specimens for 9 min. at 1300°C and cooling for 2 min until a temperature of approx. 40°C by using compressed air. A failure criterion of 20% spallation of the TBCs surface was used to evaluate the shock resistance of investigated coatings [10,19].

3. RESULTS AND DISCUSSION

3.1. Oxidation results

Oxidation behavior of the TBCs was evaluated based on measuring the weight gain during oxidation and using scanning electron microscopy. Based on the weight measurements, it was observed time-dependent increase of the weight of tested samples as a direct effect of the oxidation process which can be expressed by a polynomial function shown in Figure 4.

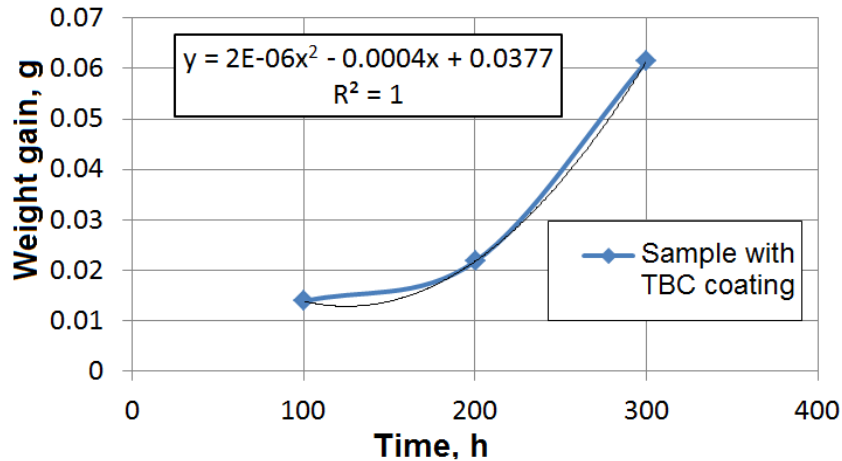
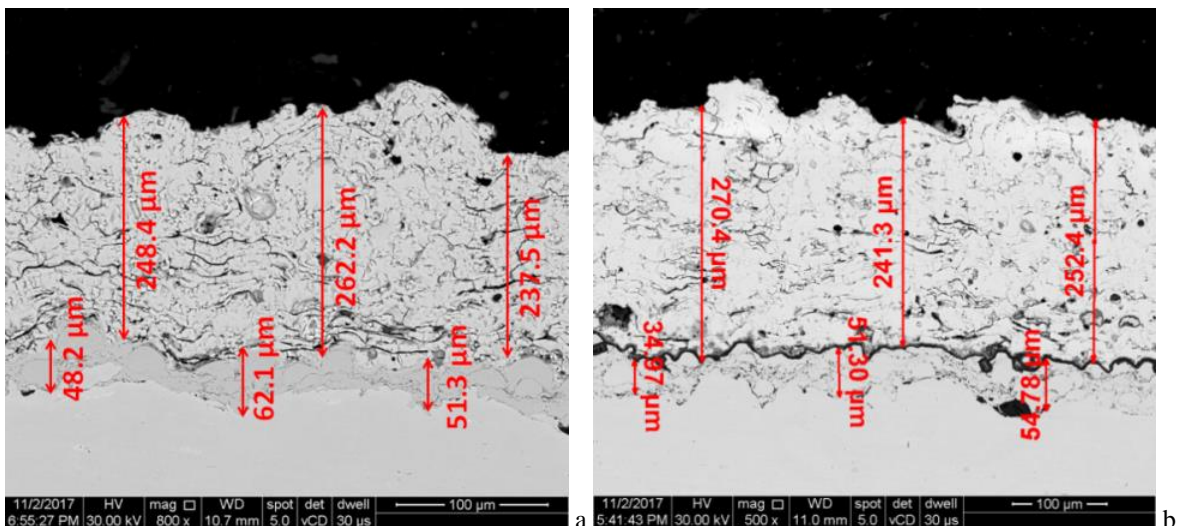


Fig. 4. Mean mass gain of the isothermal oxidized TBCs as a function of duration holding of 100, 200 and 300 hours at 1100 °C

Layer thickness measurements on reference sample showed that the metallic bond coat and ceramic top coat had thicknesses of approx. 55 μm and 250 μm, respectively. During the isothermal oxidation cycles, it was found that the thickness of the ceramic layer did not undergo significant dimensional changes. Otherwise, the thickness of metallic bond coat had a tendency to decrease with increasing the exposure times, from an average thickness of 55μm to 40μm after 300 h of isothermal oxidation (Figure 5). The decrease in thickness of the coating layer is generated by the formation of aluminum oxides (Al₂O₃) protective layer formed at the interface of bond coat/top coat, which act as oxygen diffusion barrier also known as thermally grown oxide (TGO) layer. In Figure 5a-d are presented the cross-sectional SEM images with layer thickness of TBCs in as-sprayed state (Figure 5a), and after exposure times of 100, 200 and 300 hours (Figure 5b-d).



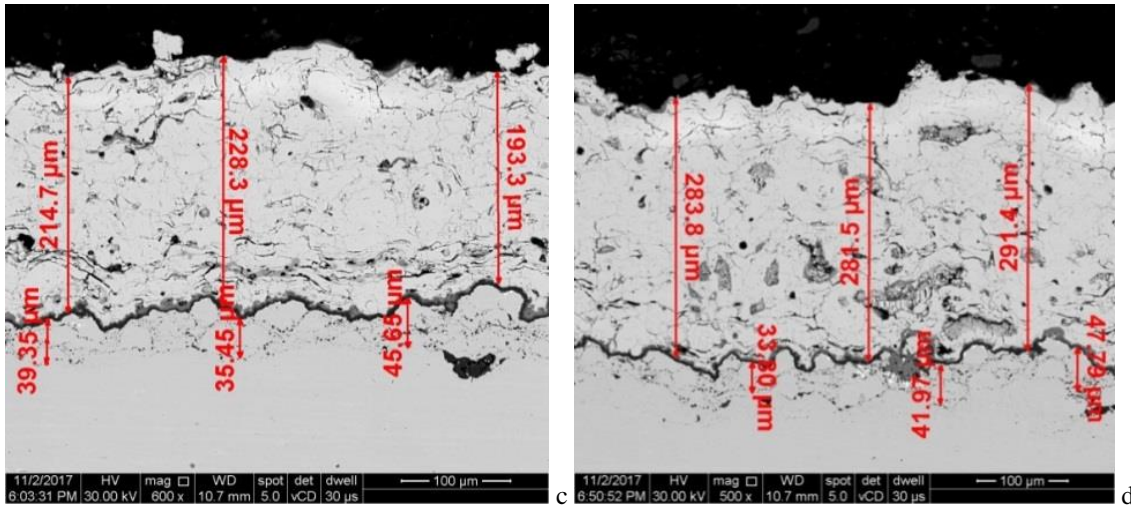


Fig. 5. SEM images with the thickness of the initial layer and the ceramic layer in the initial state (a), after 100 hours (b), 200 hours (c) and 300 hours (d)

Based on the SEM images presented in Figure 5b-d it was observed an increase of TGO layer during exposure durations. The evolution and thickness of TGO layer of oxidized TBCs are highlighted by image details in Figure 6a-d.

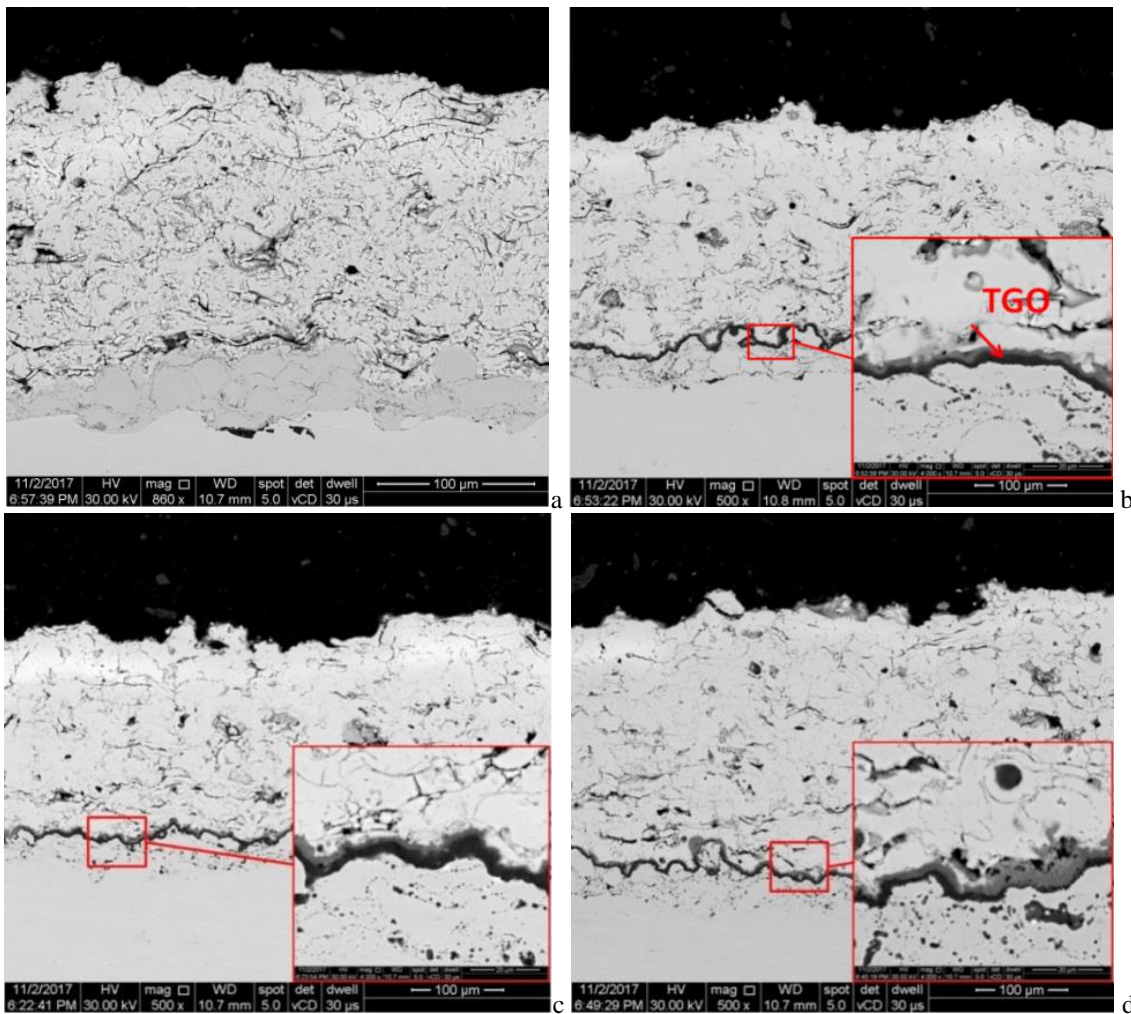


Fig. 6. SEM images with the microstructure of the TBC systems and the formation of the TGO layer at different isothermal oxidation cycles: a) initial state, b) after 100 hours, c) after 200 hours and d) after 300 hours

The SEM images presented in Figure 6a-d show the microstructure of TBC systems at different isothermal oxidation cycles and the formation of the TGO layer which is desired to consist of a homogeneously distributed, continuous and dense α -Al₂O₃[14]. Anyway, the TGO layer consists of various spinel and metallic oxides apart from α -Al₂O₃ which is the reason why the TGO has a low permeability of oxygen and a reduced protection of the bond coat from oxidizing [15-16]. Based on the experimental measurements graphically presented in the Figure 7 it was found that the thickness of the TGO layer has an increasing evolution as a function of holding times at 1100 ° C, which can be expressed by a polynomial function.

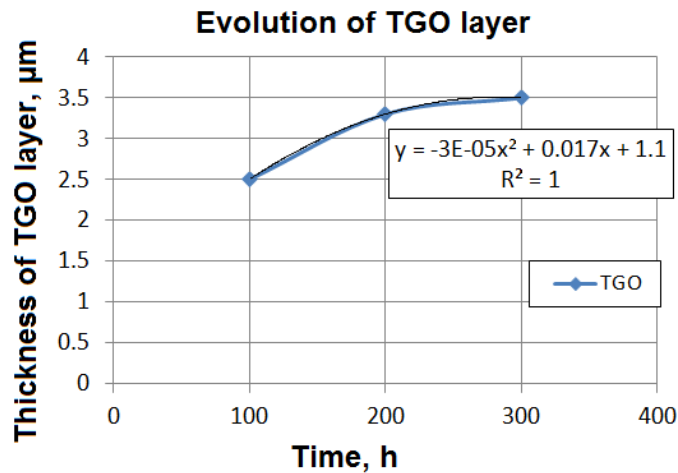


Fig. 7. The evolution of the TGO layer in the TBCs according to the holding durations at 1100°C for 100, 200 and 300 hours

The efficiency of the diffusion barrier of TBCs is largely determined by the thickness of TGO layer. The maximum thickness of TGO layer was approx. 3.5 µm after 300 hours of holding duration. Generally, the TGO layer increases with increasing the oxidation duration and temperature which induce residual stress and microcracks. When the layer thickness reaches a critical size (5-15 µm)[17], will lead to delamination of coatings, usually at the bond coat – TGO layer or TGO layer – top coat interface. In order to ensure effective protection of the bond coat and substrate, the optimum thickness of the TGO layer should be around 2 µm [18].

3.2. Thermal-Shock results

Generally, the examination of samples tested by thermal shock tests is performed visually, the coating has been damaged and can no longer fulfill the role of thermal protection. Most papers [10,19] indicate that the thermal shock testing of a TBCs is completed when 20% of its surface is exfoliated. In the case of investigated TBCs (Figure 8) it was found that after exposure of 25 cycles at max. temperature of 1300°C, no spallation was found. But, after 30 cycles, the deterioration process of sample has started after 35 cycles an approx. 20% of surface coating was exfoliated and after 46 cycles the coating was fully exfoliated.

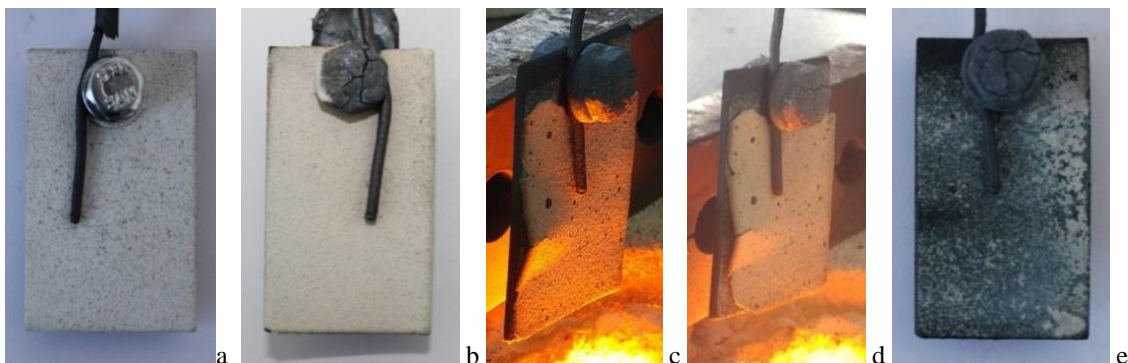


Fig. 8. The thermal shock test of samples with TBC coatings in the initial state (a), after 25 cycles (b), after 30 cycles (c), after 35 cycles (d) and after 46 cycles (e)

The relatively high stress areas associated with the geometry of the specimens also contributed to the spallation of the coatings. In the first phase the spallation of the coatings was initiated first from the edge and continued with the central area.

Based on this behavior no samples were microstructural investigated and the number of 35 thermal cycles was considered as the maximum shock resistance of TBC investigated.

4. CONCLUSIONS

In this paper, TBC with yttria-stabilized zirconia (YSZ) as top coat and NiCrAlY alloy as bond coat were tested and evaluated by isothermal oxidation tests at high temperatures and thermal shock resistance by furnace cyclic oxidation test (FCT). The oxidation tests were performed at 1100 °C with holding durations of 100, 200 and 300 hours by using an atmospheric electrical furnace. FCTs were performed at 1300 °C with holding the specimens for 9 minutes in the atmosphere of electrical furnace, and cooling by compressed air for 2 minutes until a temperature of approx. 40 °C was reached.

Based on the research and experimental results obtained, the following were found:

- In the case of samples with TBCs tested for isothermal oxidation, a layer of TGO which was formed at the bond coat-top coat interface during oxidation increased in thickness as a function of the exposure durations of 100, 200 and 300 hours. During the isothermal oxidation test, the thickness of metallic bond coat had a tendency to decrease with increasing the exposure times from an average thickness of 55 µm to 40 µm after 300 hours and the thickness of TGO increasing to 3,5 µm after 300 hours.
- During the thermal shock testing of specimens, it was found that after 30 cycles the deterioration process of sample has started, after 35 cycles approx. 20% were exfoliated and after 46 cycles the coating was fully exfoliated. It was also found that the geometry of the specimens contributed to the spallation of the coatings.

For future studies, TBC system with yttria-stabilized zirconia (YSZ) as top coat, NiCrAlY alloy as bond and In625 substrate will be tested for hot corrosion resistance.

ACKNOWLEDGEMENT

This work was carried out within POC-A1-A1.2.3-G-2015, ID/SMIS code: P_40_422/105884, “TRANSCUMAT” Project, Grant no. 114/09.09.2016 (Subsidiary Contract no. D1.3/114/18.12.2017), Project supported by the Romanian Minister of Research and Innovation.

REFERENCES

- [1] Mobarra R., Jafari A.H., Karaminezhad M., Hot corrosion behavior of MCrAlY coatings on In 738LC, Surf. Coat. Tech., 2006, 201, 2202–2207.
- [2] Xie D., Xiong Y., Wang F., Effect of an enamel coating on the oxidation and hot corrosion behavior of an HVOF sprayed CoNiCrAlY coatings, Oxidation of Metals, 2003, 59, 503-516.
- [3] Nijdam T.J., Sloof W.G., Combined pre-annealing and pre-oxidation treatment for the processing of thermal barrier coatings on NiCoCrAlY coatings, Surf. Coat. Tech., 2006, 201, 3894–3900.
- [4] Limarga A.M., Clarke D.R., Characterization of Electron Beam Physical Vapor Deposited Thermal Barrier Coatings Using Diffuse Optical Reflectance, Int. J. Appl. Ceram. Technol., 2009, 6 (3), 400–409.
- [5] Feuerstein A., Knapp J., Taylor T., Ashary V., Bolcavage A., Hitchman N., Technical and Economical Aspects of Current Thermal Barrier Coating Systems for Gas Turbine Engines by Thermal Spray and EB-PVD: A Review, Journal of Thermal Spray Technology, 2008, Vol: 17, 199-213.
- [6] L. Wang, Y. Wang, X.G. Sun, J.Q. He, Z.Y. Pan, C.H. Wang, Microstructure and indentation mechanical properties of plasma sprayed nano-bimodal and conventional ZrO₂-8wt%Y₂O₃ thermal barrier coatings, Vacuum 86 (2012) 1174-1185.
- [7] S.Q. Nusier, G.M. Newaz: Growth of interfacial cracks in a TBC/superalloy system due to oxide volume induced internal pressure and thermal loading, International Journal of Solids and Structures 37 (2000) 2151-2166.
- [8] Vaßen R., CERNUSCHI F., RIZZI G., SCRIVANI A., MARKOCSAN N., OSTERGREN L., KLOOSTERMAN A., MEVREL R., FEIST, J., NICHOLLS J., Recent Activities in the Field of Thermal Barrier Coatings Including Burner Rig Testing in the European Union, Advanced Engineering Materials, 2008, 10, No. 10, 907-921.
- [9] Kara, I. E., TBK Kaplamaların Thermal Shock Özelliklerinin İncelenmesi, Master Thesis, Sakarya University, Metalurgical and Materials Engineering Department, (in Turkish), 2008.

- [10] Bolcavage A., Feuerstein A., Foster J., Moore P., Thermal Shock Testing of Thermal Barrier Coating/Bondcoat Systems, *Journal of Materials Engineering and Performance*, 2004, Vol: 13(4), 389-397.
- [11] Traeger F., Vaßen, R., Rauwald K.H., Stover D., Thermal Cycling Setup for Testing Thermal Barrier Coatings, *Advanced Engineering Materials*, 2003, Vol: 5 (6), 429-432.
- [12] Thompson J.A., Clyne T.W., The Effect Of Heat Treatment On The Stiffness Of Zirconia Top Coats in Plasma Sprayed Zirconia Top Coats in Plasma-Sprayed TBCs, *Acta mater.*, 2001, 49, 1565–1575.
- [13] Padture, N. P., Gell, M., & Jordan, E. H. (2002). Thermal barrier coatings for gasturbine engine applications. *Science (New York, N.Y.)*, 296 (5566), 280-4
- [14] Richer P., Yandouzi M., Beauvais L., Jodoin B., Oxidation behaviour of CoNiCrAlYbond coats produced by plasma, HVOF and cold gas dynamic spraying, *Surf.Coat.Tech.*, 2010, 204, 3962–3974.
- [15] Li Y., Li C.J., Zhang Q., Yang G.J., Li C.X., Influence of TGO composition on the thermalshock lifetime of thermal barrier coatings with cold-sprayed MCrAlY bond coat,*Journal of Thermal Spray Technology*, 2010, 19 (1-2), 168-177.
- [16] Tang F., Ajdelsztajn L., Kim G.E., Provenzano V., Schoenung J.M., Effects of SurfaceOxidation during HVOF Processing on the Primary Stage Oxidation of a CoNiCrAlYCoating, *Surf.Coat.Tech.* , 2004, 185, 228-233.
- [17] Abdullah Cahit Karaoglanli, Kazuhiro Ogawa, Ahmet Türk and Ismail Ozdemir, Thermal Shock and Cycling Behavior of Thermal Barrier Coatings (TBCs) Used in Gas Turbines, chapter 10.
- [18] R. Rajendran, Gas turbine coatings – An overview, *Engineering Failure Analysis* (26)(2012) pp. 355-369.
- [19] E. Altuncu, E. I. Karaall, G. Erdogan, F. Ustel, A.Turk, The Effect of Samples Geometry and Thermal Cycling Test Type on the Thermal Shock Behaviour of Plasma Sprayed TBC, *Plasma Process. Polym.*,6 (2009) pp. S711–S7.

SYSTEM AND METHOD DESIGN FOR TBC DEGRADATION DETECTION

Tiberius-Florian FRIGIOESCU¹, Mihaela Raluca CONDRUZ^{1,2}, Alexandru PARASCHIV^{1,2}, Teodor-Adrian BADEA¹, Lucian Cosmin ZAMFIR¹, Ion IONICA³

ABSTRACT: Thermal barrier coatings (TBCs) are structures used to protect the gas turbine components during operation at high temperatures and in corrosive-erosive environment. The prediction of such component's lifetime should be determined during designing and testing phase. This paper presents a low-cost non-destructive system with its associated method that can be applied to determine the damage degree of a thermal barrier coating tested at thermal shock. The system consists in a single-board computer and a camera module that can capture and process an image of coated samples and afterwards by calculating the pixel area it determines the coating damage degree. The results obtained with the developed system were validated by manual measurements with an image processing software. It was concluded that the system can be integrated in test rig system for thermal shock testing of TBCs in order to detect the damaged produced at coating level and predict its service lifetime.

KEYWORDS: detection, TBC, single-board computer, damage, Python

1. INTRODUCTION

The need to increase the operating temperature of different gas turbine components led to development of protective ceramic layers known as thermal barrier coatings – TBCs. By applying TBCs on turbine blades it is ensured a working temperature higher than alloy's melting temperature resulting in an increase of the overall gas turbine performances [1, 2].

A careful selection of TBC system should be realized taking into account the difference between the coefficients of thermal expansion of substrate, bond coat or top coat materials. Such differences can lead to microcracking, delamination, large spallation and finally detachment when it is heated and cooled.

In order to obtain optimal TBC systems depending on the substrate, multiple experimental studies should be conducted, experiments consisting in cooling – heating cycles (thermal shock cycles) that simulate the part working conditions. Figure 1 presents a schematic illustration of the TBC system and working conditions.

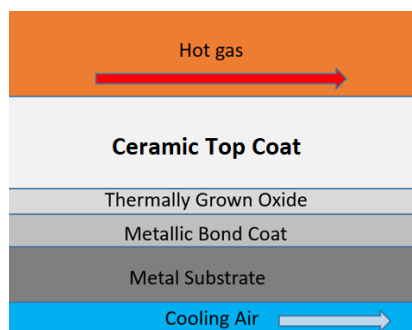


Fig. 1 The principle of the TBC system testing [1]

¹ Romanian Research and Development Institute for Gas Turbines COMOTI

² University Politehnica of Bucharest, Romania

³ SC Plasma Jet SRL

During such experiments or afterwards, many non-destructive methods are used to determine the damage degree produced in the TBC system. For example, Sayar et.al. [3] inspected TBC systems using microwaves and they observed different modifications in the coatings after high temperature exposure that can result in TBC damage.

Ogawa et.al. [4, 5] investigated the degradation of TBC used for nickel superalloys by impedance spectroscopy which can be applied to determine the physical properties and modification of the coating thickness. Flattum et.al. [6] used infrared reflectance spectroscopy in order to evaluate the degradation of TBC by studying the fingerprint region and the chemical bonding region to observe if changes and microstructural degradation were produced.

Generally, these equipment and methods are very expensive or complicated to use. Therefore, simple and more accessible methods should be developed. The present study is focused on the design, implementation and programming of a low-cost device that can monitor and analyze the damage of a TBC system which can be integrated in a test rig system for thermal shock testing.

2. THE SURFACE ANALYSIS SYSTEM

2.1 Procedure and devices

The system design shall include both physical components and auxiliaries for construction, as well as all connections between them. Furthermore, the system software was defined by the development of a programming script. The monitoring and analyzing system consist in:

- Single-board computer – SBC;
- Camera module (Resolution up to 1080p);
- Lamp;
- Relay.

During sample testing, a camera module captures an image of the tested sample. Further, the image is analyzed and processed by using the SBC with the designed script. A design scheme of the system is shown in Figure 2.

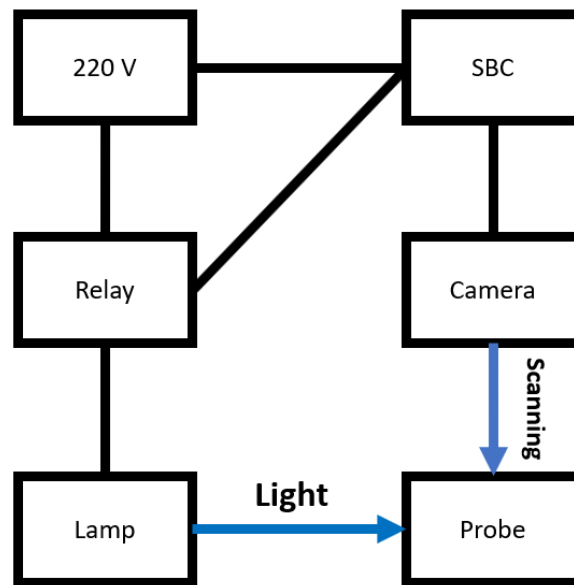


Fig. 2 Design scheme of monitoring and analyzing system

The SBC is powered by 220V AC and it contains the script programmed to take a picture with the sample's surface through the camera module. The lamp is used to illuminate the sample in order to improve the surface details. This lamp is switched on/off via the relay, which is controlled by the SBC. Figure 3 shows the designed system during testing and method implementation.

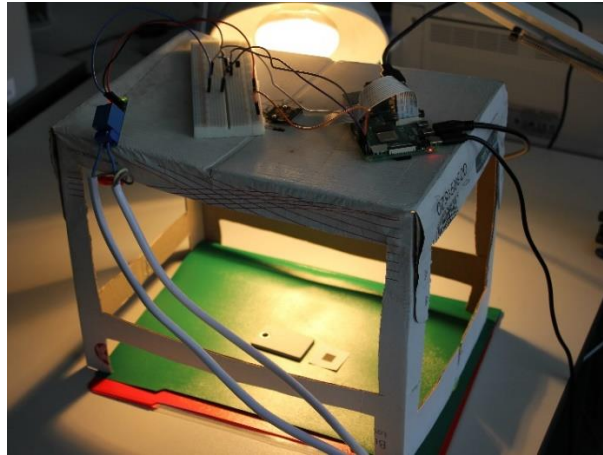


Fig. 3. Designed system during method establishment

The programming phase involved the following steps:

- Turn on the camera module;
- Close relay circuit (lamp on);
- Waiting for image stabilization (3 seconds);
- Image capture (at 1920x1080 resolution);
- Image binarization;
- Calibrate the area of a pixel;
- Coating surface measurement.

A schematic of the software logic is presented in Figure 4.

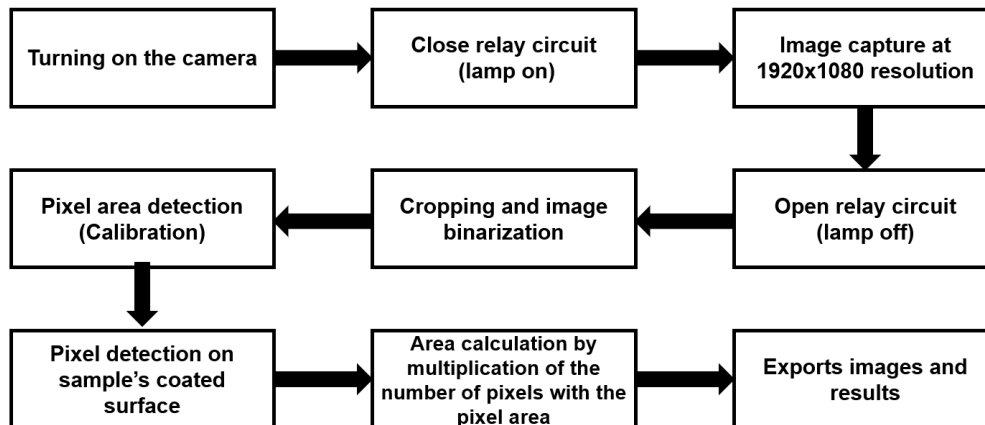


Fig. 4. Process diagram of the programmed script

When the device is switched on the SBC program closes the relay circuit and the lamp is turned on. The camera module focuses on the surface of sample for 3 seconds and afterwards takes a picture which is further binarized on the single-board computer. The SBC also operates the relay, and to process the data and display the results by using Python programming language.

To establish the method, samples with dimensions 50 x 30 x 4 mm were used. The samples consisted of a plasma-sprayed conventional TBC (yttria stabilized zirconia - ZrO_2 -6-8% Y_2O_3 - as top coat and NiCrAlY alloy as bond coat). To validate the experimental method three samples were used: one reference (as-sprayed sample with a coated area of 1500 mm²) and two samples with different damage degrees tested to determine their thermal shock resistance. The second sample was subjected to 32 thermal cycles, and the third sample underwent 53 cycles. The samples are presented in Figure 5. To calibrate the system, the reference sample and a piece of paper with a black square (area 100 mm²) were used, as it is presented in Figure 6.

The calibration procedure involves calculation of a pixel area. After capturing the image and binarizing it, the program calculates the calibration sample's area (the black square) and reads the number of pixels within it. After this step, the program divides the known square area by this number of pixels, resulting in the area of one pixel.

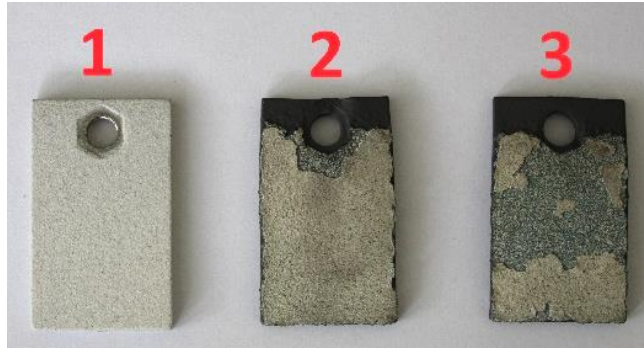


Fig. 5. Samples used for system programming and development

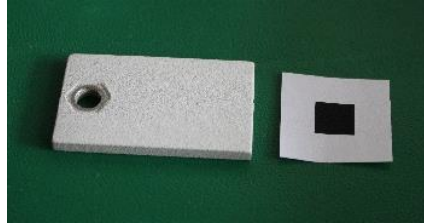


Fig. 6. System calibration

The first step in determination of the TBC damage degree is to identify the number and of pixels and the coating's surface. The number of pixels of the TBC system is determined and multiplied by the area of a pixel, resulting in the coating's surface (in mm²). Applying this procedure after each thermal shock cycle, the image binarization will highlight the coating detachment. Representative images with the system calibration and pixel detection can be observed in Figure 7.

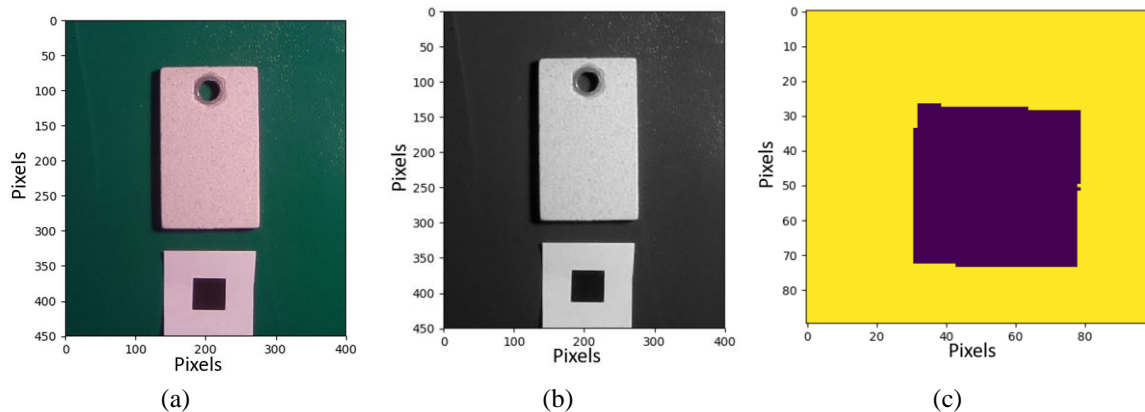


Fig. 7. Raw and processed images from programming: cropped image (a); black-white image (b); binarized image of the calibration sample (c).

A comparative analysis between these samples was performed between the results obtained using the developed system and the measurements realized with an image processing software - Scandium. Scandium was used to manually measure the area of the TBC surfaces to compare these values with the results provided by the developed low-cost device.

2.2 Results and discussions

The images with all samples were processed, the pixel area was calculated (0.05 mm²), by using the Scandium. The measurements of samples by using Scandium are presented in Figure 8 and Table 1. Based on the measurements it was determined that the TBC was degraded by 21.74% in case of the second sample and by 58.17% in case of the third sample.

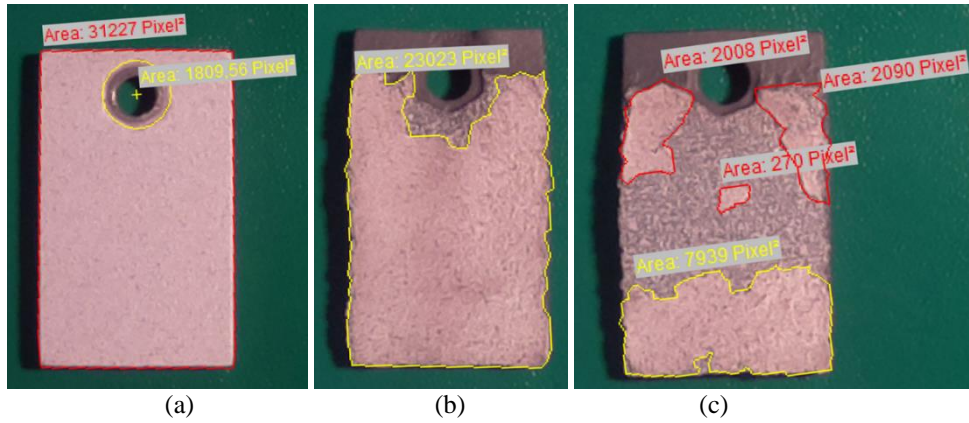


Fig. 8 Pixel area measurements made using Scandium: reference sample (a); second sample (b); third sample (c).

Table 1. Results from Scandium

Sample	1	2	3
Number of pixels coating	29418	23023	12307
Area of coating [mm ²]	1470.9	1151.15	615.35

In order to increase the accuracy of the measurements made by the designed system, a simple thresholding method was applied to binarize the images, thereby a 0.6 threshold was used for images binarization in case of reference and second sample, while a 0.65 threshold was used for the third sample image. An increase of the threshold level was applied due to the presence of coating small debris particles left on sample's surface after coating detachment which can induce significant errors during the measurements, thereby the threshold was increased in order to decrease the errors. The results obtained by the designed system are presented in Table 2 and in Figure 9.

Table 2. Results from designed system

Samples	1	2	3
Number of pixels coating	29141	21540	12229
Area of coating [mm ²]	1471.62	1122.88	634.68

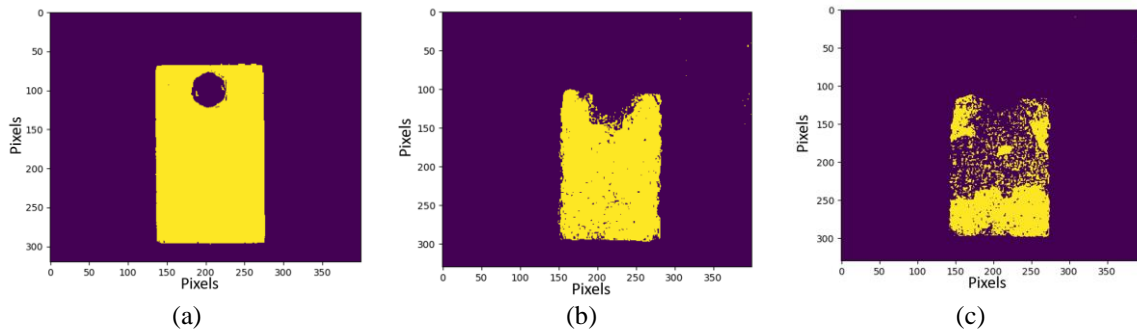


Fig. 9 Binarized images of coated sample's surfaces: reference sample (a); second sample (b); third sample (c).

Based on the measurements obtained by using the designed system, it was determined that the TBC was degraded by 23.69% in case of the second sample and by 56.87% in case of the third sample. The values recorded with the designed system are comparable with the measurements manually made with Scandium.

Obtaining these results means that the designed system can be implemented on a testing rig system. Among the changes that need to be made are the following: at the thermocouple of the cyclic test system, the SBC must be connected through a thermocouple amplifier. By this connection, the script will be modified so that every time the sample temperature drops to a temperature below 100 degrees Celsius, the current script will start running. This automates the system so that its scanning is performed after each cycle. Also, it must be processed in programming so that the results do not overlap, deleting the previous ones.

By combining these 2 systems, the user will be able to directly correlate the TBC degradation according to the cycles, everything being done automatically. In addition, a low-cost upgrade of the thermal testing system in terms of automatic control will be brought in a future work.

3. CONCLUSIONS

The article presents a low-cost system and a method designed to detect the TBC degradation degree. The components of the designed system for degradation detection, the calibration technique and measurement method were presented. Degradation detection was performed by processing images captured by a camera module. For the low-cost system validation, a sample with a TBC in as-sprayed state was used as reference and two samples with different damage degrees of the TBC (resulted after thermal shock tests). To validate the results provided by the low-cost system, manual measurements were performed on images with the same investigated samples. Based on manual measurements, it was determined that the TBC on the second sample was damaged by 21.74% and by 58.17% in case of the third sample. Similar damage values were obtained by using the designed system and method (23.69% of the second sample, 56.87% damage in case of the third sample). It can be concluded that the designed system can be integrated in a test rig system for thermal shock testing of TBCs in order to detect the amount of damaged produced at coating level and to predict its service lifetime.

ACKNOWLEDGEMENT

This work was carried out within POC-A1-A1.2.3-G-2015, ID/SMIS code: P_40_422/105884, "TRANSCUMAT" Project, Grant no. 114/09.09.2016 (Subsidiary Contract no. D1.3/114/18.12.2017), Project supported by the Romanian Minister of Research and Innovation.

REFERENCES

- [1]. D. R. Clarke, S. R. Phillpot; 2005; Thermal barrier coating materials, *Materials Today*, 8 (6), pp. 22-29
- [2]. N.P. Padture, M. Gell, E. H. Jordan; 2002; Thermal Barrier Coatings for Gas-Turbine Engine Applications, *Science*, 296 (5566), pp. 280-284
- [3]. M. Sayar, D. Seo, K. Ogawa; 2009; Non-destructive microwave detection of layer thickness in degraded thermal barrier coatings using K- and W-band frequency range, *NDT & E International*, 52(5), pp. 398-403
- [4]. K. Ogawa, D. Minkov, T. Shoji, M. Sato, H. Hashimoto; 1999; NDE of Degradation of Thermal Barrier Coating by Means of Impedance Spectroscopy, *NDT & E International*, 32(3), pp. 177-185
- [5]. K. Ogawa, T. Shoji, I. Abe, H. Hashimoto; 2000; In situ NDT of Degradation of Thermal Barrier Coatings Using Impedance Spectroscopy, *Materials Evaluation*, 58(3), pp. 476-481
- [6]. R. Y. Flattum, A. T. Cooney; 2013; Non-destructive evaluation of degradation in EB-PVD thermal barrier coatings by infrared reflectance spectroscopy, *AIP Conference Proceedings*, 1511

INCREASED PRODUCTIVITY OF WELDED JOINTS BY USING THE MIG/MAG PROCESS WITH SPINARC

Lucian-Cosmin ZAMFIR¹, Florentin CONDURACHI¹
Adrian Horia CAMPUREAN²

ABSTRACT: This article presents the SpinArc technology with application in the ship building sector. The project involves the mechanized welding of the sheets used in the ship building sector through three welding procedures, in order to obtain the optimum quality and productivity. The preliminary results show that the SpinArc technology proves a significant higher quality and productivity than the classic procedures.

KEYWORDS: welding, MIG/MAG process, wire SpinArc.

NOMENCLATURE

MIG = Metal inert gas
MAG = Metal active gas
PA = Butt welding in horizontal position
 I_s = Welding current
 U_a = Arc voltage
 V_{as} = Wire speed
 V_{sr} = Root welding speed
 V_{s1} = The welding speed of the filling layer
 S = Transverse shrinkage
 A_w = Cross-sectional area of weld
 t = Thickness of plates
 d = Root opening
 σ = Reaction stress
 E = Modulus of elasticity
 B = Width of the joint
 T_s = Total welding time
 T_{sr} = Root welding time
 T_{s1} = Welding time of the filling layer
 L_s = The length of the weld

1. INTRODUCTION

Using a model of welding gun, MA400 SpinArc (Fig. 1), with its own control system, SpinArc welding technology, developed by WeldRevolution USA, moves the welding wire in a high-speed circular motion. This process increases the productivity and quality of conventional welding procedures, such as MIG/MAG with tubular wire, solid wire or tubular wire with self-protection.

¹ Romanian Research and Development Institute for Gas Turbines COMOTI, Bucharest, Romania

² University Politehnica of Bucharest, Romania

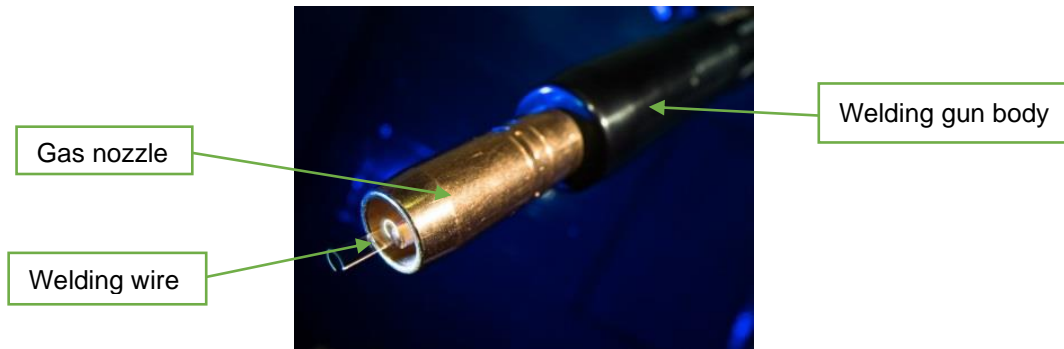


Fig. 1. Welding gun MA400 SpinArc [1]

The general advantage of the MIG / MAG welding system with SpinArc electrode is that the high speed rotation allows to increase the productivity in a variety of applications. Areas that can benefit from this welding process include the automotive industry, metal construction, general fabrication, pipelines, off-shore structure, aerospace industry, shipbuilding, storage tanks, etc..The SpinArc welding process it's easy to integrate into a standard welding equipment.

Quality is an equally important advantage of the process due to the fact that the rotation causes the spring energy to spread to the base material, thus ensuring a better penetration and a pleasant "scales" appearance.As a result, the quality is much higher than that of a weld made by classical processes.

The system works with both solid wire and tubular wire (with metallic or rutile powder core). The wire is fed by the reel of the welding source directly into the SpinArc gun. Basically it replaces the existing MIG / MAG welding gun with the MA-400 air-cooled machined gun.At its end, where the welding takes place, the wire rotates tapered. This is controlled by an engine inside the welding gun. During the welding process, the centrifugal force detaches the small droplets of molten wire and directs them to the side walls of the welded joint, creating a consistent and robust welding layer. Rotation allows high speeds of deposition.

1.1. Way of operation

The welding operator sets the standard welding parameters, such as the feed rate and the welding speed. The system works with any welding equipment, both standard and pulsed. The operator also has three possibilities of setting the rotary spring: the diameter of rotation, the speed and the direction of rotation, which can be clockwise or inverse.The diameter of rotation is set on the welding gun (Fig. 2), and the other two settings are made from the control box of the welding gun.The diameter of rotation can be adjusted from 0 to 8mm, with fine adjustment every 1mm, up to 8mm. The diameter of rotation is adjusted according to the application.In order to make a weld on large pieces, a smaller diameter of rotation will be selected, so that at the first layer a correct melting of the edges will be obtained, in order to make the root. In other cases, such as welding of corrosion-resistant materials it is better to choose a larger diameter, to obtain a thicker layer of welding.

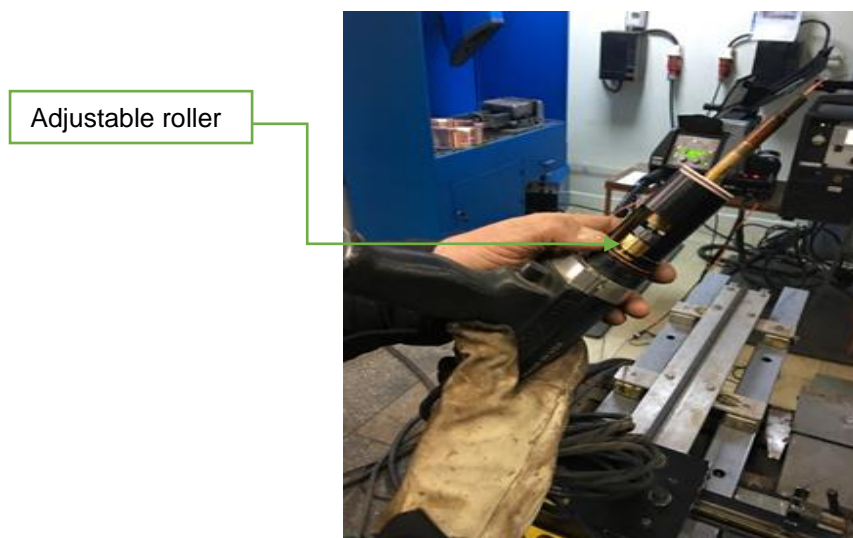


Fig. 2. Diameter adjustment system [1]

1.2. The advantages of the process

The rotary spring allows the welding of all metals in any position. This can be achieved by using solid or tubular wire with metal powders, both through the MIG / MAG welding process in pulsed current and in arc spray.

Welding in position in the spray-arc mode is almost impossible, but with SpinArc this can be done with solid or tubular wire with metallic powders, obtaining high quality welds, with a very high productivity.

Using the SpinArc system, where the centrifugal force keeps the molten metal bath in the chamfer for position welding, conventional welding and spray-arc technology with high deposition rates can be used.

Also, there is no need for the influence of slag (tubular wire with rutile core) and as a result you can use solid wire or metal core, with higher deposition rates and lower diffusible hydrogen content.

Due to the melting of the side walls, the narrow joint welding is much simpler through the rotary arch process. These types of welded joints are common in the construction of marine pipelines. At the same time, the process can be extrapolated to other areas that perform welding of thick-walled pipes and thick boards.

The part profile can be modified so that the need for chamfering is reduced or even eliminated. For example, when welding thick sheets for oil storage tanks or shipbuilding, it is often necessary to make a joint, weld on one side, then turn and weld on the other. With the SpinArc system, the chamfering operation is eliminated and the welding can be done from one side.

The stirring action of the arc in the welding bath leads to a clean appearance of the weld, with improved properties. It also allows the welding of raw materials. For nickel-based alloys or stainless steels, a convex welding cord results from the classic welding process. With the SpinArc system, the arc flattens the bath, dispersing the energy into the material. The resulting flat weld is better for a variety of applications.

2. PAPER CONTENTS

The experimental program follows:

-Compare MIG/MAG, horizontal welding, PA position, in three situations: solid wire, tubular wire and SpinArc.

-Determining the optimum welding parameters by means of the MIG / MAG process with rotary electrode for sheets used in the naval industry;

-Comparison between the productivity of the MIG / MAG process with rotary electrode and of the classic MIG / MAG process.

-Comparative determination of welding stress and deformations for the two processes;

The present paper presents the preliminary results obtained at welding in the PA position.

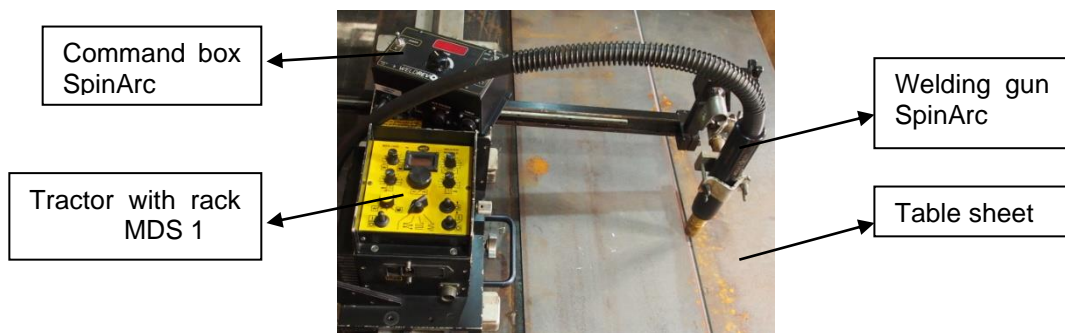


Fig. 3. Experimental stand

Comparative welding tests were performed on 500x300x10 mm samples, processed with 40 ° V joint and I joint (without machining) on ceramic root support.

The optimum parameters were determined so as to obtain a welding cord with unsuitable aspect, at which the linear energy was minimal, in order to obtain tensions and deformations as small as possible. Also, it was considered to obtain a deposition rate and to join welding speeds that will lead to the increase of the productivity compared to the classic process. **Only optimal results are presented in the paper.**

Used equipment:

-Source of welding: Phoenix 405 Synergic S – EWM,

-Welding tractor with rack: KBUG 5102- BUG-O SYSTEMS,

- Welding tractor with rack: Modular Drive System 1 – BUG-O SYSTEMS,
- Welding gun: SpinArc MA 400 gas cooled -Weld Revolution,
- Positioning device.

3. MATERIAL AND METHOD

3.1. Welding in the PA position – butt welding in horizontal plane with solid wire

The welding was done mechanically, using a KBUG 5102 rack tractor and the Phoenix 405 Synergic S. welding equipment. The type of wire used is presented in table 1. Angular pendulum was used with flanking. Root ceramic support was provided.

Table 1. Characteristics of the solid wire [2].

#	The mark of the wire	The type of the wire	Wire composition according to the catalog,%								Mean properties of the deposited weld metal according to the catalog [M21/CO ₂]				
			C	Mn	Si	P	S	Al	Cr	Ni	R _m ,	R _{p0.2} ,	A ₅ ,	KV, min.	
			Mo	V	Cu	Nb	N	B	Ti	-	Mpa	Mpa	%	J	T, °C
1	FILEUR G3	Solid (Ar/CO ₂ – CO ₂) (M21/CO ₂)	0.08	1,75	0.85	≤0,025	≤0,025	-	-	-	530-660	>460	≥24	≥70	-20
			-	-	-	-	-	-	-	-					

Dimensions of sheets metal for welded samples: 500x300x10mm with 40 ° joint. The material to be welded is a general structural steel S355. The diameter of the wire welding is 1.2mm. Welding parameters were determined experimentally based on the recommendations of the wire manufacturer. [3]

Welding was done from 2 passes:

I. Root layer:

- The program used: Root Arc.
- The parameters of the welding regim:
- Is = 158 A
- Ua= 21.1V
- Vas= 4,5 m/min
- Vsr =7.15 cm/min.
- Lp = 6mm
- Stationary on the flanks = 0,2s.



Fig. 4. PA welding root layer with solid wire

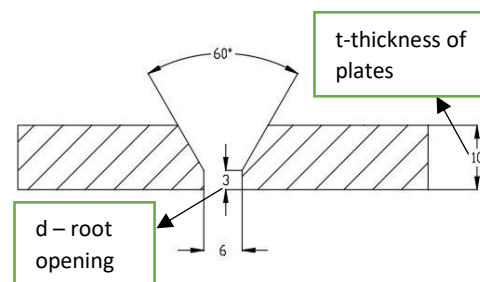


Fig.5. Solid wire welding joint dimensions

II. Second layer:

- The program used: Force Arc Pulse;
- The parameters of the welding regim:
- Is = 185A;
- Ua = 27V;
- Vas = 7 m/min;
- Vs₁ = 15 cm/min;

$L_p = 8 \text{ mm}$;
Stationary on the flanks = 0,2s.



Fig. 6. Full-shape PA welding

3.2. Welding in the PA position- butt welding in horizontal plane with tubular wire

The test was performed with the same equipment as in point 3.1. It was used for rooting tubular wire with metallic powders, and for filling layer of rutile tubular wire. The types of wires used are those in table 2.

Table 2. Additive materials used for welding with tubular wire [4, 5].

Nr . crt	The mark of the wire	The type of the wire	Wire composition according to the catalog, %								Mean properties of the deposited weld metal according to the catalog [M21/CO ₂]				
			C	Mn	Si	P	S	Al	Cr	Ni	R _m ,	R _{p0.2} ,	A ₅ ,	KV, min.	
			Mo	V	Cu	Nb	N	B	Ti	-	Mp _a	Mpa	%	J	T, °C
1.	FILEUR AMC 01	Tubular	0,06	1,40	0,35	≤0,025	≤0,025	-	-	-	530 - 660	≥460	≥22	80	-40
			-	-	-	-	-	-	-	-	-	-	-	-	-
		with metal powders (CO ₂ /Ar – CO ₂) (M21/CO ₂)	0,05	1,30	0,30	0,025	0,025	-	-	-	500 - 640	>420	>22	70	-40
			-	-	-	-	-	-	-	-	-	-	-	-	-
2.	FILEUR ARS	Tubular rutile CO ₂ /Ar (M21)	0,06	1,30	0,45	≤0,025	≤0,025	-	-	-	530 - 660	≥460	≥22	70	-20

Dimensions of sheets for welded samples: 500x300x10mm with 40 ° joint. The material to be welded is a general structural steel S355. The diameter of the wire welding is 1.2mm. Welding parameters were determined experimentally based on the recommendations of the wire manufacturer. [3]

Welding was done from 2 passes:

I. Root layer- wire Ø1,2mm tubular with metallic powders

The program used: Root Arc pulse

The parameters of the welding regime:

$I_s = 183 \text{ A}$

$U_a = 26,5 \text{ V}$

$V_{as} = 4,5 \text{ m/min}$

$V_{sr} = 10 \text{ cm/min.}$

$L_p = 6 \text{ mm}$

Stationary on the flanks = 0,2s.

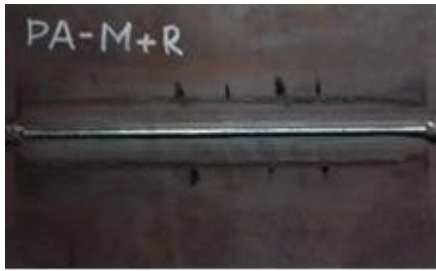


Fig. 7. The root obtained by welding with tubular wire with metal powders

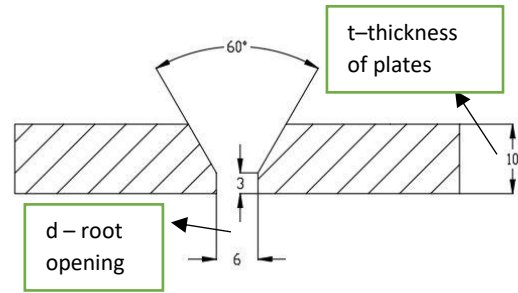


Fig.8. Tubular wire welding joint dimensions

- II. Layer II: wire Ø 1,2mm tubular rutile
 The program used: Force Arc Pulse
 The parameters of the welding regime:
 $I_s = 302A$
 $U_a = 31V$
 $V_{as} = 11m/min$
 $V_{s1} = 14,6 cm/min.$
 $L_p = 8 mm$
 Stationary on the flanks = 0,1s.

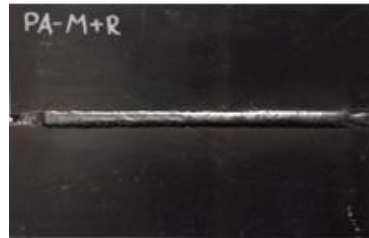


Fig. 9. Welding made of tubular wire with metallic powders

3.3. Welding in the PA positions- butt welding in horizontal plane with tubular wire through the SpinArc process.

Dimensions of sheets metal for welded samples: 500x300x10mm with I-joint (without processing). The material to be welded is a general structural steel S355. The diameter of the wire welding is 1.2mm. Welding parameters were determined experimentally based on the recommendations of the wire manufacturer. [3] Welding was performed from 2 passes using the MDS 1 tractor with linear weaver

- I. Root layer- tubular wire with metal powders, Ø 1.2mm, ceramic support.
 The program used: Root Arc
 The parameters of the welding regime:
 $I_s = 175 A$
 $U_a = 19,1V$
 $V_{as} = 7 m/min$
 $V_{sr} = 17 cm/min.$
 Rotation diameter = 4mm
 Wire rotation = 1250 rot/min



Fig.10. Root obtained through the SpinArc process

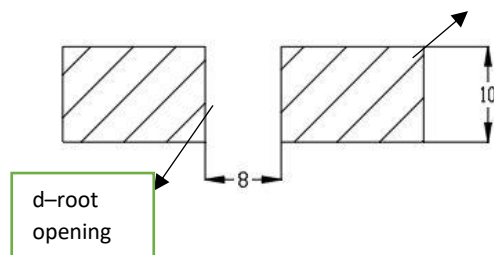


Fig.11. SpinArc welding joint dimensions

- I. Layer II: rutile tubular wire, Ø 1.2mm.
 The program used: Force Arc
 The parameters of the welding regime:
 $I_s = 250$ A
 $U_a = 23,4$ V
 $V_{as} = 9$ m/min
 $V_{s1} = 22$ cm/min.
 Rotation diameter = 5mm
 Wire rotation = 1250 rot/min



Fig. 12. Welding obtained by the mechanized SpinArc process

3.4. Calculations of transverse shrinkage and stress [6]

In literature, are proposed numerous formulas for estimating the cross-sectional contraction at the butt weld. For example, Spraragen and Ettinger suggest that the amount of transverse shrinkage in carbon and low-alloy steel welds can be estimated using the following equation (1):

$$S = 0.2 \frac{A_w}{t} + 0.05d \quad (1)$$

For the welding by the classical procedure the welding section was calculated $A_w=106\text{mm}^2$, and for the SpinArc procedure $A_w=93\text{mm}^2$. According to Fig. 5 and Fig. 8 for welding by the classical process MIG/MAG root opening $d = 8\text{mm}$ and thickness of plates $t = 10\text{mm}$. According to Fig. 11 for welding with SpinArc process root opening $d= 6\text{mm}$ and thickness of plates $t=10\text{mm}$.

Table 3. Parameters of the transverse shrinkage

	A_w [mm ²]	d [mm]	t [mm]	S [mm]
Welding by the classical MIG/MAG	106	6	10	2.208
Welding with SpinArc	93	8	10	2.074

When transverse shrinkage occurs, it causes reaction stress. This is calculated with the following equation (2):

$$\sigma = E \left(\frac{S}{B} \right) \quad (2)$$

Table 4. Parameters of the reaction stress [7]

	E [MPa]	S [mm]	B [mm]	σ [MPa]
Welding by the classical MIG/MAG	210000	2.208	600	772.8
Welding with SpinArc	210000	2.074	600	725

3.5. Calculation of the welding time [6]

The welding time is calculated with the following equations (3), (4), (5):

$$Ts = Tsr + Ts1 \quad (3)$$

$$Tsr = \frac{Lp}{Vsr} \quad (4)$$

$$Ts1 = \frac{Lp}{Vs1} \quad (5)$$

Table 5. Time for welding

	Tsr [min]	Ts1 [min]	T [min]
Welding with solid wire	7	3.33	10.33
Welding with tubular wire	5	3.42	8.42
Welding with SpinArc	2.94	2.27	5.21

4. CONCLUSIONS

The element of originality in the chosen technology consists in the fact that we combined the electrode rotation motion with the linear oscillation movement of the welding head, thus obtaining a much higher deposition rate. It can be seen from the comparative analysis of the three welding regimes used that the SpinArc welding process has the highest productivity, to which is added the fact that the chamfering operation is not necessary. Despite the fact that the boards were welded freely, no visible deformation occurs at SpinArc welding. All in all, we can conclude that SpinArc welding has the following advantages and disadvantages:

Benefits:

- High welding speed, leads to high productivity;
- From the ratio between the time obtained in the case of the classic MIG process with solid wire and the time obtained in the case of the SpinArc process, it turns out that the SpinArc process is 98% faster;
- From the ratio between the time obtained in the case of the classic MIG process with tubular wire and the time obtained in the case of the SpinArc process, it turns out that the SpinArc process is 61% faster;
- Minimum sheet deformations. In the case of welding with solid and tubular wire, the pieces suffered an angular deformation of 4°, and by the SpinArc process with tubular wire the deformation was 2°;
- Reducing the number of passes;
- Easy to use, no special schooling required.

Disadvantages:

- Special welding equipment that involves additional investments;

REFERENCES

- [1]. Woods S. – “*High-speed rotating arc welding increases productivity and quality*”.
- [2]. AWS A5.18: ER70S-6 | EN440: G46 2 M G4Si1 / G42 2 C G4Si1.
- [3]. General catalogue – *Trafilerie di citadella FILEUR*.
- [4]. AWS A5.18: E70C-6MH4 | EN 758: T46 4 M M 1 H5 / T42 4 M C 1 H5.
- [5]. AWS A5.20: E71T1MH4 | EN 758: T46 2 P M 1 H5.
- [6]. *WELDING HANDBOOK VOL. 1* Welding Science & Technology – AWS NINTH Edition.
- [7]. mec.tuiasi.ro/rm/incercari/5.htm (accessed at 25.03.2020)

REPLACEMENT OF CONVENTIONAL COUPLINGS WITH 3D PRINTED COUPLINGS

Teodor STĂNESCU¹, Nicușor-Daniel STAN¹, Gabriel BADEA¹
Eduard VASILE¹, Razvan BORCEA¹, Alexandru ILIES¹, Horațiu ȘERBESCU¹

ABSTRACT: In this article are presented the advantages and disadvantages of using additive manufacturing couplings compared to conventional couplings. Experimental measurements were made to determinate the using domains.

Keywords: couplings, 3D printing, additive manufacturing, PLA, PETG.

NOMENCLATURE

PLA – Polylactic acid
PETG – Polyethylene Terephthalate Glycol – Modified
FDM – Fused Deposition Molding
P&ID – Piping and instrumentation diagram
 V_g – Displacement
 n – Rotational speed
 p_1 – Oil pressure
 Q – Flow rate
 T – Torque

1. INTRODUCTION

With the advancement in the field of manufacturing technologies, many companies are starting to develop prototypes using the latest and most advanced technologies. For example, in the medical field, with the help of additive manufacturing, there have been various studies regarding implant problems in the bone implants field [1]. Due to the accelerated growth of the planet's population and the increasing demand for housing, the idea of printing houses came up [2].

Other studies have been carried out, including in the food industry [3]. Couplings make the permanent or alternate link between two consecutive elements of a transmission. They transmit the rotation speed and torque without modifying the movement law. [4]

Couplings can be made of a lot of materials like steel, rubber etc. In the last years, along with the 3D printing development, a lot of questions appeared about using this technology for components because complex shapes can be created without further processing. In this article are shown different types of 3D printed couplings from various plastic types (PLA, PETG). These couplings were verified using a testing configuration which is presented in Chapter 3 to establish the functionality in various fields of use (prototypes, industrial facility) etc.

¹ Romanian Research and Development Institute for Gas Turbines COMOTI

2. MATERIALS DESCRIPTION AND TESTING CONFIGURATION

2.1. Materials

Table 1 presents the mechanical characteristics and the printing parameters of the most used plastic materials.

Mechanical characteristics:

- ultimate strength;
- stiffness;
- durability;
- maximum service temperature;
- coefficient of thermal expansion;
- density.

Printing parameters:

- printability;
- extruder temperature;
- bed temperature;
- heated bed;
- material price.

Table 1. Plastic material properties for 3D printing [5]

Material	Ultimate strength [MPa]	Stiffness	Durability	Maximum service temperature [°C]	Coefficient of thermal expansion [$\mu\text{m}/\text{m}^\circ\text{C}$]	Density g/cm^3	Price (\$/kg)	Printability	Extruder temperature [°C]	Bed temperature [°C]	Heated bed
ABS	40	5/10	8/10	98	90	1.04	10-40	8/10	220-250	95-110	Required
Flexible	26-43	1/10	9/10	60-74	157	1.19-1.23	30-70	6/10	225-245	45-60	Optional
PLA	65	7.5/10	4/10	52	68	1.24	10-40	9/10	190-220	45-60	Optional
HIPS	32	10/10	7/10	100	80	1.03-1.04	24-32	6/10	230-245	100-115	Required
PETG	53	5/10	8/10	73	60	1.23	20-60	9/10	230-250	75-90	Required
Nylon	40-85	5/10	10/10	80-95	95	1.06-1.14	25-65	8/10	220-270	70-90	Required
Carbon fiber	45-48	10/10	3/10	52	57.5	1.3	30-80	8/10	200-230	45-60	Optional
ASA	55	5/10	10/10	95	98	1.07	38-40	7/10	235-255	90-110	Required
Polycarbonate	72	6/10	10/10	121	69	1.2	40-75	6/10	260-310	80-120	Required
Polypropylene	32	4/10	9/10	100	150	0.9	60-120	4/10	220-250	85-100	Required
Metal filled	20-30	10/10	4/10	52	33.75	2-4	50-120	7/10	190-220	45-60	Optional
Wood filled	46	8/10	3/10	52	30.5	1.15-1.25	25-55	8/10	190-220	45-60	Optional
PVA	78	3/10	7/10	75	85	1.23	40-110	5/10	185-200	45-60	Required

From the materials presented above only PLA and PETG were used for the manufacturing process of the couplings. The reasons are: they are very common, the printing temperatures are low, they don't discharge toxic gases while printing and also have reliable strength and a low price.

2.2. Printing settings

The printing machine used has the FDM technology and the following parameters:

- traveling speed: $\leq 180\text{mm}/\text{s}$, normal $60\text{mm}/\text{s}$;
- printing precision: $\pm 0.1\text{mm}$;
- nozzle diameter: standard 0.4mm , can be 0.2mm or 0.3mm ;
- hotbed temperature: $\leq 110^\circ\text{C}$;
- nozzle temperature: $\leq 255^\circ\text{C}$;
- filament thickness: 1.75mm ;
- layer thickness $0.1-0.4\text{mm}$.

The printing characteristics of each coupling are shown in the table below (Table 2).

Table 2. Printing settings of tested coupling

Coupling	Material	Layer thickness [mm]	Number of wall layers	Number of top/bottom layers	Infill material density	Printing temperature [°C]	Printing speed [mm/s]	Printing position
1	PLA	0,2	3	3	30%	203/52	45	transverse
2	PLA	0,2	5	5	100%	203/52	50	transverse
3	PLA	0,2	5	4	30%	203/52	50	longitudinal
4	PETG	0,2	5	4	30%	225/60	50	longitudinal

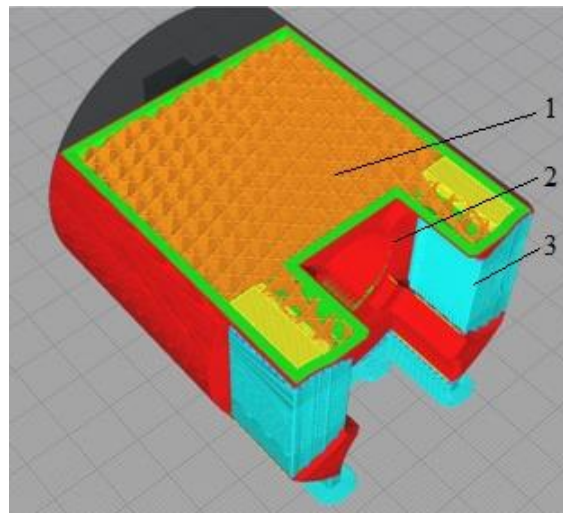
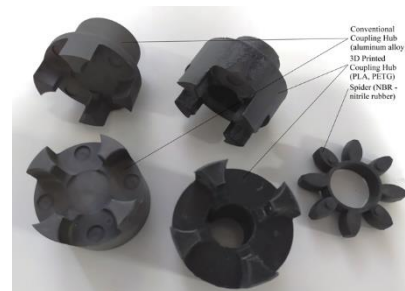


Fig. 1 3D visualization on the coupling before printing in which:
 1-The density of the filling layers; 2- Outside layers of the part;
 3-support for the layers that don't have a sitting surface.



Coupling type 1



Couplings type 2, 3 and 4



Coupling assembly type 2, 3 and 4

Fig. 2 Couplings presentation before test

2.3. Testing configuration

For the measurements, the printed couplings presented in chapter 2.2 were fitted to transmit rotation between an electric motor and the oil pump. The P&ID (Piping and instrumentation diagram) of the testing configuration is presented in figure 3.

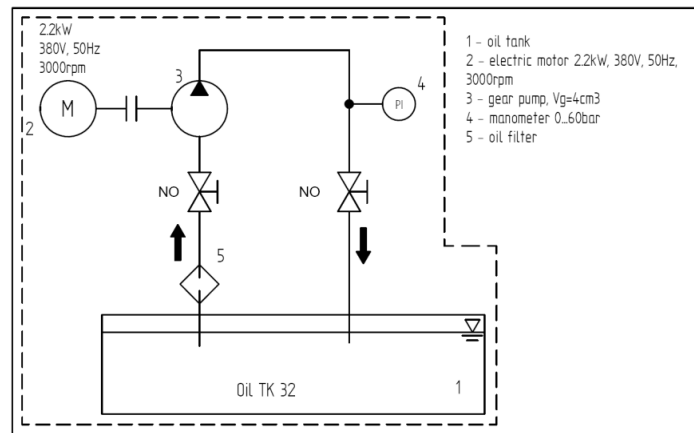


Fig.3 Piping and instrumentation diagram

3. EXPERIMENTAL RESULTS

Following the measurements on the testing configuration presented in chapter 2 the results are displayed in figure 4 and table 3. It was observed that the PLA couplings broke parallel with the printing layers and the PETG coupling cracked in the parallel key zone.



Coupling 1



Coupling 2



Coupling 3



Coupling 4

Fig.4 Couplings presentation after test

Table 3. Experimental data

Coupling	Breaking pressure [bar]	Material	Direction of printing layers	Comments
1	11	PLA	transverse	Coupling broke transversal
2	7	PLA	transverse	Coupling broke transversal
3	7	PLA	longitudinal	Coupling broke longitudinal
4	15	PETG	longitudinal	Coupling cracked in the parallel key zone

4. CALCULATION OF TORQUE BREAKING COUPLING

In order for compute maximum torque in which the couplings had broken, the following formulas have been used:

$$Q \left[\frac{m^3}{h} \right] = n[rpm] \cdot V_g[cm^3] \cdot 10^{-6} \cdot 60 \quad (1)$$

in witch: $V_g = 4 \text{ cm}^3$; $n = 2.960 \text{ rpm}$.

$$T[Nm] = \frac{V_g[cm^3] \cdot 10^{-6}}{2 \cdot \pi} \cdot p_1 \left[\frac{N}{m^2} \right] \quad (2)$$

thus: p_1 =gauge pressure.

Thereby, with the help of this relationship, the breaking torque for coupling failure have been determined. For example the torque for coupling type 1 is $T_1 = 0,64 \text{ Nm}$;for coupling type 2 and 3 is $T_2 \text{ and } 3 = 0,38 \text{ Nm}$;and for coupling type 4 is $T_4 = 0,89 \text{ Nm}$.

5. CONCLUSIONS

Following the tests, it was observed that the PLA couplings broke parallel with the printing layers and the PETG coupling only cracked.

It can be observed that for couplings 2 and 3, both made from PLA, the breaking torque is the same $T_2 \text{ and } 3 = 0,38 \text{ Nm}$ and that the direction of printing layers didn't make any difference.

The principal advantages of 3D printed couplings are the short production time and the complexity of form that can be made (compared with classical manufacturing methods that include designing, casting, milling, turning, grinding). There are only two stages for 3D printed couplings (creating the 3D model and printing it) and a large variety of shapes that cannot be reproduced by the classical methods, whether it is milling, casting or turning.

Another advantage is its reduced mass (the possibility of using them in the aeronautical field). There are disadvantages too, the main being represented by functionality, these need slow starts, without shocks, and the torque produced by the electric motor to be a reduced one. Considering that plastics are much cheaper compared to metallic, ceramic etc. and due to the elimination of many steps from the technological process the production price of the printed couplings is a low one.

Future tests will focus on finding another material, more resistant and with stronger adhesion between the deposited layers, with which to print the coupling.

REFERENCES

1. M. van Eijnatten et al., CT image segmentation methods for bone used in medical additive manufacturing, *Medical Engineering and Physics* (2017), <https://doi.org/10.1016/j.medengphy.2017.10.008>
2. Izabela Hager et al., 3D printing of buildings and building components as the future of sustainable construction, *ICEBMP* (2016)
3. Lipton, J.I, Cutler, M., Nigl, F., Cohen, D., Lipson, H., Additive Manufacturing for the Food Industry - A review, *Trends in Food Science & Technology* (2015), doi: 10.1016/j.tifs.2015.02.004
4. <http://webbut.unitbv.ro/Carti%20on-line/OM/JulaChisuLates/Col5.pdf>
5. <https://www.simplify3d.com/support/materials-guide/properties-table>

DESIGNING A HIGH EFFICIENCY ADDITIVELY MANUFACTURED HEAT EXCHANGER

Traian TIPA¹, Andrei George TOTU¹, Andrei RADU¹, Madalin DOMBROVSCI¹
Cristian OLARIU¹, Sebastian VOICU¹

ABSTRACT: Obviously, conventional manufactured heat exchangers have reached their maturity. Hence new concepts must be developed in order to enhance its traditional advantages such as specific consumption reduction in gas turbines. This paper proposes a heat exchanger concept with significant advantages in terms of weight and compactness, manufactured by Selective Laser Melting (SLM) technology using additive manufacturing, intended to increase the thermal efficiency of turboshaft engines. The proposed concept consists of a core made of corrugated tubes, which have a thin and symmetrical profile in the section, placed in the hot gas stream and through which the pressurized cold air stream pass. Due to the shape of the tubes, two advantages are introduced: a minimal flow distortion, the profile has very low drag and a high heat transfer given through the large exchange surface introduced by the tube shape.

KEYWORDS: additive manufacturing, flow simulation, heat transfer, thermal and hydraulic performance, low emissions

NOMENCLATURE

A - heat transfer area [m²]

AM - Additive manufacturing

CFD -computational fluid dynamics

K - heat transfer coefficient [W/m²K]

L - channel length[m]

M_a - air flow rate [kg/s]

M_g - gas flow rate [kg/s]

Q - heat exchanger load [W]

SLM - Selective Laser Melting

ΔT_{med} - logarithmic mean temperature difference

T₁ - compresor inlet air temperature [K]

T₂ - recuperator inlet air temperature [K]

T₃ - combustor outlet temperature [K]

T₄ - recuperator inlet gas temperature [K]

T₅ - recuperator outlet air temperature [K]

T₆ - recuperator outlet gas temperature [K]

c_p - specific heat [J/kgK]

d_e - hydraulic diameter [m]

f - friction factor

w - fluid velocity [m/s]

Greek symbols

α_{air} - convection coefficient for compressed air

α_{gas} - convection coefficient for burnt gases

ε - correction coefficient for cross-flow logarithmic mean temperature difference

δ - wall thickness [mm]

λ - thermal conductivity [W/mK]

π_c - pressure ratio

¹ Romanian Research and Development Institute for Gas Turbines COMOTI

1. INTRODUCTION

Heat exchangers transfer heat from one fluid to another while keeping the fluids from coming into contact with each other. They are widely used in power generation, space heating, refrigeration, air conditioning, and propulsion systems (with maritime and land applications). As the operating costs of the high-power engines are mostly found in the amount of fuel used, a decrease in the specific consumption leads both to the decrease of these costs and to the decrease in the amount of pollutants that are introduced into the atmosphere. A specific consumption reduction can be achieved by introducing a heat recovery system that uses the wasted energy from the exhaust gases by introducing some of it back into the system.

There are different types available like plate, bundled tube or rotary heat exchangers. In addition, heat exchangers also differ in their working principle (counter-flow, direct-flow, or cross-flow) and can consist of differently shaped plates or tubes with, for example, smooth, bucked, or rippled surfaces. A typical wall thickness reaches from 0.4 to 2.5 mm and is mainly designed to withstand blockage, corrosion, active pressure, or abrasive media. Such heat exchangers are very cost-effective [1].

In conventional heat exchangers “Fig.1”, a lot of restrictions and disadvantages exist, concerning the realizable geometry, the operating temperature, as well as the manufacturing costs [1]:

1. Heat exchanger manufactured by the combination of different planar parts is limited in the realizable design and compactness (the ratio between heat exchanging surface and total volume);
2. The assembly of the different parts can result in assembly failures;
3. The realization of mechanical and fluidic interfaces is very challenging (often, the crossflow principle is realized instead of the superior counter-flow principle because of the feeding system for the different fluid channels);
4. The joining of the different parts is often realized by brazing. But the brazing material limits the operating temperature, and the brazing process can result in leakage;
5. Because of the used standardized geometries for the parts as well as the whole heat exchanger components, their outer geometry can hardly be individualized. Furthermore, no adjustment of the outer geometry on the shape of the surrounding system can be realized;
6. Some examples of ceramic-based heat exchangers for high temperature or high corrosive or abrasion applications exist, but their design is limited because of the ceramic shaping and finishing technologies. Furthermore, the operation temperature is limited because of the needed joining additives (e.g., solders or brazes) for the different ceramic parts.



Fig.1 Conventional bundled tube heat exchangers [2]

Additive manufacturing (AM) is a new class of manufacturing technologies, which has been developed during the last three decades and keeps evolving. Based on computer-aided design (CAD) files in 3D, typically a layer-wise manufacturing process follows, which allows the realization of component designs as well as inner and outer geometries that were previously regarded as not producible. Concerning the manufacturing of heat exchanger, AM technologies open the door to overcome all of the restrictions mentioned above [1]:

1. The manufacturing of the heat exchanger as one component with integrated mechanical and fluidic interfaces becomes possible;
2. No joining steps are needed, and the same properties are available in the whole component;
3. Very complex designs can be realized, and the ratio between the heat exchanging surfaces to the total volume of the heat exchanger can be increased significantly. The increased performance allows the miniaturization of the heat exchanger;
4. The adjustment of the outer geometry becomes possible, and the required volume for the implementation of the heat exchanger and the surrounding system can be decreased;
5. AM of ceramics opens the door for complex heat exchangers for demanding applications concerning operation temperature, abrasion, or corrosion.

1.1 AM heat exchangers – a review

AM heat exchangers seem to be very interesting while prices are falling especially for AM of metal components [3]. Today, only a few designs are described or commercially available. General Electric has designed UPHEAT (Ultra Performance Heat Exchanger enabled by Additive Technology) “Fig.2”, as a part of a \$2.5 M research project. This 3D printed heat exchanger is able to operate at temperatures up to 900°C and pressures up to 250bar [4]. This product was a result of hard work in the additive manufacturing field since the first 3D printed part made by GE (a fuel nozzle) came out in 2012, the first 3D printed heat exchanger being released in 2013 [5].

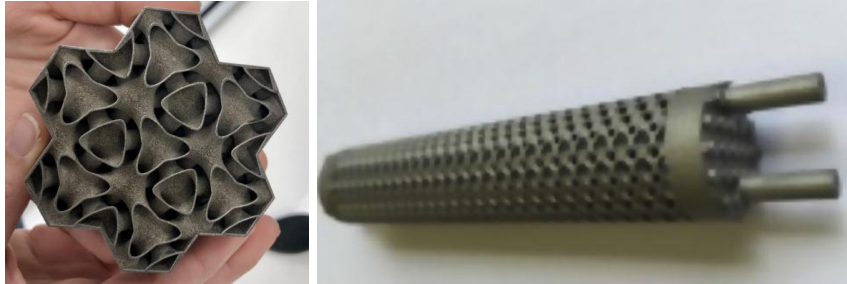


Fig. 2 GE 3-D printed milli-structured heat exchanger made from stainless steel with gyroid design [4]

Due to its large surface area/volume ratio, a heat exchanger made of aluminum AlSi10Mg “Fig.3” was able to show several benefits in comparison with a Formula 1 benchmark. The mentioned comparison revealed the advantages of the additive manufactured product: reduced weight (by 22%), it can reduce the size of existing F1 heat exchangers (by 55mm) and has a pressure drop reduction of two-thirds [6].

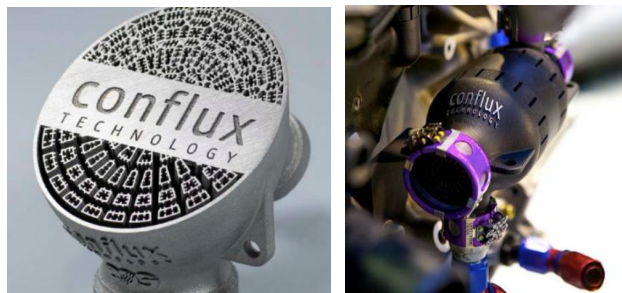


Fig. 3 Efficient Conflux Technology heat exchanger [6]

EOS and 3TRPD have designed a heat exchanger, which was manufactured with laser beam melting” Fig. 4 a. Unfortunately, they have not published any performance data for comparison. Furthermore, at Fraunhofer IFAM, a counterflow heat exchanger was developed to improve the efficiency of a micro-gas turbine system „Fig.4 b.”. The heat exchanger was particularly designed for AM, so there was no conventional way to manufacture the part. The heat exchanger combines 18 layers of channels in the limited design space. Furthermore, the complex inner channels were designed in a wave shape combined with a very small spacing to each other in order to maximize the surface for heat transfer [8].



Fig. 4 a. Additively manufactured heat exchanger by EOS and 3TRPD [7]; b. Counterflow heat exchanger manufactured by AM; left: manufactured component, right: rendering of complex internal structure inside the heat exchanger [8]

2. DESIGN STAGE

The start point in current recuperator concept design, it can be found in a primary surface tubular recuperator, made up of numerous tubes within an outer shell fabricated by MTU Aero Engines "Fig. 5". These tubes are special through its oval shape, and thanks to that they showed superior fluid flow and heat transfer characteristics.

For additively manufactured heat exchangers, a high exchange capacity is essential. It is represented by the heat flow, which can be calculated from the thermal conductivity λ , summarized in "Table 1" for different materials, the heat transfer area A, the wall thickness and the temperature difference in the heat exchanger.

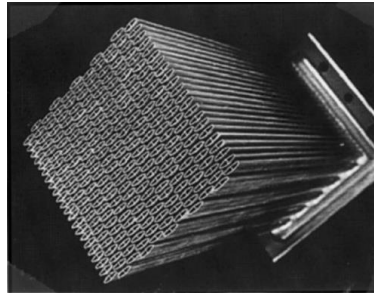


Fig.5 MTU profile tube recuperator module [9]

Table 1. Main materials used in AM [1]

Material	Thermal conductivity [W/mK]
Silver	429
Copper	401
Aluminum	237
High alloyed steel	20
Low alloyed steel	30

Even if the thermal conductivity for high alloy steel is not as good as silver or copper thermal conductivity, the favourable material proposed to be used in heat exchanger manufacturing is Inconel 625 which is a nickel-based superalloy as it is well known. The main working parameters of the heat exchanger such as maximum pressure (10 bar) or maximum temperature (~1000 K), require that heat exchanger must be very resistant. Therefore, using Inconel 625 offers good resistance to the heat exchanger and leads to the manufacturing of tubes with a minimum thickness of 0.15mm with high resistance and very lightweight.

The starting concept is represented in "Fig. 6". The heat exchanger components which achieve the heat transfer from burnt gas to compressed air must introduce minimum drag, for minimizing the overall pressure loss. It is known that airfoils have the smallest drag compared with edged objects such as flat thin fins. So, for the beginning, the model is a network of corrugated tubes (flow channels of compressed air) which have a thin symmetrical profile placed in the flow of hot gases. Using AM, some major improvements can be made regarding profile thickness and overall dimensions in order to increase the area-volume ration and reduce overall weight.

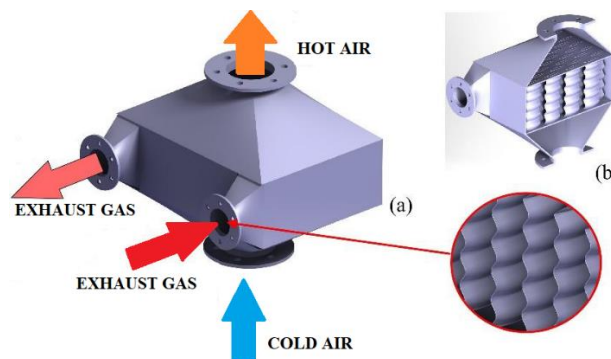


Fig. 6 Starting point design for the AM heat exchanger (a) Isometric view, (b) Section through the heat exchanger

The gases path inside of the heat exchanger is intricate in order to maximize the time spent inside. Because the compressed air pass through the system vertically, the horizontal movement of the gases leads to a so-called “cross-flow”, which offers a good thermal transfer. The usual flow speed, for both fluids, is around 10m/s in order to obtain a high energy recovery. This speed is achieved by introducing the divergent channels after the coupling flanges.

A few researches were done to see what problems can occur while the 3D printing of the recuperator concept. Therefore, for printing preparation, it must be eliminated the support layers that might appear in the interior structure affecting the flow. The optimum printing direction was determined using the existing LASERTEC 30 SLM printer control software “Fig.7”.

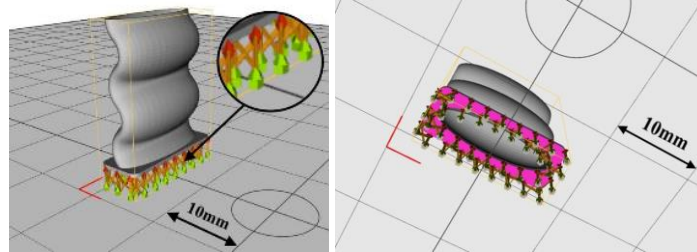
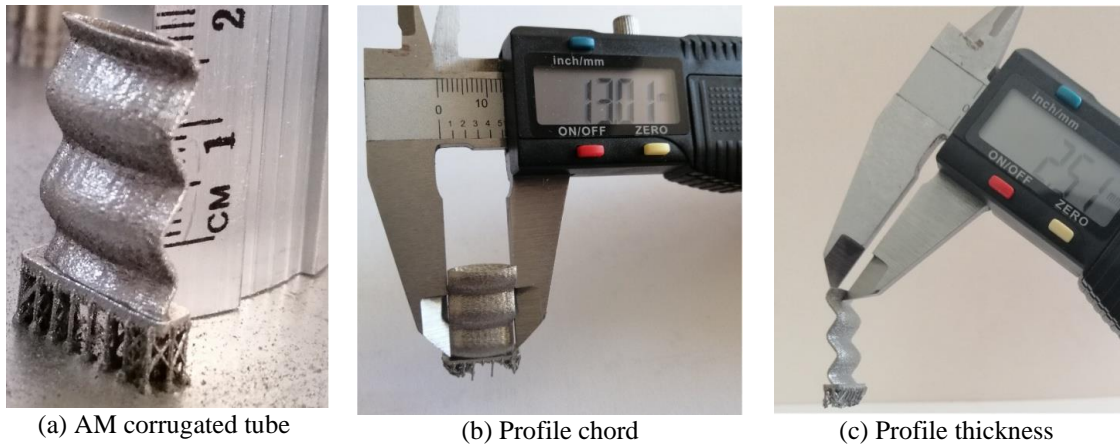


Fig.7 Printing simulation using LASERTEC 30SLM printer control software

Although the support layer is inevitable for the exterior structure, it should not appear in unwanted places leading to an increase in the structure's weight. The only favorable position resulted in the printing was the vertical one which does not affect the functioning performances. Because of the reduced wall thickness (0.2-0.4mm), the base support layer cannot be added so a small size base (4mm width, 16mm length) must be used, in the full model this representing the wall of the exchanger.

In order to verify the feasibility of the studied recuperator concept, it has been printed a corrugated tube sample “Fig.8”. The concept has proven to be achievable in terms of manufacturing technology.



(a) AM corrugated tube

(b) Profile chord

(c) Profile thickness

Fig. 8 Corrugated tube printed sample

3. HEAT TRANSFER AND PRESSURE DROP CHARACTERISTICS

The main parameters used in recuperator calculations are summarized in "Table 2".

Table 2. Design data parameters used in recuperator calculations

No.	Parameter	Values [Unit]	No.	Parameter	Values [Unit]
1	M_a	1 [kg/s]	6	T_4	1093 [K]
2	π_c	4.2	7	T_5	924 [K]
3	T_1	288 [K]	8	T_6	570 [K]
4	T_2	470 [K]	9	Q	180 [kW]
5	T_3	1457 [K]	-	-	-

One of the most vital characteristics in recuperator research is the heat transfer which can be expressed as:

$$Q = K * A * \Delta T_{med} = M_a * c_{p_a} * (T_5 - T_2) = M_g * c_{p_g} * (T_4 - T_6) = 180kW \quad [10] (1)$$

when the whole heat transfer area is $A=2.64m^2$ knowing the dimensions of the tube mentioned above. The ratio between heat transfer area and effective volume of the recuperator is $880 m^2/m^3$, which can be concluded that in a small room there is a large heat transfer area thanks to the corrugated shape of the tubes. Assuming the cross-flow arrangements, the temperature inside the recuperator was calculated with the formula for counter-flow arrangements and using a correction coefficient read from dedicated charts [10].

$$\Delta T_{med} = \varepsilon * \frac{(T_4 - T_5) - (T_6 - T_2)}{\ln\left(\frac{T_4 - T_5}{T_6 - T_2}\right)} = 71.57^\circ \quad [10] (2)$$

and the heat transfer coefficient:

$$K = \frac{1}{\frac{1}{\alpha_{air}} + \frac{\delta}{\lambda} + \frac{1}{\alpha_{gas}}} = 952.73 [W/m^2K] \quad [10] (3)$$

Another vital characteristic in recuperator research is pressure loss, especially for the recuperators used to increase microturbine efficiency when the pressure plays an important role. Inside the cold fluid channel, the pressure loss was calculated with the formula below, and the values obtained were insignificant (up to 0.02 bar, which means under 1%) which is very good for the entire assembly efficiency.

$$\Delta p = 4 * f * \frac{\rho * w^2}{2} * \frac{L}{d_e} \quad [10] (4)$$

4. 3D CFD SIMULATIONS RESULTS

For the numerical analysis, a portion of the working channel was used because obtaining qualitative results on a sector containing a row of 15 corrugated tubes is impossible. In this way, it was chosen for the analysis of heat exchange a volume containing a corrugated profiled tube. A grid consisting of structured quadrilateral elements was used near the wall and unstructured triangular elements in the remaining part of the geometry. "Fig. 9" shows a section through the mesh of the geometry used, where 9.6mil elements and 3.6mil knots were used, the mesh being thickened in the area of interest (near the wall) to better capture the heat transfer.

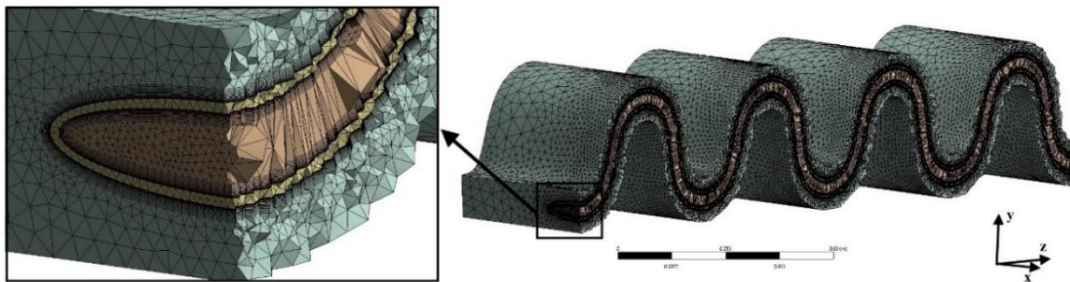


Fig. 9 Model mesh

The boundary conditions are presented in "Fig. 10". Because the heat transfer is stronger near the wall, the temperature of the fluid is slightly higher in its area. The temperatures recorded and presented in "Table 3" represent the temperature at the z coordinate in the middle of the working channel. The average temperature of the channel is actually slightly higher but not very significant. The study case was a steady one in which thermal radiation was not taken into consideration. For this case the wall is considered a surface with 0 thicknesses and the material used for the solid body was high alloyed steel (Inconel 625).

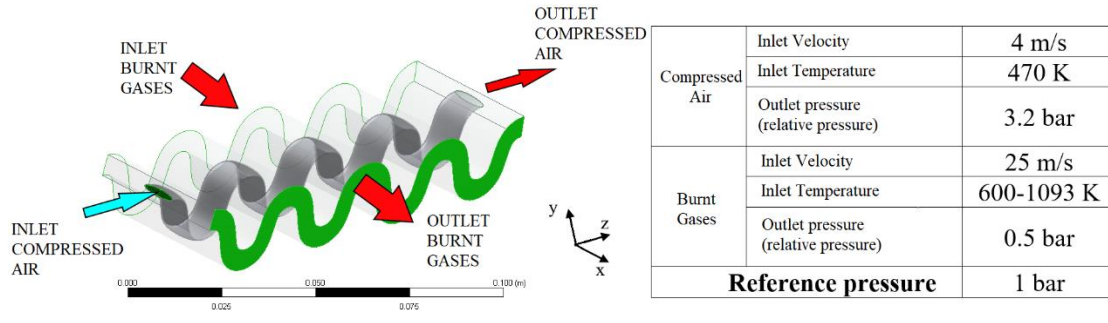


Fig. 10 Boundary conditions

Table 3. 3D CFD simulation results

z position [mm]	Cold fluid temperature				
	T ₄ =1093K	T ₄ =1000K	T ₄ =900K	T ₄ =800K	T ₄ =600K
0	470	470	470	470	470
15	510.81	505.86	500.4	493.64	480.09
30	559.11	547.32	534.44	521.76	492.02
45	605.72	588.91	569.36	549.16	503.3
60	649.16	626.76	600.85	573.69	513.74
75	691.08	662.27	631.13	596.71	523.47
90	729.23	695.04	657.01	617.29	531.61
105	763.77	725.96	682.38	636.93	539.75
120	793.47	750.9	703.14	653.16	546.12

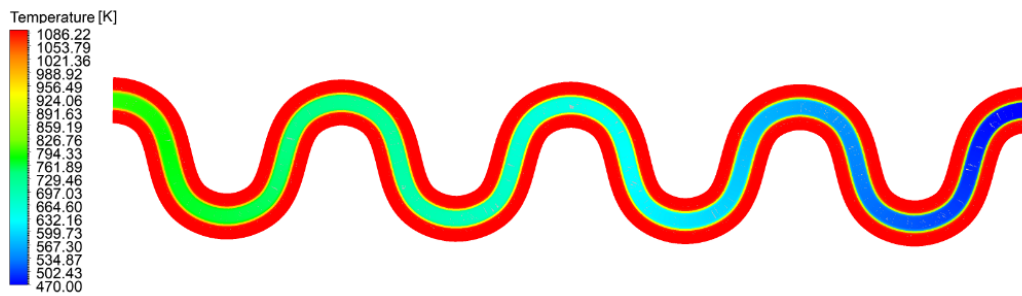


Fig.11 3D CFD heat transfer simulation

The distribution of temperatures inside the channel is as realistic as possible, the only disadvantage of the simulation of a single element is the inability to appreciate the total heat transferred by the hot fluid and the final temperature with which it exits the recuperator. As noted, the boundary condition (1093K inlet on the hot fluid) leads to temperatures similar to the outflow (10-20K less). The cases analysed are for several inlet temperatures to capture how the fluid heats up depending on its position in the recuperator.

The results presented in table 3 are shown in "Fig. 12" where the difference between the temperature of the fluid at the exit of the corrugated profiled tube can be noticed for several temperatures corresponding to different positions in the recuperator.

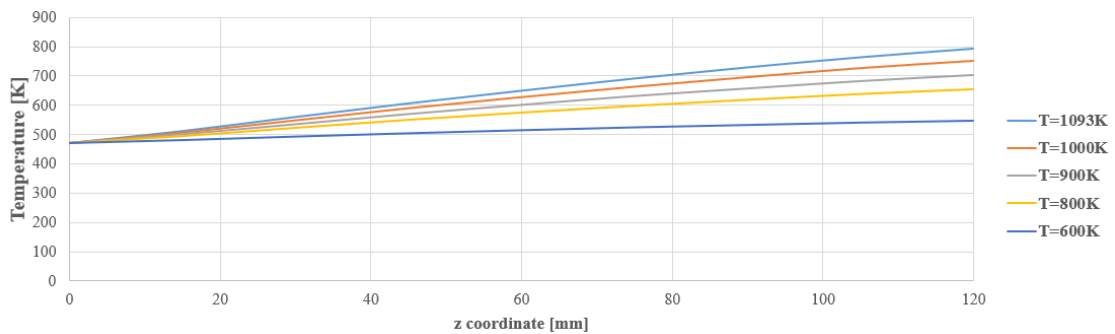


Fig.12 Heat transfer for different hot fluid inlet temperature

"Fig.13" relates the variation of the pressure of the cold fluid inside the working channel. It is noteworthy that for the discharge pressure initially set to 3.2 bar, the inlet pressure is 3.201 bar, which is quantified in a pressure loss of 0.03%.

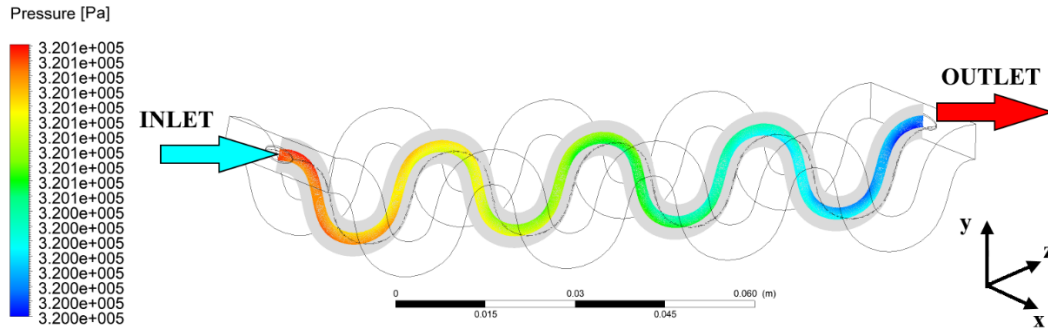


Fig. 13 Compressed air pressure distribution along working channel

Regarding pressure loss on the burnt gas side "Fig.14 a)", 2D simulations were done. The 2D simulations were performed using a gas inlet speed of 25 m/s and a temperature of 1093K and the relative outlet pressure was set to 0.5 bar ($p_{ref} = 101325 \text{ Pa}$). Each ellipse was considered as a wall of constant temperature (470K - corresponding to the inlet section of the air to be heated) and thickness 0. For a relative outlet pressure of $5 \cdot 10^4 \text{ Pa}$, it is observed that the inlet pressure in the recuperator must be $5.142 \cdot 10^4 \text{ Pa}$ which corresponds to a pressure loss on the flue gases of **2.76%**.

In future work, for a better demonstration of the recuperator's advantages regarding pressure loss on the burnt gas side, 3D simulation on the burnt gas side will be performed.

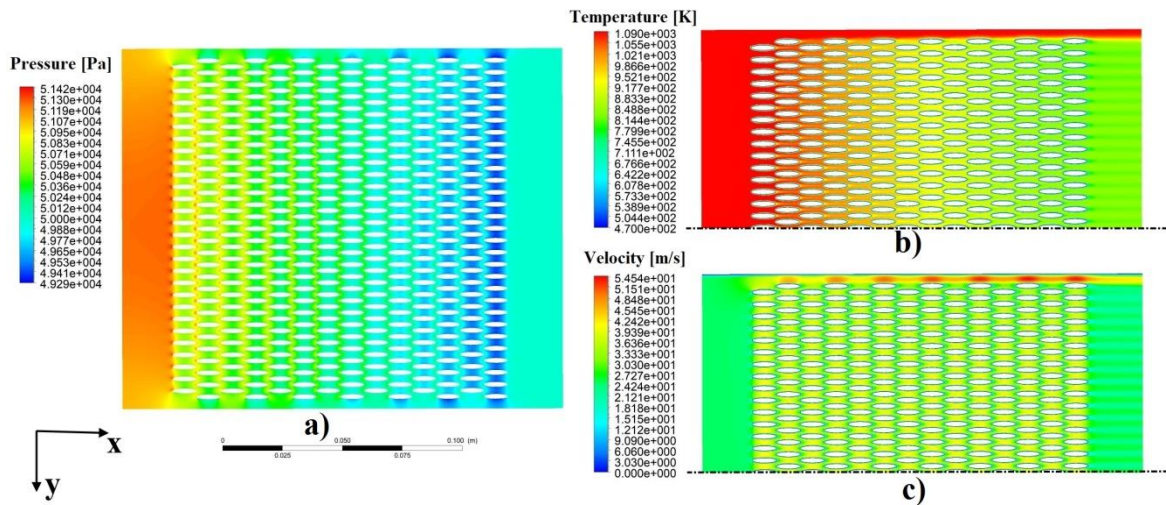


Fig. 14 2D Simulations on the burnt gas side a) Pressure loss, b) Temperature distribution, c) Fluid Velocity

5. CONCLUSIONS

In the first part, this paper provides a comprehensive review of benefits brought by using additive manufacturing technology for heat exchangers fabrication. In the second part, the paper provides the design stage including researches done to see what problems can occur while the 3D printing of the recuperator concept and how they could be solved. Analytical and numerical calculation shows the advantages brought by the recuperator concept. The surface-volume ratio obtained (almost 1000) represents an important aspect by which the recuperators made by this printing technology can have a guaranteed success.

Future research will focus on flow analysis in a complete sector in order to fully appreciate the capacity of the 3D printed recuperator.

REFERENCES

- [1]. Uwe Scheithauer, Richard Kordaß, Kevin Noack, Martin F. Eichenauer, Mathias Hartmann, Johannes Abel, Gregor Ganzer and Daniel Lordick, Potentials and Challenges of Additive Manufacturing Technologies for Heat Exchanger
- [2] Kuppam Thulukkanam, Heat Exchanger Design Handbook, Second Edition
- [3]. Langefeld R, Veenker H, Schäff C, Balzer C. Additive Manufacturing—Next generation (AMnx): Study. München. Available from: http://www.rolandberger.com/media/studies/2016-04-11-rbsc-pub-Additive_Manufacturing-next_generation.html 11 April 2016
- [4]. Essop, A. (2019, April 16th), “GE RESEARCH \$2.5 M PROJECT ATTAINS 3D PRINTED ULTRA PERFORMANCE HEAT EXCHANGER”. Retrieved from <https://3dprintingindustry.com/news/ge-research-2-5-m-project-attains-3d-printed-ultra-performance-heat-exchanger-153627/>
- [5]. https://www.pressreleasefinder.com/prdocs/2019/GE_Additive_Overview_May2019.pdf
- [6]. Boissonneault, T. (2018, October 25th), “Conflux Technology is reinventing heat exchangers with 3D printing”. Retrieved from <https://www.3dprintingmedia.network/conflux-technology-reinventing-heat-exchangers/>
- [7]. 3TRPD. Available from: <https://www.3trpd.co.uk/> [cited 16 October 2017]
- [8]. Abel J, Scheithauer U, Klemm H, Moritz T, Michaelis A. Fused filament fabrication (FFF) of technical ceramics. *Ceramic Applications*. 2018;6:2-4
- [9]. C.F. McDonald, Recuperator considerations for future higher efficiency microturbines, *Appl. Therm. Eng.* 23 (12) (2003) 1463–1487.
- [10]. Necula, H., Badea, A., Ionescu, C. Schimbătoare de căldură compacte. Editura AGIR, București, 2006

FINITE ELEMENT ANALYSIS ON TEMPERATURE DISTRIBUTION OF THERMAL BARRIER COATINGS

Tiberius-Florian FRIGIOESCU¹, Alexandru PARASCHIV¹, Mihaela Raluca CONDRUZ¹, Teodor-Adrian BADEA¹, Lucian Cosmin ZAMFIR¹, Ion IONICA²

ABSTRACT: The performance of turbojet engines is limited by the maximum temperature obtained in the combustion chamber. This thermal limitation is given by the high temperature capability of materials used for the engine components, especially for the combustion chamber and turbine blades. For thermal protection of these components and to increase their capability at high temperature, cooling systems and thermal barrier coatings (TBCs) are used. In this study, the finite element method (FEM) is used to investigate the thermal insulation behaviour of TBCs with different materials and architectures in order to identify the most promising coating which can exceed the performance of conventional TBC with yttria stabilized zirconia (YSZ) as top coat in terms of temperature drop on the substrate. Seven cases of TBC systems have been proposed for thermal analysis. Ansys Transient Thermal was used to simulate the turbine channels environment. The thermal analysis indicates that a triple-ceramic-coating system with YSZ, gadolinium zirconate ($Gd_2Zr_2O_7$, GZO) and lanthanum zirconate ($La_2Zr_2O_7$, LZO) had the highest temperature drop across the TBC system.

KEYWORDS: Finite element method (FEM), Thermal Barrier Coating (TBC), convection, conduction, heat

1. INTRODUCTION

In the combustion chamber of a gas turbine the energy generated is delivered to the working fluid [1] and the turbine blades are exposed to high mechanical loads and temperatures near or even higher than the melting point of the most advanced metallic materials [2]. Thus, two methods are used to thermally protect and maintain the blade cooled. One method is using the cooling channels with air flow from the second or third compressor stage. The second method is to use the thermal barrier coatings (TBCs) [3]. These two methods are usually used together for better efficiency of thermal protection and to increase the working temperature of the engine. An example of a turbine blade with TBC and cooling channels is shown in figure 1.

A typical TBC consists of a Ni-based superalloy substrate, a metallic bond coat (usually MCrAlY, where M is Ni, Co or Fe) and ceramic top coat based on yttria-stabilized zirconia - YSZ (ZrO_2 - Y_2O_3), deposited by atmospheric plasma spraying (APS) or electron beam physical vapor deposition (EB-PVD).

The ceramic materials are the most resistant materials at high temperatures. In a TBC system the ceramic materials act as a thermal insulation layer to protect the metallic bond coat and substrate against corrosion. The performance of a TBC system at high temperatures is strongly influenced by the thickness of ceramic layer and their thermophysical properties. The conventional YSZ thermal barrier coatings can reduce the surface temperature at least 100°C. By increasing the thickness of ceramic layer the heat transfer throughout the substrate is reduced, but also generates more residual stress in the coating due to the different thermal expansion coefficient of metallic and ceramic materials. Furthermore, during the exposure at thermal cycles, residual stress and microcracks are induced in TBCs layers which reduce the adhesion at the interface of the metallic-ceramic coat.

Another critical property of TBCs is the thermal conductivity. In order to reduce the surface temperature of the substrate (turbine blade) the ceramic top coat must have a low thermal conductivity, as much as possible. The gadolinium zirconate ($Gd_2Zr_2O_7$, GZO) and lanthanum zirconate ($La_2Zr_2O_7$, LZO) are considered the most promising materials for TBCs due to their lower thermal conductivity [1.5–1.6 W/mK] [4] than conventional YSZ ceramic 2.3 W/m·K [5].

¹ Romanian Research and Development Institute for Gas Turbines COMOTI

² Plasma Jet, Romania



Fig. 1 Thermal barrier coating on high pressure turbine blade [6]

In order to design an efficient TBC system, a numerical model has been developed to determine the temperature drop from the hot fluid to the metal surface of different TBC systems under specific thermal loading by using the heat conduction and heat convection as heat transport mechanisms.

The present study is focused to evaluate the temperature distribution and heat insulation performance of TBCs systems with single or multilayer ceramic layer with conventional YSZ, nanostructured YSZ, LZO, GZO or combinations thereof using Inconel 625 as substrate and NiCrAlY alloy as bond coat.

2. PROCEDURE DESCRIPTION

In this study, seven models of TBCs were evaluated in terms of heat insulation performance by using Ansys Transient Thermal. To highlight the temperature drop across the TBC system the raw data from Ansys were processed by using GNU Octave which is mainly used for numerical computations.

For comparison, one model, with just a metallic bond coat (E2T1) was used as a reference model. The models proposed for thermal analysis had the dimensions of 1.5 x 1.5 x 4 mm with the configurations presented in figure 2.

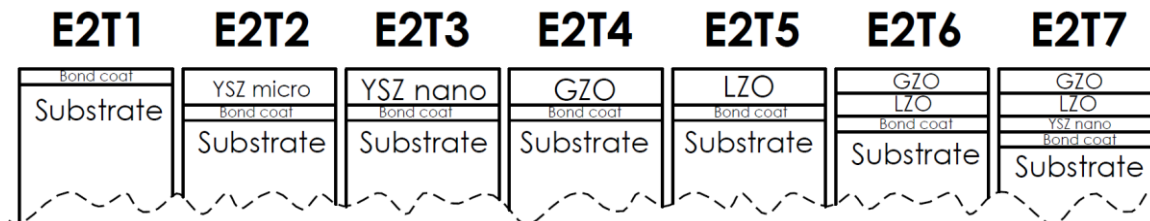


Fig. 2. The TBC systems for analysis

The purpose of this study was to evaluate by using the finite element analysis the thermal barrier performance of the thermal barrier coatings provided for high temperature components, such as burners, rotor and stator blades of gas turbines used in power plants, aircraft engines or rocket engines.

From a geometrical point of view, the strategy for all models was to have the same thickness (4 mm). Therefore, for each model the thickness of substrate was adjusted according to the number and layers thicknesses. In table 1, the dimensions of each component of the investigated models are presented.

Table 1. The dimensions of the components of TBC systems.

Thickness [mm]	E2T1	E2T2	E2T3	E2T4	E2T5	E2T6	E2T7
Substrate	3.85	3.5	3.5	3.5	3.5	3.39	3.24
Bond coat NiCrAlY	0.15	0.15	0.15	0.15	0.15	0.15	0.15
Top coat YSZ (conventional)	-	0.35	-	-	-	-	-
Top coat YSZ (nanostructured)	-	-	0.35	-	-	-	0.15
Top coat LZO	-	-	-	-	0.35	0.23	0.23
Top coat GZO	-	-	-	0.35	-	0.23	0.23

The strategy of reducing the thickness of substrate as a function of thickness of TBCs was chosen with respect to the working temperatures of blade and the centrifugal forces which increase with increasing layer thickness. The thermo-physical properties of the investigated TBC systems used for thermal analysis were identified based on a literature review [4,5,7] and presented in table 2.

Table 2. The thermo-physical properties of the layers of TBC systems [4,5,7].

Properties	Density [g/cm ³]	Thermal conductivity [W/m ² K]	Specific heat [J/gK]
Substrate IN625	8.44	23.8	0.627
NiCrAlY	7.32	10.2	0.781
YSZ (conventional)	6	2.3	0.65
YSZ (nanostructured)	4.77	2	0.505
LZO	6.05	1.5	0.42
GZO	7	1.6	0.23

In order to simulate the conditions in the turbine channels the models were heated on the coated surface by an air jet with a temperature of 1482 °C and a convection transfer coefficient of 3423 W/m²K and cooled by a lower flow air jet on the opposite side with a temperature of 556 °C and a convection transfer coefficient of 2800 W /m²K, according with F100-PW-229 engine's performance data [8-9]. Therefore, the thermal boundary conditions are described as follows and the connections between the four other sides of the depicted parallelepipeds were imposed by contact type to allow heat transfer. Therefore, the thermal boundary conditions and the connections between the four other sides of the depicted parallelepipeds were imposed by a direct contact condition that allows the heat transfer between them and are described as follows and the 4 side surfaces have the condition of an adiabatic wall:

- Initial temperature: 22°C;
- Convection on the upper surface: 3423 W/m²K, with temperature of 1482°C
- Convection on the lower surface: 2800 W/m²K, with temperature of 556°C

The heat transfer equation [10] used to correlate the heating and cooling fluid with the sample is:

$$\dot{Q} = hA(T_2 - T_1) \quad (1)$$

Where,

\dot{Q} - heat flux [W/m²]

H - heat transfer coefficient [W/m²K]

A - Surface area where the heat transfer takes place [m²]

T2 - temperature of the surrounding fluid [K]

T1- temperature of the solid surface [K]

The temperature distribution through the TBC system was determined by using the Fourier equation [10]:

$$q = -k\nabla T \quad (2)$$

Where,

q- local heat flux density [W/m²]

k- material's conductivity [W/m °K]

∇T -temperature gradient [°K /m]

The TBC coatings are anisotropic materials with different microstructure and defects such as porosities, microcraks, unmelted or partially melted particles, inclusions etc. depending on the deposition conditions and the technology used (atmospheric plasma spraying or electron beam physical vapor deposition) which have a strong impact especially on the residual stress and CTE of materials. Since the microstructure of the coatings and the deposition technology were not analyzed, the purpose of these thermal analysis was only to investigate the the temperature dropped across multilayer and multimaterial thermal barrier coatings in order to identify the most promising candidates to replace the TBC conventional with yttria-stabilized zirconia (YSZ) as ceramic layer.

For each TBC system the 3D model was introduced in the thermal system where a mesh has been made by using the MultiZone method, generating different nodes and quadrilateral elements as follows:

- E2T0: 433 475 nodes and 102 884 elements
- E2T1: 441 910 nodes and 104 040 elements
- E2T2-E2T5: 445 515 nodes and 104 040 elements
- E2T6: 453 950 nodes and 105 196 elements
- E2T7: 462 385 nodes and 106 352 elements

In figure 3 is presented the modelling process of E2T7 system (table 2) with the rendered view of the TBC system (a), structured and dense mesh (b), boundary conditions imposed (c) and the distribution of temperature gradients through the TBC system.

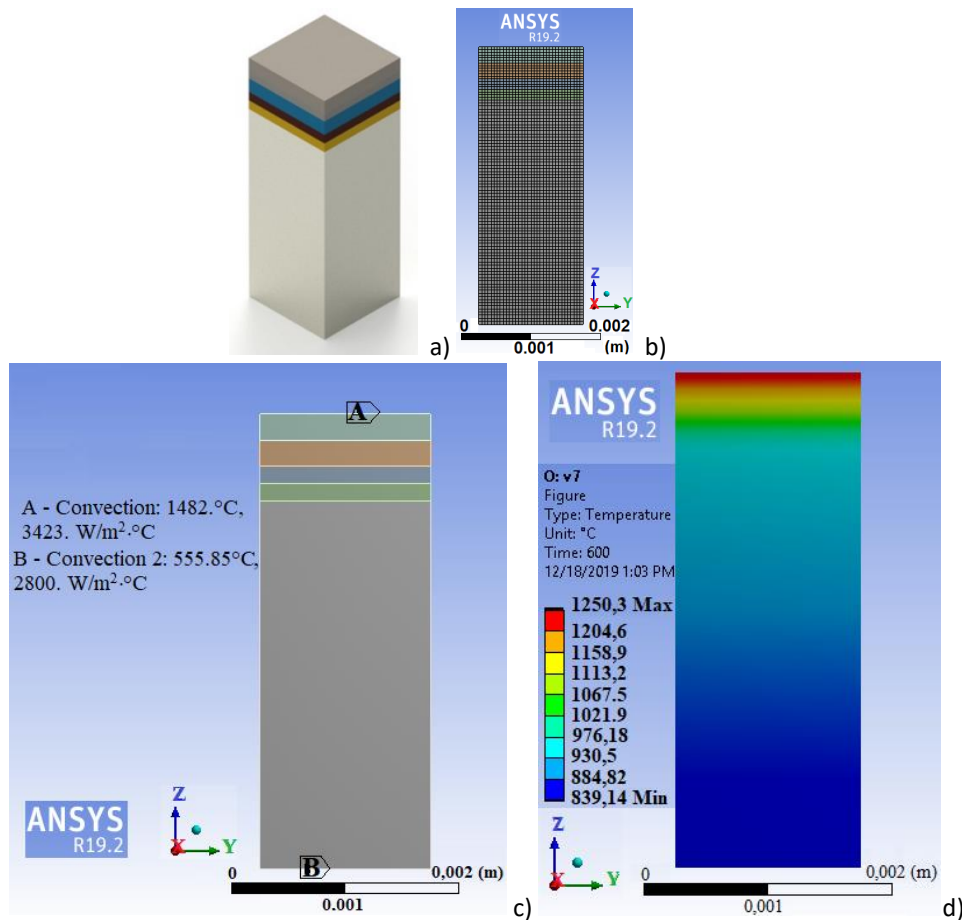


Fig. 3 The modelling process of E2T7 system: 3D model (a), meshing model (b), model with the imposed boundary conditions (c) and temperature distribution on E2T7 (d)

3. RESULTS AND DISCUSSIONS

From the *heat transfer point of view*, the part, has 2 inputs/outputs with the external environment. One area comes in contact with the hot air (where the heat flow is introduced into the system) while the second area is cooled (the heat flow coming out of the system). Based on the simulations, a distribution of the average temperature throughout the E2T7 model was generated as a function of time after 50 s (figure 4.a) and after 600 s (figure 4.b).

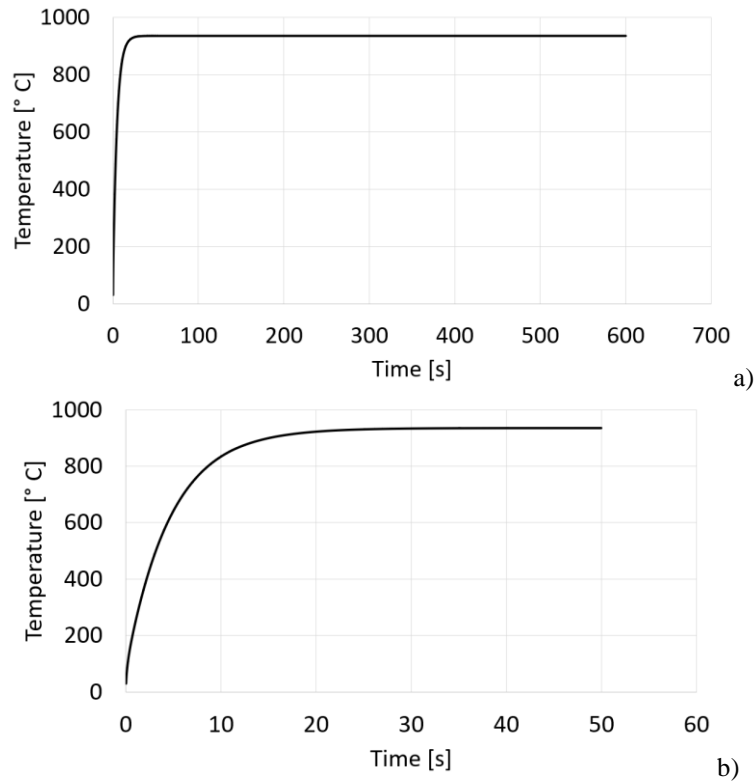
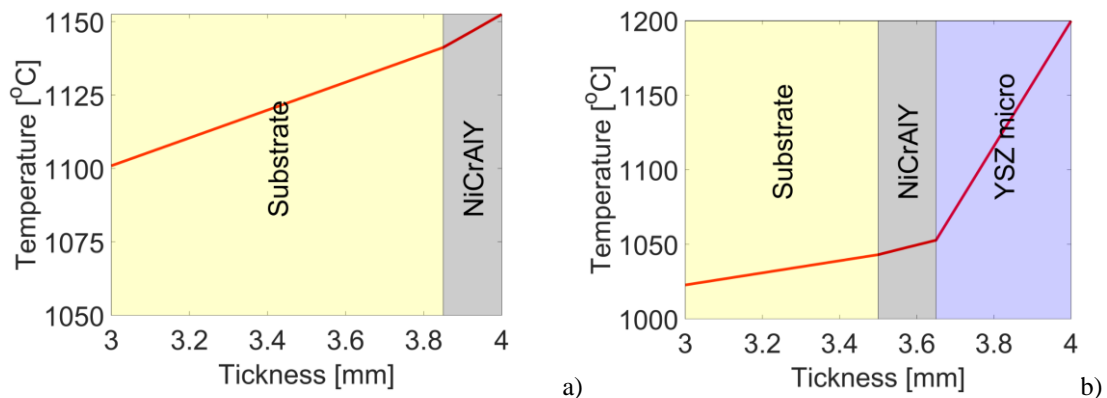


Fig. 4 Average temperature distribution in the E2T7 TBC system after 50 s (a) and after 600 s (b)

Based on the graphs presented in figure 4, it was observed that the stabilization of the temperature in the structure is achieved after a time of approximately 25 s. To highlight the temperature distribution in the cross-section at different layer thicknesses of E2T7 system a graph generated by using Octave software was presented in figure 5-g.

The graphs presented in figure 5,6 shows the temperature drops along the layers of the investigated systems. As can be seen in figure 5-g the temperature drop, across the layers of E2T7 system is major in the ceramic layers while in the metal layer and substrate the temperature drop, is very low. These slopes are governed by the thermal conductivity of each layer (Table 2). In the case of the E2T1 system with metallic layer (reference model) the temperature on the surface of substrate was 1141°C, which means a temperature drop of 341°C ($T_{\text{gas}}=1482^\circ\text{C}$) and is mainly due to the cooling by flow air jet on the opposite site of model. Regarding the systems with ceramic layer (s), the systems with LZO and GZO layers had the highest temperature drop, followed by systems with nanostructured YSZ and conventional YSZ as top coat. Compared to the reference system (E2T1), the E2T7 system had the highest temperature drop on the substrate (194°C), while the E2T2 system had the lowest temperature drop on the substrate (98°C). Regarding the TBC systems with conventional YSZ (E2T2) and nanostructured YSZ (E3T3) an increase of 31°C of temperature drop was determined in the case of TBC system with nanostructured YSZ. Any improvement in the high temperature capability of turbine components by using TBCs with nanostructured YSZ or novel multilayer of lanthanum and gadolinium zirconate may significantly increase the turbine entry temperature.



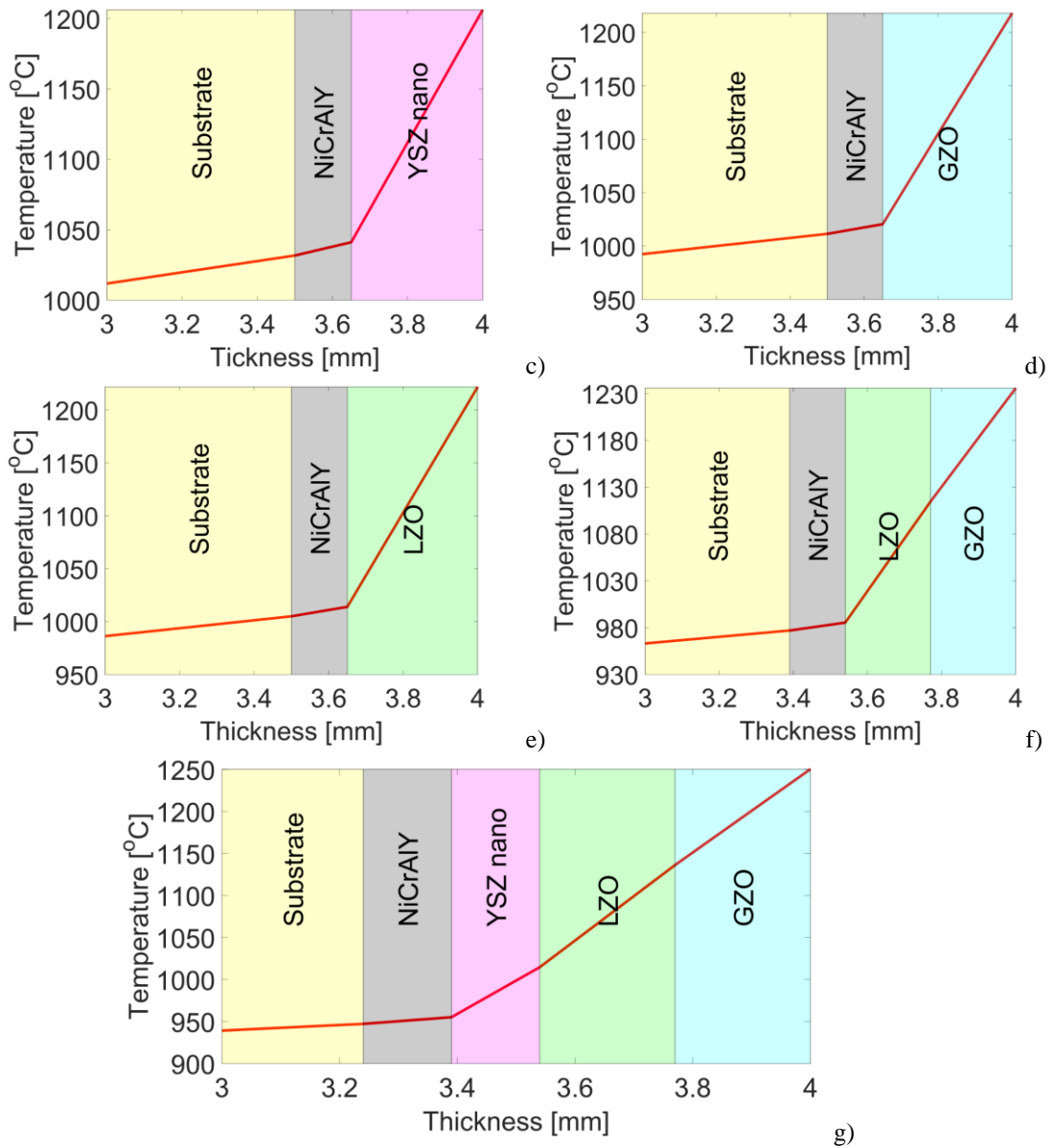


Fig. 5 Diagrams of temperature drop across the E2T1, E2T2, E2T3, E2T4, E2T5, E2T6 and E2T7 systems



Fig. 6. The maximum reached temperature of the substrate for each investigated system

By using a higher working temperature the performance of the engine will increase by increasing the nozzle speed and the flow rate driven by the engine due to the higher energy introduced into the working fluid. Based on the thermal analysis results, the temperature drop increases with increasing the thickness of ceramic layers, but, from a thermodynamic point of view, using a too thick coating on the turbine blade may cause negative effects. In order to identify an appropriate configuration and optimal layers thicknesses of a TBC system, a thermostructural simulation may be applied. However, due to the anisotropy of coatings, specific structure and defects generated during deposition by thermal spray or electron-beam physical vapor deposition the optimal TBC coatings are determined by thermal cycling.

4. CONCLUSIONS

Seven TBCs models with different materials and architectures were evaluated in terms of heat insulation performance by the finite elements model (FEM) using Ansys Transient Thermal. For the TBC systems were used different ceramic layer (layers) such as conventional and nanostructured YSZ, LZO, GZO and combinations thereof using Inconel 625 as substrate and NiCrAlY alloy as bond coat.

The E2T7 system had the highest temperature drop on the substrate (194°C), while the E2T2 system (conventional TBC) had the lowest temperature (98°C) compared to the reference system (E2T1).

Also, the TBC system with YSZ nanostructured as ceramic top coat (E2T3) had a temperature drop higher by 31°C than the TBC system with YSZ conventional as ceramic top coat (E2T2). Based on the thermal analysis the E2T7 TBC system is the most efficient coating in terms of thermal barrier.

The first simulations consisted of the analysis on parallelepipeds with the dimensions of 30 x 30 x 4 mm. Following the discretization, a single node resulted in the GZO layer (E2T7), and the thermal distribution was not conclusive according to the thermal conductivities. For these dimensions, due to the limitation of the processing power, a better mesh could not be achieved. Thus, for the present thermal analysis, the size was reduced to 1.5 x 1.5 x 4 mm, in order to increase the number of nodes along the thickness, which leads to an increase in accuracy. By doing this, 7 nodes were obtained in the GZO layer (E2T7) along its thickness. Therefore, the results led to the present ones where the slopes corresponding to each thermal conductivity of the material can be observed.

For future studies, new material concepts for the next generation of plasma-sprayed thermal barrier coatings will be evaluated in terms of heat insulation performance by the finite elements model (FEM) using Ansys Transient Thermal.

ACKNOWLEDGEMENT

This work was carried out within POC-A1-A1.2.3-G-2015, ID/SMIS code: P_40_422/105884, "TRANSCUMAT" Project, Grant no. 114/09.09.2016 (Subsidiary Contract no. D1.3/114/18.12.2017), Project supported by the Romanian Minister of Research and Innovation.

REFERENCES

- [1]. P. J. H.; 2009; The Hotter the Engine, the Better
- [2]. P. N. P., G. M. and J. E. H.; 2002; Thermal Barrier Coatings for Gas-Turbine Engine Applications
- [3]. D. R. Clarke and S. R. Phillpot; 2005; Thermal barrier coating materials
- [4]. X.Q. Cao; 2004; Ceramic materials for thermal barrier coatings, Journal of the European Ceramic Society 24
- [5]. H. Zhao; 2009; Low Conductivity Thermal Barrier Coatings, 2009, School of Engineering and Applied Science
- [6]. W.A. Kaysser; 2002; Processing of Advanced EB-PVD Thermal Barrier Coating Systems
- [7]. A. Keyvani; 2012; A comparison on thermomechanical properties of plasma-sprayed conventional and nanostructured YSZ TBC coatings in thermal cycling, Journal of Alloys and Compounds 541
- [8]. A. S. Leel, R. Singh, S. D. Probert; 2009; Modelling of the Performance of a F100-PW229 Equivalent Engine under Sea-level Static Conditions, 45th AIAA/ASME/SAE/ASEE Joint Propulsion Conference & Exhibit
- [9]. P. Laskaridis, P. Pilidis; 2015; Turbine cooling and heat transfer modelling for gas turbine performance simulation
- [10]. I. D. V. Lavine; 2007; Introduction to Heat Transfer

TEST BENCH WITH 500Nm HYDRAULIC BRAKE FOR SIMULATING NONLINEAR LOADS ON ELECTRIC ACTUATORS

Razvan CIOBANU¹, Sorin TOMESCU^{1,2}, Valentin PETRESCU^{1,2}, Adrian
UNGUREANU¹, Alexandra TARANU^{1,2}, Eduard VASILE^{1,2}, Ramona Elena
STANCIUC¹

ABSTRACT: This article presents the design and development of a test bench with a hydraulic torque brake used for simulating different nonlinear loads that can occur on electric vane actuators. The main component of the test bench is developed around a single brake disc with two radially opposed and mirrored brake callipers from the automotive industry. We chose this solution for generating resistive torque due to constraints regarding other mechanical solutions and the fact that the electrical actuators intended for this application have very low rotational speeds, thus making the use of an electrical generator as a braking element futile. The components used for the brake system were chosen such that the maximum nominal load value testing capability is 500Nm. There are many constraints when designing a non-standard brake system at this torque rating which were overcome by ingenious engineering solutions that we devised whilst developing the test bench.

KEYWORDS: Test Bench, Nonlinear, Adjustable Torque Brake, Electrical Actuators, System Dynamics, Design, Development

NOMENCLATURE

CAD – Computer Aided Design	ω – Brake disc rotational speed
D_b – Brake caliper cylinder surface area	P_f – Brake caliper hydraulic pressure
χ – Specific ratio described by equation 8	P_p – Brake master cylinder pressure
k_{rSAE} – Reduction factor according to SAE standard	R_m – Brake pad mean radius
μ_k – Kinetic friction coefficient	SAE – Society of Automotive Engineers
μ_s – Static friction coefficient	T_k – Kinetic braking torque
N – Number of brake pads per caliper	T_s – Static braking torque
N_e – Number of brake pads per caliper assembly	

1. INTRODUCTION

This article presents the design and development of a test bench with a hydraulic torque brake used for simulating different nonlinear loads that can occur on electric actuators for vanes used in combustion gas transportation and compression facilities. The design of the test bench is developed in order to be able to test any type of electrical actuator in the actuating torque range of 50 Nm up to 500 Nm, with continuous rotation, whilst being able to predefine any nonlinear load curve possible. This was achieved by implementing the use of SAE approved automotive part for the brake system such as brake disc and brake calipers and master brake pump. The difficulties that arose were defined by the facts that electrical actuators have low rotational speeds, under 1 rpm, and the brake system has to have precise non-interfering actions with torque feedback signals. Thus, the use of an electric motor as a brake generator was ruled out due to low rpm and the use of a multiplying gear box was also ruled out due to the fact that in order to reach synchronous rpm of the electric generator, the gear box, had to have a high ratio. Thus, leading to very high gear inertia resulting in the reduction

¹ Romanian Research and Development Institute for Gas Turbines COMOTI, Bucharest Romania

² University Politehnica of Bucharest, Romania

of useful range for those actuators that have limited angular ranges. The second major difficulty that arose is that the brake system had to be extremely precise and responsive.

In order to achieve such a level of braking torque we had to use two brake calipers, thus resulting in high hydraulic pressure for actuating them (16 MPa). The use of an electric pump was ruled out to the fact that it can induce micro fluctuations in the brake lines, of very small volume, resulting in a unstable brake system with low robustness and tuning capabilities. As a result, we concluded from our research that a master brake cylinder from the automotive industry will provide the best results. Another milestone was to design a case adapted hydraulic system with as less hydraulic fluid as possible in order to minimize its compressibility.

The brake master cylinder is normally, in the automotive industry, used in conjunction with a brake booster that in essence reduces the actuating force on the brake pump. To overcome this situation, we used a linear electromechanical actuator rated at a much higher actuating force than the maximum calculated brake force needed. The use of two brake calipers is also done in order to reduce the load on the electromechanical actuator, thus maintaining it in its linear response in terms of travel speed. The travel speed of the actuator is of utmost importance to be as fast as possible in order to achieve high controllability and accuracy of the brake system.

The usage of a ready-made adjustable brake solution was also ruled out as they can only achieve levels of controllability in excess of 1500 rpm and at around 2500 Nm brake torque and are mainly used in offshore oil rigs and heavy lift maritime industries.

The current market in this kind of solutions regarding test rigs for electrical actuators is very limited by means of the inability of achieving nonlinear braking characteristics. Thus, making INCDT COMOTI a future leader in terms of know-how in aspects regarding programable nonlinear test benches for electrical actuators. Other producers of such test benches only implement threshold level testing for validation and proof of own developed products, i.e. electrical actuators. The necessity of designing and developing a test bench for such a demanding level of control in terms of testing capabilities is due to the fact that this stand is part of project with a consortium of other 3rd party companies, other than the lead institute INCDT COMOTI.

2. TEST BENCH DESIGN AND DEVELOPMENT

The test stand (Fig. 1) is composed of several key elements such as tested electric actuator (ref. 1), torque transducer (ref. 2), brake system (ref. 3), actuating system (ref. 4), electronics and automation bay (ref. 5).

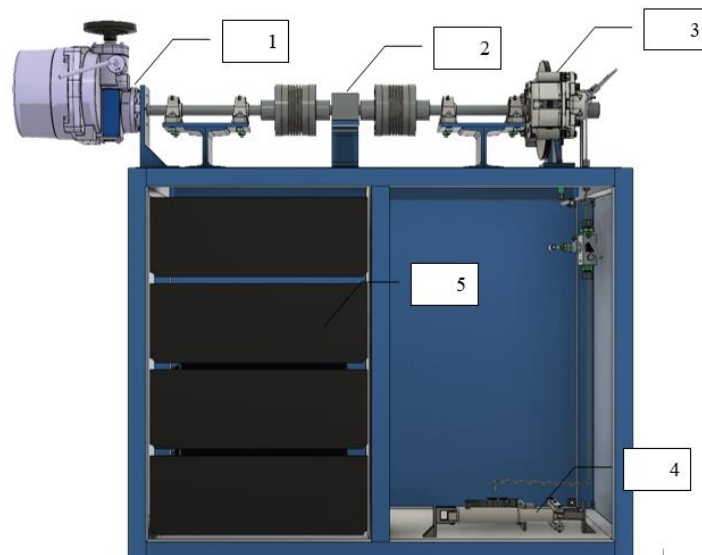


Fig. 1 Electrical actuator test bench main components and systems.

The test bench utilizes a hybrid electric and hydraulic brake system (Fig. 2) developed around a single brake master cylinder capable of providing hydraulic pressures up to 20 MPa with a linear travel of only 28 mm. The components illustrated in figure no. 2 are listed in table no. 1.

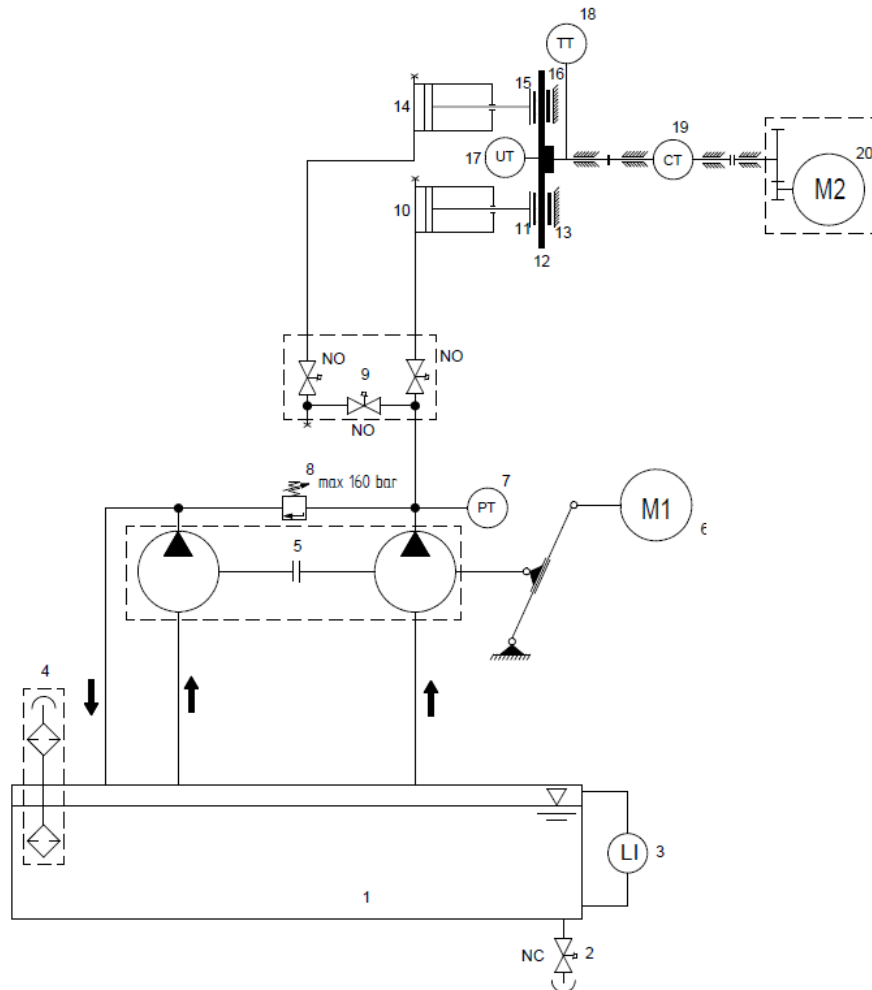


Fig. 2 Part and identification diagram for the electrohydraulic brake system.

Table 1. Brake system components.

Reference	Part and/or component
1	SAE DOT 4 hydraulic brake fluid
2	Reservoir drain tap
3	Level gauge
4	Filling and vent filter
5	Brake master cylinder
6 / M1	Electromechanical linear actuator
7	Pressure transducer
8	Safety blow-off valve
9	3-way equalisation valve manifold
10	Right brake calliper
11	Brake pad
12	Brake disc
13	Brake pad
14	Left brake calliper
15	Brake pad
16	Brake pad
17	Absolute rotary encoder for measuring rotational speed and angle
18	Pt ₁₀₀ 3 wire Resistive Temperature Device
19	Torque transducer
20 / M2	Electrical actuator

In order to design the brake system and to test if the solution can provide the intended design requirement, we had to iteratively calculate static and kinetic brake torques. For this we needed to get accurate readings and CAD measurements on all components from the brake calliper (Fig. 3 & 4), brake master cylinder (Fig. 5 & 6), brake pads (Fig. 6) and brake disc assembly (Fig. 7).

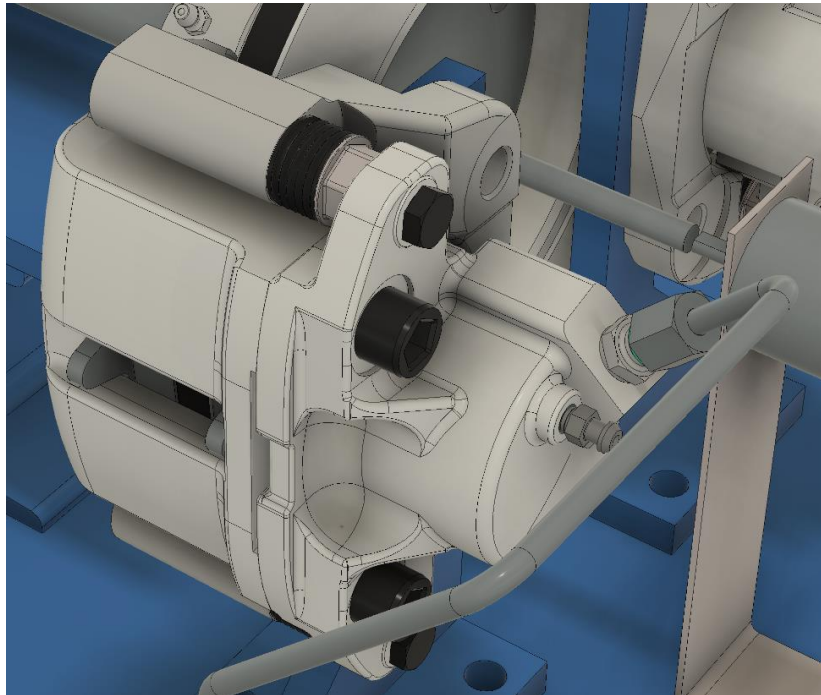


Fig. 3 CAD model of left brake caliper.

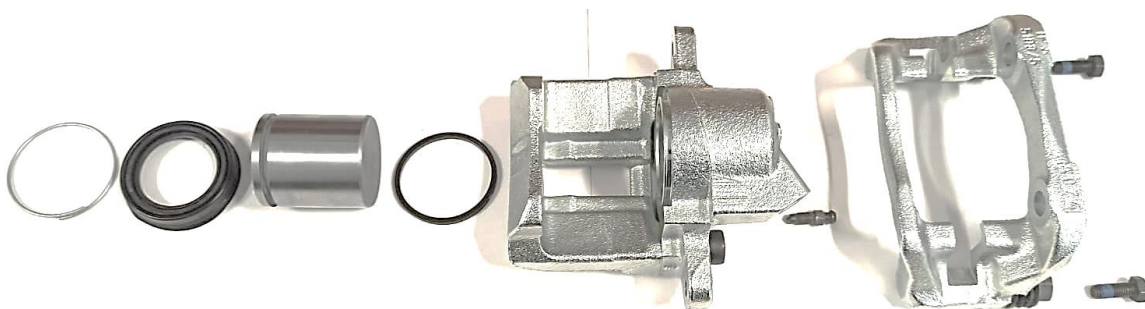


Fig. 4 Disassembled brake calliper.

The brake master cylinder is a dual output line (ref 1 / fig. 6) hydraulic pump with redundant system comprised of dual pressure generating pistons (ref 2 / fig. 6), reflow & hydraulic reservoir feed channels (ref 3 / fig. 6), dual resetting springs (ref 4 / fig. 6) and dual one-way hydraulic valves (ref 5 / fig. 6) all in an cast aluminium body (ref 6 / fig. 6).

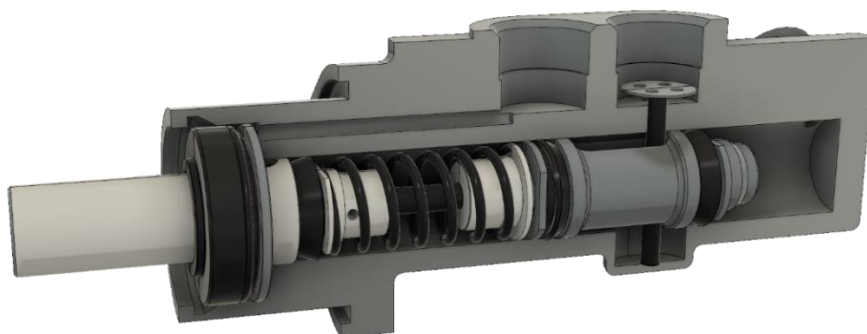


Fig. 5 CAD cutaway brake master cylinder.

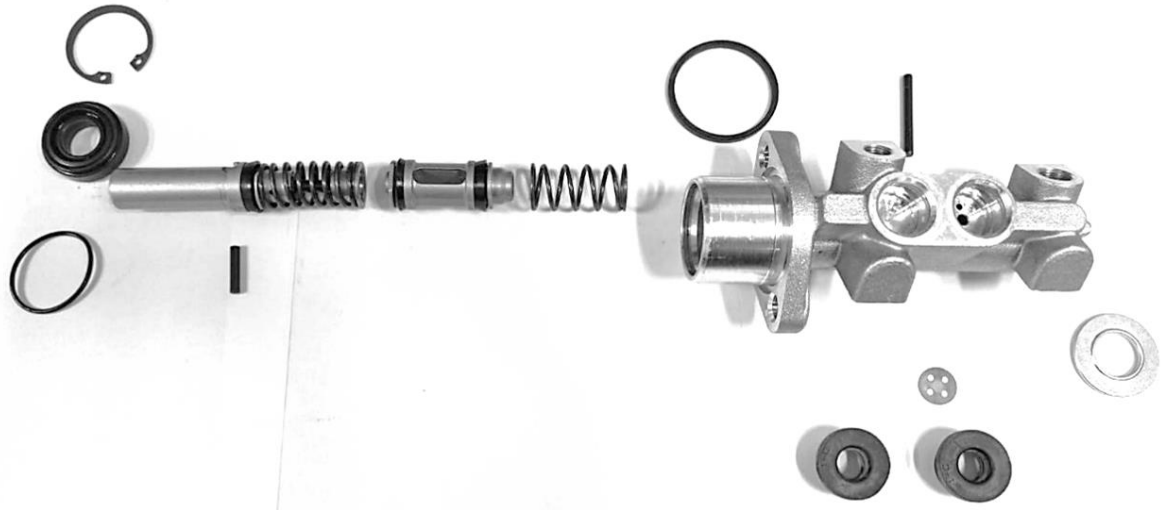


Fig. 6 Disassembled brake master cylinder pump.

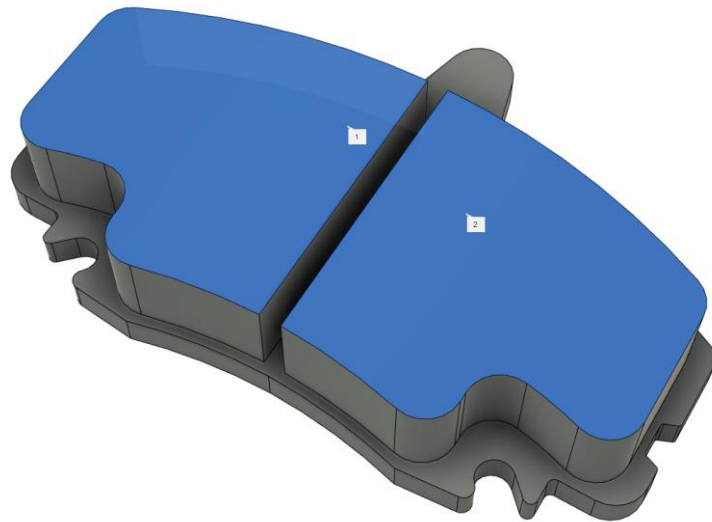


Fig. 6 Brake pads [1].



Fig. 7 Brake disc.

After we modelled all parts as CAD components, we proceeded to identify certain key sizes such brake pad surfaces, brake master cylinder bore diameter, brake calliper cylinder bore diameter, brake disc inner and outer diameters, brake pad inner, outer and mean sitting radius on the brake disc. All values and variables listed above are found centralised in table no. 2.

Table 2. Brake system parametric data.

No.	Parameter	Variable	Value	Unit
1	Brake pad surface	Bps	0.00162	m ²
2	Brake pad outer radius	Robp	0.1	m
3	Brake pad inner radius	Ribp	0.085	m
4	Brake pad mean radius	Rm	0.0925	m
5	Brake disc outer diameter	Bdod	0.236	m
6	Brake disc inner diameter	Bdid	0.140	m
7	Brake disc angular speed	Bdas	0.56	rpm
8	No. of brake callipers	Nc	2	N/A
9	No. of brake pads per calliper assembly	N	2	N/A
10	Brake calliper cylinder bore diameter	Db	0.048	m
11	Brake master cylinder bore diameter	Dp	0.0206	m

For calculating static and kinematic torque values we used equations (1) and (3) according to SAE standards and specifications that are used to design automotive brake systems for conditions (2) and (4).

$$T_s = \frac{\mu_s * P_f * \pi * D_b^2 * R_m * N}{4} \quad (1)$$

For:

$$\omega = 0 \text{ rad/s} \quad (2)$$

$$T_k = \frac{\mu_k * P_f * \pi * D_b^2 * R_m * N}{4} \quad (3)$$

For:

$$\omega \neq 0 \text{ rad/s} \quad (4)$$

Where:

$$P_f = \frac{P_p}{N_e} * 10^5 \quad (5)$$

In order to calibrate the test stand brake system and feedback-based control loop it is necessary to determine the static and kinetic friction coefficients μ_s and μ_k . Where the kinetic friction coefficient can be determined by equation (6).

$$\mu_k = \frac{\mu_s}{k_{rSAE}} \quad (6)$$

Where k_{rSAE} (of value 1.73116) is a reduction factor used to determine the kinematic friction coefficient for disc brake rotational speeds for up to 350 rpm. Parameters P_p and T_s are measured directly from the stand i.e. hydraulic line pressure and shaft torque. Thus, resulting in experimental determination of μ_s thru equation no. (7).

$$\mu_s = \frac{T_s}{\chi} \quad (7)$$

Where:

$$\chi = \frac{P_f * \pi * D_b^2 * R_m * N}{4} \quad (8)$$

The actuating force to the brake master cylinder is provided by means of linear mechanical movement from the electromechanical actuator thru a lever system (Fig. 8).

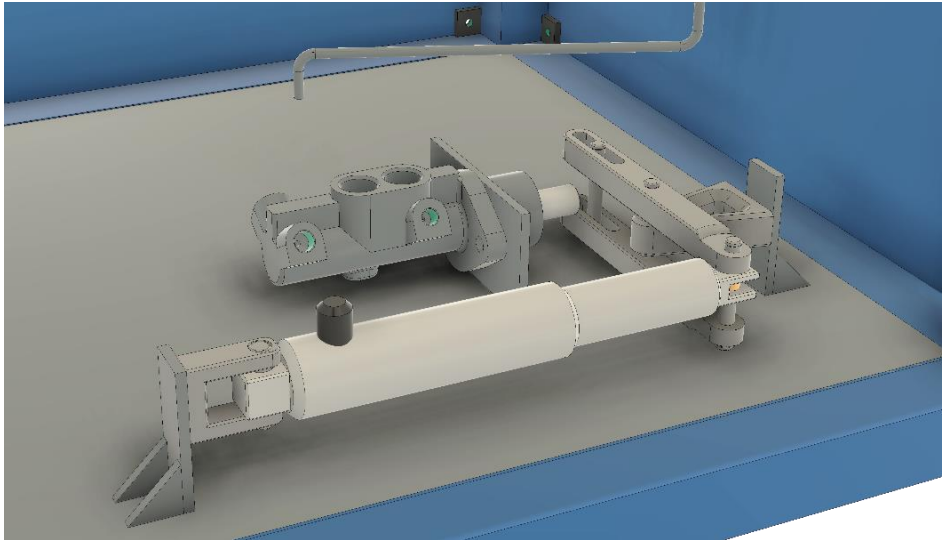


Fig. 8 Electromechanical brake master cylinder actuating system.

A single hydraulic line is used from the brake master cylinder and it is fed into a 3-way equalisation valve (Fig. 9a) which is also used as a hydraulic distributor to supply the brake callipers (Fig. 9b) with hydraulic fluid.

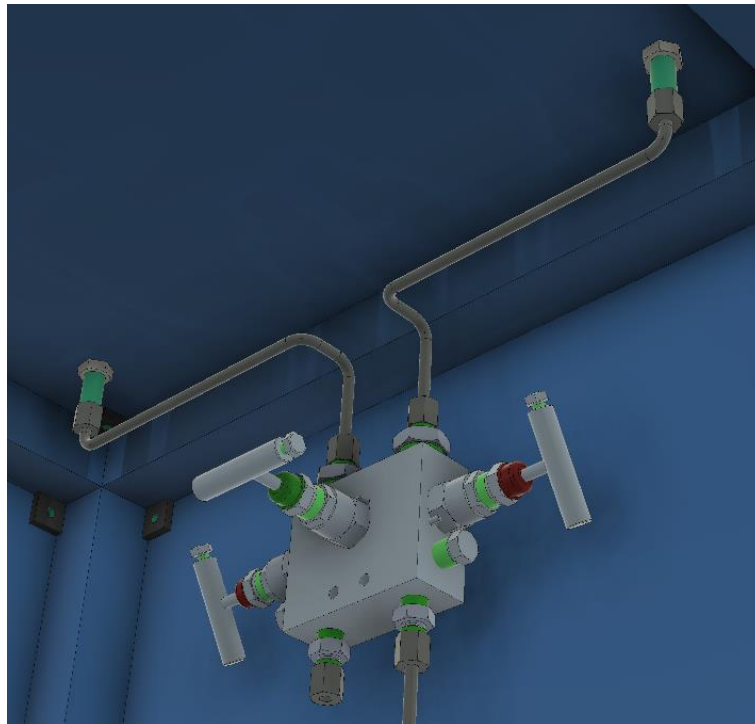


Fig. 9a 3-way equalisation valve.

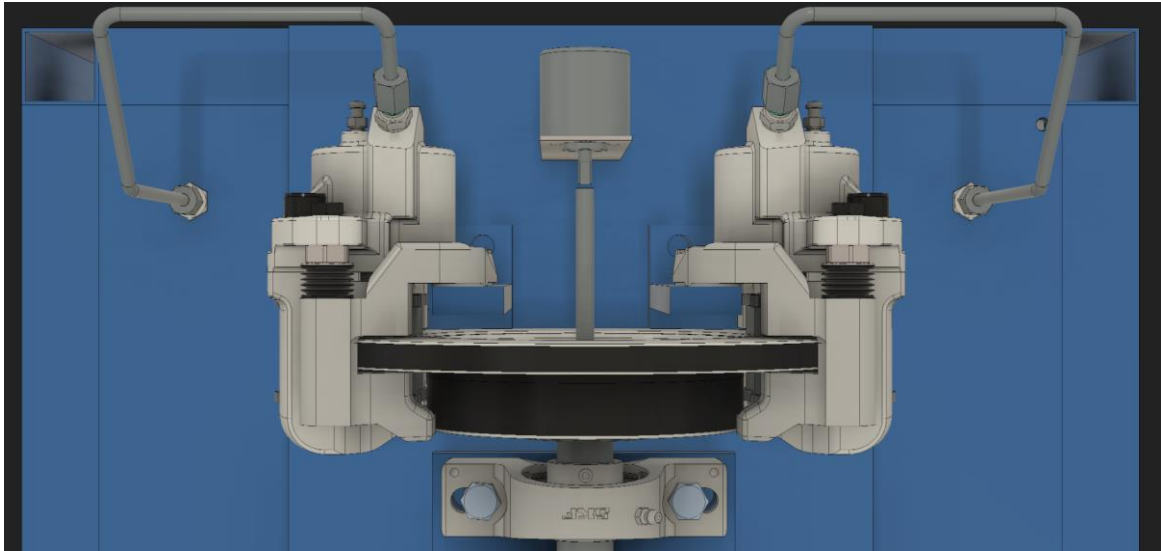


Fig. 9b Brake callipers with feed lines.

The top structure (Fig. 10) of the test bench accommodates two connection shafts for linking the electric actuator to the brake system while linking an intermediately positioned torque transducer. The torque transducer is connected to the shafts via two mechanical wedge couplings that allow free axial movement on the transducer's shaft. This is done in order to eliminate any type of parasitic loads on the transducer's shaft. The transducer shaft is an aluminium radial resistive load cell that can falsely read axial loads. The two linkage shafts are held in place by two pairs of bearings of type Sy 25 TF from SKF producer.

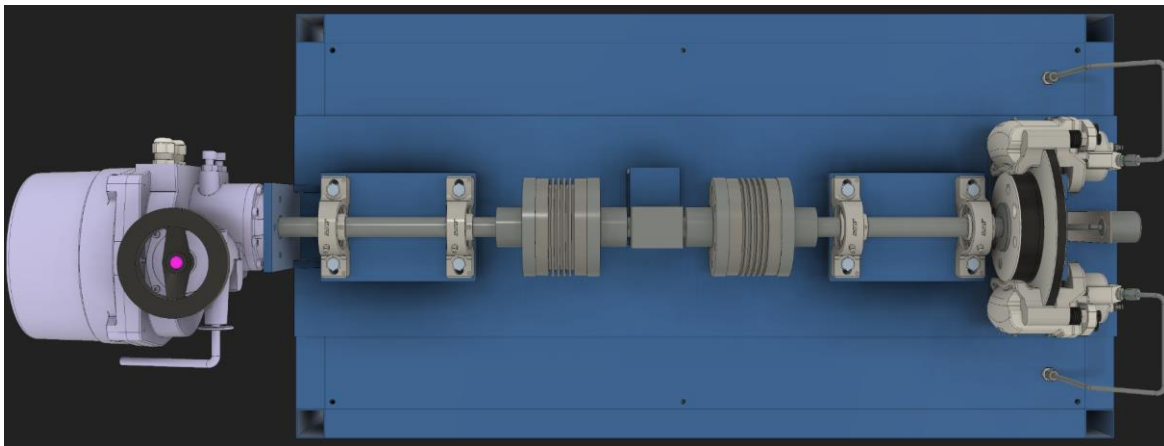


Fig. 10 Top structure layout of the electric actuator test bench.

In order to ensure proper control accuracy and robustness of the test bench brake system it is necessary to precisely calibrate the system as a whole. In order to do just that we designed a dynamic system (Fig. 11) that replicates the test stand mathematical model in terms of input vs. output for determining the static friction coefficient. This was done in MathWorks Simulink software.

As calibration logic goes, taking into account equation no. (7) we only need to generate a certain pressure level predetermined by the test stand software that is measured via a pressure transducer and use a load lever with calibrated weights to generate the desired torque, i.e. 500 Nm for the case illustrated in figure 11.

If the shaft does not rotate while nominally loaded, in order to achieve the desired torque, means that the static friction coefficient is bigger than anticipated. Shaft rotation will be measured via an absolute rotary encoder and if there is no rotation what so ever the software will start to reduce brake pressure until angular movement is detected.

When angular movement is detected, the software will record the hydraulic line pressure threshold at which it started to rotate and only then compute the corrected and calibrated value for the static friction coefficient.

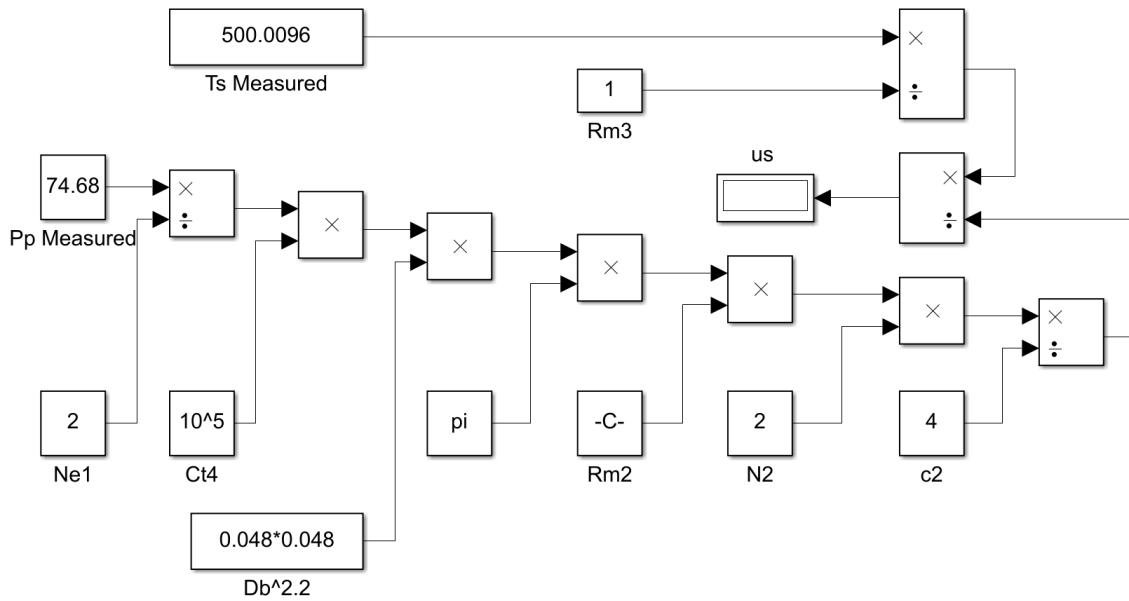


Fig. 11 Calibration block diagram for determining static friction coefficient.

Knowing the exact value of the static friction coefficient is needed in order to determine the real output command for the PID (Proportional Integrator Derivative) controller corrected with the torque transducer signal (Fig. 12). Accuracy of the input command signal for the brake system controller directly leads to final system performance. Thus, all mechanical, hydraulic and electrical systems have been modelled and taken into account in order to achieve a very robust controller for the test stand.

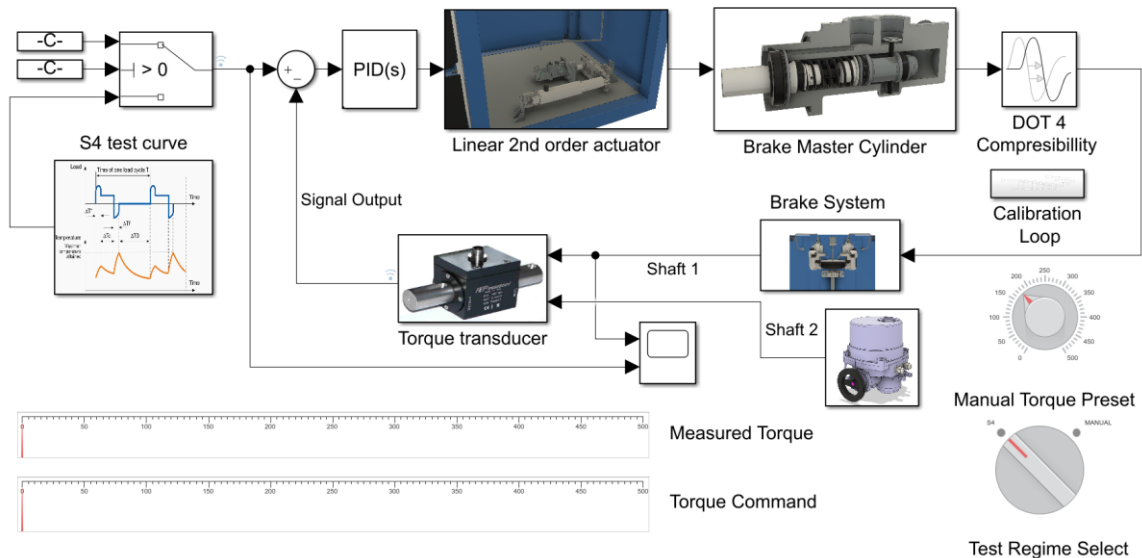


Fig. 12 Test bench system block diagram with control loop and command interface.

Considering the earlier mentioned equations and the test bench block diagram we were able to plot the dependencies of hydraulic pressure with static and kinetic braking torque (Fig. 13).

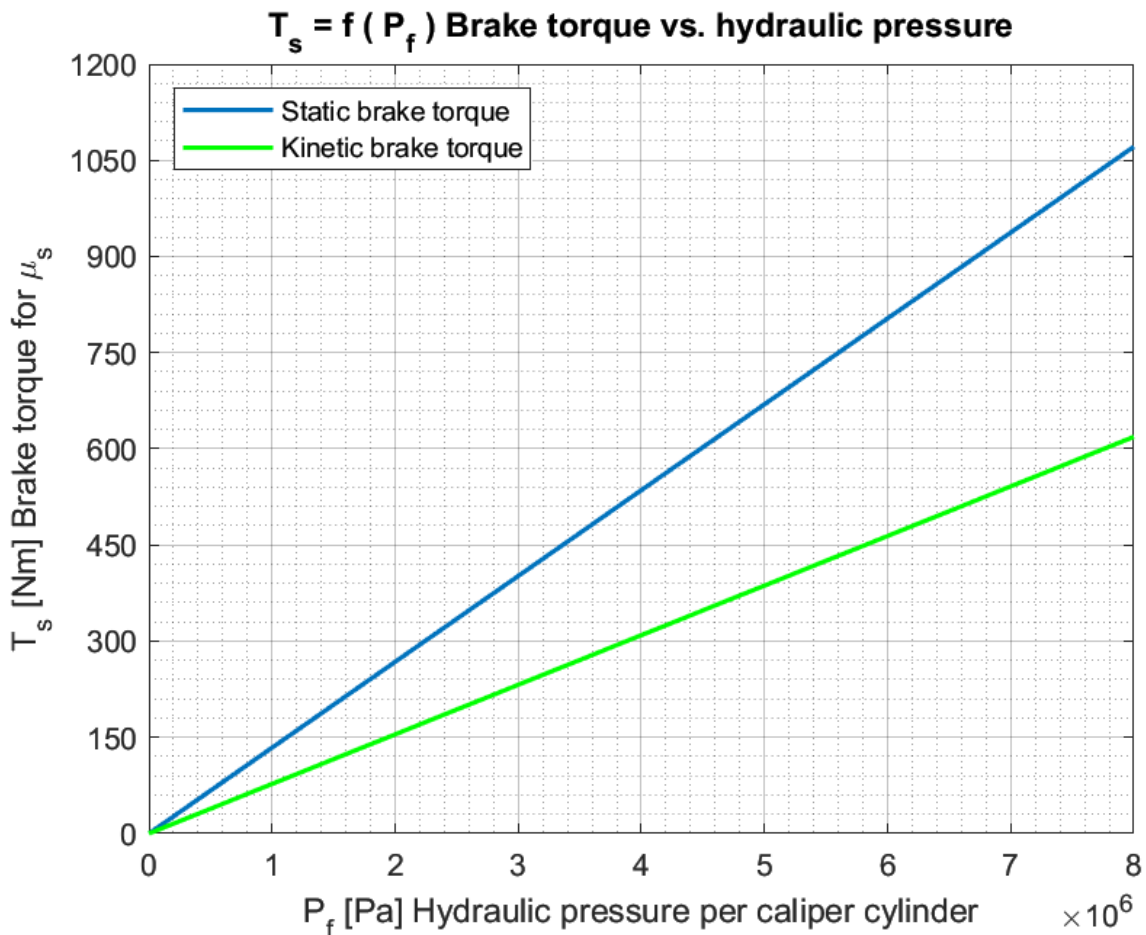


Fig. 13 Brake torque vs. hydraulic brake system pressure per caliper.

As seen in the graph from figure 13, the static braking torque (blue line) can reach values of up to 1050 Nm and the kinetic braking torque (green line) can achieve just over 600 Nm, well beyond the 500 Nm required design threshold.

For the test bench we used a Compact Logix 5380 (commercial name) Allen-Bradley (producer name) (Fig. 14) programmable logic controller. This controller is equipped with two analogue input modules, single digital input module and single digital output module.



Fig. 14 Test bench system block diagram with control loop and command interface [2].

The test bench implements the use of 19-inch 4U (Fig. 15) (standard size of 4-unit heights) stacked four one on top another. We chose this solution as to the traditional automation cabinet due to the ability to minimise as much as possible all electronics and automation equipment cabinet volume. The use of such a system ensures that any excess technological space is reduced to a bare minimum in order to assure proper heat dissipation and ventilation. Also, it makes the test stand more versatile in terms of maintenance as all racks are essentially line replaceable units thus resulting also in a reduction in time and financial losses.



Fig. 15 19” 4U rack’s [3].

For designing the electrical diagram, it was necessary to develop a cable management solution in order to maximise the individual internal space of each rack. We started by populating the racks with all electronic hardware until we achieved a maximum surface usage after we proceeded with the electrical connections between each and every rack and other auxiliary equipment. The cable management diagram for the whole test bench is illustrated in figure 16.

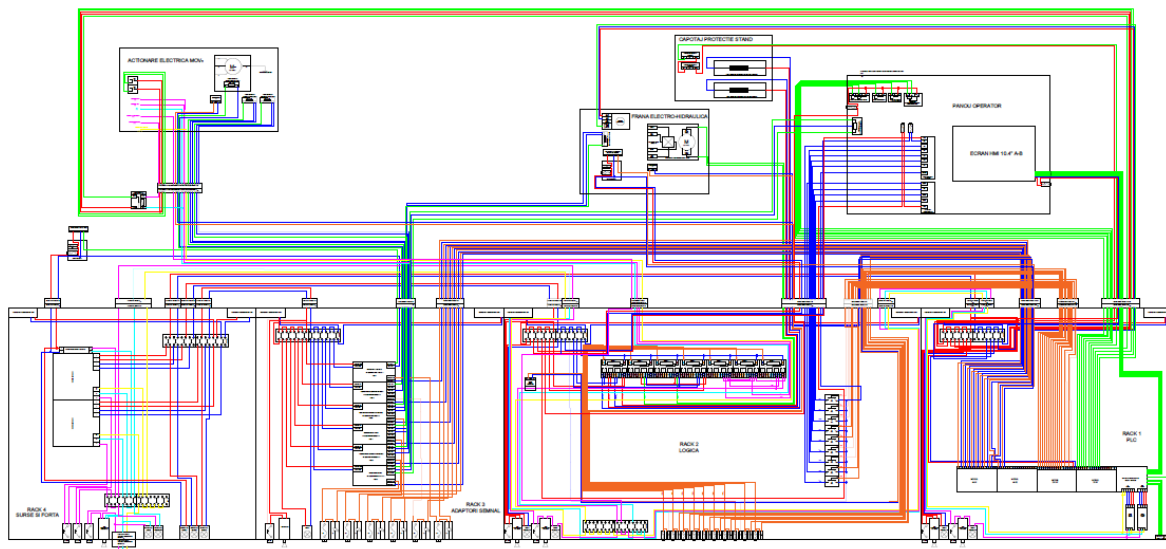


Fig. 16 Test bench cable management diagram.

As a secondary benefit of implementing such a compact and concentrated automation cabinet is a reduction in build time, material loss and very high electrical connection reliability achieved via the use of military grade type MIL-C 5015 rapid connector that in term translates into minimal junction usage.

The racks are numbered from one to four from top to bottom and are equipped as per table no. 3.

Table 3. Rack designation.

Rack number	Designation
1	Allen-Bradley Compact Logix Controller and input/output modules
2	Relay and Transistor-Transistor-Logic command blocks
3	Signal conversion blocks
4	Alternating and Direct current power supply and distribution

All the racks are equipped with two direct current fans that turn on over a 45°C threshold in order to ensure proper heat management thru induced ventilation. In order to make an easy troubleshoot system we designated on all the rack panels fuse sockets for ease of replaceability that also use caution beacons to indicate correct or faulty operation of a certain system. The control panel is designed so that it concentrates all command and control devices such as switches, potentiometers and the human machine interface with a 10.4-inch touch sensitive display. The human machine interface from Allen-Bradley (Fig. 17) is externally supplied via 24 V direct current and uses a standard Ethernet RJ-45 plug for full duplex data transfer between itself and the Compact Logix Controller.



Fig. 17 Allen-Bradley human machine interface touch screen for the test bench control panel [4].

Taking into account that the test bench is designed for research, development and knowledge transfer applications we also designed a chassis (Fig. 18) built out of 40 x 40 mm T-slot aluminium extrusion profiles. This allows for a more versatile platform in terms of adaptability between different types of electric actuator other than those designated for the current application.

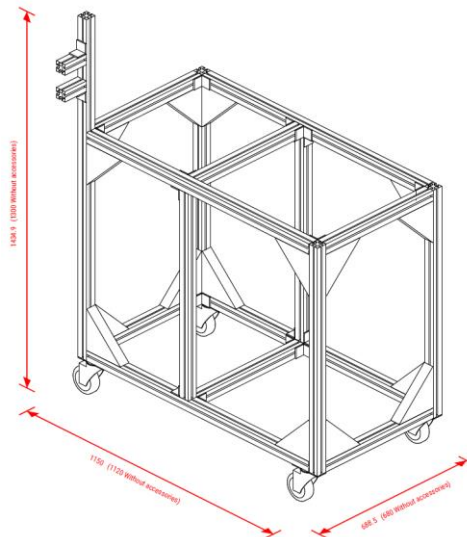


Fig. 18 T-slot 4040 series aluminium extrusion profile test bench chassis [5].

3. CONCLUSIONS

The article addresses the constraints and requirements in the design and development of an electric actuator test bench capable of simulating nonlinear vane loads. The challenges that we faced were related to developing a variable brake system at rotational speeds under one rpm. This challenge was overcome by implementing the use of a hybrid electromechanical and hydraulic brake system designed with SAE approved automotive parts. Through mathematical modelling of the test bench components, through calculations and through CAD modelling we've successfully validated the concept of the test bench for electric vane actuators described in the article. The next stage in this project consists in building the described test bench as a demonstrator for experimental validation. For further research and development in terms of optimisation we are studying the usage of an artificial intelligence controller for tuning and calibration of the brake system in order to account for static friction coefficient variations due to mechanical wear.

ACKNOWLEDGEMENT

The present research data is part of the "POC" Research and Knowledge Transfer Programs, supported by the Romanian Ministry of Research and Innovation, project number 132/23.09.2016 acronym EPAVREDI

“Echipament performant pentru actionarea vanelor din rețeaua de distribuție și transport a gazelor combustibile”.

REFERENCES

- [1] <https://moto-dynamic.com/img/2009/brake-pads-front-renault-dacia-oryginal-410607115.jpg>
- [2] <https://www.plchardware.com/Products/RA-5069-L310ER.aspx>
- [3] <https://www.pulsar.pl/>
- [4] https://www.rockwellautomation.com/ro_RO/overview.page
- [5] Courtesy of <https://item.engineering/> online design application
- [6] <https://books.google.ro/books?id=yeEkBAAAQBAJ&pg=PA55&lpg=PA55&dq=sae+j1703+compressibility&source=bl&ots=kLXH4rK90m&sig=ACfU3U0ok5YwO3E6GH8HqYZZkzb40P-nnA&hl=en&sa=X&ved=2ahUKEwjypexmvHnAhXNbMAKHc9PAbeEQ6AEwFHoECA0QAQ#v=onepage&q=sae%20j1703%20compressibility&f=false>
- [7] R. Herman; 2019; Solving Differential Equations Using Simulink
- [8] A. M. Khatkhate, E. Keller; 2006; Modelling and System Identification of an Experimental Apparatus for Anomaly Detection in Mechanical Systems; Department of Mechanical Engineering, The Pennsylvania State University, University Park, PA 16802-1412, United States;
- [9] M. Witters, J. Sweres; 2009; Optimal experiment design for the black box identification of a semi-active damper; Department of Mechanical Engineering, Katholieke Universiteit Leuven, Celestijnenlaan 300B, B-3001 Heverlee, Belgium;
- [10] M. Deflorian, S. Zaglauer; 2011; Design of Experiments for nonlinear dynamic system identification; The International Federation of Automatic Control Milano (Italy);
- [11] A. Khalil, G. El-Bayoumi; 2013; Flight Dynamics, Stability and Control of a Flexible Airplane; Conference: 15th International Conference on Aerospace Sciences & Aviation Technology (ASAT – 15) At: Cairo, Egypt;

STRESS REDUCTION METHODS FOR CENTRIFUGAL IMPELLERS

Andrei-George TOTU¹, Daniel-Eugeniu CRUNȚEANU², Andreea-Cătălina DOBRE¹,
Mihail SIMA¹

ABSTRACT: Centrifugal compressors are a crucial component of jet engines and the current trends of increasing propulsion systems performance include increasing the pressure ratio so that the mechanical demands to which the rotor is subjected also increase. The aim of the paper is to highlight how geometry optimization can lead to weight reduction while obtaining a very good mechanical behavior (under mechanical stress and vibration).

KEYWORDS: centrifugal compressor, jet engine, weight optimization, mechanical stress, vibration

NOMENCLATURE

f- frequency	R_1 - boss main radius
f_e -excitation frequency	UAV-unmanned aerial vehicle
f_{st} - static frequency	α - thermal expansion coefficient
g- blade root maximum thickness	β - coefficient for vibration modes
n_s -rotational speed in rot/s	ρ - density
sc-safety coefficient	σ_{02} - yield stress
A- area	$\sigma_{1,2,3}$ - principal stress in direction 1,2 or 3
D- cylindrical rigidity	σ_{ech} - equivalent stress
E- modulus of elasticity	σ_{max} - maximum stress
FEA- finite element analysis	σ_v -von Misses stress
FEM- finite element method	σ_A - allowable stress
J- moment of inertia	σ_R - radial stress
K- number of excitation factors	σ_T - tangential stress
K_f - coefficient for static frequency	ω - angular velocity
N_{tr} - total number of sections	[] _i - index corresponding to section i

1. INTRODUCTION

In the field of modern aviation, the main applications of centrifugal compressors are microjet engines, APUs or turboshaft engines (which require relatively low flow rates compared to the high dilution turbofan engines). Numerous studies are being conducted on impeller optimization methods, as this is the element with the greatest influence in the centrifugal compressor assembly [1]. Regarding compressors with low flow rates, around 1 kg/s [2], the tendency is to increase the pressure ratio (reaching values of 10) which implies the use of very high rotational speeds leading to transonic peripheral speeds at the impeller tip [3]. Since in the field of aviation safety is a priority, each component of the engine must be well designed and tested to ensure its functionality at the desired parameters. For compressors with usual pressure ratio and flow rates, most development directions are aimed at increasing efficiency, reducing component weight, increasing operating range, lowering production costs, while maintaining acceptable safety limits [4], [5]. This paper aims to lead to some results (at least qualitative) that can be taken into account when designing a centrifugal rotor. The optimization from the design stage is very important since testing the centrifugal compressors on the test bench is very expensive,

¹ Romanian Research and Development Institute for Gas Turbines COMOTI, Bucharest, Romania

² University Politehnica of Bucharest, Romania

taking into account the fact that a modal analysis (as opposed to the aerodynamic resistance and performance tests) requires a lot more advanced equipment (specific to optical interferometry [6]). Thus, the most convenient analysis that can be performed is a numerical one, using a FEM analysis, qualitatively confirmed by a theoretical analysis combined with semi-empirical formulae.

2. MAIN FORCES ACTING ON THE IMPELLER

The angular velocities combined with the torsion of the blades lead to the occurrence of both tensile and bending forces. Using radial blades is the simplest way to reduce the overall load on the impeller because the forces acting on them are generated by the pressure difference (pressure side – suction side) and by the main component of the centrifugal force acting in the radial direction (low bending force). In terms of aerodynamic performance, the radial blades are slightly disadvantageous, but for a simplified structural calculation they are desirable. In the current paper, a geometry with radial blades (except for the anterior part) will be used in order to better correlate the results obtained from the finite element analysis with the theoretical calculation. If the impeller is considered to be a rotating disk, the forces acting on an area element are represented in fig. 1 (b).

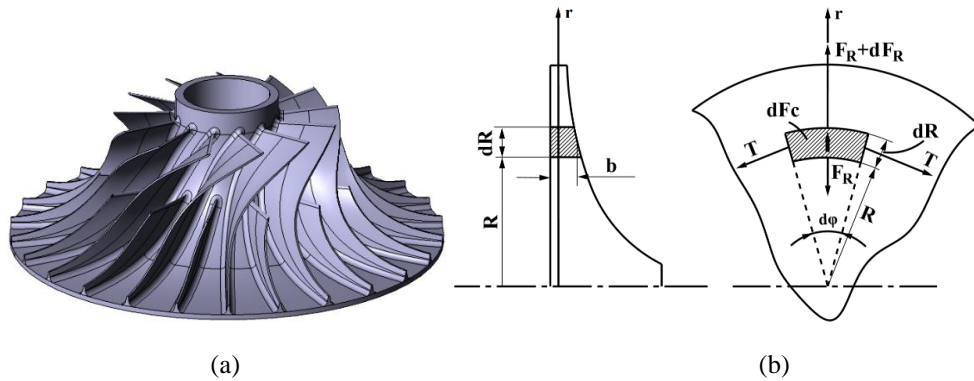


Fig.1. (a) Impeller used in the following analysis, (b) Forces acting on an area element [1], [7]

Radial and tangential stresses can be written in differential form [7]

$$\begin{aligned} d\sigma_R &= \sigma_T \frac{dR}{R} - \sigma_R \left(\frac{dR}{R} + \frac{db}{b} \right) - \rho\omega^2 R^2 \frac{dR}{R} \\ d\sigma_T &= \sigma_T \left(-\frac{dR}{R} + \frac{dE}{E} \right) + \sigma_R \left(-\mu \frac{db}{b} - \mu \frac{dE}{E} + \frac{dR}{R} \right) - \mu\rho\omega^2 R^2 \frac{dR}{R} - Ed(\alpha t) \end{aligned} \quad (1)$$

and the equivalent stress can be found using

$$\sigma_{ech} = \sqrt{\sigma_R^2 + \sigma_T^2} \quad (2)$$

The analytical calculation of vibration implies the consideration of the radial blade with a cantilever plate and the semi-empirical formula can be used [7]

$$f_{st} = \frac{17.5}{l^2} \left(\frac{E \cdot J}{\rho \cdot A} \right)^{\frac{1}{2}} \quad (3)$$

and for the rotating disk, the frequencies corresponding to a certain number of diameters and circles of nodes are determined by summing on the sections considered in the structural calculation using [7]

$$\frac{1}{f^2} = K_f \sum_{i=1}^{N_{tr}} \frac{1}{f_i^2}$$

$$f_i = \frac{\beta}{2\pi \cdot R_{mi}^2} \sqrt{\frac{D_i}{\rho \cdot b_i}}$$
(4)

Unlike analytical calculation, finite element analysis no longer uses semi-empirical or empirical coefficients but is based on solving a system of differential equations (static equations - Navier-Cauchy equations, geometric equations - Saint Venant equations, physical equations - generalized Hooke's Law) which eliminates the dependency of the conditions used to determine those coefficients.

The von Mises equation (for principal stresses) used in FEA is presented in relation (5). [8],[9]

$$\sigma_v = \sqrt{\frac{1}{2}[(\sigma_1 - \sigma_2)^2 + (\sigma_2 - \sigma_3)^2 + (\sigma_3 - \sigma_1)^2]}$$
(5)

3. VIBRATION AND STRESS EVALUATION

For the vibration and stress evaluation, the centrifugal rotor described in [1] is used, which is part of a compressor that is supposed to equip a microjet engine for a UAV. The impeller has a diameter of 250mm and is designed to operate at 40000rpm. The FEM analysis was performed in several steps. For the proper use of computer resources, only a rotor sector was used which consists of a blade and a splitter. Because it is an aviation specific centrifugal compressor, the aerograde materials used for the finite element analysis are the following: 7075 aluminum alloy and Ti6Al4V titanium alloy whose properties are presented in Table 1.

Table 1. Properties of the materials used

Parameter	7075 Aluminum Alloy		Ti6Al4V Titanium Alloy	
	Value	Unit	Value	Unit
ρ	2810	kg/m ³	4430	kg/m ³
E	71.7	GPa	114	GPa
σ_{02} (at 20°C)	572	MPa	950	MPa
σ_{02} (at 150°C)	380	MPa	700	MPa
μ	0.33	-	0.31	-

As is well known in the field of numerical simulations, the use of a periodic element (disk sector) does not introduce additional errors to the final result [11]. For the analyzed sector (with the symmetry condition applied at the cut faces), the two cylindrical channels of diameter 5mm and depth 25mm were not taken into account. For the vibrational analysis, the complete geometry (once the final solution - material and geometry was established), to which the notches were added.

The boundary conditions are represented by the cylindrical symmetry on the radially cut faces, the axial fixation on the nut fitting surface and the cylindrical fixation on the shaft surface and the speed at which the rotor was calculated is 40000 rpm.

In the work [1] it was tried (in the first place) the simulation of a sector consisting of a blade and a splitter (without hub) but the fixation at the base introduced additional stress that does not appear normally. FEA were performed using the specialized programs PATRAN (for pre and post processing) and NASTRAN (for the calculation itself).

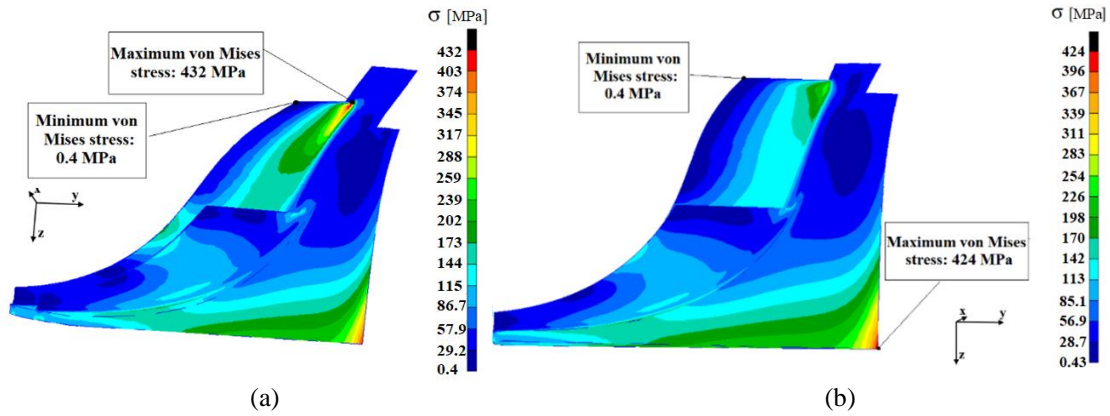


Fig.2. (a) Baseline aluminum rotor, $g=1\text{mm}$, (b) Baseline aluminum rotor, $g=2\text{mm}$ [1]

4. OPTIMIZATION CRITERIA

Although the stress that appears in the rotor is relatively small, it is observed that there is a region where the allowable stress is exceeded (according to table 1 and fig. 2). Because the centrifugal force is directly proportional to the density, it is obvious that changing the material does not greatly alter the stress distribution. It is correct that the use of other material with better mechanical properties would lead to a better σ_A / σ_{\max} ratio but the use of the material is not fully exploited. In order to do so, two modifications can be made to the impeller: it can either be cut from the base of the rotor (which leads to a weight reduction) -fig.3a or a boss (protrusion) (fig. 3b and 3c) can be made in the area of high stress.

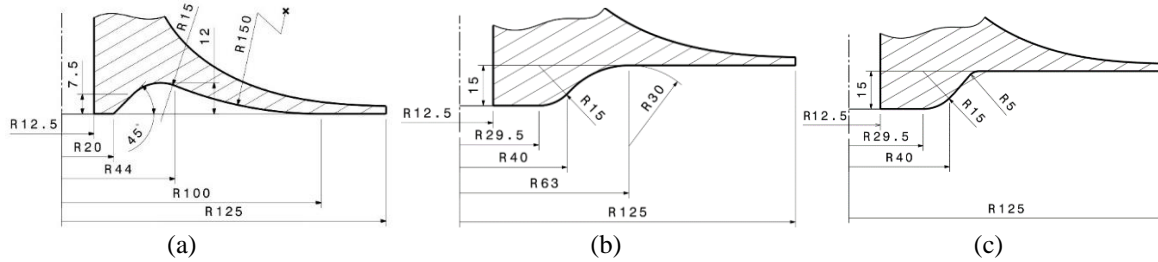


Fig.3. Modifications made to the impeller [1]

Applying cutting solution (a), the stress that appears in the bladed sector is shown in fig. 4.

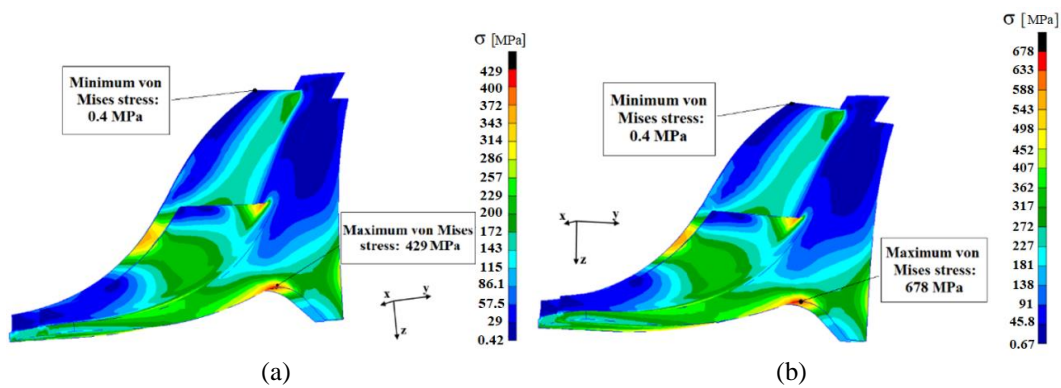


Fig.4. Impeller with cut base (a) Al7075 rotor stress, (b) Ti6Al4V rotor stress [1]

For the rotor made of aluminum alloy, a different distribution of material stress is observed compared to the initial geometry, but the maximum stress that appears is obviously above the creep limit. Changing the material for the same new geometry results in a σ_A / σ_{\max} ratio over 1 but this is not satisfactory.

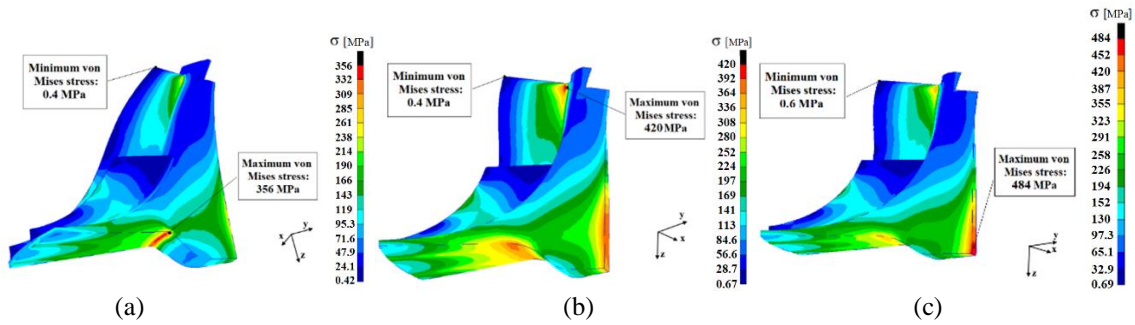


Fig.5. Impeller with boss (a) Al7075 ($R_1=5\text{mm}$) rotor stress, (b) Al7075 ($R_1=30\text{mm}$) rotor stress (c) Ti6Al4V ($R_1=30\text{mm}$) rotor stress [1]

On the one hand the alternative with the boss (fig. 5) is better than the one with the cut, in the case of aluminum alloy, on the other hand for the titanium alloy the results are very good but at the expense of increasing the weight of the rotor and the overall price.

Summarizing the obtained results, it is observed in table 3 that there are geometries that satisfy the resistance condition (safety coefficient > 1). In addition to the numerical results, the maximum stress resulting from the analytical calculation (table 2) was added by using the method of solving the differential equations (1) which is described in [7].

Table 2. Maximum stress in baseline rotor (finite element vs theoretical)

Geometry	σ_A [MPa]	analytical		finite element	
		σ_{\max} [MPa]	sc [-]	σ_{\max} [MPa]	sc [-]
Baseline Al alloy rotor	380	247.5	1.53	424	0.89
Baseline Ti alloy rotor	700	404.6	1.73	668	1.04

Table 3. Maximum stress in modified impeller

Geometry	σ_A [MPa]	σ_{\max} [MPa]	sc [-]	Rotor weight [kg]
Baseline Al alloy rotor	380	424	0.89	2.017
Baseline Ti alloy rotor	700	668	1.04	3.18
Al alloy cut impeller	380	429	0.88	1.878
Ti alloy cut rotor	700	678	1.03	2.961
Al alloy boss rotor ($R=5\text{mm}$)	380	356	1.06	2.45
Al alloy boss rotor ($R=30\text{mm}$)	380	420	0.9	2.45
Ti alloy boss rotor ($R=30\text{mm}$)	700	484	1.44	3.862

To verify that the most advantageous solution is fully usable, the radial and axial displacements for the model made of titanium alloy are shown in figure 6. The maximum radial displacement is observed to be about one tenth of a millimeter, which is a value in the usual range. The minimum axial displacement is (as expected) on the fixing surface with the nut and maximum in the area of minimum thickness (at the top of the blade).

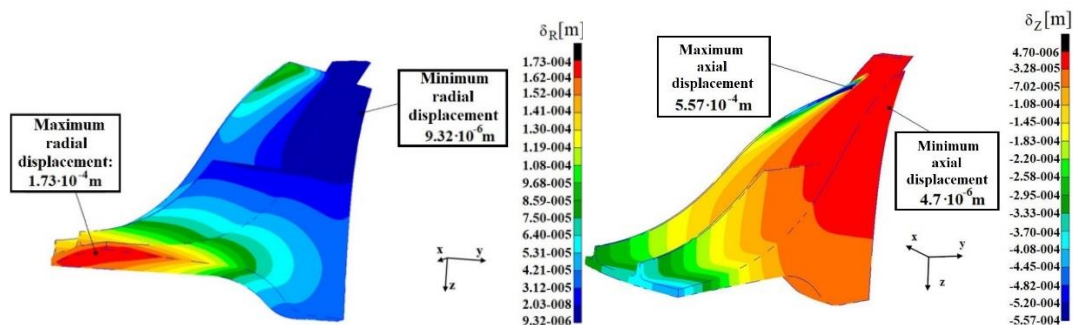


Fig.6. Displacement of the rotor in radial and axial direction

It is necessary to determine the static and dynamic frequencies because at certain rotor speeds it can happen that an excitation frequency equals the vibrational frequency of the rotor and the resonance phenomenon occurs. For the optimum solution of the rotor (the Ti rotor with the boss), the static and dynamic frequencies of the rotor were determined analytically (using relations (3) and (4)) and numerically (using FEA) and represented in Table 4. For the analytical determination of static frequencies, the model of the disc with a central hole, fixed at the center and free at the edges [7] was used, which corresponds to the boundary conditions imposed in the FEM analysis. Figure 7 shows the modes of vibration using the Lanczos method (with normalization parameter set for unit amplitude). The method uses eigenvalues so that the obtained values do not offer a quantitative value but a qualitative representation, because each eigenvector multiplied by a constant gives an eigenvector as well [10].

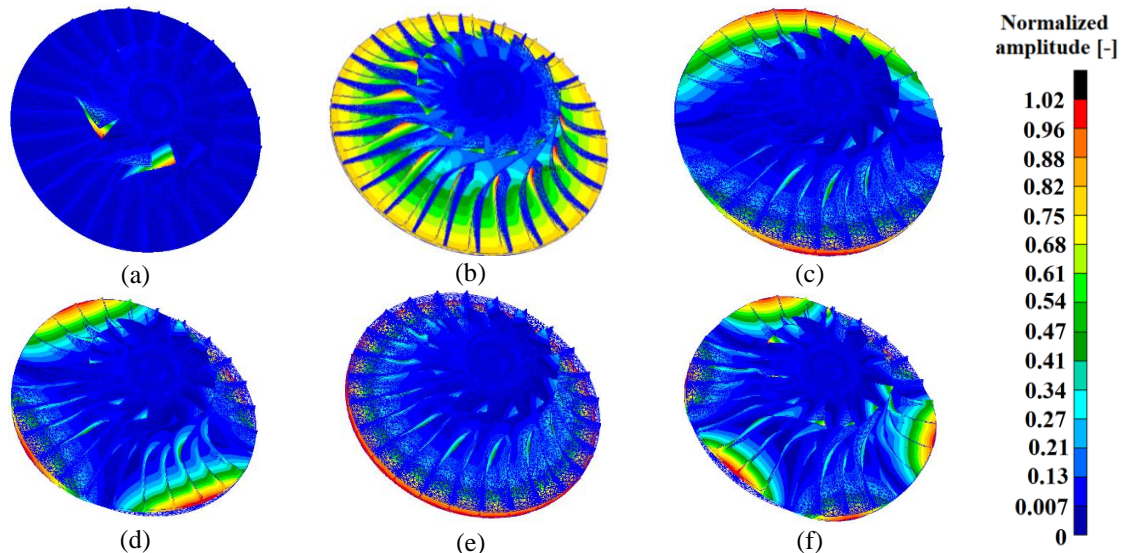


Fig.7. Impeller vibration modes (a) 1757.3Hz, (b) 3312.2Hz, (c) 3787.6Hz, (d) 3891.5Hz, (e) 3979.9Hz, (f) 4115.7Hz [1]

Table 4. Static frequencies analytically determined

Nodal circles	Nodal diameters			
	0	1	2	3
0	2997.2 Hz	3652.7 Hz	4308.1 Hz	9991.1 Hz
1	16745.1 Hz	16425.4 Hz	27895.2 Hz	42522 Hz

Table 5. Static and dynamic frequencies

Percentage of max rpm	Frequency [Hz]					
	Mode 1 (blades)	Mode 2.1 (disk torsion)	Mode 3 (first nodal diameter)	Mode 4 (second nodal diameter)	Mode 2.2 (zero nodal diameters)	Mode 5 (third nodal diameter)
0	1757.3	3312.2	3787.6	3891.5	3979.9	4115.7
50	1920.2	3347	3840.7	3960.9	4029.2	4205.9
100	2069.2	3381.5	3892.5	4028.6	4077.4	4293.7
110	2097.6	3388.3	3902.7	4041.9	4086.9	4311

In order to justify the need for vibration analysis, it is necessary to draw the frequency-rotational speed diagram (Campbell diagram) [12], [13]. By determining the excitation frequencies using the relation (6), where K represents the number of excitatory factors (number of mounting/stator blade or number of injectors from the combustion chamber), critical speeds can be determined and precautionary measures can be taken to avoid an operating regime with high vibration amplitudes, possibly long-term destructive. [7]

$$f_e = K \cdot n_s \tag{6}$$

Because the number of excitatory factors may vary, the usual values for microjet engines were chosen: 3 and 4 for stator blades and 5-7 for the number of injectors and the excitation frequencies determined using these values are represented in the Campbell diagram (Figure 8).

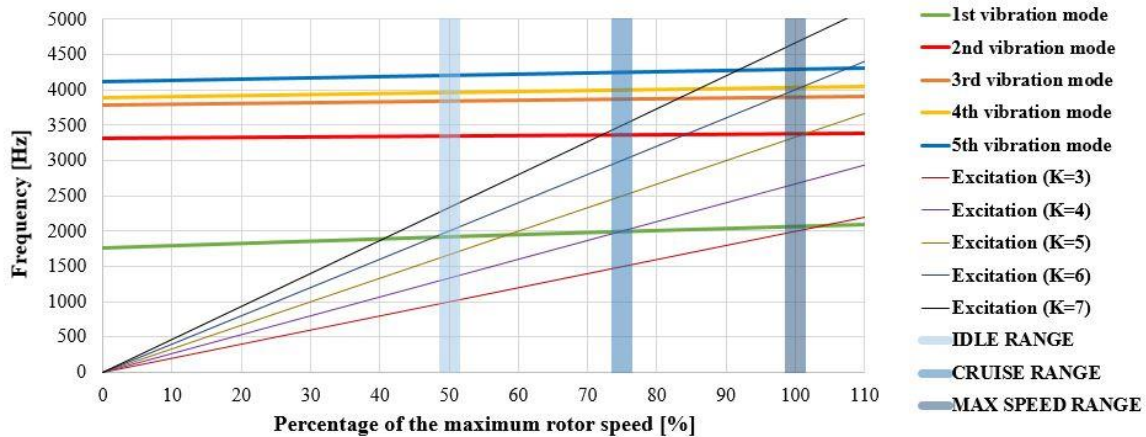


Fig.8. Campbell diagram

From the analysis of the diagram represented in figure 8 it can be concluded that, for the used compressor geometry, some of the critical speeds are found in the continuous operating range. For $K = 6$ there is a resonance in the idle domain and another one near the maximum regime, for $K = 4$ there is a resonance at the corresponding speed of 75% of the maximum speed and $K = 3$ and $K = 5$ are dangerously close to the maximum speed zone. It should be taken into account that when designing the whole engine assembly, using a number of elements corresponding to those previously mentioned must be avoided.

5. CONCLUSIONS

An optimization can be made regarding the centrifugal rotor by cutting the bottom of the impeller which leads to a 7% weight reduction compared to the full rotor and a more uniform distribution of high stress intensity but the maximum stress value remains close to the same value as that of the baseline. This procedure cannot be applied to all materials, observing the analyzed case that it is also necessary a material with special properties which leads to higher costs. The variant with boss is less beneficial in terms of weight but allows the use of materials with weaker mechanical properties. In the most favorable case (Ti alloy rotor), a maximum stress decrease of 27.5% was obtained for a weight gain of 21%. It was also observed that the simplified analytical calculation leads to an optimistic result (with high safety coefficients) but for the real case, with complicated geometry, leads to the appearance of areas that cannot be highlighted by the applied calculation procedure. It is obvious that the best solution for the current application was the one with the boss followed by the cutting solution and the baseline. A combination of the first two solutions will be analyzed in future work. Regarding vibration analysis, it was observed that a very small thickness of the blade root leads to the appearance of some vibration forms on the blade before the it appears on the disk. This should be avoided because the vibration of the blades at low frequencies, combined with their high flexibility can lead to quite large amplitudes that can favor material fatigue and cracks in the area of high material stress.

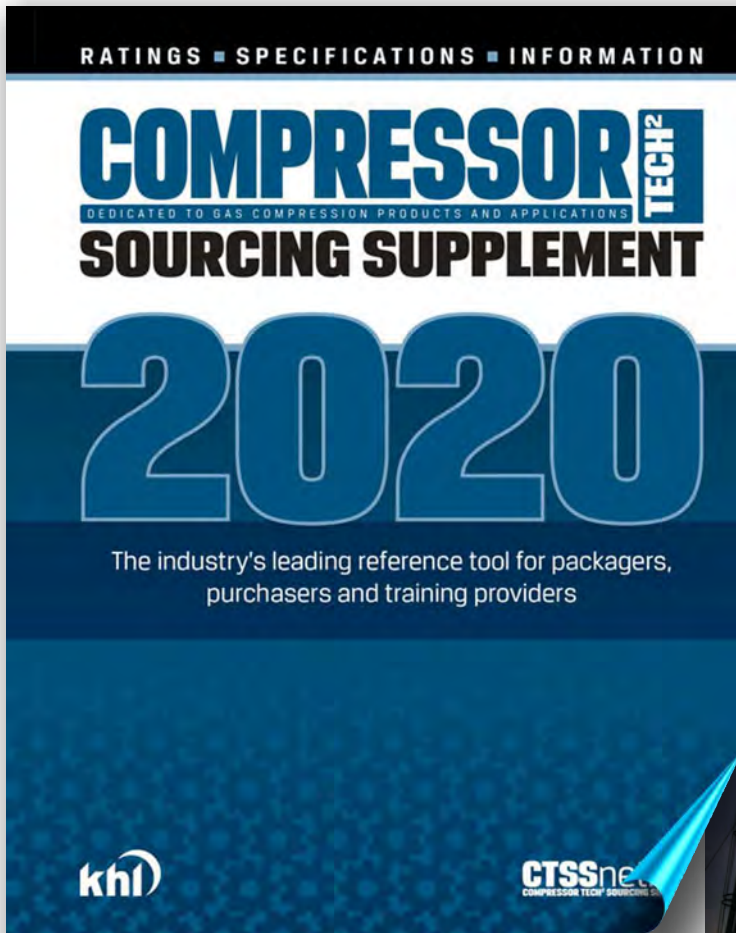
Future work will be focused on a parametric study on the influence of different material removal or addition at the bottom of the disk for different common materials used in centrifugal compressors along with a material fatigue analysis.

ACKNOWLEDGEMENT

This work represents a summary of the results obtained in the bachelor degree paper [1] of the main author, carried out under the coordination of a teaching staff within the UPB and support from COMOTI.

REFERENCES

- [1] Totu A.G.; 2019; “Calculul de rezistență și vibrații pentru un compresor centrifugal”, Bachelor Degree Paper, UPB
- [2] Drăgan V., Dumitrescu O., Malael I., Porumbel I., Gherman B., Pușcașu C. , “Turbulence model sensitivity on steady state mapping of a very high pressure ratio compressor stage”, ICNPAA 2018 World Congress, AIP Conf. Proc. 2046, 020024-1–020024-7; 2018; <https://doi.org/10.1063/1.5081544>
- [3] Cuciumița C. F., “Computation of Thermodynamic Cycle for Novel Detonation Aircraft Engine”, CEAS 2015 paper no. 180
- [4] Sorokes J. M., Kuzdzal M. J., “Centrifugal compressor evolution”, 2010, *Proceedings of the thirty-ninth turbomachinery symposium*
- [5] Sorokes J. M., “Selecting a Centrifugal Compressor”, June 2013, American Institute of Chemical Engineers (AIChE) and Dresser-Rand
- [6] Haupt U., Bammert K., Rautenberg M., “Blade Vibration on Centrifugal Compressors Blade Response to Different Excitation Conditions”, 1985, Institute of Turbomachinery, University of Hannover, Germany
- [7] Manole I., Crunțeanu D., “CALCULUL MOTOARELOR AEROREACTOARE”, 2016, Politehnica Press, ISBN 978-606-515-714-9
- [8] Presură A., “Stări de solicitare ce apar în structurile neconvenționale ale navelor cu dublu înveliș”, 2017, Teză de doctorat, Universitatea “Dunărea de Jos”, Galați
- [9] Băgnaru D. Gh., “Elemente de teoria elasticitatii și calculul placilor”, 2010, Editura SITECH, Craiova, ISBN 978-606-530-949-4
- [10] Bostic S.W., “Lanczos eigensolution method for high-performance computers”, 1991, NASA Technical Memorandum 1104108, <https://ntrs.nasa.gov/search.jsp?R=19910023212>
- [11] Zu-Qing Q., „Model order reduction techniques: with Applications in Finite Element Analysis”, 2004, ISBN 18-523-3807-5
- [12] Hassemann H., Hagelstein D., Rautenberg M., “Coupled Vibration of Unshrouded Centrifugal Compressor Impellers. Part I: Experimental Investigation”, 2000, International Journal of Rotating Machinery, Vol. 6, No. 2, pp. 101-113
- [13] Tamrakar R., Mittal N.D., “Campbell diagram analysis of open cracked rotor”, 2016, Engineering Solid Mechanics No. 4, pp. 159-166



The Compression Technology Sourcing Supplement (CTSS) is an annual comprehensive resource for comparative technical information on gas compressors, drivers and related machinery, systems and services.

Contents include:

- Basic machinery specification tables from all major machinery manufacturers.
- Selected excerpts from the Gas Processors Suppliers Association Engineering Data Book, 13th Ed. covering gas compression machinery fundamental principles, operation and applications.
- Manufacturer and vendor advertising sections offering additional product data, support information, ordering information and service capabilities.

The CTSS targets packagers, purchasers and training providers of gas compression products, technologies and systems. It includes ratings, specifications and editorial for all compressors and prime-movers. This information can also serve as a tutorial for anyone that needs information on the equipment found in a compressor package.

The markets covered in the CTSS include gas machinery used for onshore and offshore wellhead gas gathering, vapor recovery, natural gas transmission, gas storage, gas treatment, refineries and chemical and petrochemical plants. Service and support activities associated with gas handling machinery are also a part of the CTSS.

CTSSnet.net
 COMPRESSOR TECH² SOURCING SUPPLEMENT

COMOTI'S EXPERIENCE IN OIL AND GAS INDUSTRY EQUIPMENTS

NATURAL GAS COMPRESSION EQUIPMENTS
 using helical compression units (screw compressors).

NATURAL GAS AND AIR CENTRIFUGAL COMPRESSORS:

- natural gas compression installations equipped with supercharger set;
- electrical centrifugal gas compressors;
- electrically actuated air centrifugal compressors.

EXPANDERS
 for recovering the expansion energy of natural gas with production of electricity.

HIGH EFFICIENT GENERATION OF ELECTRIC AND THERMAL POWER WITH GAS TURBINES (CHP)
 by the implementation of the first co-generation power plants in Romania.

DESIGN, PRODUCTION, TESTING, AUTOMATION, MAINTENANCE, SERVICE, SPARE PARTS

COMOTI
 ROMANIAN RESEARCH & DEVELOPMENT INSTITUTE FOR GAS TURBINES

2200 Iuliu Maniu Ave., 061126 Bucharest 6, ROMANIA
 Phone: +40 21 434 01 98; +40 21 434 02 40
 Fax: +40 21 434 02 41
 e-mail: contact@comoti.ro
 www.comoti.ro



COMOTI - Romanian R&D Institute
 for Gas Turbines 87

2200 Iuliu Maniu Ave
 061126 Bucharest
 ROMANIA
 Phone: +4 021 434 02 40
 Fax: +4 021 434 02 41
 Email: contact@comoti.ro
 www.comoti.ro

Acoustical Pulsation Analysis
Bearings, Tilting Pad
Blades & Nozzles, Gas Turbines
Blowers
Compressor Condition Monitoring
Compressor Sets, Electrically Engine-Driven
Compressor Sets, Gas Turbine-Driven
Compressor Sets, Natural Gas Engine-Driven
Compressor Valve Condition Monitoring
Compressors, Air
Compressors, Centrifugal



The only specialized company that integrates
such activities as

scientific research,
design,
manufacturing,
testing,
experimental activities,
technologic transfer and
innovation

in the field of aircraft and industrial gas turbines and
high speed bladed machinery.

220D Iuliu Maniu Ave., 061206 Bucharest, ROMANIA,
P.O. 76, P.O.B. 174

Phone: (+4)021/434.01.98, (+4)021/434.02.31, (+4)021/434.02.40
Fax: (+4)021/434.02.41, e-mail: contact@comoti.ro

www.comoti.ro